

Copyright
by
Sean Patrick Carney
2020

The Dissertation Committee for Sean Patrick Carney
certifies that this is the approved version of the following dissertation:

**Numerical Multiscale Methods for Boundary Layer
Problems in Fluid Dynamics**

Committee:

Björn Engquist, Supervisor

Robert D. Moser

Yen-Hsi Tsai

Irene M. Gamba

Todd J. Arbogast

**Numerical Multiscale Methods for Boundary Layer
Problems in Fluid Dynamics**

by

Sean Patrick Carney

DISSERTATION

Presented to the Faculty of the Graduate School of
The University of Texas at Austin
in Partial Fulfillment
of the Requirements
for the Degree of

DOCTOR OF PHILOSOPHY

THE UNIVERSITY OF TEXAS AT AUSTIN

May 2020

Dedicated to all of the educators in my life.

Acknowledgments

Firstly, thank you to my parents, my very first educators, for their love and support throughout my life and in particular during my time as a graduate student. Thank you also to my family, including my brother, grandparents, cousins, and aunts and uncles, as well as my close friends for their love and support.

Thank you to my advisor, Björn Engquist, for his guidance throughout my time at UT Austin. I am truly grateful for his patience, sense of humor, and willingness to share his deep knowledge of applied and computational mathematics, science, and philosophy.

Thank you to Robert D. Moser for welcoming me into the PECOS group despite not being “officially” registered an advisor. I am grateful for our regular, weekly meetings during which I learned from his expertise in fluid dynamics, computational science, and multiscale modeling, and from his perspective on academic life.

Thank you also to Todd Arbogast, Irene Gamba, and Richard Tsai for serving on my doctoral committee. I appreciate the time they took to read this manuscript and offer suggestions for improvements.

Thank to Ann S. Almgren for welcoming me as a graduate research assistant at the Lawrence Berkeley National Lab’s Center for Computational

Science and Engineering for two summers in a row. Thank you also to John B. Bell for his mentorship during those two summers. I am thankful for the time he invested in my growth as a computational scientist. His patience and willingness to impart his knowledge in stochastic modeling, physics of fluids at the mesoscale, numerical PDE, and high-performance computing are truly appreciated.

Thank you to my teachers at Detroit Catholic Central High School for first kindling my intellectual curiosity in philosophy and physics, especially Mr. Robert Scheuermann, Mr. Jason Jones, and Mr. Neal Alpiner.

Thank you to all of my instructors in the physics and mathematics departments at the University of Michigan for their time and patience. Thank you to Dr.'s Vanessa Sih, Yuri Popov, Farkhod Eshmatov, Weiyi Zhang, Tim Chupp, Dante Amidei, Georg Raithel, Mark Newman, Charlie Doering, James Wells, and Joel Smoller for their excellent courses, and to Evelyn Lunasin, Henriette Elvang, Jean Krisch, Robert Deegan, and Stephen DeBacker for their instruction and especially their guidance as I navigated my undergraduate studies.

Thank you additionally to my fellow undergraduates at Michigan, including but not limited to, Kyle Gordon, Nick Kern, Alex Trujillo, Pavel Okun, Jenn Smith, Josh Schudel, and Mike Mills. Without your comaraderie, help and friendship I never would have survived my undergraduate studies.

Thank you also to Dr. Divakar Viswanath for the guidance and in-

struction, especially for helping me prepare a competitive graduate school application, helping me find a suitable REU summer program, and for introducing me to Bertrand Russell's philosophical writings. Without his aid I never would have ended up in a mathematics graduate program. Additionally, thank you to my undergraduate mentor Dr. Smadar Karni and her student Dr. David Prigge for their tireless efforts to introduce me to research in applied and computational mathematics. Without their kind patience, enthusiasm, and willingness to involve me in their clever problem solving, I never would have pursued further research opportunities.

Thank you to all my instructors at UT, especially Hans Koch, Alexis Vasseur, Gordan Žitković, Arie Israel, Mihai Sîrbu, Thaleia Zariphopoulou and Rachel Ward for their time and effort. Thank you also to Sandra Catlett, Elisa Bass, Jenny Kondo, as well as Dan Knopf, Kui Ren, Thomas Chen, and Tim Perutz for their help and support as I navigated life as a graduate student.

Thank you to my elder academic siblings Christina Frederick, Yoon-sang Lee, and Yunan Yang for their friendship and perspective throughout my time in graduate school. Thank you also to Myoungkyu Lee for his gracious help with installing and modifying the PoongBack code on multiple machines, and for his sharing of post-processing Python scripts and LaTeX source code. Without his patience and tolerance for my often foolish questions, I would have never been able to make progress in my research.

I am especially grateful to my fellow graduate students in the fall 2014 cohort—Martin Bobb, Natasa Dragovic, Abe Frei-Pearson, Spencer Johnson,

Dan Kubala, Jonathan Lai, Frank Lin, Zhao Liu, Clark Pennie, Isabelle Scott, Logan Stokols, Yuri Sulyma, Anna Szczekutowicz, Milica Taskovic Dussinger, Xiaoxia Wu, Yijing Wu, Chuwei Zhang, and Xikai Zhao— for their comaraderie, support in the prelim courses and exams, and help making Austin a home for the past six years. Thank you also to my officemates Will Carlson and especially to Andy Ma for their companionship and discussions about mathematics, sports, and life. Thanks also to Henry Cappel, Simon D’alton, Michael Hott, Joe Jackson, Eric Korman, JR Lagade, Andrew Lee, Allison Miller, Christine Ngan, Matt Novack, Tynan Ochse, Eddie Tiernan, Mike Wade, and Billy Warner for sharing with me their support, friendship, and love of basketball.

Thank you to the my friends and fellow graduate students in the CSEM program. To Prakash Mohan and Gopal Yalla I am extremely grateful for the time spent traveling together to the APS DFD conferences and comaraderie while navigating the landscape of turbulence research. Thank you also to Max Bremer, Sam Estes, Tyler Masthay, Clark Pederson, Teresa Portone, Bryan Reuter, Tim Smith, Sid Wahhal, Anna Yespenko for their friendship and help sharpening my skills in computational science.

Lastly, thank you to my fellow graduate research assistants at the CCSE over the past two summers, especially David Akinyemi, Kevin Luna, Yuexia Luna Lin, Guy Moore, Matea Santiago, and Jack Wakefield. Thank you also to researchers Daniel Ladiges, Katherine Klymko and Tess Smidt, and especially to Andy Nonaka and Alejandro Garcia for making my time in the Bay area productive and enjoyable.

Numerical Multiscale Methods for Boundary Layer Problems in Fluid Dynamics

Sean Patrick Carney, Ph.D.

The University of Texas at Austin, 2020

Supervisor: Björn Engquist

Physical processes typically occur over a wide range of scales in space and time. In many instances it is computationally preferable to couple models with differing levels of physical description for different portions of the domain in space and/or time. Such multiscale, hybrid strategies allow for an accurate representation of important physical phenomena where necessary while ensuring a feasible overall computational cost. In general, every multiphysics problem is different, and for every coupling strategy there are nontrivial mathematical and algorithmic details that must be worked out. However, many problems share similar features, for instance, asymptotically thin boundary layers and nonlinear interactions across scales, and sometimes strategies developed for one problem can be successfully applied to a related, but different area.

This thesis develops numerical strategies for the accurate and efficient simulation of multiscale, boundary layer problems arising in fluid dynamics.

Considered are four different physical models, namely viscous laminar flow over a rough surface, high Reynolds number wall-bounded turbulent flow, electrokinetic flows over charge-conducting surfaces, and upscaling in porous media flow. The first three of these situations typically involve asymptotically small, physical boundary layers while the fourth can involve computational boundary layers as a result of modeling artifacts.

The numerical strategies are presented in the context of the heterogeneous multiscale method (HMM), which generally involves coupling a coarse-scale, macroscopic solver for bulk dynamics to a fine-scale, microscopic solver for the small and/or fast scales in space and/or time. The first section contains a coupled method for rough-wall laminar flow. The second describes a reduced-order, microscale model for the near-wall eddies present in high Reynolds number wall bounded turbulence. The third section concerns the application of stochastic, multiscale partial differential equation model known as Fluctuating Hydrodynamics to the mesoscale dynamics of electrokinetic flows. Finally, the fourth contains a method for reducing the nonphysical, boundary or “resonance” error term that arises in the numerical homogenization of multiscale elliptic operators as in, for example, the modeling of porous media flows or steady state heat conduction.

All sections contain a description of and motivations for the problem, numerical examples of the model presented, and a discussion of future research and open problems to be addressed.

Table of Contents

Acknowledgments	v
Abstract	ix
List of Tables	xv
List of Figures	xvi
Chapter 1. Introduction	1
1.1 Multiscale Problems	1
1.2 Multiscale Modeling	3
1.2.1 Multiscale methods	4
1.3 Heterogeneous Multiscale Methods	5
1.4 Summary of Research Work and Outline of Dissertation	7
1.4.1 Rough-wall laminar flow	8
1.4.2 Wall-bounded, incompressible turbulent flows	9
1.4.3 Electrokinetic flows	11
1.4.4 Cell resonance error in numerical homogenization	12
Chapter 2. Viscous Laminar Flow Over Rough Surfaces	13
2.1 Introduction	13
2.2 Homogenization Theory for Laminar Flow Over Rough Surfaces	16
2.2.1 Preliminary definitions	17
2.2.2 Asymptotic analysis	18
2.3 Heterogeneous Multiscale Method for Laminar Flow Over a Rough Surface	26
2.3.1 Multiscale flow model	27
2.3.2 Algorithm for the coupled system	31
2.3.3 Boundary conditions for the microscopic systems	33

2.3.4	Convergence theory for domains with periodic roughness	35
2.4	Numerical Results	39
2.4.1	Flow in a channel with periodic roughness	42
2.4.2	Nonsquare domain with periodic roughness	43
2.4.3	Flow in a channel with non-periodic roughness	49
2.4.4	Flow in a channel with quasi-periodic roughness	50
2.4.5	Flow over a backwards facing step	53
Chapter 3.	Wall Bounded Turbulent Viscous Flow	59
3.1	Introduction to Wall Bounded Turbulence	59
3.2	Multiscale Strategies for Wall Bounded Turbulence	62
3.3	Near Wall Patch (NWP) Microscale Model	65
3.3.1	Notation	65
3.3.2	Motivation: computational boundaries	66
3.3.3	Mathematical formulation	67
3.3.4	Physical parameters	70
3.3.5	Computational parameters	73
3.3.6	Numerical implementation and resolution	74
3.3.7	Statistical convergence	75
3.4	Numerical Results	75
3.4.1	Mean velocity and shear stresses	76
3.4.2	Energy spectral density	79
3.4.3	Universality of small scales	86
3.4.4	Production	90
3.4.5	Dissipation, pressure strain and transport	91
3.5	NWP Discussion	93
3.5.1	Summary: modeling assumptions and limitations	93
3.5.2	Potential future work: model applications	95
3.5.3	Boundary layer growth: adverse pressure gradients	97
3.6	Slow-Grow NWP	103
3.6.1	Introduction & modeling assumptions	103
3.6.2	Multiscale asymptotic analysis	104
3.6.3	Slow-growth model equations of motion	108
3.6.4	Velocity-vorticity formulation	111

Chapter 4. Electrokinetic Flows	117
4.1 Multiscale Nature of Electrolyte Solutions	117
4.2 Macroscopic Continuum Model for Electrolytes	119
4.2.1 Electro-osmosis (EO)	121
4.2.2 Induced-charge electro-osmosis	126
4.2.3 Thermal fluctuations in nonequilibrium systems, stochastic PDEs, and Fluctuating Hydrodynamics	128
4.2.4 Fundamental electrolyte scaling: breakdown of continuum model at walls	135
4.3 Hybrid Particle-Continuum Stochastic Electrolyte Model	137
4.3.1 Model equations	138
4.3.2 Particle-particle, particle-mesh (P3M) description	142
4.3.3 Temporal integration	150
4.3.4 Numerical results	154
4.4 Discussion: Potential Multiscale Modeling for Wall Bounded Electrokinetic Flows	159
4.5 Room Temperature Ionic Liquids (RTILs)	162
4.6 Low Mach Number Fluctuating Hydrodynamics Model for RTILs	166
4.6.1 Formulation	166
4.6.2 Derivation of reversible stress term	170
4.6.3 Numerical methods	175
4.6.4 Spatial Discretization	175
4.6.5 Temporal Discretization	179
4.7 RTIL Simulation Results	181
4.7.1 Parameter Calibration	181
4.7.2 Bulk morphology	184
4.7.3 Double Layer Capacitance	189
4.7.4 Electroosmotic shear flow	194
4.7.5 Discussion	196

Chapter 5. Reduction of the cell resonance error in numerical homogenization	200
5.1 Introduction	200
5.2 Averaging Kernels	205
5.3 Reduction of the Cell Resonance Error: $d = 1$	210
5.3.1 Numerical strategy, $d = 1$	215
5.4 Numerical Results, $d = 1$	215
5.5 Numerical Strategy, $d \geq 2$	220
5.6 Computational Cost and Discussion	222
Bibliography	225

List of Tables

3.1	Prescribed mean pressure gradient and the resulting total momentum flux τ_{tot} at $y = L_y$ for the three model cases presented. The favorable pressure gradient parameters were selected to match the channel data posted to https://turbulence.oden.utexas.edu/ . 72	
3.2	Summary of simulation parameters consistent for all simulation cases; ψ is the prescribed value for the Neumann boundary condition in (3.1). N_x and N_z refer to the number of Fourier modes, while N_y is the number of B-spline collocation points. $\Delta x = L_x/N_x$ and similarly for Δz . Δy_w is the collocation point spacing at the wall.	75
3.3	Input parameters for an application of the NWP model to an APG flow are shown in the column NWP- β 1 and compared to the previous values for the cases presented in section 3.4.	100
4.1	RTIL properties of [DMPI+][F6P-] at standard conditions from NIST database https://ilthermo.boulder.nist.gov/ ; ion diffusion coefficients from [89, 213]	182
4.2	Parameters used in the simulation	182
4.3	The radius corresponding to the maximum value of the structure factor, k_r , and the associated pattern feature scale, $\ell = \pi/k_r$ as a function of κ	189
5.1	Comparison of the computational cost associated to reducing the cell resonance error below some fixed tolerance for some of the microscale problems proposed in the literature. Here the decay rate $s = \min\{p+1, q+2\}$ for averaging kernel $K \in \mathbb{K}^{-p,q}$ is assumed to generalize for the case $d \geq 2$ in the present work. The averaging kernels in the hyperbolic solver from [14] are defined slightly differently than those in the present work, but the meaning of q is identical.	224

List of Figures

2.1	Semi-infinite domain Y with boundary $\partial Y = \{y \in \mathbb{R}^2 y_2 = \varphi(y_1)\}$ for some periodic function φ	17
2.2	Domain Ω^ϵ with periodic, sinusoidal roughness modulated by a smooth function.	17
2.3	(a) Example domain Ω^ϵ (....) containing several Ω_j^{mic} (—). (b) One instance of a micro domain Ω_j^{mic}	27
2.4	Sketches of the rough domains used to test the numerical method.	41
2.5	Horizontal component of the flow u_1 versus x_1 plotted at various heights x_2 for the domain shown in 2.4a.	43
2.6	Shear $\partial u_1 / \partial x_2$ versus x_1 plotted at various heights x_2 for the domain shown in 2.4a.	44
2.7	Horizontal component of the flow u_1 versus x_1 plotted at various heights x_2 for the domain shown in 2.4b.	46
2.8	Vertical component of the flow u_2 versus x_1 plotted at various heights x_2 for the domain shown in 2.4b.	47
2.9	Shear $\partial u_1 / \partial x_2$ versus x_1 plotted at various heights x_2 for the domain shown in 2.4b.	48
2.10	Horizontal component of the flow u_1 versus x_1 plotted at various heights x_2 for the domain shown in 2.4c.	50
2.11	Shear $\partial u_1 / \partial x_2$ versus x_1 plotted at various heights x_2 for the domain shown in 2.4c.	51
2.12	Horizontal component of the flow u_1 versus x_1 plotted at various heights x_2 for the domain shown in 2.4d.	53
2.13	Shear $\partial u_1 / \partial x_2$ versus x_1 plotted at various heights x_2 for the domain shown in 2.4d.	54
2.14	Horizontal component of the flow u_1 versus x_1 plotted at the values $x_2 = \epsilon/4, \epsilon/2, \epsilon, 2\epsilon, 4\epsilon, 0.55$ for the domain shown in 2.4e.	57
2.15	Shear $\partial u_1 / \partial x_2$ versus x_1 plotted at the values $x_2 = \epsilon/2, \epsilon, 2\epsilon, 4\epsilon, 0.55$ for the domain shown in 2.4e.	58

3.1	Unfiltered, high-pass (SS), and low pass (LS) portion of the turbulent kinetic energy scaled in viscous units with $k_{\text{cut}}\delta_\nu = 0.00628$ ($\lambda_{\text{cut}}/\delta_\nu = 1000$) for a channel flow at various Re_τ (green: $Re_\tau = 550$, blue: $Re_\tau = 1000$, red: $Re_\tau = 2000$, black: $Re_\tau = 5200$). The contributions from the large scales increases with Re_τ , but the contribution from the small scales is largely independent of Re_τ . Figure reproduced from [143] with permission.	61
3.2	For some fixed outer length scale of interest δ , the physical size of the near wall patch shrinks as Re_τ increases ($Re_\tau^1 < Re_\tau^2$). Here δ could represent, for instance, the characteristic size of the computational domain of a large eddy simulation.	62
3.3	The fluid is subject to periodic boundary conditions at the (dash-dotted) side walls, constant Dirichlet/Neumann conditions at the upper boundary $y = 2H$, and the no-slip condition at the wall $y = 0$, as described in (3.1). In addition to the constant pressure gradient assumed to be present in the near wall layer, the model includes an auxiliary pressure gradient in a “fringe region” to account for momentum transport at the computational boundary $y = 2H$	68
3.4	Blue: model total stress $\tau_{\text{model}}^+(y^+) = \partial U^+ / \partial y^+ - \langle u'v' \rangle^+$; Red: target total stress $\tau_{\text{target}}^+ = 1 + y^+ dP^+ / dx^+$; Green: Primitive $F^+(y^+)$ of forcing function f^+ ; Black: $\tau_{\text{model}}^+(y^+) + F^+(y^+)$; Cyan: total stress for a simulation <i>without</i> the forcing function f^+ ; for all the three model cases listed in table 3.1.	72
3.5	Statistical convergence for the model cases listed in table 3.2–solid lines: Absolute error $ \tau_{\text{model}}^+(y^+) - \tau_{\text{target}}(y^+) $, where $\tau_{\text{model}}^+ = \partial U^+ / \partial y^+ - \langle u'v' \rangle^+$ and $\tau_{\text{target}}^+ = 1 + y^+ dP^+ / dx^+$; dashed lines: Standard deviation of the estimated statistical error for τ_{model}^+ in the region $y^+ \in [0, 300]$	76
3.6	Mean velocity U^+ (left) and the indicator function $\beta^+ = y^+ \partial_{y^+} U^+$ (right) versus $\log(y^+)$. The black dashed-dotted vertical line marks $y^+ = 300$, and the red dashed-dotted lines plot the law-of-the-wall $U^+ = y^+$ and $U^+ = (1/\kappa) \log(y^+) + B$, where $\kappa = 0.384$ and $B = 4.27$ [141].	77
3.7	(a) Reynolds stress $-\langle u'v' \rangle^+$ and (b) the filtered Reynolds stress $-\langle u'v' \rangle_{SS}^+$ (defined by (3.18)) as a function of $\log(y^+)$, discussed in section 3.4.3. The black dashed-dotted vertical line marks $y^+ = 300$	78
3.8	Comparison of log-polar and “log-Cartesian” coordinates. Figure reproduced from Lee and Moser [143] with permission.	81

3.9	Two-dimensional spectra of the streamwise velocity variance $\langle u'u' \rangle^+$ in log-polar coordinates, as defined by equation (3.14). $\lambda^+ = 10$ on the outermost dotted circle and increases by a factor of 10 for each dotted circle moving inward.	82
3.10	Two-dimensional spectra of the wall-normal velocity variance $\langle v'v' \rangle^+$ in log-polar coordinates, as defined by equation (3.14). $\lambda^+ = 10$ on the outermost dotted circle and increases by a factor of 10 for each dotted circle moving inward.	83
3.11	(Left) The shaded gray region indicates the subset (in the first quadrant) of wavespace \mathcal{K}_{SS} defined by (3.15). (Right) the corresponding region defined instead by the circular, L^2 filter (3.16) used in [143].	87
3.12	Velocity variances $\langle u'_\alpha u'_\alpha \rangle^+$ (top) and the corresponding high-pass filtered quantities $\langle u'_\alpha u'_\alpha \rangle_{SS}^+$ (bottom) as a function of $\log(y^+)$	88
3.13	Two-dimensional, premultiplied spectra $y^+(E_{11}^\varphi)^+$ in log-polar coordinates, as defined by equation (3.14). $\lambda^+ = 10$ on the outermost dotted circle and increases by a factor of 10 for each dotted circle moving inward.	92
3.14	Profiles of the premultiplied $\langle u'u' \rangle$ production \mathcal{P}_{11}^+ versus $\log(y^+)$ in the region $y^+ \in [0, 300]$	93
3.15	Profiles of $\langle u'^2 \rangle$, $\langle v'^2 \rangle$, and $\langle w'^2 \rangle$ dissipation as log densities.	94
3.16	Mean velocity U^+ (left) and the indicator function $y^+ \partial_{y^+} U^+$ (middle) versus $\log(y^+)$, and total stress τ_{tot}^+ (right) versus y^+ . The black dashed-dotted vertical line marks $y^+ = 300$	101
3.17	Reynolds stress profiles versus $\log(y^+)$. The black dashed-dotted vertical line marks $y^+ = 300$	102
3.18	Mean stress budget for the $\beta = 1$ APG DNS of Kitsios et al. [127]. The linear, black curve is the sum of all the terms.	110
4.1	Cartoon description of electro-osmosis; image borrowed from [211].	122
4.2	Electro-osmotic plug flow velocity profile u is proportional to the electric potential $\Phi - \Phi_{wall}$ as in equation (4.11). Here E_0 is the external electric field strength, and μ is the fluid viscosity.	125
4.3	Cartoon description of induced charge electro-osmosis; image borrowed from [205].	127
4.4	Alternating current ICEO.	129

4.5	2D illustration courtesy of Daniel Ladiges (LBNL) of the discretization of the $\nabla \cdot \mathcal{W}^s$ term from equation (4.30). Random numbers Z are generated at the faces of control volumes around the points where velocities u are defined so that the divergence may be calculated.	153
4.6	Radial distribution for a molarity of 0.1M. The upper plot shows the pair correlation for ions of like charge, also indicated is the Debye length. The lower plot shows the pair correlation for ions of opposite charge. The solid line shows the approximate analytical solution given by (4.96), the squares show the numerical result from the SHIBA mode. These results were collected using a bin width of 0.025 nm, with a sample size of 50,000—the simulation was run for 100,000 steps, with the first 50,000 steps used for equilibration. Note that some points have been omitted for visual clarity. The grid size was set such that the total diffusion of species α was 14.7% wet and 85.3% dry, and for species β , 12.9% wet and 87.1% dry. This corresponds to $\Delta r = 1\text{nm}$, with a $32 \times 32 \times 32$ cell periodic domain.	157
4.7	Radial distribution for a molarity of 1.0M. The upper plot shows the pair correlation for ions of like charge, also indicated is the Debye length. The lower plot shows the pair correlation for ions of opposite charge. The solid line shows the approximate analytical solution given by (4.96), the boxes and circles show numerical result from the SHIBA model. The numerical parameters are the same as those described for figure 4.6, except that two different grid resolutions are shown. The red circles show the case where the grid size was set such that the total diffusion of species α was 14.7% wet and 85.3% dry, and for species β , 12.9% wet and 87.1% dry. This corresponds to $\Delta r = 1\text{nm}$, with a $16 \times 16 \times 16$ cell periodic domain. The black squares show the case for which the grid size was set such that the total diffusion of species α was 58.9% wet and 41.1% dry, and for species β , 51.8% wet and 41.2% dry. This corresponds to $\Delta r = 0.25\text{nm}$, with a $32 \times 32 \times 23$ cell periodic domain.	158
4.8	Cartoon depiction of proposed heterogeneous multiscale model for a channel configuration.	161
4.9	Time evolution of cation concentration profiles illustrating structural pattern formation at $t = 1, 2, 5$, and 10 ns for $\kappa = 1 \times 10^{-11}\text{ cm}^{-2}$. All figures in this paper use the same colorbar unless otherwise noted.	185
4.10	Time evolution of pattern formation as in Figure 4.9 with uncharged species ($z = 0$) at $t = 1, 2, 5$, and 10 ns . In this case the regions will continue to coarsen.	185

4.11	Cation concentration profiles from three-dimensional simulations (interior cut-out image). The left panel shows the stable pattern ($t = 10$ ns) reached by the RTIL; compare with the last frame in Figure 4.9. The other two panels show the evolution of pattern formation of the cation concentration in three dimensions for the uncharged case at $t = 2$ ns and $t = 5$ ns; compare with the second and third frames in Figure 4.10.	186
4.12	Cation concentration profiles illustrating spinodal decomposition for the $t = 50$ ns configuration for $\kappa = 0.5, 1.5, 2.0$, and $2.5 \times 10^{-11} \text{ cm}^{-2}$, respectively. Compare to final image in Figure 4.9. We note that the colorbar for the $\kappa = 2.5 \times 10^{-11} \text{ cm}^{-2}$ case only has been changed to range from 0.4 to 0.6 in order to see the structure.	187
4.13	Structure factor in logscale for the cation concentration, $S(\mathbf{k})$ for $\kappa = 1 \times 10^{-11} \text{ cm}^{-2}$ (left) and $\kappa = 2 \times 10^{-11} \text{ cm}^{-2}$ (right). The radius of the ring, k_r , is inversely proportional to the morphological feature size as $\ell \sim \pi/k_r$. The anisotropic ring in the right panel is consistent with the striped features favoring a single orientation in physical space, as seen in the third panel in Figure 4.12.	188
4.14	Cation concentrations for capacitance simulations. Electrode wall voltages (top and bottom) are $\pm 2, 8, 32$, and 128 V.	191
4.15	Horizontally-averaged potential for the capacitance cases in Figure 4.14.	192
4.16	Differential capacitance as a function of electrode potential compared to theory (4.179).	193
4.17	Cation concentrations for ± 8 V capacitance simulations. (Left) Stochastic simulation, (Middle) deterministic simulation with an initial stochastic perturbation, and (Right) purely deterministic simulation.	194
4.18	Horizontally-averaged potential for the cases in Figure 4.17. The perturbed deterministic case has a large amplitude near the walls due to the horizontal striping, but the same wavelength as the stochastic case. The purely deterministic case has striping features with smaller wavelength.	195
4.19	Time evolution of the cation concentration in the RTIL under electroosmotic shear; images are at $t = 0, 2, 5$, and 20 ns.	196
5.1	Results for $a^\epsilon(x) = 1.1 + \cos(2\pi x/\epsilon)$. (Blue) $K \in \mathbb{K}^{-2,2}$; (Green) $K \in \mathbb{K}^{-2,3}$; (Red) $\mathcal{O}(\epsilon/\eta)$; (Magenta) $\mathcal{O}(\epsilon/\eta)^5$	217

5.2	Results for the discontinuous, oscillatory step-function $a^\epsilon(x) = 3\chi_{[0,\epsilon/2)}(x) + 4\chi_{[\epsilon/2,\epsilon)}(x)$, periodically extended to \mathbb{R} . (Yellow) $K \in \mathbb{K}^{-1,1}$; (Blue) $K \in \mathbb{K}^{-1,2}$; (Green) $K \in \mathbb{K}^{-1,3}$; (Red) $\mathcal{O}(\epsilon/\eta)$; (Magenta) $\mathcal{O}(\epsilon/\eta)^2$	218
5.3	Results for the quasi-periodic oscillatory function $a^\epsilon(x) = (2.2 + \sin(2\pi x/\epsilon) + \sin(\sqrt{2} 2\pi x/\epsilon))^{-1}$. (Blue) $K \in \mathbb{K}^{-2,1}$; (Green) $K \in \mathbb{K}^{-2,2}$; (Red) $\mathcal{O}(\epsilon/\eta)$; (Magenta) $\mathcal{O}(\epsilon/\eta)^4$	218
5.4	Absolute values of various smoothing kernels shown on a log-scale as a function of $x \in [1, 2]$. (Green) $K \in \mathbb{K}^{0,1}$; (Red) $K \in \mathbb{K}^{-2,2}$; (Blue) $K \in \mathbb{K}^{-1,3}$; (Magenta) $K \in \mathbb{K}^{-7,7}$. The local extrema of K grow as a function of (p, q) .	219
5.5	Results for $a^\epsilon(x) = 1.1 + \cos(2\pi x/\epsilon)$. (Blue) $K \in \mathbb{K}^{-7,7}$; (Red) $\mathcal{O}(\epsilon/\eta)$; (Magenta) $\mathcal{O}(\epsilon/\eta)^9$	219

Chapter 1

Introduction

1.1 Multiscale Problems

Physical models in the mathematical sciences are typically derived for and applied to a problem with some set of length and time scales. For example, Einstein’s theory of general relativity describes systems of enormously massive objects over astronomically large distances. The theory of quantum mechanics has proven to be an incredibly successful model for physical systems at minuscule, atomic length scales. At more intermediate, “everyday” length scales, Newton’s laws of motion apply to a wide variety of problems in science and engineering.

Generally speaking, macroscopic models have a limited range of applicability, and outside of that range they are inaccurate. For example, Newtonian mechanics cannot describe how a laser works, which instead requires the laws of quantum mechanics. In contrast, microscopic models can in principle be accurately applied to a wider variety of systems, but it oftentimes is difficult to extract from them useful information or predictions.

It is sometimes sensible to ignore the fine-scale features in some description of a physical system. For example, in a cup of water sitting stationary

on a table, we know that at microscopic scales the liquid is composed of molecules that are in constant motion, bombarding one another at a rate that depends on the liquid's temperature. Those details are totally irrelevant at the macroscale, however; their collective, average motion simply amounts to a liquid that just sits there until further disturbed. More practically, the mean motion of a large hurricane occurs over hundreds of miles, and in storm forecasting it is of course more important to know approximately where a hurricane will hit land than the precise direction and strength of the wind on any particular city block.

There are many situations, however, in which the dynamics of physical processes that occur at small length and rapid time scales directly impact the dynamics of a process evolving over much larger and slower scales in space and time, respectively. For example, the mechanics of cracks and fractures in solid materials depend on the breaking of chemical bonds at molecular length scales. Another example is the phenomenon of fluid turbulence, which was famously first depicted by Leonardo da Vinci and can be observed in the chaotic motion of river rapids, the vortical twirls of a tornado, and the intricate storm patterns visible in the gas giant Jupiter. In aerodynamics, the forces of drag and lift on an aircraft depend crucially on the dynamics of vortical motions in a thin region near the aircraft's body whose size is on the order of millimeters in thickness.

Problems that contain a large separation of dynamically relevant scales are challenging for modeling, analysis, and numerical simulation. Applying

a high-fidelity model is often infeasible, as the computational power required for a full description of the problem can exceed that which even the world’s largest and most powerful supercomputers can offer. In contrast, macroscale models are more computationally feasible; oftentimes, however, they are unsatisfactory because of their failure to account for the effect of the smallest and fastest scales in the problem. Multiscale modeling then is an attempt to arrive at a compromise between these two approaches by combining the speed and efficiency of macroscale models with the accuracy of microscale models.

1.2 Multiscale Modeling

Multiscale mathematical models typically take one of two forms. As defined in E’s text [70], the first is a Type A problem where local defects or singularities, such as boundary layers or discontinuities, are isolated or contained to some small region of a spacetime domain. In this case, a macroscale model is sufficient for the majority of the domain, and a microscale model is only necessary near the local defects. The second is a Type B problem in which a microscale problem is needed throughout a domain in order to supplement or replace entirely some aspect of macroscale model. In both settings, a crucial issue to address is the precise way in which the macro and microscale models are coupled. A principal challenge in multiscale modeling is to sort out the precise mathematical and algorithmic details for a given coupling strategy.

Coupling strategies are typically implemented either concurrently or sequentially. The former approach obtains missing information in the macro

and microscale models “on the fly” as a computation proceeds, as is done in Car-Parrinello molecular dynamics [39]. The latter approach consists of precomputing information to be passed from the macro to microscale model, or vice-versa, and it is sometimes referred to as parameter passing. The choice for one approach or the other depends on accuracy and efficiency, and typically it is informed by how much is known about the physics of the macroscale dynamics.

1.2.1 Multiscale methods

Some classical examples of multiscale analytic methods are the method of matched asymptotic (or perturbative) expansions, averaging and homogenization theory for ordinary and partial differential equations, respectively, and renormalization group techniques. At their core, both Fourier and wavelet analysis are also multiscale techniques that decompose functions or signals at different scales.

On the computational side, classical multiscale techniques include multigrid methods, adaptive mesh refinement algorithms, domain decomposition methods, fast Fourier and wavelet transforms, fast multipole methods, the method of Ewald summation, and particle-particle, particle-mesh methods.

Some examples of methods specifically designed for problems with multiple scales include the multiscale finite element method of Hou et al. [72], the previously mentioned method of Car-Parrinello molecular dynamics, the quasicontinuum method developed by Ortiz and collaborators [209], and the

equation-free technique due to Kevrekidis et al. [121]. There are of course many, many other examples, and a much more thorough survey can be found in E’s book [70] and references therein.

1.3 Heterogeneous Multiscale Methods

In addition to the methods mentioned above, the heterogeneous multiscale method (HMM) is a general framework for designing multiscale algorithms that aims to capture the macroscopic behavior of a system without resolving the microscopic details in their entirety. It is the framework through which much of the work in this dissertation will be presented; hence we describe it in some detail below, noting however that comprehensive introductions to and reviews of HMM can be found in [6, 68, 69]

Under the assumption of scale separation in the underlying physical system, HMM couples macroscopic simulations to local, microscopic simulations so that the simulation has an overall computational complexity independent of the fine scale. Suppose there is a general model for the macroscopic state of a physical system that can be expressed as $M(\Psi, D) = 0$, where D represents the macroscopic data necessary for the model to be complete. Then the main goal of HMM is to approximate D by solving microscale problems locally in space and/or time that are constrained by the macroscopic solution. If the microscale problem is denoted by $m(\psi, d) = 0$, where the data d represents the input from the macroscopic system, then the HMM can be succinctly expressed

as

$$\begin{aligned} M(\Psi, D) &= 0, & D &= D(\psi) \\ m(\psi, d) &= 0, & d &= d(\Psi). \end{aligned} \tag{1.1}$$

With a macroscopic solver in hand, the procedure is to first constrain the micro simulation to be consistent with local macro data: $d = d(\Psi)$. After solving for ψ in the micro domain, the missing macro data is estimated using the results from the micro simulation: $D = D(\psi)$.

The HMM framework has been applied to fluid simulation problems before. For instance, in [186], Wen and E model fluid-fluid and fluid-solid interactions in which the standard boundary conditions for a continuum fluid are no longer accurate and must be inferred from microscopic models, such as molecular dynamics (MD). Using such a microscopic model throughout the entire computational domain is prohibitively expensive, due to the disparate spatial and temporal scales between the continuum and molecular dynamics involved. Instead, local molecular dynamic simulations are computed only along the interfaces for which a boundary condition is needed. In the language of (1.1) above, the model is

$$M(\Psi, D) = \begin{cases} \rho \mathbf{u}_t + \nabla \cdot \tau = 0, & \tau = \tau(\mathbf{q}_i, \mathbf{p}_i) \\ \nabla \cdot \mathbf{u} = 0 \end{cases} \tag{1.2}$$

$$m(\psi, d) = \begin{cases} m_i \frac{d}{dt} \mathbf{q}_i = \mathbf{p}_i \\ \frac{d}{dt} \mathbf{p}_i = \mathbf{F}_i, & \mathbf{p}_i(t=0) = \mathbf{p}_i(\mathbf{u}), \end{cases} \tag{1.3}$$

the point being that the usual stress tensor

$$\tau = \rho \mathbf{u} \otimes \mathbf{u} + p I + \tau_d, \quad \tau_d = \mu (\nabla \mathbf{u} + \nabla \mathbf{u}^T) \tag{1.4}$$

can be replaced with a more accurate model coming from the MD simulation where it is needed, and the MD simulation is initialized to be consistent with the local values of the continuum velocity.

While not initially proposed as an example of HMM, the method of Superparameterization proposed by Grabowski [90] and developed by Majda and others [91, 153, 154, 156] is a multiscale method for the simulation of atmospheric flows that fits into the framework of HMM. The original idea of the method is to couple local computations for the turbulent transport quantities to a global macroscopic model for the atmosphere. The local computations impose artificial scale separation in both space and time between the large scale energetic motions and the small scale fluctuations and hence allow for a reduced computational cost.

We mention also recent work by Lācis and Bagheri for determining the effective boundary condition at the interface between a free fluid and a porous medium [135]. The method fits in the HMM framework and is quite similar to the one proposed in Chapter 2 here; the coefficients in a generalized Beavers-Joseph law are determined by solving Stokes problems in a microscale domain containing a unit cell of the porous media.

1.4 Summary of Research Work and Outline of Dissertation

The development of a heterogeneous multiscale model for a multiscale system involves positing both a macroscale and microscale model and then

detailling the precise way in which the two are coupled.

1.4.1 Rough-wall laminar flow

The first chapter details a multiscale model for viscous fluid flow over rough surfaces. The physical model considered is the two dimensional, stationary Navier-Stokes equations

$$-\nu \Delta u^\epsilon + u^\epsilon \nabla u^\epsilon + \nabla p^\epsilon = f \quad (1.5)$$

$$\nabla \cdot u^\epsilon = 0 \quad (1.6)$$

in some domain Ω^ϵ whose boundary contains small oscillations of characteristic wavelength and amplitude $0 < \epsilon \ll 1$. The flow field is assumed to satisfy the no slip condition $u^\epsilon = 0$ along the rough boundary $\partial\Omega^\epsilon$. Even in the low Reynolds number, laminar case, the boundary roughness introduces small oscillations in the solution u^ϵ that make a full description computationally expensive. An HMM technique is proposed that couples together two Navier-Stokes models: fine scale solvers localized to the rough boundary and a macroscopic solver for the bulk flow in a domain with a smooth boundary. The local, fine-scale problems account for the geometry of the roughness, and they in turn supply the slip amount for an effective, macroscopic boundary condition of Robin-type, as inspired by mathematical homogenization theory. The convergence of the algorithm is investigated, and numerical examples illustrate its utility in a variety of test cases.

1.4.2 Wall-bounded, incompressible turbulent flows

The second chapter is concerned with the multiscale dynamics of wall-bounded, turbulent viscous incompressible flows, as described by the time-dependent Navier-Stokes equations

$$\partial_t u + u \nabla u + \nabla p - \frac{1}{Re} \Delta u = f \quad (1.7)$$

$$\nabla \cdot u = 0 \quad (1.8)$$

for $Re \gg 1$.

Wall turbulence is ubiquitous in nature; virtually every object that moves on planet earth passes through a fluid. Viscous friction between the object and fluid molecules then induces stresses on the fluid, often leaving turbulent vortices in the object's wake.

Wall bounded turbulent flows are difficult to compute because they contain asymptotically small, dynamically important boundary layers. The direct simulation of such flows incurs a computational cost proportional to $\mathcal{O}(Re_\tau^4)$, where Re_τ is the so-called friction Reynolds number [165]. A standard macroscale approximation technique for the simulation of turbulent flows is called Large Eddy Simulation (LES). For LES to be applicable to realistic aeronautical or atmospheric flows, e.g., it requires a model for the effect of the small-scale, near-wall dynamics on the bulk turbulence [30, 181], typically referred to in the fluid dynamics literature as a wall-model.

An HMM-type approach to computing wall-bounded turbulent flows, then, would have a suitably defined Large Eddy Simulation (equipped with a

subgrid model) as the macroscale model $M(\bar{u}, \bar{p}, D)$, where \bar{u}, \bar{p} are the low-pass filtered velocity and pressure fields, while D is the missing wall-model that supplies, for instance, a wall shear stress boundary condition necessary for the LES model to be complete. The work of Sandham et al. [194] is an example of such a model.

Building off of the “quasi-DNS” component of Sandham et al.’s work, this chapter details a reduced-order, microscale computational model $m(u, p, d)$ for the small-scale flow dynamics, where the model inputs d are a local pressure gradient and large-scale total stress. After a description of the model formulation, numerical experiments are presented that illustrate the model’s flow statistics compare favorably to those generated by direct numerical simulation (DNS) in the cases of favorable and negligible pressure gradients for a range of Reynolds numbers Re_τ . In contrast to the increasing cost of DNS as a function of Re_τ , the computational cost for the model to obtain those statistics is independent of such restrictions.

An application of the model to a flow with a strong adverse pressure gradient then demonstrates a more refined formulation is required to model the effect of boundary layer growth on mean flow statistics. Asymptotic analysis is then presented and a “slow-grow” model for such situations is proposed. Ultimately this results in the addition of another model input ϵ which models the growth of the mean wall shear in the streamwise direction. Finally, a derivation of the slow-grow model’s equations of motion in the well known vorticity-velocity formulation of Kim, Moin, and Moser [126] is presented.

1.4.3 Electrokinetic flows

Electrolyte solutions, such as seawater, are fundamentally important to the fields of microfluidic engineering, colloid science, molecular biology, battery technologies, and membrane technologies.

Ionic liquids (ILs), such as molten NaCl, are another class of liquids that can conduct electricity. Because the solvent in an IL *is* the charged ions, they exhibit intriguing physical properties, such as an extremely low vapor pressure pressure. In particular there exist complex hydrocarbons that are high-viscosity liquids at room temperature. Such room temperature ionic liquids (RTILs) are known to phase separate in cations and anions, making them attractive for such industrial applications as super-capacitors, batteries, lubrication of micro-electromechanical machines, dye-sensitive photoelectrochemical cells, and gating devices.

Flows of electrolyte solutions and ionic liquids are often termed electrokinetic flows, and they are difficult to model both analytically and numerically because their dynamics occur over a disparate range of temporal and spatial scales.

This chapter presents a few different modeling strategies for electrolytes and ionic liquids. Firstly, a continuum model is used to numerically simulate two important wall bounded electrokinetic flow phenomena, electro-osmosis and induced charge electro-osmosis. These simulations motivate a simple scaling analysis which shows a continuum representation is fundamentally inappro-

priate for the charged ion density field in the near wall region. A multiscale, hybrid particle-continuum model is then proposed. After detailing the hybrid model, we present a numerical example for verification. Lastly, we present a stochastic partial differential equation model for RTILs in the Fluctuating Hydrodynamics framework.

1.4.4 Cell resonance error in numerical homogenization

In the numerical homogenization of multiscale elliptic operators, one often needs to take an average of the solution to a microscale problem m whose input is the local value of some oscillatory data a^ϵ . Both the boundary conditions and domain size of the microscale problem play an important role in the accuracy of the homogenization procedure. In particular, imposing naive boundary conditions leads to a $\mathcal{O}(\epsilon/\eta)$ error in the computation, where ϵ is the characteristic size of the microscopic fluctuations in the heterogeneous media, and η is the size of the microscopic domain. This so-called “cell resonance” error can dominate the discretization error incurred in the numerical solution to both the macroscopic M and microscopic problem m , polluting the entire homogenization scheme. Based on the simple observation that this error oscillates as a function of domain size η , this chapter presents a procedure that reduces the cell resonance error to $\mathcal{O}(\epsilon/\eta)^r$, where r can be made arbitrarily large through the use of special averaging kernels. Rigorous analysis and numerical experiments showcase the utility of the approach for use in multiscale numerical methods.

Chapter 2

Viscous Laminar Flow Over Rough Surfaces

2.1 Introduction

Standard partial differential equations for viscous flow such as the Stokes and Navier-Stokes equations naturally have no slip boundary conditions. The velocity vector $u = 0$ at the boundary.

There are cases where this is not accurate. At a slip line where two immiscible fluids meet at a solid boundary is one example [67]. The fluid molecules actually slide along the boundary near the slip line. Another example is gas at very low pressure.

Even when the no slip boundary condition is valid, it can generate an asymptotic separation of energetic scales, manifest in the form of boundary layers. Such boundary layer flows are challenging both for analysis and numerical computation. Some examples include high Reynolds number wall bounded flows, electro-kinetic flows over charged surfaces, and viscous flow over a rough surface or a porous bed.

In such cases, it may be better in a computation to replace the no slip boundary condition by an effective boundary condition, or wall law. Ideally, the wall law captures the effect of the asymptotic small scales on the

large scales. Computing in a domain without the small scale structure then results in a large reduction in the degrees of freedom necessary in a simulation. Sometimes wall laws can be rigorously derived from first principles; examples include the Navier-slip law for flows over a rough surface [111] and the Beavers-Joseph-Saffman interface law for flows over porous beds [110]. In other cases one has to resort to physical intuition or engineering wisdom in order to derive effective boundary conditions. Classical examples include the logarithmic law-of-the-wall [162] and the electro-osmotic slip velocity (and associated zeta potential) [206] for wall bounded turbulent and electro-kinetic flows, respectively.

The focus in this chapter will be on laminar flow with a rough boundary that varies with characteristic amplitude and period $0 < \epsilon \ll 1$. Surface roughness plays an important role in a variety of physical applications, such as in geophysical fluid dynamics [34, 177] or in the reduction of skin friction drag. The morphology of a swordfish's sword, shark dermal denticles, and riblets on the Stars and Stripes yacht in the 1987 America's Cup finals are all examples of the latter [35, 161]. The problem is also quite well understood mathematically; see for example the series of studies [8, 12, 20, 47, 111].

The basic goal is to model the effect of the rough boundary on the flow in the domain interior and thus remove the ϵ -scale from the problem. Computational techniques based on domain decomposition and asymptotic homogenization theory have been previously proposed for this purpose [8, 9]. Similar strategies have also been explored for compressible flows over rough

surfaces [58] and for shape optimization with the purpose of minimizing drag for both laminar and turbulent incompressible flows, assuming the roughness is within the viscous sublayer [78, 79].

Our goal is to derive the Navier-slip effective boundary condition by a local high-resolution simulation coupled to the coarser scale simulation in the interior following the framework of the heterogeneous multiscale method (HMM) [6, 68, 69]. This coarser scale simulation will use the effective boundary condition.

The HMM framework has been applied to the slip line problem mentioned above. The local high-resolution model is then molecular dynamics. The outer coarser scale model is the Navier-Stokes equations, which gets an effective boundary condition at the slip line from the molecular dynamics simulation, [69, 186].

The method proposed here for laminar flow over a rough boundary is similar to domain decomposition, but it uses the Robin-type boundary condition from the mathematical homogenization theory. In the academic setting of periodic roughness, it is designed to reproduce the slip amount from the theory. However, no assumption of local flow periodicity is made, in contrast to [9], and hence the coupling procedure can work in more general settings.

The structure of this chapter is as follows. The problem of laminar, viscous flow over a rough boundary is introduced in section 2.2. Since the analysis of the multiscale method introduced in section 2.3 relies on the asym-

potic expansions performed in [8], the analysis is repeated in a slightly more general setting. Lastly, numerical results in section 2.4 illustrate not only that the method reproduces the theoretical wall law predicted from the homogenization theory when applicable, but that it also performs well in more general settings.

2.2 Homogenization Theory for Laminar Flow Over Rough Surfaces

There exists a large amount of mathematical results available in the literature concerning the asymptotic behavior of laminar incompressible flow in the presence of a rough boundary; see [8, 10–12, 15, 20, 47, 111], and references therein. Although there are differing physical assumptions and levels of mathematical rigour associated to each work, all justify the use of a Robin-type condition on a smooth boundary near the original rough boundary. The slip constant α in the wall law

$$u = \alpha \frac{\partial u}{\partial n} \quad (2.1)$$

(where n is the unit vector normal to the smooth boundary) depends on the average of a local corrector that decays exponentially in the fast variable. As noted above, the removal of the ϵ -scale of the problem is of practical use, as the number of mesh nodes in a numerical simulation that would be needed for a full treatment of the problem is drastically reduced.

Below we give some preliminary definitions necessary to describe two-dimensional viscous, laminar flow in a rough domain. Since the asymptotic

analysis of [8] is used for the convergence analysis of the multiscale algorithm presented in section 2.3, it is reproduced below in a slightly more general setting—namely that of periodic roughness that is modulated by a smooth function.

2.2.1 Preliminary definitions

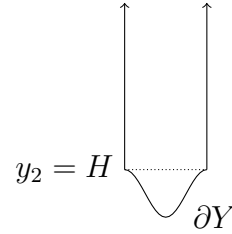


Figure 2.1: Semi-infinite domain Y with boundary $\partial Y = \{y \in \mathbb{R}^2 | y_2 = \varphi(y_1)\}$ for some periodic function φ .

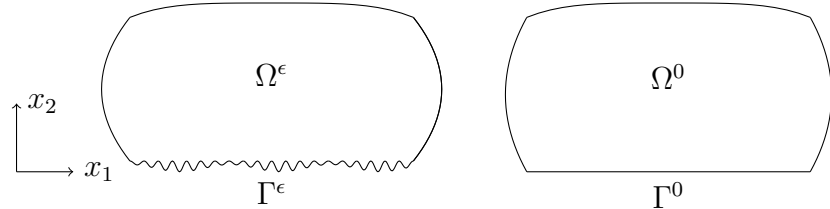


Figure 2.2: Domain Ω^ϵ with periodic, sinusoidal roughness modulated by a smooth function.

Let $\varphi : \mathbb{R} \rightarrow \mathbb{R}$ be a bounded, Lipschitz continuous, periodic function with maximum value $H := \|\varphi\|_\infty$ that satisfies $\varphi(N) = H$ for every $N \in \mathbb{Z}$, and $\varphi(y + 1) = \varphi(y) \geq 0 \forall y \in \mathbb{R}$. Let ϵ be some fixed small parameter, $0 < \epsilon \ll 1$, and define $\varphi^\epsilon(x_1) := \epsilon\varphi(x_1/\epsilon)$. For smooth, bounded function $\beta : \mathbb{R} \rightarrow \mathbb{R}$ that is independent of ϵ , define $\zeta^\epsilon(x_1) := \beta(x_1)\varphi^\epsilon(x_1)$ to be the

function that parameterizes the rough boundary. Without loss of generality, assume that $\|\beta\|_\infty = 1$ for ease of exposition below. Further assume that $\beta \geq 0$ so that $\zeta^\epsilon(x_1) \geq 0 \ \forall x_1 \in \mathbb{R}$.

Let $Y = \{(y_1, y_2) \in [0, 1] \times \mathbb{R} \mid y_2 \geq \varphi(y_1)\}$ be a domain containing a periodic “cell” of φ , semi-infinite in the vertical direction with boundary $\partial Y = \{y \in \mathbb{R}^2 \mid y_2 = \varphi(y_1)\}$; for example, see figure 2.1.

Let $\Theta^\epsilon = \{(x_1, x_2) \in \mathbb{R}^2 \mid x_2 \geq \zeta^\epsilon(x_1)\}$ be the semi-infinite domain contained in the upper half plane $x_2 \geq 0$ in \mathbb{R}^2 , and let Ω be a bounded domain in \mathbb{R}^2 made of one piece that intersects the line $\{x_2 = 0\}$. Take $\Omega^0 = \Omega \cap \{x_2 > 0\}$, and let $\Gamma^0 = \partial\Omega^0 \cap \{x_2 \geq 0\}$. Finally, take $\Omega^\epsilon := \Theta^\epsilon \cap \Omega^0$, so that Ω^ϵ has a rough boundary Γ^ϵ with characteristic amplitude and wavelength ϵ ; for example, see figure 2.2. Note that $\overline{\Omega^\epsilon} \rightarrow \overline{\Omega^0}$ as $\epsilon \rightarrow 0$.

2.2.2 Asymptotic analysis

With Ω^ϵ in hand, consider the following stationary Navier-Stokes problem

$$\begin{aligned} \mathcal{L}(u^\epsilon, p^\epsilon) := u^\epsilon \nabla u^\epsilon - \nu \Delta u^\epsilon + \nabla p^\epsilon &= f && \text{in } \Omega^\epsilon \\ \nabla \cdot u^\epsilon &= 0 && \text{in } \Omega^\epsilon \\ u^\epsilon &= 0 && \text{on } \partial\Omega^\epsilon. \end{aligned} \tag{2.2}$$

Note that other combinations of well-posed boundary conditions are possible, so long as the no slip condition $u^\epsilon = 0$ is imposed on the rough wall Γ^ϵ .

The authors in [8] consider the regime of high Reynolds number, laminar stationary flow; in this case, the flow exhibits Prandtl boundary layers

of characteristic size $\mathcal{O}(\sqrt{\nu})$ [40]. Assuming $|\Omega^0| = \mathcal{O}(1)$, they hypothesize that the effects of surface roughness on the mean flow will be contained in the boundary layer when

$$\epsilon \ll \sqrt{\nu}. \quad (2.3)$$

For simplicity of the asymptotic analysis, the authors take $\nu = \mu\epsilon$, $\mu = \mathcal{O}(1)$, which we consider in this section as well. For other choices of ν that still satisfy (2.3), different asymptotic expansions must be considered. As in [8], we take $\nu = \mu\epsilon$ and assume the system (2.2) has a unique smooth solution.

The goal of the asymptotic analysis is to derive an effective boundary condition similar to (2.1). The starting point is to search for approximations to (u^ϵ, p^ϵ) of the form

$$u^\epsilon \approx u^0(x) + \epsilon u_{BL}^1(x, x/\epsilon) \quad (2.4)$$

$$p^\epsilon \approx p^0(x) + \epsilon p_{BL}^1(x, x/\epsilon), \quad (2.5)$$

where (u^0, p^0) satisfy

$$\begin{aligned} \mathcal{L}(u^0, p^0) &= f && \text{in } \Omega^0 \\ \nabla \cdot u^0 &= 0 && \text{in } \Omega^0 \\ u^0 &= 0 && \text{on } \partial\Omega^0, \end{aligned} \quad (2.6)$$

and (u_{BL}^1, p_{BL}^1) are boundary layer correctors.

Consider first the error that arises when u^0 does *not* satisfy the no slip condition along the rough boundary Γ^ϵ . For $x^0 \in \Gamma^0$, $x^0 + \zeta^\epsilon(x_1^0)e_2 \in \Gamma^\epsilon$, a

Taylor expansion and the no slip condition give

$$\begin{aligned} u^0(x^0 + \zeta^\epsilon(x_1^0)e_2) &= \overbrace{u^0(x^0)}^{=0} + \zeta^\epsilon(x_1^0) \frac{\partial u^0}{\partial x_2}(x^0) + \frac{1}{2} (\zeta^\epsilon(x_1^0))^2 \frac{\partial^2 u^0}{\partial x_2^2}(\xi(x^0)) \\ &= \epsilon \beta(x_1^0) \varphi(x_1^0/\epsilon) \frac{\partial u^0}{\partial x_2}(x^0) + \mathcal{O}(\epsilon^2), \end{aligned} \quad (2.7)$$

so that to leading order in ϵ , the error on the rough boundary Γ^ϵ is given as the product of a function of the macroscopic, “slow” variable x^0

$$\beta(x_1^0) \frac{\partial u^0}{\partial x_2}(x^0) \quad (2.8)$$

and a periodic function of the microscopic, “fast” variable x^0/ϵ

$$\varphi(x_1^0/\epsilon). \quad (2.9)$$

Since the no-slip condition implies $\partial u_1^0 / \partial x_1 = 0$ along the smooth wall Γ^0 , the continuity equation implies

$$\frac{\partial u^0}{\partial x_2}(x^0) = \frac{\partial u_1^0}{\partial x_2}(x^0) e_1, \quad x^0 \in \Gamma^0. \quad (2.10)$$

This motivates an ansatz for the boundary layer correctors of the form

$$u_{BL}^1(x, y) = \beta(x_1) \frac{\partial u_1^0}{\partial x_2}(x_1, 0) (\chi(y) - \bar{\chi}) \quad (2.11)$$

$$p_{BL}^1(x, y) = \beta(x_1) \frac{\partial u_1^0}{\partial x_2}(x_1, 0) \pi(y) \quad (2.12)$$

where $x = (x_1, x_2)$, χ is a periodic function of $y := x/\epsilon$, and $\bar{\chi}$ is a constant vector. Using the formal differentiation rule

$$\nabla \Phi(x, x/\epsilon) = \nabla_x \Phi(x, y) + \frac{1}{\epsilon} \nabla_y \Phi(x, y), \quad (2.13)$$

inserting (2.4) and (2.5) into \mathcal{L} , and grouping together terms of similar asymptotic order gives

$$\mathcal{L}(u^0 + \epsilon u_{BL}^1, p^0 + \epsilon p_{BL}^1) - f = \mathcal{L}(u^0, p^0) - f \quad (2.14)$$

$$+ \beta(x_1) \frac{\partial u_1^0}{\partial x_2}(x_1, 0) (-\mu \Delta_y \chi + \nabla_y \pi) \quad (2.15)$$

$$+ \beta(x_1) \frac{\partial u_1^0}{\partial x_2} u^0 \cdot \nabla_y \chi + \mathcal{O}(\epsilon) \quad (2.16)$$

$$= \beta(x_1) \frac{\partial u_1^0}{\partial x_2}(x_1, 0) (-\mu \Delta_y \chi + \nabla_y \pi) + \mathcal{O}(\epsilon^{1/2}). \quad (2.17)$$

The term in (2.16) is $\mathcal{O}(\epsilon^{1/2})$ or smaller throughout Ω^0 because (i) u^0 is $\mathcal{O}(\epsilon)$ near Γ^0 , (ii) $\nabla_y \chi$ decays exponentially fast as x_2/ϵ grows, as guaranteed a posteriori by 2.2.1, and (iii) by assumption of the Prandtl boundary layer scales, $\partial u_1^0 / \partial x_2 = \mathcal{O}(\nu^{-1/2}) = \mathcal{O}(\epsilon^{-1/2})$. Hence, if (χ, π) are chosen such that

$$-\mu \Delta_y \chi + \nabla_y \pi = 0, \quad (2.18)$$

then the approximations (2.4) and (2.5) will be $\mathcal{O}(\epsilon^{1/2})$ pointwise in Ω^0 . A similar computation gives

$$\nabla \cdot (u^0 + \epsilon u_{BL}^1) = \beta(x_1) \frac{\partial u_1^0}{\partial x_2}(x_1, 0) \nabla_y \cdot \chi + \mathcal{O}(\epsilon) \quad (2.19)$$

which implies χ should be made divergence free:

$$\nabla_y \cdot \chi = 0. \quad (2.20)$$

Lastly, consider again the pointwise error on the rough boundary $x = x^0 + \zeta^\epsilon(x_1^0)e_2 \in \Gamma^\epsilon$. In contrast to (2.7), the error on Γ^ϵ for the approximation

(2.4) is:

$$\begin{aligned} u^0(x) + \epsilon u_{BL}^1(x, x/\epsilon) &= \epsilon \beta(x_1^0) \left(\varphi(x_1^0/\epsilon) \frac{\partial u_1^0}{\partial x_2}(x_1^0, 0) e_1 \right. \\ &\quad \left. + \frac{\partial u_1^0}{\partial x_2}(x_1^0, 0) (\chi(x/\epsilon) - \bar{\chi}) \right) + \mathcal{O}(\epsilon^2) \end{aligned} \quad (2.21)$$

(note $x_1 = x_1^0$). Hence, one could enforce the boundary condition

$$\chi(x/\epsilon) - \bar{\chi} = -\varphi(x_1/\epsilon) e_1, \quad x \in \Gamma^\epsilon \quad (2.22)$$

in order to eliminate the $\mathcal{O}(\epsilon)$ error terms. The resulting problem for (χ, π) in the periodic cell Y becomes

$$\begin{aligned} -\mu \Delta_y \chi + \nabla_y \pi &= 0 && \text{in } Y \\ \nabla_y \cdot \chi &= 0 && \text{in } Y \\ \chi(y) - \bar{\chi} &= -\varphi(y_1) && y \in \partial Y \\ \chi - \bar{\chi} &\in H_{\text{per}}^1(Y) \\ \pi &\in L_{\text{per}}^2(Y). \end{aligned} \quad (2.23)$$

It can be shown, however, that in general the problem (2.23) has no solutions. Borrowing an example from [8], simply take $\varphi(y_1) = C > 0$. Instead, the Dirichlet condition in (2.23) can be modified so that only

$$\chi(y) = -\varphi(y_1), \quad y \in \partial Y \quad (2.24)$$

is enforced. In order to ensure that (2.4) is $\mathcal{O}(\epsilon^2)$ on Γ^ϵ , replace (u^0, p^0) with (u^1, p^1) , where u^1 satisfies

$$u^1(x^0) = \epsilon \beta(x_1^0) \bar{\chi} \frac{\partial u_1^1}{\partial x_2}(x_1^0), \quad x^0 \in \Gamma^0. \quad (2.25)$$

This is exactly the desired effective boundary condition, or wall law, of the form (2.1). Accordingly, the $\partial u_1^0 / \partial x_2(x_1, 0)$ term in boundary layer correctors (2.11) and (2.12) must be replaced with $\partial u_1^1 / \partial x_2(x_1, 0)$; the analysis above, however, is unchanged since both expressions are $\mathcal{O}(\nu^{-1/2})$ near Γ^0 , and hence asymptotically equivalent.

In summary, the approximations

$$\begin{aligned} u^\epsilon(x) &\approx u^1(x) + \epsilon\beta(x_1) \frac{\partial u_1^1}{\partial x_2}(x_1, 0) (\chi(x/\epsilon) - \bar{\chi}) \\ p^\epsilon(x) &\approx p^1(x) + \epsilon\beta(x_1) \frac{\partial u_1^1}{\partial x_2}(x_1, 0) \pi(x/\epsilon), \end{aligned} \quad (2.26)$$

where (u^1, p^1) satisfy

$$\begin{aligned} \mathcal{L}(u^1, p^1) &= f && \text{in } \Omega^0 \\ \nabla \cdot u^1 &= 0 && \text{in } \Omega^0 \\ u^1(x) - \epsilon\beta(x_1)\bar{\chi} \frac{\partial u_1^1}{\partial x_2}(x) &= 0 && x \in \Gamma^0 \\ u^1 &= 0 && \text{on } \partial\Omega^0 \setminus \Gamma^0 \end{aligned} \quad (2.27)$$

and (χ^1, π^1) satisfy

$$\begin{aligned} -\mu\Delta_y\chi + \nabla_y\pi &= 0 && \text{in } Y \\ \nabla_y \cdot \chi &= 0 && \text{in } Y \\ \chi(y) &= -\varphi(y_1) && y \in \partial Y \\ \chi - \bar{\chi} &\in H_{\text{per}}^1(Y) \\ \pi &\in L_{\text{per}}^2(Y). \end{aligned} \quad (2.28)$$

are $\mathcal{O}(\epsilon^{1/2})$ in Ω^0 and $\mathcal{O}(\epsilon^2)$ on Γ^0 . In the linear (Stokes) case, it has been shown that the above approximations are one order (in $\epsilon^{1/2}$) better than

(u^0, p^0) ; similar results have also been obtained for Maxwell's equations in a rough domain—see [10, 11, 15].

The following two theorems are due to Achdou et al. The first gives rigorous backing to the assertion that the local correctors (u_{BL}^1, p_{BL}^1) decay exponentially fast in the fast variable x/ϵ , so that the term (2.16) resulting from the insertion of the asymptotic expansions (2.4) and (2.5) into \mathcal{L} is indeed $\mathcal{O}(\epsilon^{1/2})$.

Theorem 2.2.1. [8] *Let $\mathcal{S}_{\text{per}}(Y)$ denote the space of all functions in Y that decay exponentially fast in y_2 , as well all of their derivatives, and are 1-periodic in y_1 . Then there exists a unique pair of functions (χ, π) and a unique vector $\bar{\chi} \in \mathbb{R}^2$ such that $\chi - \bar{\chi} \in (H_{\text{per}}^1(Y))^2 \cap (\mathcal{S}_{\text{per}}(Y))^2$, $\pi \in L^2_{\text{per}}(Y) \cap \mathcal{S}_{\text{per}}(Y)$ and (2.28) is satisfied in a weak sense. Furthermore, $\bar{\chi}$ is horizontal,*

$$\bar{\chi} = |\bar{\chi}| e_1. \quad (2.29)$$

Note 2.2.1 also ensures the wall law (2.25) is of slip and no-penetration type for the horizontal and vertical component of u^1 , respectively. The second theorem provides a bound on the size of the constant $-\bar{\chi}$ and is crucial for the well posedness of the effective problem (2.27) and hence for its numerical approximation as well.

Theorem 2.2.2. [8] *Let $H := \max_{y \in \partial Y} y = \|\varphi\|_\infty$. Then the constant $-\bar{\chi}$ satisfies the bound*

$$0 \leq -\bar{\chi} \leq H.$$

As a result, the problem (2.27) is ill-posed; its variational form contains the term

$$\frac{\mu}{\beta\bar{\chi}} \int_{\Gamma^0} u_1^1 v_1 \, ds \quad (2.30)$$

where v is a test function, which is not coercive when $\bar{\chi} < 0$. For this reason, the effective problem is instead

$$\begin{aligned} \mathcal{L}(u^1, p^1) = f &\quad \text{in } \Omega_{\epsilon H}^0 \\ \nabla \cdot u^1 = 0 &\quad \text{in } \Omega_{\epsilon H}^0 \\ u^1(x) - \epsilon \beta(x_1)(\bar{\chi} + H) \frac{\partial u_1^1}{\partial x_2}(x) = 0 &\quad x \in \Gamma_{\epsilon H}^0 \\ u^1 = 0 &\quad \text{on } \partial\Omega^0 \setminus \Gamma_{\epsilon H}^0, \end{aligned} \quad (2.31)$$

where

$$\Omega_{\epsilon H}^0 = \Omega^0 \cap \{x_2 \geq \epsilon H\}, \quad \Gamma_{\epsilon H}^0 = \{x + (0, \epsilon H), x \in \Gamma^0\}, \quad (2.32)$$

so that $\Omega_{\epsilon H}^0 \subset \Omega^\epsilon \subset \Omega^0$. A Taylor expansion of the effective boundary condition (2.25) implies that the approximation

$$u^1(x) + \epsilon \beta(x_1) \frac{\partial u_1^1}{\partial x_2}(x_1, \epsilon H) (\chi(x/\epsilon) - \bar{\chi}) = \mathcal{O}(\epsilon^2), \quad x \in \Gamma_{\epsilon H}^0 \quad (2.33)$$

still holds.

In conclusion, when discussing the convergence of the multiscale scheme in section 2.3 below, the desired target, homogenized solution is the one satisfying (2.31).

2.3 Heterogeneous Multiscale Method for Laminar Flow Over a Rough Surface

We now describe a heterogeneous multiscale method (HMM) for the efficient computation of the effective boundary condition, or wall law, for the case of laminar flow over a rough surface. After some preliminary definitions, the multiscale model is introduced before an algorithm for its practical solution is described. Analysis of the algorithm in the setting of periodic roughness then demonstrates the method's convergence to the homogenized solution from [8] described in section 2.2.

Consider a translation of the domains Ω^ϵ and $\Omega_{\epsilon H}^0$ defined in section 2.2.1 and (2.32) by ϵH units in the negative x_2 direction, where $H = \|\varphi\|_\infty$ as before, so that

$$(x_1, x_2) \mapsto (x_1, x_2 - \epsilon H); \quad (2.34)$$

note that $\Omega_{\epsilon H}^0 \subset \Omega^\epsilon$ still holds after the translation. Define Ω^{mac} to be the resulting translation of $\Omega_{\epsilon H}^0$, and for simplicity continue to refer to the translation of Ω^ϵ as Ω^ϵ (and similarly for Γ^ϵ). In addition, rename $\Gamma_{\epsilon H}^0$ —the flat part of the boundary of Ω^{mac} defined by (2.32)—to be simply Γ .

Consider also a collection of points $\{s_1, s_2, \dots, s_J\}$, each $s_j \in \mathbb{R}$, and assume $|s_j - s_{j+1}| \geq \epsilon$ for each j . Define the micro-domains Ω_j^{mic} to be the domains bounded by the curves $x_1 = s_j$ on the left, $x_1 = s_j + \epsilon$ on the right, $x_2 = \gamma > 0$ above, and $\{(x_1, x_2) | x_2 = \zeta^\epsilon(x_1) - \epsilon H\}$ below. The lower curve is simply the portion of Γ^ϵ from $x_1 = s_j$ to $s_j + \epsilon$. Denote this portion of the micro-domains $\partial\Omega_{j,\text{noslip}}^{\text{mic}}$, as this is where the physical wall is located. Denote

the remaining portion of the boundary $\partial\Omega_{j,D}^{\text{mic}} = \partial\Omega_j^{\text{mic}} \setminus \partial\Omega_{j,\text{noslip}}^{\text{mic}}$. Lastly, take γ to be $\mathcal{O}(\epsilon)$. See figure 2.3 for an example of such a configuration.

Remark 2.3.1. In order for the micro-domain problems defined below to be well-posed, the corners of the Ω_j^{mic} domains should be mollified; such technical details are not considered here.

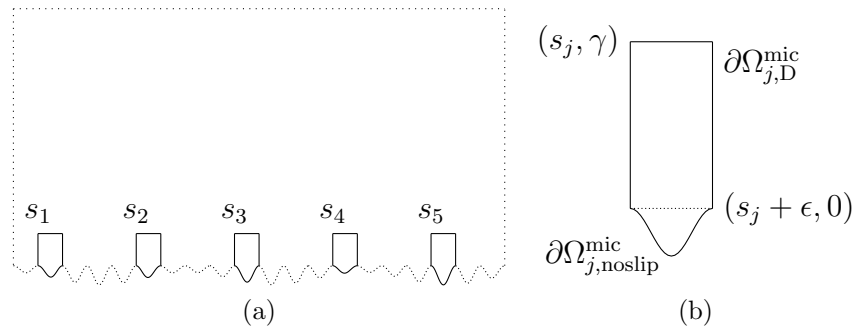


Figure 2.3: (a) Example domain Ω^ϵ (....) containing several Ω_j^{mic} (—). (b) One instance of a micro domain Ω_j^{mic} .

2.3.1 Multiscale flow model

The purpose of the multiscale model is to efficiently produce an approximation U to the true, oscillatory flow u^ϵ by enforcing U satisfy a wall law of the form from the homogenization theory

$$U = \alpha \frac{\partial U_1}{\partial x_2} e_1 \quad (2.35)$$

on Γ , the boundary of the smooth domain Ω^{mac} . The missing data necessary for the model to be complete is the coefficient α in the wall law. The strategy utilized in [8] consists of simply precomputing the solution χ to a (truncated)

cell problem and then taking its average $\bar{\chi}$. This constant (plus some amount $\delta \geq \epsilon H$, in light of theorem 2.2.2) is then taken to be the missing data α . The precomputing step is possible because the cell problem depends only on the geometry of the roughness.

In contrast, the model defined below to estimate α involves coupling a Navier-Stokes system posed in the macroscopic domain Ω^{mac} to J separate Navier-Stokes systems posed in microscopic domains Ω_j^{mic} , $1 \leq j \leq J$. Similar to the cell problem from the homogenization theory, the microscopic systems account for the geometry of the rough surface. They are additionally constrained however to match the averaged local flow values of the macroscopic system, which allows for a more accurate representation of the effect of surface roughness on the macroscopic flow. Furthermore, the inclusion of the nonlinear term allows for convective effects not captured by the cell problem's linear Stokes system. In each Ω_j^{mic} , the ratio of the average flow and the average flow gradient (the shear) is computed. These values are interpolated, and the resulting function is then used for the slip amount α in (2.35). The coupled system is thus designed to reproduce the effective boundary condition from the homogenization theory whenever it is applicable, but also to perform favorably in more general situations to which the theory does not apply.

Define first the macro and microscopic systems, as well as a projection, smoothing, and interpolation operator.

Definition 2.3.1. Let $M(U, P, \alpha)$ define the following PDE system parame-

terized by the slip amount α and posed in Ω^{mac} :

$$\begin{aligned}
-\nu \Delta U + U \nabla U + \nabla P - f &= 0, & \text{in } \Omega^{\text{mac}} \\
\nabla \cdot U &= 0, & \text{in } \Omega^{\text{mac}} \\
U - \alpha \frac{\partial U_1}{\partial x_2} e_1 &= 0, & \text{on } \Gamma \\
U &= 0, & \text{on } \partial\Omega^{\text{mac}} \setminus \Gamma
\end{aligned} \tag{2.36}$$

Note that in general α can vary along Γ so that $\alpha = \alpha(x_1)$.

Definition 2.3.2. Let $m_j(u^j, p^j, \Upsilon_j)$ define the PDE system posed in Ω_j^{mic} and parameterized by the Dirichlet boundary condition $\Upsilon_j : \partial\Omega_{j,D}^{\text{mic}} \rightarrow \mathbb{R}^2$:

$$\begin{aligned}
-\nu \Delta u^j + u^j \nabla u^j + \nabla p^j - f &= 0, & \text{in } \Omega_j^{\text{mic}} \\
\nabla \cdot u^j &= 0, & \text{in } \Omega_j^{\text{mic}} \\
u^j &= \Upsilon_j, & \text{on } \partial\Omega_{j,D}^{\text{mic}} \\
u^j &= 0 & \text{on } \partial\Omega_{j,\text{noslip}}^{\text{mic}}
\end{aligned} \tag{2.37}$$

Note that for well-posedness, Υ_j must satisfy

$$\int_{\partial\Omega_{j,D}^{\text{mic}}} \Upsilon_j \cdot n \, ds = 0. \tag{2.38}$$

Furthermore, let $\{s_n\}_{n=1}^\infty \in \partial\Omega_{j,D}^{\text{mic}}$ be some convergent sequence whose limiting point $\sigma = (s_j, 0)$ or $\sigma = (s_j + \epsilon, 0)$. Then Υ_j should also satisfy

$$\lim_{n \rightarrow \infty} \Upsilon_j(s_n) = 0 \tag{2.39}$$

for continuity with the no slip condition posed along $\partial\Omega_{j,\text{noslip}}^{\text{mic}}$.

Definition 2.3.3. For a sufficiently regular class of functions \mathcal{S} , let

$$\pi_j : \mathcal{S}(\Omega^{\text{mac}}) \rightarrow \mathcal{S}(\partial\Omega_{j,D}^{\text{mic}}) \tag{2.40}$$

Then for some $f \in \mathcal{S}(\Omega^{\text{mac}})$, let $\pi_j(f)$ satisfy the properties (2.38) and (2.39).

This projection operator is the mechanism by which the micro-domain is constrained by the macroscopic solution U . Note that simply taking the trace of U along $\partial\Omega_{j,D}^{\text{mic}}$ is not appropriate, since even though the conservation of mass property (2.38) holds, the constraint (2.39) will not. π_j of course is not uniquely defined by these constraints, however two specific definitions will be proposed below—one for the specific case of periodic roughness and horizontal macro flow, and another for more general settings.

Definition 2.3.4. For integrable $u : \mathbb{R}^2 \rightarrow \mathbb{R}$ and $y \in \mathbb{R}$, define the operator

$$\langle u \rangle(x, y) := \int_x^{x+\epsilon} u(s, y) ds \quad (2.41)$$

which integrates u in the horizontal direction along a small, ϵ -sized strip $[x, x + \epsilon]$ at fixed height y .

Definition 2.3.5. For collection of J points $\{(s_1, \alpha_1), \dots, (s_J, \alpha_J)\}$, $(s_j, \alpha_j) \in \mathbb{R}^2$, define

$$\mathcal{I}((s_1, \alpha_1), \dots, (s_J, \alpha_J)) : \mathbb{R}^{2 \times J} \rightarrow C(\mathbb{R}) \quad (2.42)$$

to be a piecewise continuous polynomial interpolant based on the given points.

Using the above definitions, the multiscale flow model is formally defined as follows; given a collection of points $\{s_j\}_{j=1}^J$ along the rough domain Γ^ϵ , find (U, P) and $((u^1, p^1), \dots, (u^J, p^J))$ satisfying the coupled system of

equations:

$$M(U, P, \alpha) = 0 \quad (2.43)$$

$$m_j(u^j, p^j, \Upsilon_j) = 0, \quad 1 \leq j \leq J \quad (2.44)$$

$$\Upsilon_j = \pi_j(U), \quad 1 \leq j \leq J \quad (2.45)$$

$$\alpha_j = \langle u_1^j \rangle(s_j, 0) / \langle \partial u_1^j / \partial x_2 \rangle(s_j, 0), \quad 1 \leq j \leq J \quad (2.46)$$

$$\alpha = \mathcal{I}((s_1, \alpha_1), \dots, (s_J, \alpha_J)). \quad (2.47)$$

A key feature of the method clearly is the specification of the locations $\{s_1, \dots, s_J\}$ of the micro-domains Ω_j^{mic} . A general strategy is to choose to simulate at a location s_j where either the roughness varies nontrivially or the macroscopic flow is qualitatively different, or both. For Poiseuille type channel flow with periodic roughness, for instance, only one micro-domain covering a single periodic roughness element is necessary. In more realistic applications for which the surface roughness is nonperiodic and additionally varies over macroscopic length scales, the micro-domain should be chosen large enough to cover a few of the estimated correlation lengths, or approximate periods. They should also be placed frequently enough along Γ^ϵ to capture its large-scale, macroscopic variations. The numerical examples in section 2.4 are chosen to approximate such situations.

2.3.2 Algorithm for the coupled system

In practice, the coupled, stationary system (2.43)-(2.47) is solved iteratively. Let $\tau > 0$ be some fixed tolerance, and let the subscript (k) denote

the value of a quantity at the k^{th} iteration of the procedure.

Starting from an initial guess $\alpha_{(0)} = 0$ (i. e. no slip along Γ), the macro-problem is solved for $U_{(0)}$. The J micro-problems are then solved, and a new estimate for the slip amount $\alpha_{(1)}$ is obtained. If the relative difference between the new and old slip amount is smaller than τ , the iteration is terminated, and one final solve for the macroscopic solution U is required. Otherwise, the procedure is repeated. 1 details the method more precisely.

Algorithm 1 Compute macroscopic approximation (U, P) to (u^ϵ, p^ϵ)

Inputs: $\{s_1, \dots, s_J\}, \tau$

```

1:  $\alpha_{(0)} \leftarrow 0$ 
2: solve  $M(U_{(0)}, P_{(0)}, \alpha_{(0)}) = 0$ 
3: for  $k = 1, 2, 3, \dots$  do
4:   for  $j = 1, \dots, J$  do
5:      $\Upsilon_j \leftarrow \pi_j(U_{(k-1)})$ 
6:     solve  $m_j(u_{(k)}^j, p_{(k)}^j, \Upsilon_j) = 0$ 
7:
8:      $\alpha_j \leftarrow \langle u_{1,(k)}^j \rangle(s_j, 0) / \langle \partial u_{1,(k)}^j / \partial x_2 \rangle(s_j, 0)$ 
9:   end for
10:   $\alpha_{(k)} \leftarrow \mathcal{I}((s_1, \alpha_1), \dots, (s_J, \alpha_J))$ 
11:  if  $\|\alpha_{(k)} - \alpha_{(k-1)}\|_\infty < \tau$  then
12:    terminate loop
13:  else
14:    solve  $M(U_{(k)}, P_{(k)}, \alpha_{(k)}) = 0$ 
15:     $U_{(k-1)} \leftarrow U_{(k)}$ 
16:  end if
17: end for
18: solve  $M(U_{(k)}, P_{(k)}, \alpha_{(k)}) = 0$ 
19: Return:  $(U_{(k)}, P_{(k)})$ 

```

Remark 2.3.2. Since the microscopic systems $m_j(u^j, p^j, \Upsilon_j)$ are independent of one another, they are trivially parallelizable.

Remark 2.3.3. If the relative error tolerance $\tau = \epsilon^2$ is prescribed, 1 is observed in practice to terminate after only one iteration; that is, the condition $|\alpha_{(1)} - \alpha_{(2)}| < \epsilon^2$ always holds. This statement is justified in 2.3.4 below and is observed in all cases reported in section 2.4. Hence, the outermost for-loop in algorithm 1 can actually be terminated at line 12 for $k = 1$.

2.3.3 Boundary conditions for the microscopic systems

Given some macroscopic flow U , each of the microscopic problems depends on the boundary condition from the projection operator

$$u^j = \Upsilon_j = \pi_j(U), \quad \text{on } \partial\Omega_{j,D}^{\text{mic}}. \quad (2.48)$$

In the case when U is horizontal, i.e. the vertical component of the velocity vector is zero (or at least asymptotically small compared with the horizontal component), then the boundary condition can be simplified to a “free stream” condition along the upper computational boundary $x_2 = \gamma$

$$u^j = \langle U \rangle(s_j, \gamma) e_1 \quad (2.49)$$

and periodic boundary conditions at $x_1 = s_j$ and $x_1 = s_j + \epsilon$. In this case π_j maps to functions on $\partial\Omega_{j,D}^{\text{mic}} = \{(x_1, x_2) | s_j \leq x_1 < s_j + \epsilon, x_2 = \gamma\}$.

In more general situations in which the macroscopic flow has nontrivial dependence on x_1 and/or a nontrivial vertical component, a more general approach is needed. We propose to prescribe quadratic Dirichlet conditions for both the horizontal and vertical components of the velocity along each of

the three faces of $\partial\Omega_{j,D}^{\text{mic}}$ (those that intersect $x_1 = s_j$, $x_1 = s_j + \epsilon$ and $x_2 = \gamma$).

Let

$$\Gamma_1^{\text{mic}} = \{(x_1, x_2) | 0 \leq x_2 \leq \gamma, x_1 = s_j\} \quad (2.50)$$

$$\Gamma_2^{\text{mic}} = \{(x_1, x_2) | s_j \leq x_1 \leq s_j + \epsilon, x_2 = \gamma\} \quad (2.51)$$

$$\Gamma_3^{\text{mic}} = \{(x_1, x_2) | 0 \leq x_2 \leq \gamma, x_1 = s_j + \epsilon\} \quad (2.52)$$

be the left, upper, and right computational boundaries of the micro-domain (the dependence of each Γ^{mic} on j is implied). Then there are two quadratic profiles for each boundary, each with three coefficients to be determined, and hence 18 total constraints are needed. Let u_k and v_k be the quadratic profile for the horizontal and vertical component of the flow at Γ_k^{mic} , $k = 1, 2, 3$. The no slip requirement (2.39) gives four constraints

$$0 = u_1(s_j, 0) = v_1(s_j, 0) = u_3(s_j + \epsilon, 0) = v_3(s_j + \epsilon, 0). \quad (2.53)$$

Additionally, enforce that the mass flux across each Γ_k^{mic} is the same as the macroscopic mass flux

$$\int_{\Gamma_1^{\text{mic}}} u_1 \, ds = \int_{\Gamma_1^{\text{mic}}} U \cdot n \, ds \quad (2.54)$$

$$\int_{\Gamma_2^{\text{mic}}} v_2 \, ds = \int_{\Gamma_2^{\text{mic}}} U \cdot n \, ds \quad (2.55)$$

$$\int_{\Gamma_3^{\text{mic}}} u_3 \, ds = \int_{\Gamma_3^{\text{mic}}} U \cdot n \, ds. \quad (2.56)$$

Since U is divergence free, these imply conservation of mass along the micro-domain boundaries

$$\int_{\Gamma_1^{\text{mic}}} u_1 \, ds + \int_{\Gamma_2^{\text{mic}}} v_2 \, ds + \int_{\Gamma_3^{\text{mic}}} u_3 \, ds = 0, \quad (2.57)$$

hence satisfying requirement (2.38). This gives three more conditions. In order to completely specify the quadratic profiles, one more condition each is needed for u_1 and u_3 , two more conditions are needed for v_1 , v_2 , and v_3 , and three conditions are needed for u_2 . For continuity, enforce

$$u_1(s_j, \gamma) = u_2(s_j, \gamma) = U(s_j, \gamma) \cdot e_1 \quad (2.58)$$

$$v_1(s_j, \gamma) = v_2(s_j, \gamma) = U(s_j, \gamma) \cdot e_2 \quad (2.59)$$

$$u_2(s_j + \epsilon, \gamma) = u_3(s_j + \epsilon, \gamma) = U(s_j + \epsilon, \gamma) \cdot e_1 \quad (2.60)$$

$$v_2(s_j + \epsilon, \gamma) = v_3(s_j + \epsilon, \gamma) = U(s_j + \epsilon, \gamma) \cdot e_2, \quad (2.61)$$

which leaves one more condition each for v_1 , u_2 , and v_3 . Adding one more interpolation point for each

$$v_1(s_j, \gamma/2) = U(s_j, \gamma/2) \cdot e_2 \quad (2.62)$$

$$u_2(s_j + \epsilon/2, \gamma) = U(s_j + \epsilon/2, \gamma) \cdot e_1 \quad (2.63)$$

$$v_3(s_j + \epsilon, \gamma/2) = U(s_j + \epsilon, \gamma) \cdot e_2. \quad (2.64)$$

ensures the Dirichlet conditions are thus uniquely determined along each Γ_k^{mic} , which defines the projection operator π_j . The method is tested in section 2.4.

2.3.4 Convergence theory for domains with periodic roughness

Next we show that if one assumes (i) periodic roughness in the macroscopic domain (i.e. $\beta = 1$) and (ii) the solution u to the microscopic problem (2.37) can be expanded in the form

$$u = \bar{u} + u^{\text{loc}} + \mathcal{O}(\epsilon^2), \quad (2.65)$$

as in section 2.2, then the HMM algorithm reproduces the slip constant $\epsilon(\bar{\chi} + H)$ from [8] up to an asymptotic error of $\mathcal{O}(\epsilon^{3/2})$. Here \bar{u} is assumed to satisfy the effective boundary condition

$$\bar{u} = \epsilon(\bar{\chi} + H) \frac{\partial \bar{u}_1}{\partial x_2} e_1 \quad (2.66)$$

on Γ , and

$$u^{\text{loc}} = \epsilon \frac{\partial \bar{u}_1}{\partial x_2}(x_1, 0) (\chi(x/\epsilon) - \bar{\chi}) \quad (2.67)$$

in Ω^{mic} , where $\chi - \bar{\chi}$ solves the cell problem (2.23).

If only one micro-simulation is performed at some $x_1 = z$, then by definition the slip amount is given by (2.46):

$$\alpha = \frac{\langle \bar{u}_1 \rangle(z, 0) + \langle u_1^{\text{loc}} \rangle(z, 0) + \mathcal{O}(\epsilon^3)}{\langle \partial \bar{u}_1 / \partial x_2 \rangle(z, 0) + \langle \partial u_1^{\text{loc}} / \partial x_2 \rangle(z, 0) + \mathcal{O}(\epsilon^3)}, \quad (2.68)$$

where $\langle \mathcal{O}(\epsilon^2) \rangle = \mathcal{O}(\epsilon^3)$ is used.

Assume for now (it will be shown below) that, up to an error of $\mathcal{O}(\epsilon^{5/2})$ (respectively $\mathcal{O}(\epsilon^{3/2})$), the integral of u_1^{loc} (resp. $\partial u_1^{\text{loc}} / \partial x_2$) vanishes. Then the above expression reduces to

$$\alpha = \frac{\langle \bar{u}_1 \rangle(z, 0) + \mathcal{O}(\epsilon^{5/2})}{\langle \partial \bar{u}_1 / \partial x_2 \rangle(z, 0) + \mathcal{O}(\epsilon^{3/2})}. \quad (2.69)$$

The integrand in the term $\langle \bar{u}_1 \rangle(z, 0)$ in the numerator

$$\langle \bar{u}_1 \rangle(z, 0) = \int_z^{z+\epsilon} \bar{u}_1(s, 0) ds \quad (2.70)$$

can be Taylor expanded about the point z

$$\bar{u}_1(s, 0) = \bar{u}_1(z, 0) + \frac{\partial \bar{u}_1}{\partial x_1}(z, 0)(s - z) + \frac{\partial^2 \bar{u}_1}{\partial x_1^2}(\xi(s), 0)(s - z)^2/2, \quad (2.71)$$

which yields

$$\langle u_1^{m,1} \rangle(z, 0) = \epsilon \bar{u}_1(z, 0) + \mathcal{O}(\epsilon^2), \quad (2.72)$$

after insertion into the integration operator $\langle \cdot \rangle$. A similar computation for the $\langle \partial \bar{u}_1 / \partial x_2 \rangle(z, 0)$ term in the denominator produces

$$\left\langle \frac{\partial \bar{u}_1}{\partial x_2} \right\rangle(z, 0) = \epsilon \frac{\partial \bar{u}_1}{\partial x_2}(z, 0) + \mathcal{O}(\epsilon^{3/2}). \quad (2.73)$$

where the Prandtl boundary layer scale assumption $\partial \bar{u}_1 / \partial x_2(z, 0) = \mathcal{O}(\epsilon^{-1/2})$ is made, as in 2.2.2. As a result,

$$\begin{aligned} \alpha &= \frac{\epsilon \bar{u}_1(z, 0) + \mathcal{O}(\epsilon^2)}{\epsilon \partial \bar{u}_1 / \partial x_2(z, 0) + \mathcal{O}(\epsilon^{3/2})} = \frac{\epsilon(\bar{\chi} + H) + \mathcal{O}(\epsilon^{3/2})}{1 + \mathcal{O}(\epsilon)} \\ &= \epsilon(\bar{\chi} + H) + \mathcal{O}(\epsilon^{3/2}) \end{aligned} \quad (2.74)$$

where the final equality results from

$$\frac{1}{1+x} = 1 + \mathcal{O}(x), \quad |x| < 1, \quad (2.75)$$

which gives the desired result. It remains to show that

$$\begin{aligned} |\langle u_1^{\text{loc}} \rangle(z, 0)| &\leq C_1 \epsilon^{5/2} \\ |\langle \partial u_1^{\text{loc}} / \partial x_2 \rangle(z, 0)| &\leq C_2 \epsilon^{3/2}. \end{aligned} \quad (2.76)$$

First consider $|\langle u_1^{\text{loc}} \rangle| = \left| \left\langle \epsilon \frac{\partial \bar{u}_1}{\partial x_2}(s, 0) (\chi_1(x/\epsilon) - \bar{\chi}) \right\rangle \right|$. By definition,

$$\bar{\chi} = \hat{\chi}_1(k=0, y_2) = \int_0^1 \chi_1(y_1, y_2) dy_1, \quad \forall y_2 \geq 0, \quad (2.77)$$

i.e. $\bar{\chi}$ is the zeroth Fourier mode of χ and is independent of y_2 . Observe that if $\partial \bar{u}_1 / \partial x_2(s, 0)$ were constant in s , then $\langle u_1^{\text{loc}} \rangle(z, 0) = 0$ would result. Instead,

a Taylor expansion of $\partial\bar{u}_1/\partial x_2(s, 0)$ about the point z gives

$$\left| \left\langle \epsilon \frac{\partial \bar{u}_1}{\partial x_2}(s, 0) \left(\chi_1(s/\epsilon) - \bar{\chi} \right) \right\rangle (z, 0) \right| \quad (2.78)$$

$$\leq \epsilon \left| \frac{\partial \bar{u}_1}{\partial x_2}(z, 0) \right| \cdot \overbrace{\left| \langle \chi_1 - \bar{\chi} \rangle(z, 0) \right|}^{=0} \quad (2.79)$$

$$+ \epsilon \left| \frac{\partial^2 \bar{u}_1}{\partial x_2 \partial x_1}(z, 0) \right| \cdot |\langle (s-z)(\chi_1 - \bar{\chi}) \rangle(z, 0)| \quad (2.80)$$

$$+ \epsilon \left| \left\langle \frac{\partial^3 \bar{u}_1}{\partial x_2 \partial x_1^2}(\xi(s), 0) \frac{(s-x)^2}{2} (\chi_1 - \bar{\chi}) \right\rangle (z, 0) \right|. \quad (2.81)$$

Further bounding the above

$$(2.80) \leq \epsilon \left| \frac{\partial^2 \bar{u}_1}{\partial x_2 \partial x_1}(z, 0) \right| \int_z^{z+\epsilon} |(s-z)| |\chi_1(s/\epsilon, 0) - \bar{\chi}| ds \\ \leq \frac{\epsilon^3}{2} \left| \frac{\partial^2 \bar{u}_1}{\partial x_2 \partial x_1}(z, 0) \right| \cdot \sup_{y_1 \in [0, 1]} |\chi_1(y_1, 0) - \bar{\chi}| = \mathcal{O}(\epsilon^{5/2}), \quad (2.82)$$

$$(2.81) \leq \frac{\epsilon^4}{6} \sup_{s \in [z, z+\epsilon]} \left| \frac{\partial^3 \bar{u}_1}{\partial x_2 \partial x_1^2}(\xi(s), 0) (\chi_1(s/\epsilon, 0) - \bar{\chi}) \right| = \mathcal{O}(\epsilon^{7/2}).$$

shows that $\left| \langle u_1^{\text{loc}} \rangle(z, 0) \right| \leq C_1 \epsilon^{5/2}$. To bound the integral of $\partial u_1^{\text{loc}}/\partial x_2$, first note that again, if $\partial\bar{u}_1/\partial x_2(s, 0)$ were constant in s , then

$$\left\langle \frac{\partial u^{\text{loc}}}{\partial x_2} \right\rangle (z, 0) = \epsilon \frac{\partial \bar{u}_1}{\partial x_2} \left\langle \frac{\partial}{\partial x_2} (\chi_1 - \bar{\chi}) \right\rangle (z, 0) \quad (2.83)$$

$$= \frac{\partial \bar{u}_1}{\partial x_2} \int_z^{z+\epsilon} \frac{\partial \chi_1}{\partial y_2}(s/\epsilon, 0) ds \quad (2.84)$$

$$= \frac{\partial \bar{u}_1}{\partial x_2} \frac{d}{dy_2} \int_z^{z+\epsilon} \chi_1(s/\epsilon, 0) ds \quad (2.85)$$

$$= 0 \quad (2.86)$$

by the Leibniz rule. Instead, expand $\partial\bar{u}_1/\partial x_2$ in a Taylor series to get

$$\left| \left\langle \epsilon \frac{\partial \bar{u}_1}{\partial x_2}(s, 0) \frac{\partial \chi_1}{\partial x_2} \right\rangle(z, 0) \right| \leq \epsilon \left| \frac{\partial \bar{u}_1}{\partial x_2}(z, 0) \right| \cdot \overbrace{\left| \left\langle \frac{\partial \chi_1}{\partial x_2} \right\rangle(z, 0) \right|}^{=0} \quad (2.87)$$

$$+ \epsilon \left| \frac{\partial^2 \bar{u}_1}{\partial x_2 \partial x_1}(z, 0) \right| \cdot \left| \left\langle (s - z) \frac{\partial \chi_1}{\partial x_2} \right\rangle(z, 0) \right| \quad (2.88)$$

$$+ \epsilon \left| \left\langle \frac{\partial^3 \bar{u}_1}{\partial x_2 \partial x_1^2}(\xi(s), 0) \frac{(s - z)^2}{2} \frac{\partial \chi_1}{\partial x_2} \right\rangle(z, 0) \right|, \quad (2.89)$$

which can be bounded as follows

$$(2.88) \leq \frac{\epsilon^2}{2} \left| \frac{\partial^2 \bar{u}_1}{\partial x_2 \partial x_1}(z, 0) \right| \cdot \sup_{y_1 \in [0, 1]} \left| \frac{\partial \chi_1}{\partial y_2}(y_1, 0) \right| = \mathcal{O}(\epsilon^{3/2}) \quad (2.90)$$

$$(2.89) \leq \frac{\epsilon^3}{6} \sup_{s \in [z, z+\epsilon]} \left| \frac{\partial^3 \bar{u}_1}{\partial x_2 \partial x_1^2}(\xi(s), 0) \right| \cdot \sup_{y_1 \in [0, 1]} \left| \frac{\partial \chi_1}{\partial y_2}(y_1, 0) \right| = \mathcal{O}(\epsilon^{5/2}) \quad (2.91)$$

as desired.

In summary, we have shown that for domains with periodic roughness, the slip constant α defined by the HMM scheme equals the slip constant $\epsilon(\bar{\chi} + H)$ from [8], plus a perturbation of $\mathcal{O}(\epsilon^{3/2})$. The result relies on the validity of the asymptotic analysis of [8] in the microscopic domain, and in particular assumes that the mean flow is smooth.

2.4 Numerical Results

We now present numerical tests of the HMM scheme both in situations where the periodic homogenization theory is applicable and where it is not. All computations are performed using the open source finite element package FEniCS [149, 150], and all meshes are generated using Gmsh [84]. In the first

four cases considered, $\epsilon = 0.025$ and $|\Omega^{\text{mac}}| = \mathcal{O}(1)$, and $\nu = 1$. Strictly speaking, this set of parameters is not in the asymptotic regime analyzed in section 2.2; however, the assumption (2.3) certainly holds. Different values are prescribed for the final example of a backwards facing step and are detailed below. In all cases, the parameter defining the upper boundary of the microscopic domain $\gamma = 4\epsilon$.

All discretizations are performed with the Taylor-Hood elements, i.e. P_2 and P_1 basis functions for the velocity and pressure fields, respectively [92, 138], and the resulting discrete nonlinear system is solved with Newton's method, using the solution to the corresponding Stokes problem as the initial guess.

The direct numerical simulation (DNS) of the full problem (2.2) is computed with a large number of elements and is compared with (i) the 1st order approximation satisfying the no slip condition along Γ and (ii) the HMM approximation satisfying the coupled system (2.43)-(2.46), both of which are computed on the same mesh. The coupled HMM system is solved iteratively, using 1. The tolerance τ for the relative error between successive slip amounts α is set to be $\tau = \epsilon^2$.

In all cases, the HMM solution is clear improvement over the first order, no slip approximation; it captures the average effect of roughness on the flow. Of particular note is the final example of a backwards facing step, for which the HMM solution correctly captures the effect of the roughness on the size of the recirculation bubble.

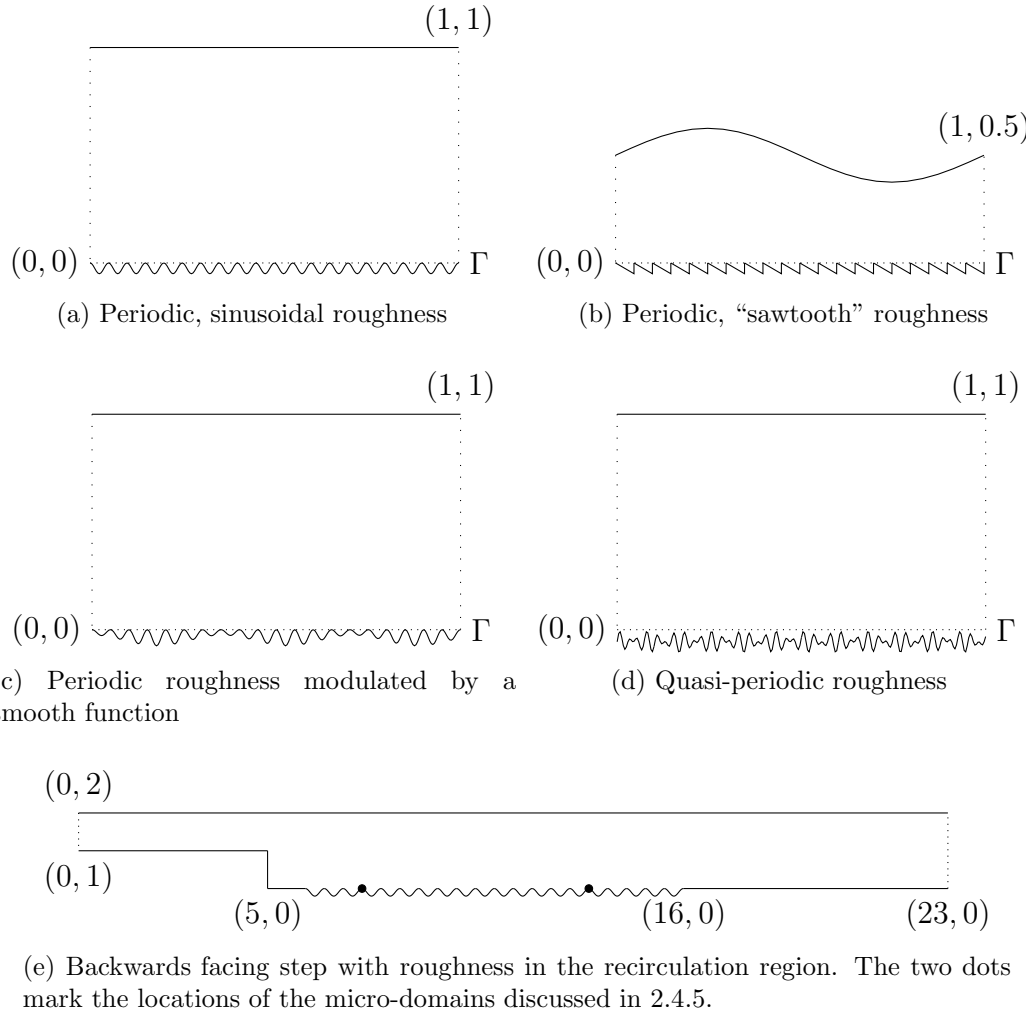


Figure 2.4: Sketches of the rough domains used to test the numerical method.

2.4.1 Flow in a channel with periodic roughness

First consider a channel domain with periodic roughness, as in 2.4a. The macroscopic domain is simply $\Omega^{\text{mac}} = [0, 1]^2$, and the roughness is parameterized by the function $\varphi^\epsilon(x_1) = \epsilon/2(\cos(2\pi x_1/\epsilon) - 1)$. The no slip condition is applied at the upper boundary $x_2 = 1$, and periodic boundary conditions are applied on the left/right boundaries. A constant pressure gradient $-\nabla p = (1 \ 0)^T$ drives the flow from left to right. Ω^ϵ is discretized with 50554 cells, while the discretization of Ω^{mac} and Ω^{mic} contain only 3200 and 927 cells, totaling $6.3\% + 1.8\% = 8.1\%$ the amount of rough domain cells.

In the setting just described, the macroscopic solution U is one dimensional. Only the horizontal component of the flow is nonzero, and it only depends on the wall-normal variable x_2 . In this case, only one micro-domain is needed, and periodic boundary conditions can be prescribed along the left/right computational boundaries of the micro-domain ($x_1 = s$ and $x_1 = s + \epsilon$) for simplicity, as discussed in section 2.3.3. The free stream condition (2.49) is then applied along the upper computational boundary $x_2 = 4\epsilon$.

Figures 2.5 and 2.6 plot u_1 and $\partial u_1 / \partial x_2$, respectively, as functions of x_1 for various values of x_2 near the wall. Also computed was an HMM solution using the more general strategy for the projection operator π_j defined by the constraints (2.53)-(2.64) (not pictured). The resulting slip amount differed from the one computed with periodic boundary conditions in the micro domain only by 0.9%. It is interesting to note, however, that the micro-domain flow u_1 along the line $x_2 = 0$ over which the average is taken has a lower value in

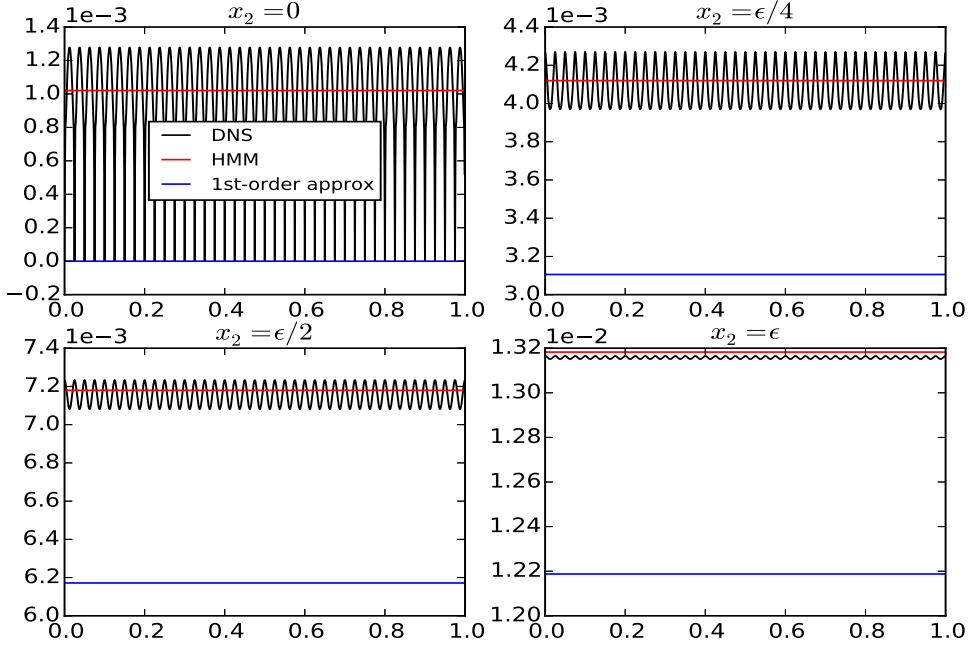


Figure 2.5: Horizontal component of the flow u_1 versus x_1 plotted at various heights x_2 for the domain shown in 2.4a.

the Dirichlet case than in the periodic case. Accordingly, the shear $\partial u_1 / \partial x_2$ is lower as well.

2.4.2 Nonsquare domain with periodic roughness

Next, consider a nonsquare macroscopic domain with periodic, “sawtooth” roughness as shown in 2.4b. Let $h(x_1) := 0.5 - 0.125 \sin(2\pi x_1)$. Then

$$\Omega^{\text{mac}} = \{(x_1, x_2) | 0 \leq x_1 \leq 1, 0 \leq x_2 \leq h(x_1)\}. \quad (2.92)$$

The roughness is parameterized by the periodic function $\varphi^\epsilon(x_1) = -3\epsilon/4(x_1/\epsilon - \lfloor x_1/\epsilon \rfloor)$. The no slip condition is applied on the domain’s upper, curved boundary, and periodic boundary conditions are applied on the left/right boundaries.

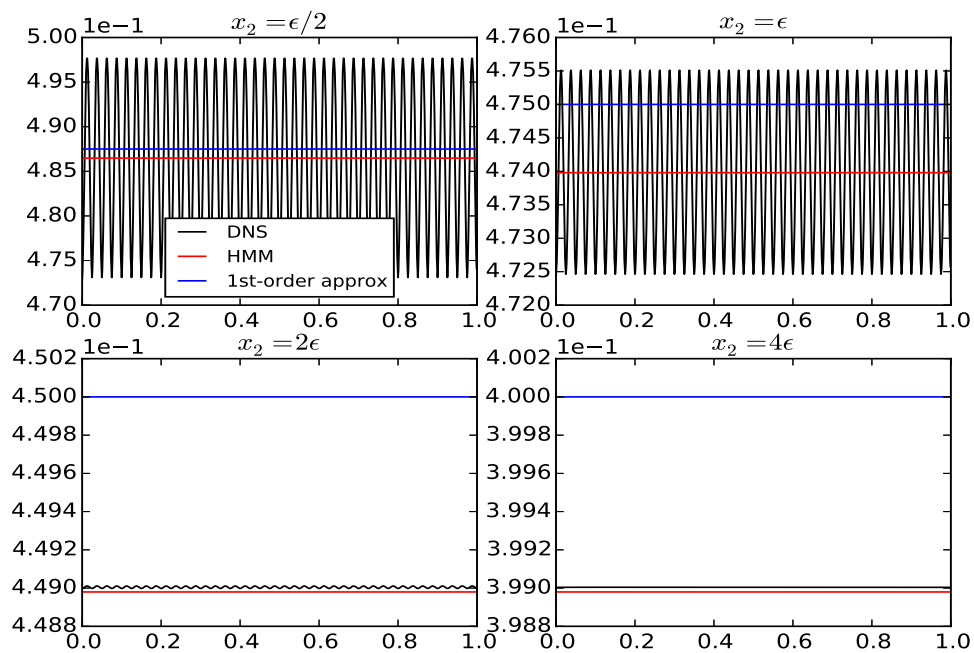


Figure 2.6: Shear $\partial u_1 / \partial x_2$ versus x_1 plotted at various heights x_2 for the domain shown in 2.4a.

A constant body force $f = (1 \ 0)^T$ drives the flow from left to right. Ω^ϵ is discretized with 41898 cells, while Ω^{mac} is discretized with only 1854 cells and each of the five discretized Ω^{mic} domains below contain 903 cells, totaling $4.4\% + 11.0\% = 15.4\%$ the amount of rough domain cells.

To compute the HMM approximations, we use algorithm 1 and set

$$\{s_1, s_2, s_3, s_4, s_5\} = \{0, 0.25, 0.5, 0.75, 1\} \quad (2.93)$$

chosen to capture influence of the macroscopic curvature of Ω^{mac} . The percent difference between the largest and smallest resulting values of slip amounts is a negligible 0.3%, indicating that simply performing one micro-solve at a single s_j is sufficient in this case.

In contrast to the previous example, the macroscopic flow U is not one dimensional, i.e. both U_2 and $\partial U_1 / \partial x_1$ are nonzero, as can be seen from the DNS curve in figures 2.7 and 2.8. However, since at $x_2 = 4\epsilon$ the horizontal component of the flow is approximately one order of magnitude larger than the vertical component for a given x_1 , it is reasonable to attempt to approximate the vertical component as being zero and compute with periodic boundary conditions and the free-stream condition (2.49).

Similar to the previous numerical example in section 2.4.1 a difference of about one percent is observed between the slip amount computed this way and the slip amount using the more general projection $\pi_j(U)$.

The results in figures 2.7 and 2.9 again show u_1 and $\partial u_1 / \partial x_2$ versus x_1 for various values of x_2 .

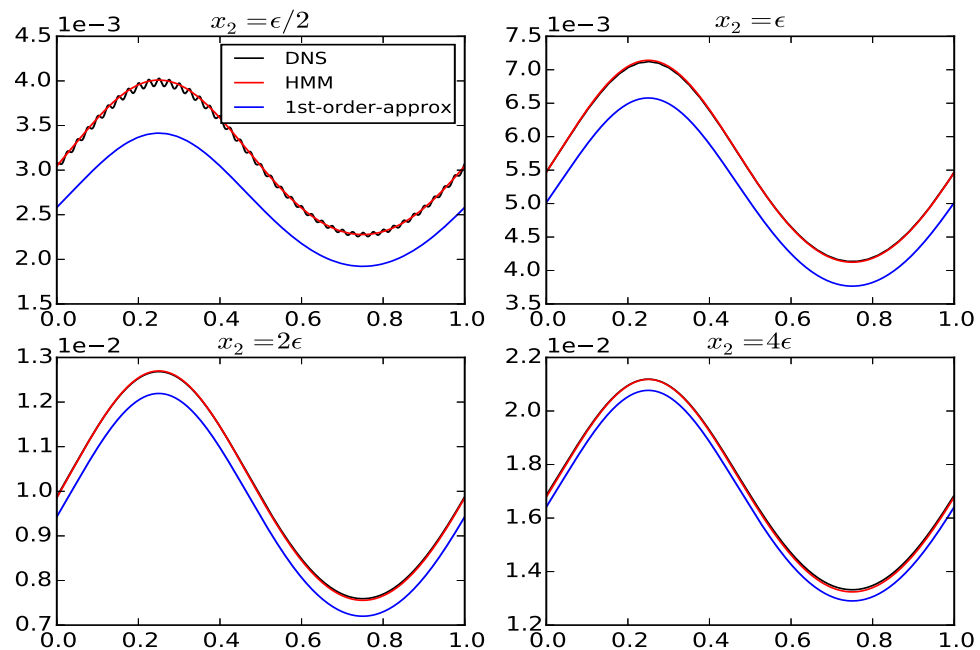


Figure 2.7: Horizontal component of the flow u_1 versus x_1 plotted at various heights x_2 for the domain shown in 2.4b.

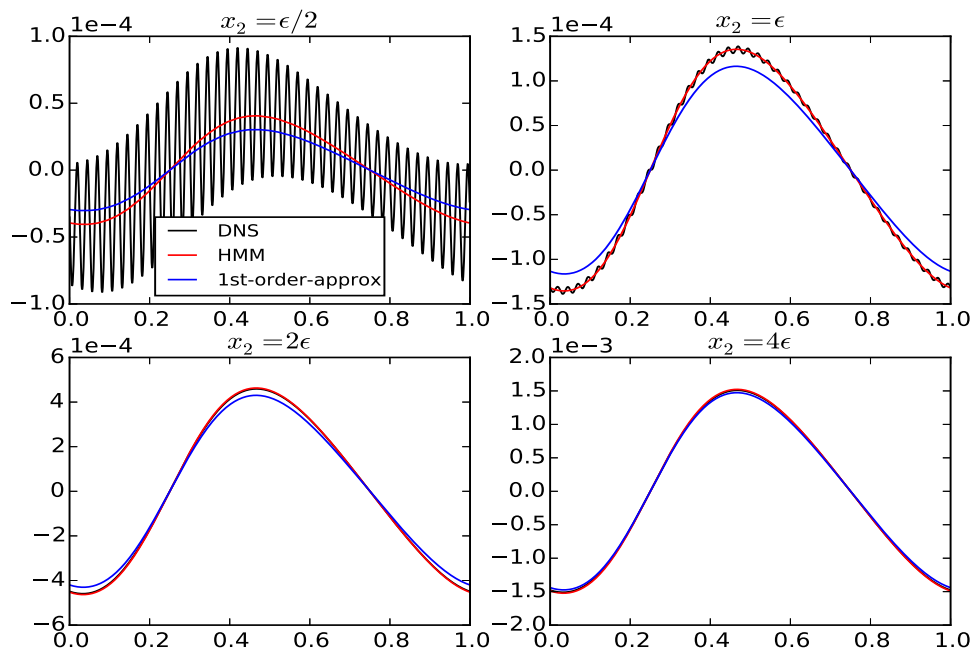


Figure 2.8: Vertical component of the flow u_2 versus x_1 plotted at various heights x_2 for the domain shown in 2.4b.

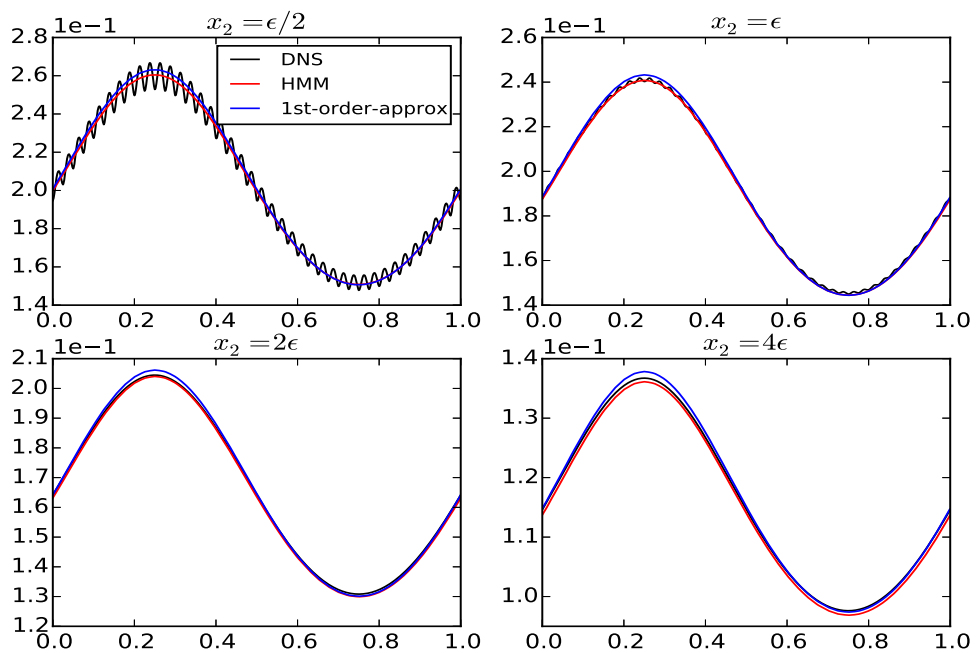


Figure 2.9: Shear $\partial u_1 / \partial x_2$ versus x_1 plotted at various heights x_2 for the domain shown in 2.4b.

2.4.3 Flow in a channel with non-periodic roughness

Consider again $\Omega^{\text{mac}} = [0, 1]^2$, but now let the roughness be parameterized by

$$\zeta^\epsilon(x_1) = \beta(x_1)\varphi^\epsilon(x_1) \quad (2.94)$$

$$\beta(x_1) = \sin^2\left(\sqrt{2}2\pi x_1\right) + 0.5 \quad (2.95)$$

$$\varphi^\epsilon(x) = \epsilon/2(\cos(2\pi x_1/\epsilon) - 1), \quad (2.96)$$

so that the periodic roughness is modulated by a smooth function as shown in 2.4c. The no slip condition is applied at $x_2 = 1$, periodic boundary conditions are enforced at $x_1 = 0$ and $x_1 = 1$, and a uniform pressure gradient $-\nabla p = (1 \ 0)^T$ drives the flow from left to right. Ω^ϵ is discretized with 51210 cells, while Ω^{mac} is discretized with only 3200 cells and the sum of the discrete cells in the 7 separate micro domains below totals 9779, amounting to $6.3\% + 12.8\% = 19.1\%$ of the rough domain cells.

Algorithm 1 is used with

$$\{s_1, s_2, s_3, s_4, s_5, s_6, s_7\} = \{0, 0.15, 0.35, 0.525, 0.675, 0.875, 0.975\} \quad (2.97)$$

chosen to capture the large scale curvature of β . The asymptotic analysis presented in section 2.2.2 suggests it is sufficient to simply compute in a single microscopic domain with roughness parameterized only by φ^ϵ and then multiply the resulting slip amount by $\beta(x_1)$ in the effective boundary condition (2.35). However, we chose to apply the general HMM algorithm to mimic the situation in which an analytic formula for β is not known.

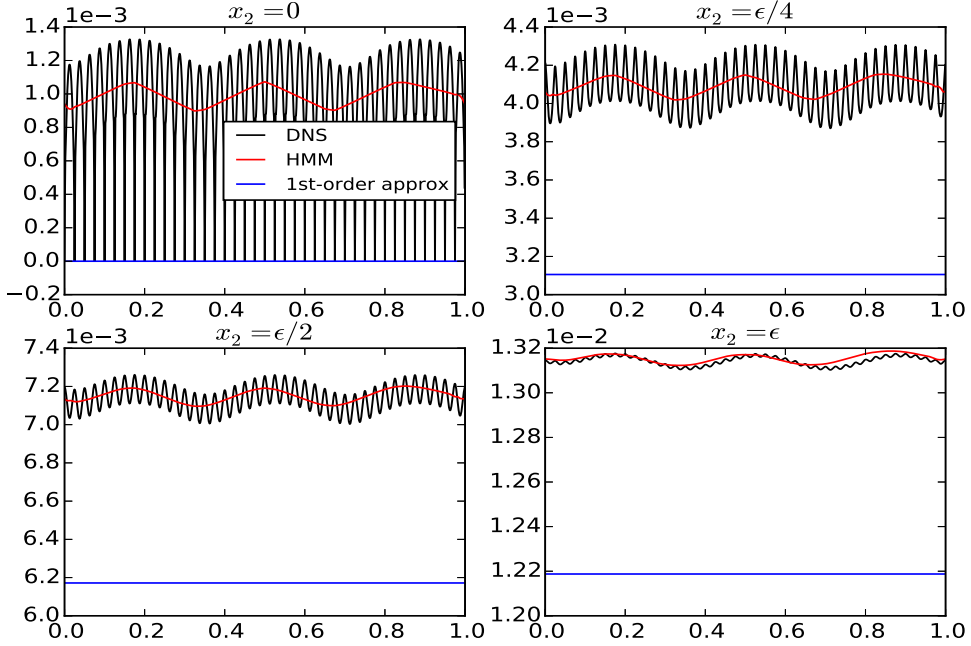


Figure 2.10: Horizontal component of the flow u_1 versus x_1 plotted at various heights x_2 for the domain shown in 2.4c.

In this case, the percent difference between the largest and smallest slip amounts is a non-negligible 23.4%. Figures 2.10 and 2.11 illustrate the success of the HMM method in capturing the horizontal dependence of the slip amount.

2.4.4 Flow in a channel with quasi-periodic roughness

Consider now a rough boundary parameterized by the quasi-periodic function

$$\varphi(x_1/\epsilon) = \epsilon/3 \left(\sin(\sqrt{2} \cdot 2\pi x_1/\epsilon) + \sin(2\pi x_1/\epsilon) - 2.25 \right), \quad (2.98)$$

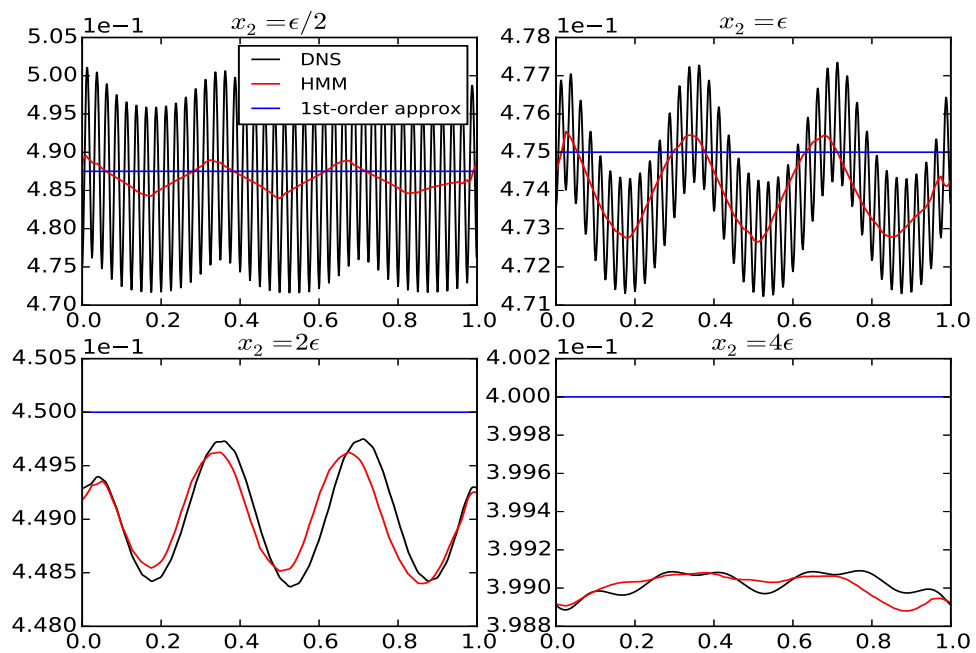


Figure 2.11: Shear $\partial u_1 / \partial x_2$ versus x_1 plotted at various heights x_2 for the domain shown in 2.4c.

like the one displayed in figure 2.4d. As in sections 2.4.1 and 2.4.3, $\Omega^{\text{mac}} = [0, 1]^2$, and no slip is applied at $x_2 = 0$. For both Ω^ϵ and Ω^{mac} , periodic boundary conditions are applied at $x_1 = 0$ and $x_1 = 1$. For u^ϵ this is only an approximation, since φ^ϵ is not truly periodic, which explains the spurious boundary layers in the DNS solution near $x_1 = 0$ and $x_1 = 1$, as seen in figures 2.12 and 2.13.

The same problem is encountered in the micro-domain if periodic boundary conditions are prescribed. Instead, we use the Dirichlet boundary conditions defined by the projection operator π_j with constraints (2.53)-(2.64). In this case the no slip condition (2.53) is applied at the more general locations $(s_j, \varphi^\epsilon(s_j))$ and $(s_j + L, \varphi^\epsilon(s_j + L))$, where L is the generalized horizontal length of the micro-domain. In any case it is best to take $L > \epsilon$ in order to capture a few “correlation lengths” of φ^ϵ .

The computations shown in figures 2.12 and 2.13 are performed with one micro domain at $s_1 = 0.481561$ and length $L = 5\epsilon$. Ω^ϵ is discretized with 65568 cells, while Ω^{mac} and Ω^{mic} are discretized with 3280 and 5028 cells, totaling $5\% + 7.7\% = 12.7\%$ the amount of rough domain cells.

We note also that if one still wants to use periodic boundary conditions, another option is to further increase the horizontal domain length L and then replace the averaging operator in definition 2.3.4 with

$$\langle u \rangle(x, y) = \int_x^{x+L} K(s)u(s, y) ds \quad (2.99)$$

where K is smooth function that has compact support, integrates to unity,

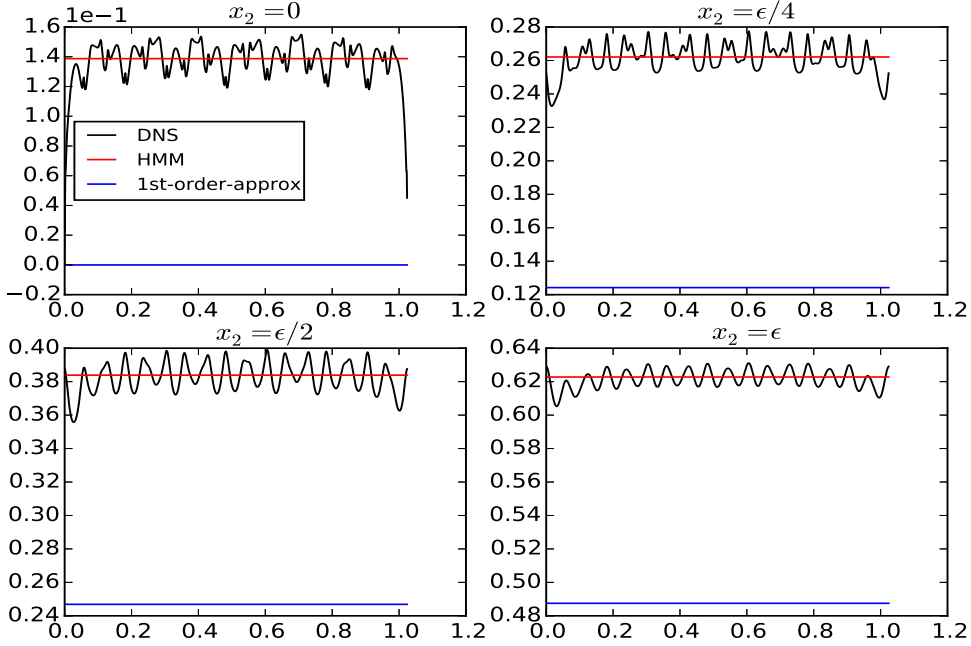


Figure 2.12: Horizontal component of the flow u_1 versus x_1 plotted at various heights x_2 for the domain shown in 2.4d.

and satisfies some vanishing moment conditions. Such kernels are well known in the numerical homogenization community [14, 74, 86] and probably would be useful in realistic applications beyond the academic test cases presented here.

2.4.5 Flow over a backwards facing step

Consider now flow over a backwards facing step with periodic roughness after the step, as in figure 2.4e. The roughness is parameterized by the function

$$\varphi^\epsilon(x) = \epsilon/2 (\cos(2\pi x_1/\lambda) - 1), \quad (2.100)$$

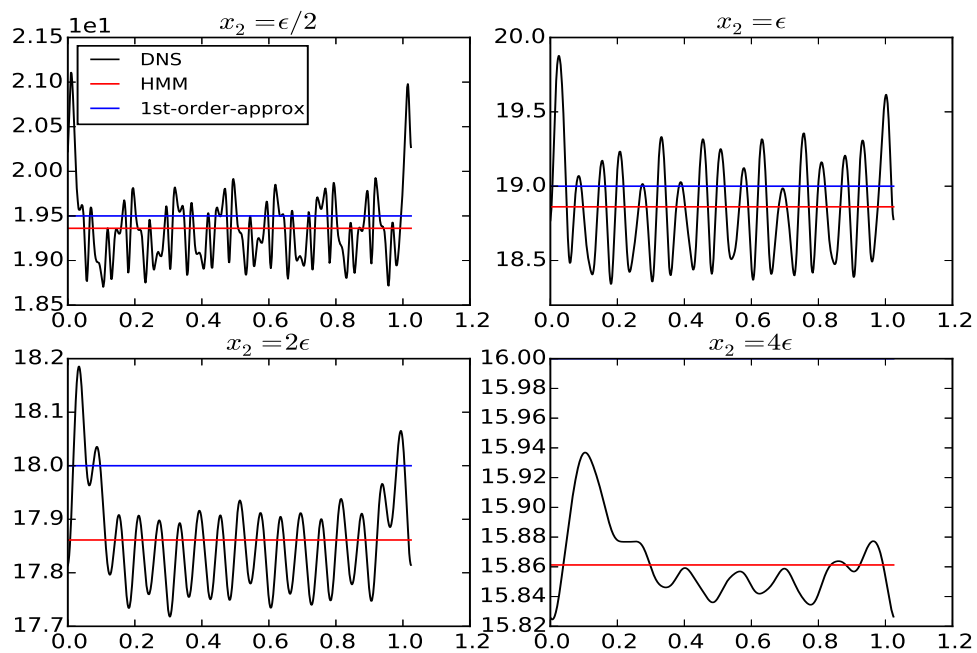


Figure 2.13: Shear $\partial u_1 / \partial x_2$ versus x_1 plotted at various heights x_2 for the domain shown in 2.4d.

similar to section 2.4.1 but with a larger wavelength $\lambda = 2.5\epsilon$. We are primarily interested in the effect of the roughness on the flow after the step. Hence for simplicity there is no roughness in the inflow region prior to the step, and the roughness does not cover the full horizontal extent of the domain, simplifying both inflow and outflow conditions. In this case, both viscosity $\nu = 0.1$ and $\epsilon = 0.1$, and the horizontal length of the domain is $L = 23$. A Poiseuille inflow profile drives the flow, and the Reynolds number based on the profile is $Re = 150$. At this value, some recirculation after the step is expected. A zero-stress condition is applied at the outflow $x_1 = 23$: $\nabla u - pI = 0$, and for both the full DNS solution and the 1st order approximation, the no slip condition is applied on all other domain boundaries. The HMM solution, of course, however satisfies the slip condition (2.36).

Algorithm 1 is used with two points $\{s_1, s_2\} = \{7.5, 13.5\}$ (marked with black dots in 2.4e) chosen to lie (i) closer to the step, and hence within the recirculation bubble, and (ii) farther away from the step, after the bubble. Given $\{\alpha_1, \alpha_2\}$ at these micro domain locations, the slip amount is given as a piecewise linear interpolant

$$\alpha(x_1) = \mathbb{1}_{[6,16]}(x_1)\mathcal{I}_{\text{linear}}((6, 0), (7.5, \alpha_1), (13.5, \alpha_2), (16, 0))(x_1) \quad (2.101)$$

where $\mathbb{1}$ is the indicator function, and $x_1 = 6$ and $x_1 = 16$ are the points at which the roughness begins and ends, and hence before and after which there should be no slip. In retrospect a piecewise constant interpolant $\mathcal{I}_{\text{constant}}$ in the region $6 \leq x_1 \leq 16$ would be more appropriate, since (2.101) does not

capture the slip amount as far out in x_1 as it should. Another option would be to simply perform micro simulations at more points $s_j \in [6, 16]$ along the roughness.

In this case the more general projection $\pi_j(U)$ is applied in both micro-domains. Because of the fluid recirculation, there is a nontrivial mass flux along the upper computational boundary $x_2 = 4\epsilon$ of the micro-domain at $s_1 = 7.5$. This results in a 10.2% difference in the slip amounts computed at $s_1 = 7.5$ and $s_2 = 13.5$. As a result, the HMM solution correctly captures the effect of roughness on the size of the recirculation bubble, something the 1st-order approximation fails to do. Figures 2.14 and 2.15 illustrate the utility of constraining the micro-domains to match the local macroscopic solution.

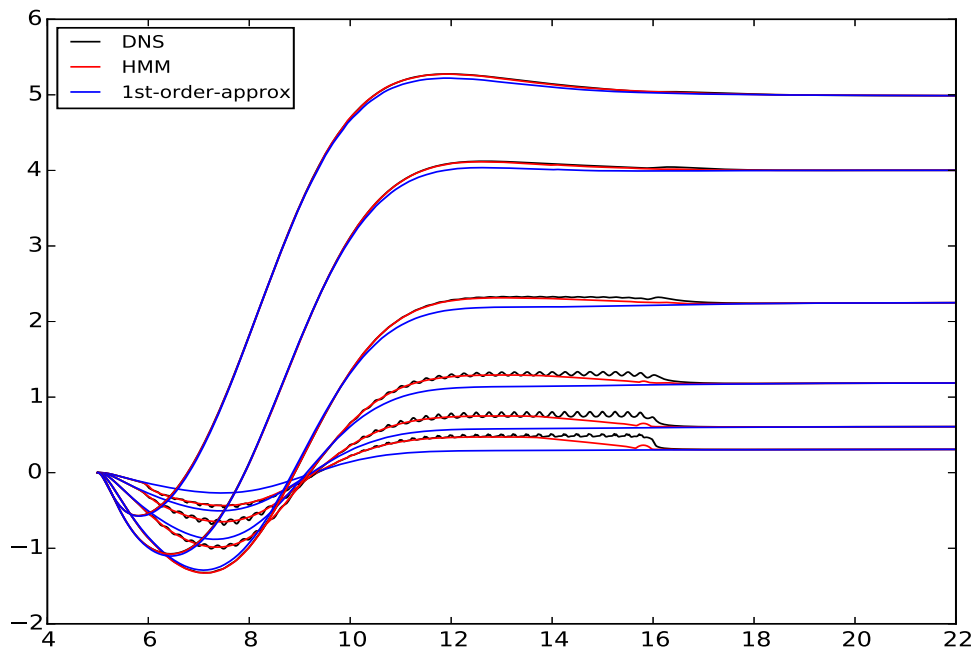


Figure 2.14: Horizontal component of the flow u_1 versus x_1 plotted at the values $x_2 = \epsilon/4, \epsilon/2, \epsilon, 2\epsilon, 4\epsilon, 0.55$ for the domain shown in 2.4e.

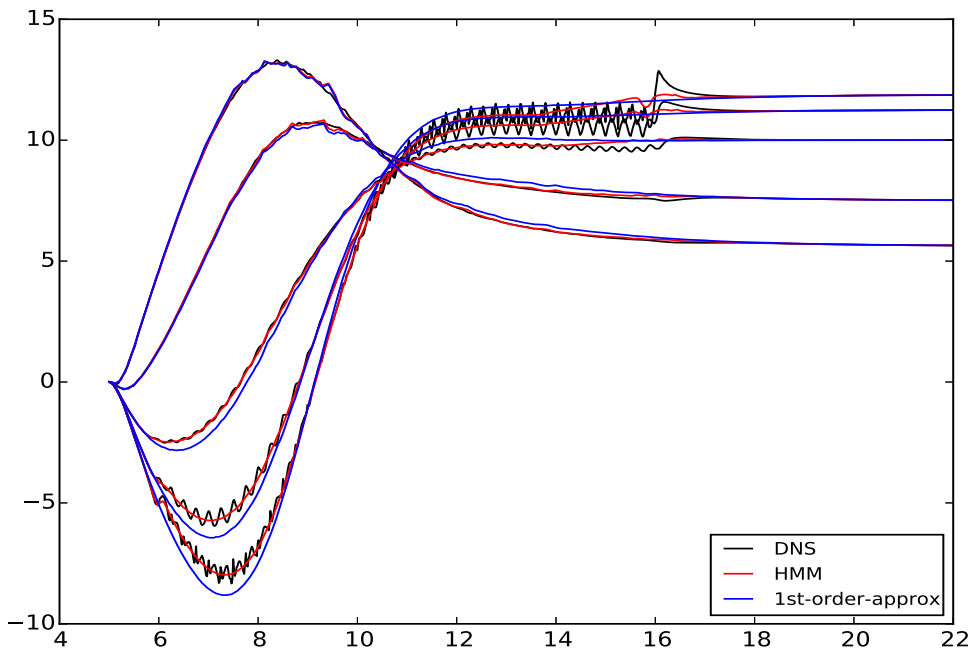


Figure 2.15: Shear $\partial u_1 / \partial x_2$ versus x_1 plotted at the values $x_2 = \epsilon/2, \epsilon, 2\epsilon, 4\epsilon, 0.55$ for the domain shown in 2.4e.

Chapter 3

Wall Bounded Turbulent Viscous Flow

3.1 Introduction to Wall Bounded Turbulence

¹High Reynolds number wall bounded turbulent shear flows are characterized by a separation of scales between the flow in the near wall region, in which mean viscous stresses play an important role, and the flow farther away from the wall, where mean viscous effects are largely negligible. This separation of scales is quantified by the friction Reynolds number $Re_\tau = \delta/\delta_\nu$, where δ is the characteristic length scale of the shear layer, such as a channel half-width, a pipe radius, or a boundary layer thickness, and $\delta_\nu = \nu/u_\tau$ is the viscous length scale, where ν is the kinematic viscosity of the fluid, $u_\tau = \sqrt{\tau_w/\rho}$, τ_w is the mean wall shear stress, and ρ is the fluid density. Both the direct numerical simulation (DNS) and large eddy simulation (LES) of such wall bounded turbulent flows are expensive, as the spatial degrees of freedom required to resolve the near wall layer scale as $\mathcal{O}(Re_\tau^{2.5})$ and $\mathcal{O}(Re_\tau^2)$ for DNS and LES, respectively [165]. For a large class of flows of technological importance, this cost is prohibitive, even on modern high-performance computing systems.

¹The results in this chapter were obtained in collaboration with Robert D. Moser and Björn Engquist.

Thanks to advances in experimental techniques and computational power, the understanding of the physics of wall bounded flows has increased greatly since the earliest investigations by Hagen, Darcy, and Reynolds [48, 93, 187], and the later work by Millikin [162]. It is well known that there is an autonomous near wall cycle of self sustaining mechanisms [96, 112, 115], involving low and high speed streamwise velocity streaks and coherent structures of quasi-streamwise vorticity. Due to a hydrodynamic instability, the streamwise streaks become sinuous and produce regions of large streamwise vorticity. The vortical structures are advected by the mean velocity and give rise to more streamwise velocity streaks, thus repeating the cycle. Jiménez and Pinelli [116] showed that this cycle of near wall dynamics persists without any input from the turbulence farther away from the wall. Moreover, if any element of the cycle is suppressed, the near wall turbulent kinetic energy (TKE) decays, and the flow becomes laminar. However, the large-scale structures in the outer layer do modulate the turbulent fluctuations in the near wall region [80, 108, 158], leaving their “footprint” on the autonomous cycle. This results, for instance, in an Re_τ -dependent peak of the turbulent kinetic energy in the near wall region (see figure 3.1). Their influence increases with increasing Re_τ [53].

Recently, Lee and Moser [143] performed spectral analysis of channel flow DNS data for several different Re_τ (ranging from approximately 550 to 5200) to investigate the relative importance of different length scales to the production, transport, and dissipation of TKE. Their results suggest that the

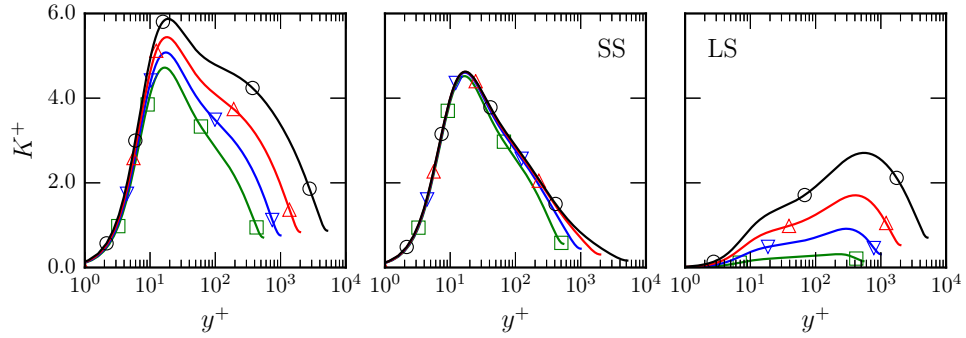


Figure 3.1: Unfiltered, high-pass (SS), and low pass (LS) portion of the turbulent kinetic energy scaled in viscous units with $k_{\text{cut}}\delta_\nu = 0.00628$ ($\lambda_{\text{cut}}/\delta_\nu = 1000$) for a channel flow at various Re_τ (green: $Re_\tau = 550$, blue: $Re_\tau = 1000$, red: $Re_\tau = 2000$, black: $Re_\tau = 5200$). The contributions from the large scales increases with Re_τ , but the contribution from the small scales is largely independent of Re_τ . Figure reproduced from [143] with permission.

small scales in the near wall region behave universally. Indeed, when the energy spectrum is high-pass filtered to only include contributions from wavenumbers with magnitude larger than some $k_{\text{cut}}\delta_\nu = 0.00628$ (corresponding to a wavelength $\lambda_{\text{cut}}/\delta_\nu = 1000$), the resulting energy is found to be independent of Re_τ , as shown in figure 3.1. Similar results were also obtained in [193] for experimental data ranging from $Re_\tau \approx 6000 - 20000$. These works, along with those mentioned above, indicate that the near wall region has universal small scales, independent of Re_τ . The large scale portion of the near wall turbulence, however, is the result of eddies whose size and influence on the turbulent statistics depend on Re_τ .



Figure 3.2: For some fixed outer length scale of interest δ , the physical size of the near wall patch shrinks as Re_τ increases ($Re_\tau^1 < Re_\tau^2$). Here δ could represent, for instance, the characteristic size of the computational domain of a large eddy simulation.

3.2 Multiscale Strategies for Wall Bounded Turbulence

Because of the strict resolution requirements for the accurate direct simulation of turbulent flows, multiscale computational approaches are often the only feasible way to simulate flows of interest in aerodynamics or atmospheric physics, for example. The traditional approaches of Reynolds-Averaged Navier Stokes (RANS) and Large Eddy Simulation (LES), as well as variants such as Partially-Averaged Navier Stokes (PANS) and Detached Eddy Simulation (DES) all rely on a multiscale decomposition of the turbulent velocity fields. These approaches can be and often are combined with other traditional multiscale computational ideas such as adaptive mesh refinement and domain decomposition; see the book by Sagaut et al. [190] for a review.

A difficulty with applying a multiscale framework like HMM to turbulent flows is that it relies on scale separation, while in turbulence this is generally lacking. Given our understanding of the physics of wall-bounded flows specifically, however, it is sensible to design a multiscale approach to

simulating wall bounded turbulent flows that consists of a macroscale model for the Re_τ dependent eddies and a microscale model for the small scale, near wall universal motions; this is essentially the computational paradigm of wall-modeled Large Eddy Simulation (WMLES). Many traditional wall modeling approaches, detailed for example in the reviews of Piomelli and Balaras [181] and Bose et al. [30], can be viewed within the HMM framework. The macroscale model $M(\Psi, D) = 0$ is the filtered Navier-Stokes equations equipped with some subgrid stress model, and the missing data D is a boundary condition at the wall. The microscale model $m(\psi, d) = 0$ could be the logarithmic law-of-the-wall or the Prandtl boundary layer equations, which can take as input d the instantaneous LES velocity \bar{u} (or its gradient $\nabla \bar{u}$) and the LES pressure \bar{p} and in turn estimate the boundary condition D for the LES model.

Other notable multiscale approaches to simulating wall turbulence in the HMM framework include the work of Pasquarelli et al. [175] and Tang and Akhavan [210], in which large eddy simulations are coupled to minimal flow unit simulations. Additionally, Sandham et al. [194] coupled a macroscopic, LES channel flow simulation to a set of microscopic, quasi-DNS (QDNS) simulations localized to the channel walls. The coupling was done concurrently, and the results from each local-in-time run of the microsimulation produced a wall-shear stress which was then interpolated throughout the entire channel and passed to the LES as a boundary condition.

The microscale, QDNS simulations of Sandham et al. provide the mo-

tivation for the current work, in which we endeavor to design a computational model of the universal small scales of turbulent, wall bounded flows in the case of a locally constant mean pressure gradient. In contrast to their work, we focus exclusively on designing the high-fidelity, microscale model and do not explicitly couple it with a macroscopic flow solver, such as RANS or LES. The reasons for this are twofold. Firstly, the viewpoint espoused here is that developing a microscale model that can precompute macroscopic flow quantities of interest, such as mean wall or Reynolds shear stresses, is more appropriate than one that is run on-the-fly. Secondly, it must be recognized that designing and implementing a mathematically coherent and physically accurate LES model for wall turbulence is highly nontrivial. As expressed by William Layton [personal communication], LES is truly “up for grabs” and any group with both strong results and mathematical support will “move the dial to their definition of LES”. Indeed the community’s understanding of the interplay between physical modeling, numerical schemes, and implementation on modern HPC architectures is still evolving; see Sagaut’s excellent book [191], as well as the Ghosal and Moin paper [85] and the more recent work by Yalla et al. [224], for enlightening discussions of these issues.

Accordingly, we describe here a reduced order, computational model of the universal near-wall small scales of turbulent, wall bounded shear flows in the case of a locally constant mean pressure gradient. The primary goal is to accurately represent the contribution of the small scales to the near wall turbulent statistics at a reduced cost relative to a DNS of the entire flow field.

The model is formulated to simulate wall bounded turbulence only in a near wall, rectangular domain Ω localized to the boundary. The size of the domain scales in viscous units, so that as Re_τ increases, the domain shrinks in size relative to the size of the overall flow, as illustrated in figure 3.2, but the number of computational degrees of freedom remains fixed. The primary application target is to generate data to inform a pressure-gradient-dependent wall model for a suitably defined large eddy simulation as suggested, for example, by Coleman et al. [44]. A complementary approach using experimental data is the inner-outer predictive model developed by Mathis et al. [159]. Additionally, the model approach could potentially be used to efficiently study more complicated physics in the near wall region, such as heat transfer, chemical reactions, turbophoresis, or surface roughness.

Section 3.3 below contains a description of the computational model for favorable and negligible constant pressure gradient flows; section 3.4 provides a comparison between the statistics generated by the model and the corresponding quantities from DNS for these cases, and section 3.5 offers a discussion and recommendation for future work.

3.3 Near Wall Patch (NWP) Microscale Model

3.3.1 Notation

In the following discussion, the velocity components in the streamwise (x), wall-normal (y) and spanwise (z) directions are denoted as u , v , and w , respectively, and when using index notation, these directions are labeled 1,

2, and 3, respectively. The expected value is denoted with angle brackets (as in $\langle \cdot \rangle$), and upper case U and P indicate the mean velocity and pressure, so that $\langle u_i \rangle = U_i$. The velocity and pressure fluctuations are indicated with primes, e.g. $u_i = U_i + u'_i$. Partial derivatives shortened to ∂_i signify $\partial/\partial x_i$, differentiation in the direction x_i . The mean advective derivative is $D(\cdot)/Dt = \partial_t(\cdot) + U_j \partial_j(\cdot)$, where Einstein summation notation is implied. In general, repeated indices imply summation, with the exception of repeated Greek indices. Lastly, the superscript ‘+’ denotes non-dimensionalisation with the kinematic viscosity ν and the friction velocity u_τ .

3.3.2 Motivation: computational boundaries

The goal of the computational model is to simulate the turbulent small scales in the near wall region as a function of pressure gradient only in a small, rectangular domain localized to the boundary. This necessarily means placing nonphysical computational boundaries in a region of chaotic, highly nonlinear dynamics. In addition to the standard no-slip condition at the lower boundary $y = 0$, the use of periodic boundary conditions at the side-walls is well established, assuming the flow is statistically homogeneous in these directions. The problem of prescribing appropriate boundary conditions at the upper computational boundary, however, is nontrivial [27, 190]. Once a mathematically well posed condition is prescribed, care must be taken to prevent the approximation inherent in the boundary condition from polluting the turbulent dynamics in the domain’s interior. To address this issue, the model augments the near wall

computational domain with a “fringe region.” In this fringe region, the flow is externally forced to account for the mean flux of momentum through the upper computational boundary that is precluded by the boundary conditions imposed there. The inclusion of such a region increases the computational cost of the model, but it provides the momentum transport needed to create the “correct environment” for the evolution of turbulence in the near wall region. In this way, the fringe region mollifies the effect of the nonphysical computational boundary. Similar techniques are used for designing inflow/outflow conditions in the DNS of turbulent boundary layers [45, 122, 199, 223], for example, as well as in molecular dynamics simulations, often referred to as a “heat-bath” or “thermostat” [26, 225].

If one is interested in the turbulent statistics resulting from a constant pressure gradient near wall region out to a wall-normal height of $y \approx H$, the fringe region consists of a layer from $H \leq y \leq 2H$ in which a horizontally uniform streamwise forcing is applied, as illustrated in figure 4.4.

3.3.3 Mathematical formulation

The near wall patch (NWP) model is defined by the equations of motion and boundary conditions in the rectangular domain $\Omega = [0, L_x] \times [0, L_y] \times$

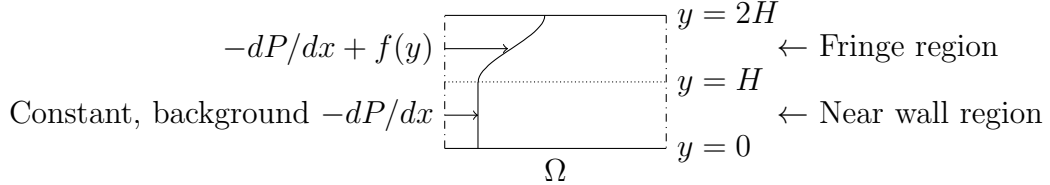


Figure 3.3: The fluid is subject to periodic boundary conditions at the (dash-dotted) side walls, constant Dirichlet/Neumann conditions at the upper boundary $y = 2H$, and the no-slip condition at the wall $y = 0$, as described in (3.1). In addition to the constant pressure gradient assumed to be present in the near wall layer, the model includes an auxiliary pressure gradient in a “fringe region” to account for momentum transport at the computational boundary $y = 2H$.

$[0, L_z]$:

$$\left\{ \begin{array}{ll} \partial_t u_i + u_j \partial_j u_i + \partial_i p' - \nu \partial_j \partial_j u_i = f_i - \partial_i P & \text{in } \Omega \\ \partial_i u_i = 0 & \text{in } \Omega \\ \partial_i P = dP/dx \quad \delta_{i1} \text{ is constant} & \text{in } \Omega \\ u_i \text{ periodic in } x \text{ and } z \text{ directions} & \text{in } \Omega \\ u_i = 0 & y = 0 \\ v = \partial_y w = 0 & y = L_y \\ \partial_y u = \psi \in \mathbb{R} & y = L_y \\ f_i(x, y, z, t) = f(y) \delta_{i1} & \text{in } \Omega. \end{array} \right. \quad (3.1)$$

These are simply the forced incompressible Navier Stokes equations on a periodic domain in the wall-parallel directions, with the no-slip boundary condition at $y = 0$ (the wall), and no-flow through and constant viscous tangential traction $\nu \psi$ in the streamwise direction (x) specified at the top $y = L_y$. The term dP/dx models the mean pressure gradient in the real turbulent flow being modeled, while p' is the NWP model’s pressure field that evolves in time and space to maintain incompressibility. It only remains to specify ψ and the

forcing function $f(y)$. The former represents the viscous flux of mean momentum through the top, and the latter is a source of streamwise momentum that makes up for the missing turbulent flux of mean streamwise momentum through the upper computational boundary, owing to the boundary conditions that imply that the Reynolds stress vanishes there.

The forcing function $f(y)$ is non-zero only in the fringe region $y > L_y/2$, and is constructed such that

$$\int_0^{L_y} f(y) dy = -\tau_{\text{turb}}, \quad (3.2)$$

where τ_{turb} is the turbulent flux of mean momentum through $y = L_y$ in the turbulent flow being modeled.

In the real turbulent flow with a constant mean pressure gradient, the mean streamwise momentum equation integrated over $[0, L_y]$ yields:

$$-\frac{dP}{dx}L_y + \left(\nu \frac{\partial U}{\partial y} \Big|_{y=L_y} - \tau_{\text{turb}} \right) - \tau_w = 0 \quad (3.3)$$

$$\implies \tau_w = -\frac{dP}{dx}L_y + \tau_{\text{top}}, \quad (3.4)$$

where statistics are assumed to be homogeneous in both the stream and spanwise directions. The term in parentheses, τ_{top} , is the total momentum flux (viscous plus turbulent) through $y = L_y$, and it, along with dP/dx , determines the mean wall shear stress τ_w .

The mean streamwise stress balance for the NWP model system (3.1) is

$$\nu \frac{\partial U}{\partial y} - \langle u'v' \rangle + \int_0^y f(s)ds = y \frac{dP}{dx} + \tau_w. \quad (3.5)$$

The boundary conditions in (3.1) and the constraint (3.22) imply that at $y = L_y$, (3.5) becomes

$$\nu\psi + \int_0^{L_y} f(s)ds = L_y \frac{dP}{dx} + \tau_w \quad (3.6)$$

$$\implies \tau_w = -\frac{dP}{dx} L_y + \nu\psi - \tau_{\text{turb}}, \quad (3.7)$$

so that for fixed L_y , the parameters ν , τ_{turb} , ψ , and dP/dx determine τ_w . Dimensional analysis therefore implies that there is a two-parameter family of possible turbulent flows to model.

By specifying ψ and τ_{turb} so that $\nu\psi - \tau_{\text{turb}} = \tau_{\text{top}}$, the NWP model's mean stress balance augmented with the forcing function f (3.7) will be consistent with that of the real turbulent flow being modeled (3.4).

3.3.4 Physical parameters

The total mean stress at $y = L_y$ is given by

$$\tau_{\text{tot}} := \nu\psi - \tau_{\text{turb}}. \quad (3.8)$$

In wall units, τ_{tot} is simply a function of dP^+/dx^+ :

$$\tau_{\text{tot}}^+ = 1 + L_y^+ \frac{dP^+}{dx^+}. \quad (3.9)$$

The pressure gradient dP^+/dx^+ is thus one parameter defining a model case, and its values for the three cases presented—two favorable pressure gradient cases and one zero pressure gradient case—are shown in table 3.1. The values for τ_{tot}^+ are also shown for convenience, but of course they are simply determined via (3.9).

The second parameter to define a NWP model case is ψ^+ ; it determines the portion of τ_{tot}^+ that comes from mean viscous stress. For all of the statistics reported in section 3.4, however, the actual value of ψ^+ used was found to be insignificant. For each case listed in table 3.1, an initial ψ_{dns}^+ was determined from available DNS data. Results were then compared from runs with $\psi^+ = \psi_{\text{dns}}^+$, $\psi^+ = 2\psi_{\text{dns}}^+$, $\psi^+ = \psi_{\text{dns}}^+/2$, and $\psi^+ = 0$, and the differences were found to be negligible. Hence, there is really only a one-parameter family of possible turbulent flows to explore with the model, and for simplicity, ψ^+ is set to zero.

Figure 3.4 illustrates the statistically converged stress balances for these model cases. Included in the figure is a stress profile resulting from simulating the equations of motion (3.1) *without* the extra momentum flux provided by the auxiliary pressure gradient f (the cyan curve). In that case, a similar analysis to that shown in equations (3.5)–(3.7) above shows that the statistically converged stress profile is simply a linear function with values $\tau_w^+ = 1$ and ψ^+ at $y^+ = 0$ and $y^+ = L_y^+$, respectively. It is clear that this stress profile is in poor agreement with the target profiles (3.9), which is to be expected, since $\psi^+ = 1/(\kappa L_y^+)$ in the log-region. Moreover, this discrepancy increases with decreasing dP^+/dx^+ (corresponding to increasing Re_τ when comparing to a channel flow), illustrating the utility of including the extra momentum flux provided by the auxiliary forcing term f .

Case name	NWP1000	NWP5200	NWPzpg
$-dP^+/dx^+$	$(1000.512)^{-1}$	$(5185.89)^{-1}$	0
τ_{tot}^+	0.4003	0.8843	1

Table 3.1: Prescribed mean pressure gradient and the resulting total momentum flux τ_{tot} at $y = L_y$ for the three model cases presented. The favorable pressure gradient parameters were selected to match the channel data posted to <https://turbulence.oden.utexas.edu/>.

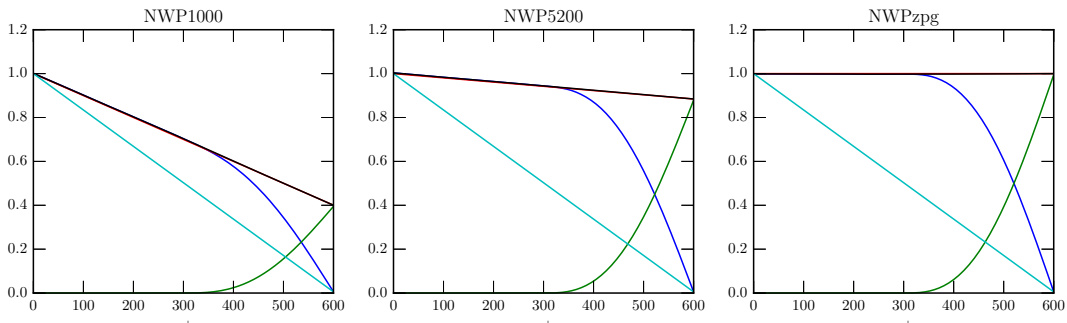


Figure 3.4: Blue: model total stress $\tau_{\text{model}}^+(y^+) = \partial U^+ / \partial y^+ - \langle u'v' \rangle^+$; Red: target total stress $\tau_{\text{target}}^+ = 1 + y^+ dP^+/dx^+$; Green: Primitive $F^+(y^+)$ of forcing function f^+ ; Black: $\tau_{\text{model}}^+(y^+) + F^+(y^+)$; Cyan: total stress for a simulation *without* the forcing function f^+ ; for all the three model cases listed in table 3.1.

3.3.5 Computational parameters

The remaining model parameters, consistent for all three simulation cases, are summarized in table 3.2. The size of the rectangular domain Ω is taken to be $L_x^+ = L_z^+ = 1500$ and $L_y^+ = 600$; these values, while somewhat arbitrary, were determined through a combination of numerical experimentation and the spectral analysis of Lee and Moser [143]. Their work suggests that the contributions to the turbulent kinetic energy from modes with wavelengths $\lambda^+ < 1000$ are universal and Re_τ -independent in a region below a wall-normal distance of approximately $y^+ = 300$. Accordingly, $L_y^+ = 2 \cdot 300 = 600$ is chosen to allow for a sufficiently large fringe-region to mollify the effect of the nonphysical computational boundary at $y = L_y$ (see figure 4.4), and both L_x^+ and L_z^+ are taken to be at least 1000.

For the domain size in the stream/spanwise directions, there generally is a balance between computational cost and the accuracy of the model, as defined by a comparison of the model's energy spectral density with that of large scale DNS. In particular, a variety of domain sizes were tested, ranging from $L_x^+ = L_z^+ = 1000$ to approximately 3500. Increasing L_x and L_z results in better agreement of the model's low-wavenumber, large-scale portion of the energy spectral density with the corresponding portion computed from DNS. The high-wavenumber, small-scale portion of the model's energy density, however, was insensitive to the domain size, so long as L_x and L_z were not taken to be too close to $L_x^+ = L_z^+ = 1000$. In particular, $L_x^+ = L_z^+ = 1500$ was found to be the smallest domain size capable of reproducing the universal

small-scales discussed in section 3.4.3.

Given some target turbulent flux of mean momentum τ_{turb} , the auxiliary forcing f must satisfy (3.22), but it is otherwise unconstrained. For the simulations reported here, f is defined explicitly to be

$$f(y) = \begin{cases} 4\tau_{\text{turb}}/L_y^4 (L_y - 2y)^2 (5L_y - 4y), & y \in [L_y/2, L_y] \\ 0, & y \in [0, L_y/2], \end{cases} \quad (3.10)$$

which was chosen to satisfy $f(L_y/2) = f'(L_y/2) = f'(L_y) = 0$.

3.3.6 Numerical implementation and resolution

The model (3.1) is solved numerically using the velocity-vorticity formulation due to Kim, Moin, and Moser [126] and is described in more detail in section 3.6.4. The equations of motion are discretized with a Fourier-Galerkin method in the stream/spanwise directions and a seventh order B-spline collocation method in the wall-normal direction [31, 134, 141]. They are integrated in time with a low-storage, third order Runge-Kutta method that treats diffusive and convective terms implicitly and explicitly, respectively [204]. The numerical resolution in both space and time is consistent with that of DNS. The number of Fourier modes, and hence the numerical resolution, used in each simulation is listed in table 3.2, and can be compared with, for instance, table 1 in [141]. In addition, the collocation point spacing in the wall-normal direction is similar to previous DNS studies; the total number of collocation points N_y is taken to be equal to the number of collocation points below $y^+ = 600$ in [141]. They are then distributed in the near wall region according to the same (shifted and rescaled) stretching function.

ψ^+	$L_x^+ = L_z^+$	L_y^+	N_x	N_z	N_y	Δx^+	Δz^+	Δy_w^+
0	1500	600	120	256	192	12.5	5.86	0.002817

Table 3.2: Summary of simulation parameters consistent for all simulation cases; ψ is the prescribed value for the Neumann boundary condition in (3.1). N_x and N_z refer to the number of Fourier modes, while N_y is the number of B-spline collocation points. $\Delta x = L_x/N_x$ and similarly for Δz . Δy_w is the collocation point spacing at the wall.

The model is implemented with a modified version of the PoongBack DNS code [140, 144], and the initial condition is taken from a restart file from a DNS run that is truncated to fit in Ω at the resolutions listed in table 3.2 and modified to satisfy the boundary conditions 3.1.

3.3.7 Statistical convergence

The method of Oliver et al. [171] is used to assess the uncertainty in the statistics reported due to sampling noise. For each pressure gradient case, statistics are collected by averaging in time until the estimated statistical uncertainty in the mean stress profiles is less than a few percent. For the cases in table 3.2 reported here, the sampling error is less than three percent, as shown in figure 3.5.

3.4 Numerical Results

The statistics reported here were computed from the three near wall patch model cases NWP1000, NWP5200, and NWPzpg and are compared to available DNS data. The favorable pressure gradient cases are compared to the

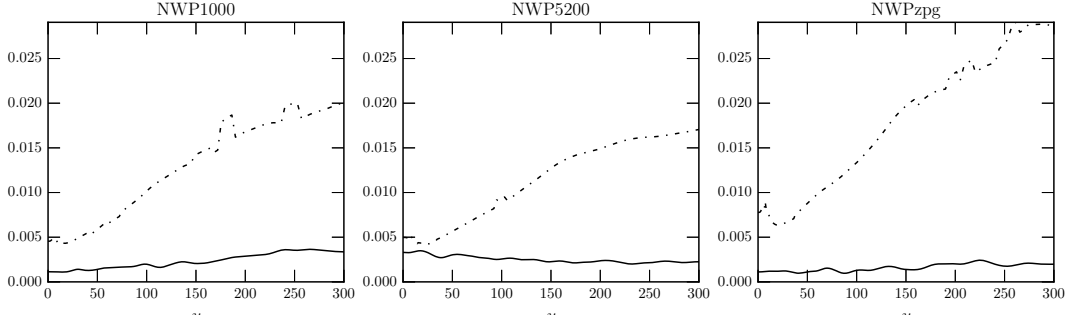


Figure 3.5: Statistical convergence for the model cases listed in table 3.2—solid lines: Absolute error $|\tau_{\text{model}}^+(y^+) - \tau_{\text{target}}(y^+)|$, where $\tau_{\text{model}}^+ = \partial U^+ / \partial y^+ - \langle u'v' \rangle^+$ and $\tau_{\text{target}}^+ = 1 + y^+ dP^+ / dx^+$; dashed lines: Standard deviation of the estimated statistical error for τ_{model}^+ in the region $y^+ \in [0, 300]$.

corresponding channel flow DNS of [141, 143] at $Re_\tau = 1000$ and $Re_\tau = 5200$ —referred to below as LM1000 and LM5200—whose statistics are available at <https://turbulence.ices.utexas.edu>. The zero pressure gradient case is compared to the turbulent boundary layer DNS described in [29, 199, 201]; the data used for comparison corresponds to the streamwise location at which $Re_\tau = 2000$, and can be found at https://torroja.dmt.upm.es/turbdata/blayers/high_re/. It is referred to below as SJM2000.

3.4.1 Mean velocity and shear stresses

The most basic requirement of any model of near wall turbulence is to correctly capture the equilibrium velocity profile and the associated mean wall shear stress. Figure 3.6 demonstrates that the near wall patch (NWP) model’s

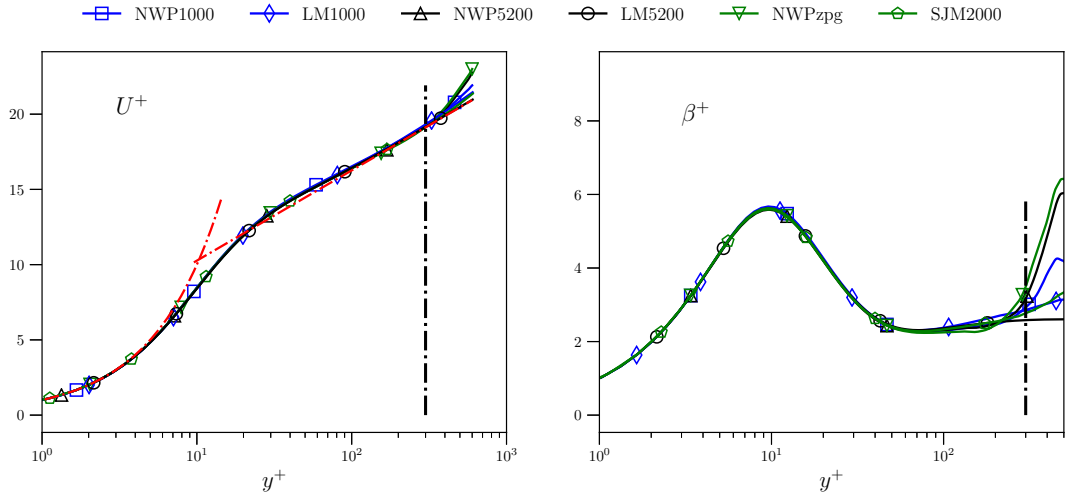


Figure 3.6: Mean velocity U^+ (left) and the indicator function $\beta^+ = y^+ \partial_{y^+} U^+$ (right) versus $\log(y^+)$. The black dashed-dotted vertical line marks $y^+ = 300$, and the red dashed-dotted lines plot the law-of-the-wall $U^+ = y^+$ and $U^+ = (1/\kappa) \log(y^+) + B$, where $\kappa = 0.384$ and $B = 4.27$ [141].

mean velocity U^+ and log-law indicator function

$$\beta^+(y^+) := y^+ \frac{\partial U^+}{\partial y^+} \quad (3.11)$$

agree with their DNS counterparts. The relative error in U^+ is less than 0.6% for $y^+ \in [0, 300]$, and the error is similarly small for β^+ in the range $y^+ \in [0, 100]$. However, there is mild disagreement of β in the range $y^+ \in [100, 300]$. As expected, the profiles diverge for $y^+ > 300$. The NWP model's Reynolds shear stress $\langle u'v' \rangle$ is in excellent agreement with that of the DNS in the region $y^+ \in [0, 300]$, as expected given the agreement of the mean velocity; see figure 3.7. For the channel cases, the error is less than 0.5%, and for the zero pressure gradient case the error is below 4%. In the former, the total stress at $y = L_y$

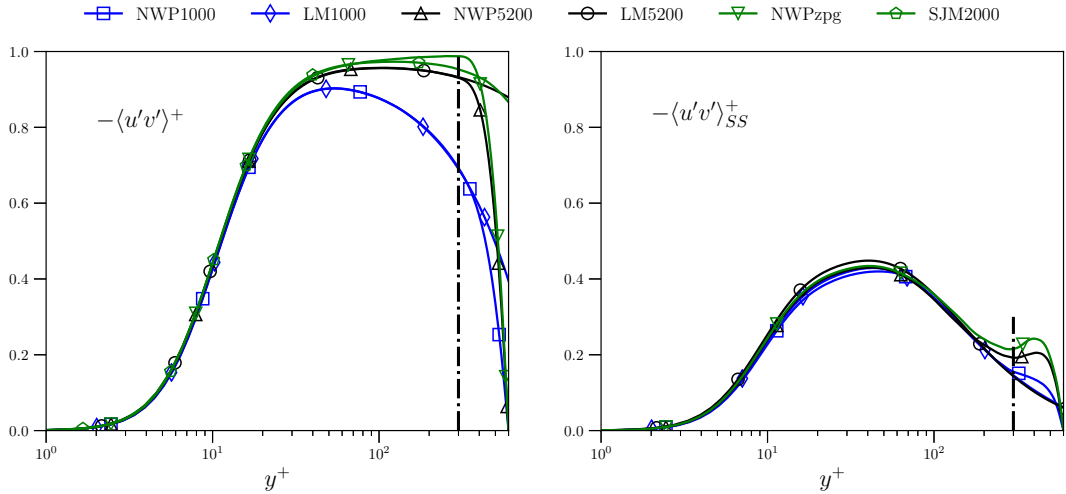


Figure 3.7: (a) Reynolds stress $-\langle u'v' \rangle^+$ and (b) the filtered Reynolds stress $-\langle u'v' \rangle_{SS}^+$ (defined by (3.18)) as a function of $\log(y^+)$, discussed in section 3.4.3. The black dashed-dotted vertical line marks $y^+ = 300$.

is known analytically as $\tau_{\text{tot}}^+ = 1 + L_y^+ dP^+/dx^+$ and is used to define $f(y)$ in (3.22), (3.8), and (3.9). In the latter, the same relations are used, though they are approximate due to the streamwise growth of the near wall layer in a boundary layer. This may explain the relatively larger discrepancy between the $\langle u'v' \rangle$ profiles for the boundary layer. In both instances, recall that $\langle u'v' \rangle$ necessarily vanishes at the upper computational boundary as a consequence of the boundary condition $v = 0$ in (3.1). The accuracy of the Reynolds shear stress profiles in spite of this condition demonstrates the utility of the forcing function f in enabling momentum transport to the near wall region $y^+ \in [0, 300]$.

3.4.2 Energy spectral density

For two points $(x, y, z), (x', y, z') \in \mathbb{R} \times [0, 2\delta] \times \mathbb{R}$ in an infinitely long channel, define the separation distances $r_x = x - x'$ and $r_z = z - z'$. For a turbulent flow that is statistically homogeneous in the stream and spanwise directions, the two point correlation tensor

$$R_{ij}(r_x, y, r_z) := \langle u'_i(x + r_x, y, z + r_z) u'_j(x, y, z) \rangle \quad (3.12)$$

is a function only of r_x , y , and r_z . Taking the Fourier transform of (3.12) in the variables r_x and r_z defines the spectral density $E_{ij}(k_x, y, k_z)$, which encodes the average contribution to the Reynolds stress tensor from different length scales as a function of the wall-normal variable y . The Reynolds stress tensor can be recovered by taking the limit $(r_x, r_z) \rightarrow (0, 0)$ in (3.12), or by integrating the spectral density over all wavenumbers

$$\langle u'_i u'_j \rangle(y) = \int \int E_{ij}(k_x, y, k_z) dk_x dk_z. \quad (3.13)$$

For a wall bounded flow in a full size domain, the low-wavenumber contributions to the Reynolds stress represent the mean influences of the large scale structures on the near wall dynamics. As is well known [108, 142, 143, 158, 193], these low-wavenumber features of the near wall flow depend on Re_τ . In contrast, there is evidence that the high-wavenumber (small-scale) contributions to the Reynolds stress profiles are universal and independent of Re_τ [143, 193]. By design, the NWP model's domain size does not allow accurate representation of the very large-scale structures known to exist in the near wall

region, and thus one cannot expect its Reynolds stress profiles to agree with those computed from DNS (with the exception of the shear stress $\langle u'v' \rangle$, as discussed in section 3.4.1). Instead, one expects the NWP model to correctly capture the dynamics of the universal small scales elucidated by [193] and [143] associated with the autonomous cycle of [116].

To determine whether or not this is the case, the model's spectra E_{ij} are compared to their DNS counterparts. The spectra are visualized in so-called log-polar coordinates [143], in which the wavenumber magnitude $k = \sqrt{k_x^2 + k_z^2}$ is represented on a logarithmic scale. For fixed wall-normal location, the log-polar coordinates are defined as

$$\begin{aligned} k_x^\# &:= \frac{k_x}{k} \log_{10} \left(\frac{k}{k_{\text{ref}}} \right) \\ k_z^\# &:= \frac{k_z}{k} \log_{10} \left(\frac{k}{k_{\text{ref}}} \right) \end{aligned} \quad (3.14)$$

where k_{ref} is an arbitrary reference wavenumber that must be smaller than the smallest nonzero wavenumber included in the spectrum, taken here to be $k_{\text{ref}}^+ = 1/50\,000$. Two advantages of these coordinates are that lines of constant k_z/k_x have slopes of k_z/k_x , and lines of constant magnitude k map to circles. In this way, the orientation and alignments of the Fourier modes are easily interpreted; see figure 3.8 for a visualization and [143] for a more detailed discussion.

The two-dimensional spectral densities of the streamwise and wall-normal velocity variances are shown in figures 3.9 and 3.10, respectively. The spectra are visualized at the wall-normal locations $y^+ = 15$, $y^+ = 100$

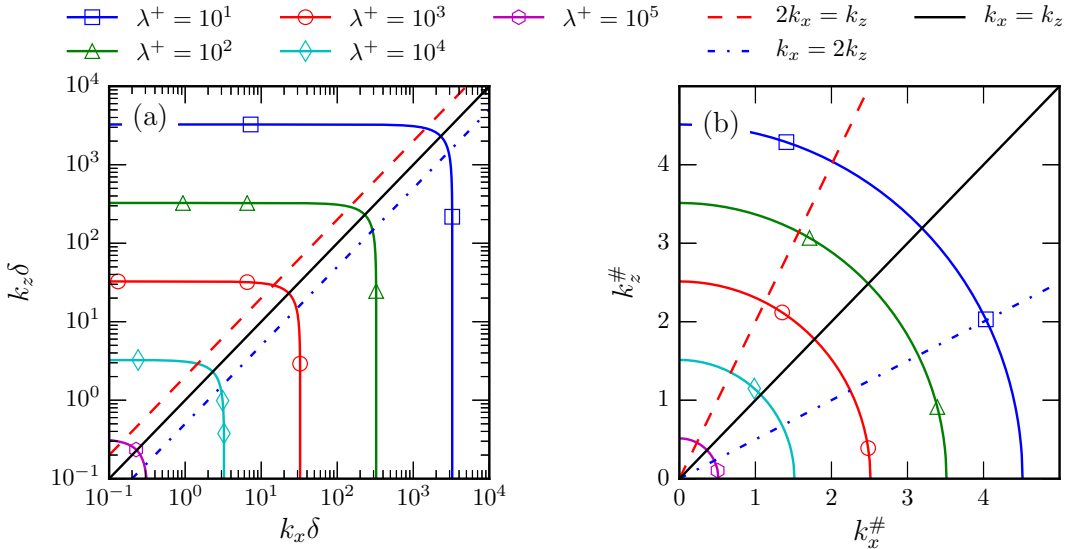


Figure 3.8: Comparison of log-polar and “log-Cartesian” coordinates. Figure reproduced from Lee and Moser [143] with permission.

and $y^+ = 300$ for the favorable pressure gradient simulations NWP1000, NWP5200, LM1000, and LM5200.

In each of the cases, the streamwise velocity spectra E_{11} consist primarily of energy concentrated along the $k_z^{\#}$ axis, with Fourier modes for which $k_z/k_x \gtrsim 10$ [143]. These correspond to structures that are strongly elongated in the streamwise x -direction, such as the well-known, near wall low and high speed streaks. The channel flow data LM1000 and LM5200 (columns two and four in figure 3.9) show that this energy exhibits two distinct features. The first is an “inner energy site” [193], a triangular shaped region in the near wall layer $y^+ \approx 15$ distributed primarily between wavelengths $\lambda^+ = 100$ and $\lambda^+ = 1000$ that can be attributed to the autonomous near wall dynamics described by

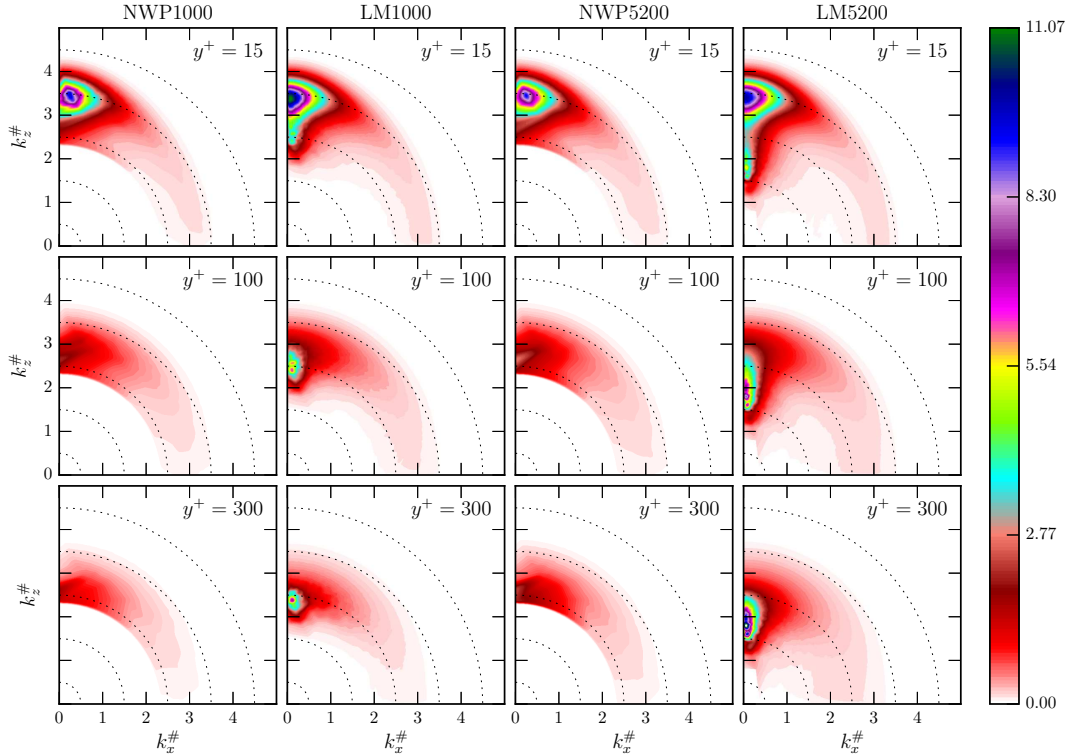


Figure 3.9: Two-dimensional spectra of the streamwise velocity variance $\langle u'u' \rangle^+$ in log-polar coordinates, as defined by equation (3.14). $\lambda^+ = 10$ on the outermost dotted circle and increases by a factor of 10 for each dotted circle moving inward.

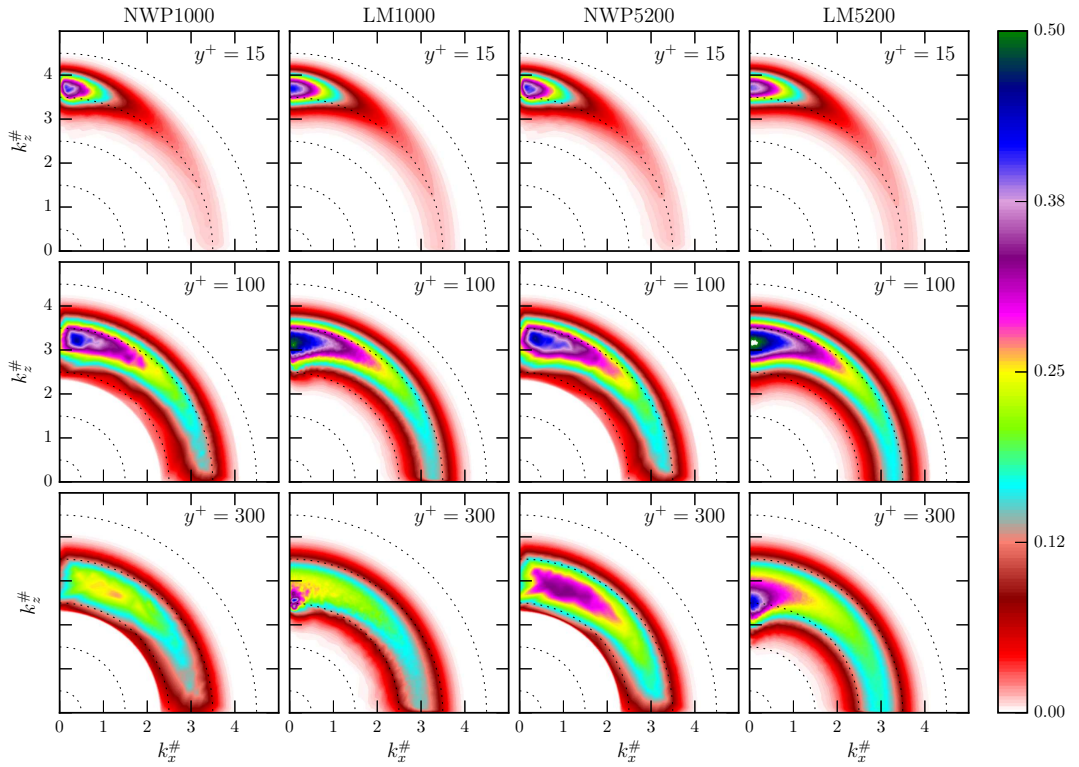


Figure 3.10: Two-dimensional spectra of the wall-normal velocity variance $\langle v'v' \rangle^+$ in log-polar coordinates, as defined by equation (3.14). $\lambda^+ = 10$ on the outermost dotted circle and increases by a factor of 10 for each dotted circle moving inward.

[96, 112, 116], and others. The model E_{11} spectra, shown in columns one and three in figure 3.9, qualitatively reproduce the inner energy site, suggesting that it captures the dynamics of the near wall, small scale energetic motions.

The second feature is a concentration of energy at relatively low wavenumbers (in the range $1000 < \lambda^+ < 10\,000$) along the $k_z^\#$ axis at each of the wall-normal locations $y^+ = 15$, $y^+ = 100$, and $y^+ = 300$. These are due to the very large scale motions (VLSMs) imposed from the outer layer flow described by [108] and [158]. These VLSMs contribute energy in the near wall region around $y^+ = 15$, and farther away from the wall they are responsible for the majority of the turbulent kinetic energy. As both y^+ and Re_τ increase, the energy becomes more concentrated and is found at larger wavelengths, consistent with the attached eddy hypothesis of [214]. In addition, the VLSMs modulate the near wall cycle through nonlinear interactions, creating large scale variations in the local wall shear stress that result in local variations in the dominant (most-energetic) wavelength [143]. Consequently, the spectral peak of the inner energy site for the DNS data is reduced and “smeared out” as a function of Re_τ . For example, the $Re_\tau = 5200$ peak is about ten percent lower than the $Re_\tau = 1000$ peak.

By design, the NWP model can only support modes with wavelengths less than or equal to $L_x^+ = L_z^+ = 1500$, meaning the VLSMs present in real wall bounded turbulence are not represented by the model. As a result, there is no energy associated with such large scale structures; the concentration of energy at low wavenumbers along the $k_z^\#$ axis (corresponding to wavelengths

$\lambda^+ \gtrsim 1000$) present in the DNS spectra is not present in that of the model. This is true both in the near wall region and farther away from the wall at $y^+ = 100$ and $y^+ = 300$.

Furthermore, the NWP model does not capture the nonlinear modulations of the autonomous cycle by the VLSMs. For instance, even though the model represents wavenumbers along the $\lambda^+ = 1000$ band, its spectra is not simply a spectral truncation of the DNS spectra. Additionally, the peak of the inner energy site is nearly identical for the two model cases, differing by only a few percent. These differences between spectra of the model and DNS highlight the important role the VLSMs play in the turbulent near wall layer.

The E_{22} spectra are largest in the wavenumber regions in which the E_{11} spectra are peaked, as discussed in [143]. Additionally, the distribution of energy generally becomes more isotropic with increasing wall-normal distance y^+ . Figure 3.10 shows that the DNS energy density E_{22} is primarily, but not exclusively, located at the small scales, i. e. at wavenumbers $\lambda^+ < 1000$. Because the NWP model adequately resolves such structures, its energy density E_{22} is in overall good agreement with the DNS spectra, especially in the near wall region. Farther away from the wall the agreement is not as good since the DNS spectra are peaked at lower wavenumbers. Accordingly, the model's unfiltered $\langle v'v' \rangle$ profiles shown in figure 3.12 show excellent agreement with the corresponding DNS profiles in region $y^+ \in [0, 300]$; they are nearly identical for $y^+ \lesssim 50$ and only display slight discrepancies for $y^+ \in [50, 300]$.

Lastly, fidelity of the NWP model's energy density E_{33} (not shown) in

reproducing the DNS spectra is similar to the E_{11} spectra. It clearly approximates the small scales in the near wall region well, but it fails to capture the modulation by the large scale structures at each wall-normal location.

3.4.3 Universality of small scales

To better quantify the universality of the small scales and assess the NWP model's ability to reproduce them, the energy spectral density is high-pass filtered and then integrated to measure the energy residing in the small scales. Let \mathcal{K} denote the set of wavenumbers supported by a simulation, and let $k_{\text{cut}} = 2\pi/\lambda_{\text{cut}}$ with $\lambda_{\text{cut}}^+ = 1000$. Define \mathcal{K}_{SS} to be the subset of \mathcal{K} with the property that $(k_x, k_z) \in \mathcal{K}_{SS}$ if

$$\min\{|k_x|, |k_z|\} > k_{\text{cut}}, \quad (3.15)$$

visualized in figure 3.11 (left). The \mathcal{K}_{SS} sets are meant to contain large wavenumbers associated with the universal small scales. Here k_{cut} is chosen based on the two-dimensional spectra in [143], where it is observed that the energy associated with the autonomous cycle has $\lambda^+ < 1000$.

Note the high-pass filter (3.15) is slightly different than the L^2 filter

$$\sqrt{k_x^2 + k_z^2} > k_{\text{cut}} \quad (3.16)$$

used in [143] and visualized in figure 3.11 (right). In particular, the wavenumbers on the axis $k_x = 0$ (respectively $k_z = 0$) with $k_z > k_{\text{cut}}$ (resp. $k_x > k_{\text{cut}}$) are filtered out by (3.15) but not by (3.16). These axes contain the NWP

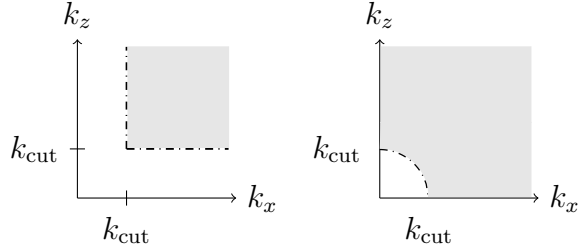


Figure 3.11: (Left) The shaded gray region indicates the subset (in the first quadrant) of wavespace \mathcal{K}_{SS} defined by (3.15). (Right) the corresponding region defined instead by the circular, L^2 filter (3.16) used in [143].

model's approximation to the large scale motions present in a DNS that do not "fit" in the near wall patch domain. Such motions correspond to wavenumbers smaller than $2\pi/L_x = 2\pi/L_z$, and they are not well represented by the NWP model. Hence, they are filtered out by (3.15). The approximation can be improved by increasing L_x and L_z (confirmed by numerical tests), although this of course increases the model's overall computational cost.

Given \mathcal{K} and \mathcal{K}_{SS} , the Reynolds stresses are

$$\langle u'_i u'_j \rangle(y) = \sum_{(k_x, k_z) \in \mathcal{K}} E_{ij}(k_x, y, k_z), \quad (3.17)$$

and the small scales energy can be quantified as

$$\langle u'_i u'_j \rangle_{SS}(y) = \sum_{(k_x, k_z) \in \mathcal{K}_{SS}} E_{ij}(k_x, y, k_z). \quad (3.18)$$

The velocity covariance $\langle u'v' \rangle$ and variances $\langle u'_\alpha u'_\alpha \rangle$, $\alpha = 1, 2, 3$ and their high-pass filtered counterparts are shown in figures 3.7 and 3.12, respectively. As previously mentioned, the model's unfiltered $\langle u'v' \rangle$ and $\langle v'v' \rangle$ profiles both agree quite well with the corresponding DNS profiles. The model's

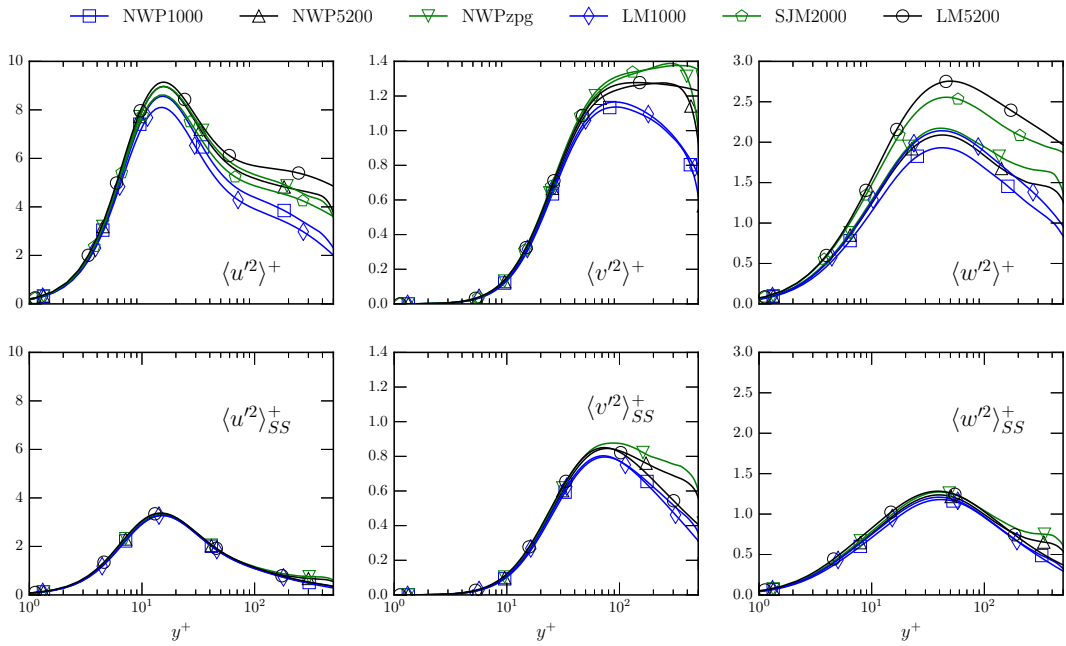


Figure 3.12: Velocity variances $\langle u'_\alpha u'_\alpha \rangle^+$ (top) and the corresponding high-pass filtered quantities $\langle u'_\alpha u'_\alpha \rangle_{SS}^+$ (bottom) as a function of $\log(y^+)$.

streamwise and spanwise velocity variances, however, display nontrivial discrepancies with the DNS profiles, as expected from the observed differences in the two dimensional spectra. In contrast, the model's high-pass filtered profiles all show excellent agreement with the high-pass filtered DNS quantities. In all cases the agreement is excellent in the region $y^+ \in [0, 100]$, although there are some relatively mild discrepancies for $y^+ \in [100, 300]$. Moreover, it is clear that the high-pass filtered quantities are nearly Re_τ independent; the collapse of the $\langle u'u' \rangle_{SS}$ profiles is particularly convincing. Although two-dimensional spectra data is not available for the zero-pressure gradient DNS case SJM2000, the $\langle u'_i u'_j \rangle_{SS}$ profiles computed from the case NWPzpg are included for completeness; they display the same universal behavior as the favorable pressure gradient flows. These observations lend support to the conclusion that the small scales in the near wall region are universal, and that the difference in the Reynolds stress profiles as a function of Re_τ is due to the increasing influence of the VLSMs. Previous results of this type obtained in both [143] and [193] involve high-pass filtering the *entire* turbulent flow field, in which there are nonlinear interactions between wavenumbers across all the scales of motion. It is particularly remarkable, however, that the NWP model reproduces the universal behavior of the small scales *without* the dynamic modulation of the near wall autonomous cycle by the large scale structures.

3.4.4 Production

The production of turbulent kinetic energy in a wall bounded flow is primarily due to the large mean velocity gradient in the wall normal direction $\partial U / \partial y$. In a flow that is homogeneous in the stream/spanwise directions with $V = W = 0$, the only $\langle u'_\alpha u'_\alpha \rangle$ term with a nonzero production is $\langle u' u' \rangle$; it is given by

$$\mathcal{P}_{11} = -2 \frac{\partial U}{\partial y} \langle u' v' \rangle. \quad (3.19)$$

The two dimensional spectra of \mathcal{P}_{11} is accordingly defined as

$$E_{11}^P(k_x, y, k_z) := -2 \frac{\partial U}{\partial y}(y) E_{12}(k_x, y, k_z). \quad (3.20)$$

The spectral analysis of channel flow data in [143] demonstrated that in contrast to the near wall energy spectra E_{11} , the near wall production spectra E_{11}^P contains only a high wavenumber peak (see columns two and four in figure 3.13). It follows that the large scales in the near wall region, and hence the energy that they contain, are due to energy transport (either in y or in scale), rather than local production. This observation suggests that the NWP model should be able to capture the near wall energy production, even though the VLSMs are not present. The production spectra shown in figure 3.13 show that this is indeed true. At both $y^+ = 15$ and $y^+ = 30$, the NWP1000 and NWP5200 spectra are qualitatively similar to that of DNS, including the regions of negative production occurring over a range of scales around $\lambda^+ = 100$. Farther away from the wall, the large scale structures increasingly influence the energy production, and their influence increases with Re_τ . At $y^+ = 300$, the

large scale influences dominate the DNS production spectra, and the model is not able to reproduce such low wavenumber features.

The one-dimensional, premultiplied production profiles are shown in figure 3.14, and they are consistent with the aforementioned observations regarding the two-dimensional spectra. The DNS profiles are approximately Re_τ -independent for $y^+ \lesssim 70$, the corresponding model profiles show strong agreement for $y^+ \lesssim 100$, and they begin to show modest discrepancies for $y^+ \gtrsim 200$.

3.4.5 Dissipation, pressure strain and transport

After being produced by the mean, turbulent kinetic energy is redistributed across scales and velocity components, transported both towards and away from the wall, and ultimately dissipated by viscosity. The relative strength, or importance, of these processes as a function of wall-normal distance can be measured by the terms in the Reynolds stress budget equation [182]. Exhaustive analyses of the behavior of these terms for wall bounded flows can be found in [18, 106, 143, 163, 164, 188], and other references therein. A general conclusion to be drawn from these works is that, similar to the production and velocity variances, the small scale contributions to the terms in the budget equation are universal in the near wall region, and differences in the profiles as a function of Re_τ can be attributed to modulations by large scale motions. As a consequence, the terms in the budget equation produced by the model are seen to compare favorably with those produced by DNS in

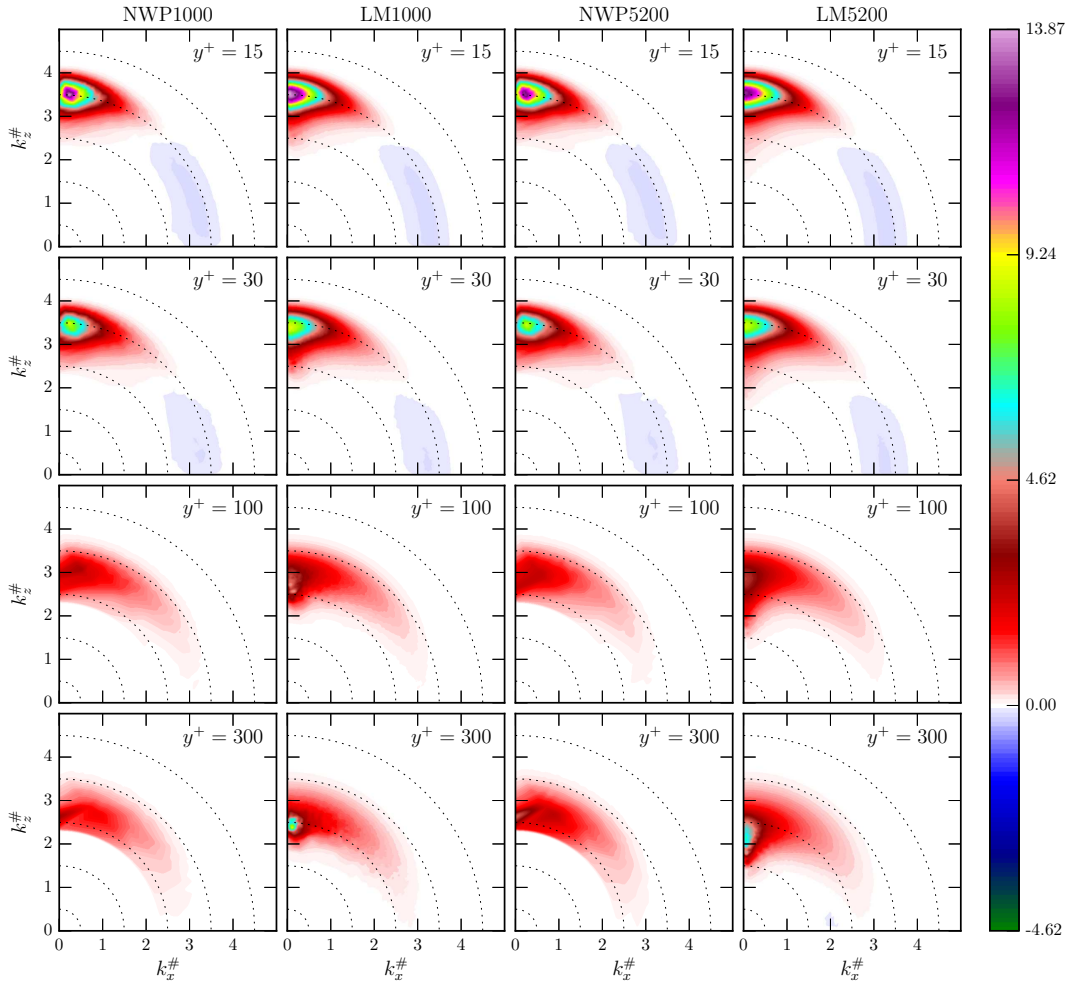


Figure 3.13: Two-dimensional, premultiplied spectra $y^+ (E_{11}^{\mathcal{P}})^+$ in log-polar coordinates, as defined by equation (3.14). $\lambda^+ = 10$ on the outermost dotted circle and increases by a factor of 10 for each dotted circle moving inward.

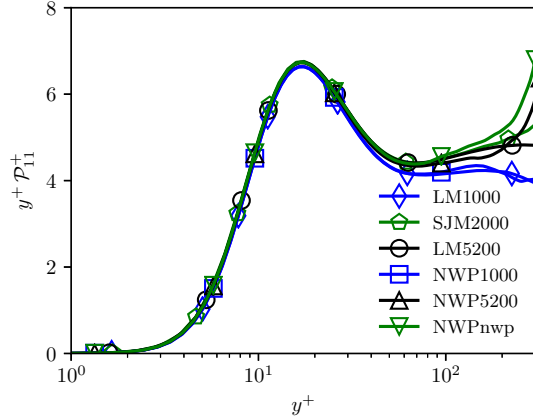


Figure 3.14: Profiles of the premultiplied $\langle u'u' \rangle$ production \mathcal{P}_{11}^+ versus $\log(y^+)$ in the region $y^+ \in [0, 300]$.

the region $y \in [0, 300]$. The model's premultiplied dissipation

$$\epsilon_{\alpha\alpha} = -2\nu \left\langle \frac{\partial u'_\alpha}{\partial x_k} \frac{\partial u'_\alpha}{\partial x_k} \right\rangle \quad (3.21)$$

profiles shown in figure 3.15, for example, are in good agreement with the corresponding DNS profiles in the range $y^+ \in [0, 100]$, show modest departures from the DNS profiles for $y^+ \in [100, 300]$, and completely diverge for $y^+ > 300$, as expected. The pressure strain and viscous, pressure, and turbulent transport terms (not displayed), all feature similar or better agreement than the dissipation profiles.

3.5 NWP Discussion

3.5.1 Summary: modeling assumptions and limitations

The near wall patch (NWP) computational model of wall bounded turbulence described here consists of a rectangular domain $\Omega = [0, L_x] \times [0, L_y] \times$

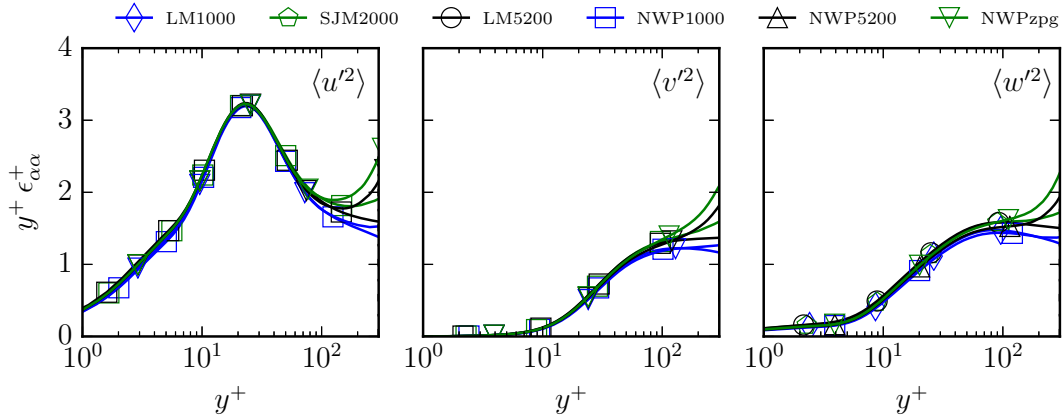


Figure 3.15: Profiles of $\langle u'^2 \rangle$, $\langle v'^2 \rangle$, and $\langle w'^2 \rangle$ dissipation as log densities.

$[0, L_z]$ whose size scales in viscous units. Similar to the simulations of Jiménez and Pinelli [116], the NWP model seeks to isolate wall turbulence from the influence of very large scale motions present both farther away from and down to the wall. The model is cheap relative to a full DNS because it does not include wavenumbers associated with length scales larger than its domain size in the wall parallel directions, and is intended to simulate turbulence out to a wall normal distance of $L_y^+/2 = 300$.

The underlying modeling assumption of the NWP is that the total mean shear stress τ_{tot} at the upper computational domain boundary—the wall normal location $y = L_y$ —is known. The ansatz is that by accounting for the flux of mean momentum through the upper domain boundary, the model provides the correct “environment” for the near wall turbulence to evolve. This is ultimately accomplished by augmenting the Navier-Stokes equations with a forcing function f that depends only on the wall-normal variable y and is

constrained to satisfy

$$\int_0^{L_y} f dy = \tau_{\text{tot}}. \quad (3.22)$$

This constraint is derived by considering the mean momentum balance

$$-\nu \partial_y^2 U + \partial_y \langle u'v' \rangle + \frac{dP}{dx} = 0 \quad (3.23)$$

for a constant pressure gradient flow that is statistically homogeneous in the stream and spanwise directions.

The results in section 3.4 demonstrate that for negligible and mild favorable pressure gradient flows, the model achieves the primary modeling objective of generating accurate near wall statistical quantities. In particular, the mean velocities and their derivatives, the small scale contribution to the turbulent kinetic energy, and the production, dissipation and transport terms in the Reynold's stress budget equation are found to be in close agreement with the statistics from available DNS.

3.5.2 Potential future work: model applications

Firstly, the reduced order near wall patch model designed here could be used to economically perform numerical experiments on wall turbulence, as for example when Jiménez and Pinelli [116] tested dynamical theories of time-dependent near wall processes by modifying the equations of motion to suppress various candidate processes: “numerics can be profitably used in ways which do not necessarily aim to duplicate real experiments, and...it is precisely the ability of numerical techniques to simulate ‘impossible’ physics that makes them a tool of choice in unravelling the physics of complex systems.”

In that direction, a potentially valuable application could be to conduct relatively inexpensive computational studies of the interaction between near wall turbulence and more complicated physical processes such as heat transfer, chemical reactions, turbophoresis, or roughness effects. Understanding the interaction of the near wall, small scale fluctuations with such processes can be important, for example, in turbomachinery, atmospheric modeling, combustion modeling, and oceanography.

The second recommended application of the NWP model is for calibrating macroscale turbulence models, such as RANS, Partially-Averaged Navier-Stokes (PANS), or LES. Depending on the precise mathematical definition of such a macroscale model, as well as its numerical implementation, the NWP microscale model could tabulate the missing data necessary for the macro model to be complete. This could be exceptionally useful in the cases when the turbulence model includes e.g. thermal convection, Lagrangian particles, or chemical reactions.

Lastly, it is reasonable to ask if the current microscale model can be applied to flows with fewer dimensions of statistical, spatial homogeneity, for instance, for boundary layers with significant evolution of the mean quantities in the streamwise direction. This occurs in flows with adverse or strong favorable pressure gradients, for example, and is important for understanding flow separation in aerodynamics.

In section 3.5.3 below we present a comparison of the NWP model's statistics to those of a recent direct numerical simulation of a self-similar, mild

adverse pressure gradient flow due to Kitsios et al. [127]. In contrast to the mean velocity and total shear stress profiles, the model's Reynolds shear stress $\langle u'v' \rangle$ profile does not exhibit the same consistency with the DNS data as in the zero and favorable pressure gradient cases. This inaccuracy in turn affects the production of turbulent kinetic energy. Below we offer a physical diagnosis of the problem based on the mean momentum balance, and then propose an extension to the NWP formulation in section 3.6 based on asymptotic analysis of the Navier-Stokes equations.

3.5.3 Boundary layer growth: adverse pressure gradients

In contrast to the channel flow simulations of Lee and Moser [143], the equations of motion and numerical method employed in the self-similar, adverse pressure gradient (APG) DNS of Kitsios et al. [127] result in a dynamical system that is homogeneous in the spanwise direction, but not in the streamwise direction.

To compare the NWP model's statistics with those from DNS requires an estimate for the pressure gradient dP/dx . This in turn determines τ_{tot} by enforcing the relation $\tau_{\text{tot}}^+ = 1 + dP^+/dx^+ L_y^+$, and this parameter constrains the forcing function f through (3.22). Kitsios et al. performed DNS of three separate cases corresponding to three values of a nondimensional pressure gradient β defined to be

$$\beta = \frac{\delta}{\tau_w} P'_e, \quad (3.24)$$

where τ_w is the mean wall shear stress, δ is a displacement thickness, and P'_e

is a farfield pressure gradient. Their values of $\beta = 0, 1$, and 39 correspond to zero, mild adverse, and strong adverse pressure gradient flows. Note that the limiting case $\beta \rightarrow \infty$ corresponds to a separated flow.

The focus in this section is on the $\beta = 1$ case. The values of the NWP model inputs τ_{tot}^+ and dP^+/dx^+ corresponding to this case are listed in table 3.3 under the column NWP- $\beta 1$ and were estimated in the following way (note: the rest of the computational inputs are exactly as they were for the zero and favorable pressure gradient cases and listed in table 3.2). Consider the mean streamwise momentum balance for the APG DNS flow; because statistics are no longer homogeneous in the streamwise direction, one has

$$-\nu (\partial_y^2 U + \partial_x^2 U) + U \partial_x U + V \partial_y U + \partial_x \langle u' u' \rangle + \partial_y \langle u' v' \rangle + \partial_x P = 0. \quad (3.25)$$

Integrating from the wall $y = 0$ to some wall-normal location y gives

$$\nu \partial_y U - \langle u' v' \rangle - \int_0^y (U \partial_x U + V \partial_y U + \partial_x \langle u' u' \rangle - \nu \partial_x^2 U) ds = \tau_w + \int_0^y \partial_x P ds \quad (3.26)$$

For each fixed streamwise location x^* in the so-called computational “domain of interest” (DOI), the statistics from an online database² can be used to compute each term on the left hand side (LHS) of equation (3.26). To a superb approximation, the total LHS is a linear function in the range $y^+ \in [0, 600]$,

²https://bridges.monash.edu/articles/Statistics_of_Beta_0_1_39_Turbulent_Boundary_Layer_DNS/ 8790785

meaning that in the near wall region, $\partial_{x^+} P^+$ is constant and

$$\begin{aligned} \frac{\partial U^+}{\partial y^+} - \langle u'v' \rangle^+ & - \int_0^{y^+} \left(U^+ \frac{\partial U^+}{\partial x^+} + V^+ \frac{\partial U^+}{\partial y^+} + \frac{\partial \langle u'u' \rangle^+}{\partial x^+} - \frac{\partial^2 U^+}{(\partial x^+)^2} \right) ds^+ \\ & = 1 + \partial_{x^+} P^+ y^+ := \tau_{\text{tot}}^+, \end{aligned} \quad (3.27)$$

where the ‘+’ superscript denotes nondimensionalization with respect to ν and the friction velocity u_τ at the location x^* . At $y^+ = 600$, $\tau_{\text{tot}}^+ = 4.60$ was estimated at the arbitrarily chosen $x^* \in \text{DOI}$, corresponding to a pressure gradient $dP^+/dx^+ = 0.006$.

The mean velocity U^+ and indicator function $y^+ \partial U^+ / \partial y^+$ profiles for the case NWP- β 1 are shown in the left and middle panels of figure 3.16. They are shown alongside the corresponding target profiles computed from the APG DNS, as well as the zero pressure gradient cases NWP-zpg and SJM2000 for comparison. The maximum relative error in the mean profile for the APG case is around 6.5% for $y^+ \in [0, 300]$; for comparison the same error is about 1% in the ZPG case.

The mean total stress profiles for these cases are shown in the right panel of 3.16. To be explicit, the APG quantities being compared are

$$\begin{aligned} \tau_{\text{tot,dns}}^+ &= \frac{\partial U^+}{\partial y^+} - \langle u'v' \rangle^+ \\ & - \int_0^{y^+} \left(U^+ \frac{\partial U^+}{\partial x^+} + V^+ \frac{\partial U^+}{\partial y^+} + \frac{\partial \langle u'u' \rangle^+}{\partial x^+} - \frac{\partial^2 U^+}{(\partial x^+)^2} \right) ds^+ \end{aligned} \quad (3.28)$$

$$\tau_{\text{tot,nwp}}^+ = \frac{\partial U^+}{\partial y^+} - \langle u'v' \rangle^+. \quad (3.29)$$

The relative error between these two profiles is less than 2% in the region $y^+ \in$

Case name	NWP-1000	NWP-5200	NWP-zpg	NWP- β 1
$-dP^+/dx^+$	$(1000.512)^{-1}$	$(5185.89)^{-1}$	0	-0.006
τ_{tot}^+	0.4003	0.8843	1	4.60

Table 3.3: Input parameters for an application of the NWP model to an APG flow are shown in the column NWP- β 1 and compared to the previous values for the cases presented in section 3.4.

[0, 300]; for comparison the relative error between NWP-zpg and SJM2000 is about 4%.

The agreement between total stress and mean velocity profiles indicate that, as before, the auxiliary forcing term f successfully transports momentum to the near wall region. However, because the model is necessarily statistically homogenous in the streamwise direction, the distribution of the shear stress is off; the lower left panel of figure 3.17 shows that the Reynolds shear stress $\langle u'v' \rangle$ does not match in the region $y^+ \in [0, 300]$ as in the zero and favorable pressure gradient cases. In the real APG turbulent boundary layer, the momentum transport from the far field turbulence is, on average, deposited across the mean viscous shear $\nu \partial U / \partial y$, the Reynolds shear $-\langle u'v' \rangle$ and the streamwise terms

$$-\int_0^y \left(U \frac{\partial U}{\partial x} + V \frac{\partial U}{\partial y} + \frac{\partial \langle u'u' \rangle}{\partial x} - \frac{\partial^2 U}{\partial x^2} \right) ds; \quad (3.30)$$

in other words, the momentum transport results in the change of statistics in the streamwise direction. The innaccuracy of the NWP model's Reynolds shear $-\langle u'v' \rangle$ negatively impacts production of turbulent kinetic energy, as observed in the $\langle u'_\alpha u'_\alpha \rangle$ profiles in figure 3.17.

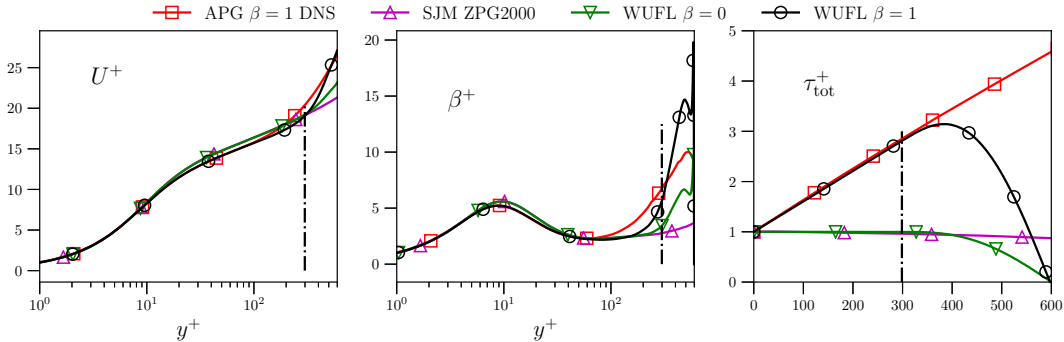


Figure 3.16: Mean velocity U^+ (left) and the indicator function $y^+ \partial_{y^+} U^+$ (middle) versus $\log(y^+)$, and total stress τ_{tot}^+ (right) versus y^+ . The black dashed-dotted vertical line marks $y^+ = 300$.

The problem of accounting for boundary layer growth in a turbulence simulation has been addressed before by Spalart [203] in his DNS of a spatially evolving flat plate boundary layer. The ansatz underlying his work is that “both the thickness of the boundary layer and the energy level of the turbulence vary slowly as functions of [the streamwise variable] x .” Multiscale asymptotic analysis ultimately then results in a set of $\mathcal{O}(\epsilon)$ ‘growth terms’ that are added to the usual Navier Stokes equations. A key result of this analysis is that the flow variables describing the local state of the boundary layer satisfy periodic boundary conditions, and hence, Fourier methods can be applied.

Inspired by Spalart’s work, we propose in section 3.6 below a “slow-growth” refinement to the near wall patch model for flows with boundary layer growth. The asymptotic analysis leading to the derivation of the model is presented, and the resulting equations of motion in the Kim-Moin-Moser velocity-vorticity formulation [126] are described.

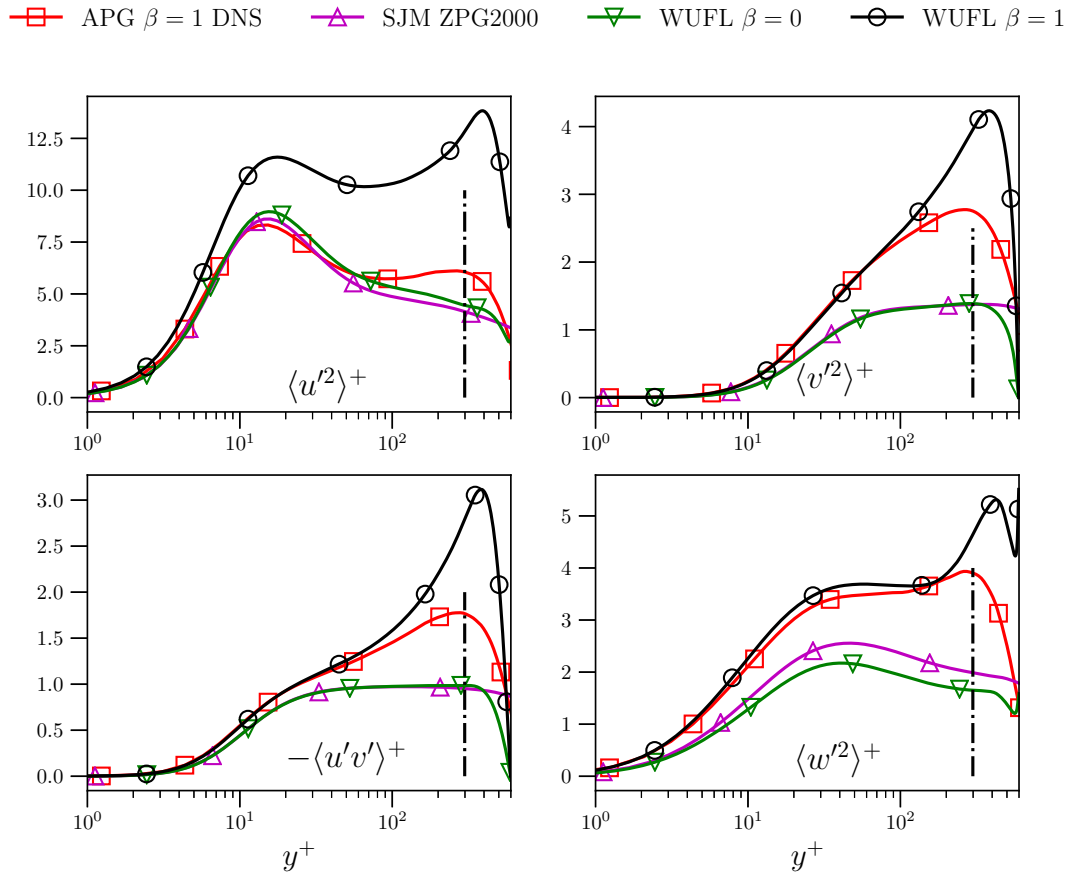


Figure 3.17: Reynolds stress profiles versus $\log(y^+)$. The black dashed-dotted vertical line marks $y^+ = 300$.

3.6 Slow-Grow NWP

3.6.1 Introduction & modeling assumptions

Firstly, let $l_\nu = \nu/u_\tau$ be the viscous length scale. For a spatially developing flow, it will depend on the streamwise variable x ; let \bar{l}_ν denote the value at some location \bar{x} . Define

$$\epsilon = \frac{\bar{l}_\nu}{L} \quad (3.31)$$

where L is the length scale that characterizes derivatives in the streamwise direction and is defined here to be

$$L^{-1} = \frac{\partial u_\tau}{\partial x}(\bar{x}) \frac{1}{u_\tau(\bar{x})} = \frac{\partial \log(u_\tau)}{\partial x}(\bar{x}). \quad (3.32)$$

Assume $\epsilon \ll 1$ and define $X = \epsilon x$.

Define also the new coordinates

$$(x, y, z) \mapsto (x, u_\tau(X)/\nu y, z) := (x, \eta, z) \quad (3.33)$$

so that derivatives become:

$$\frac{\partial}{\partial x} = \frac{\partial}{\partial X} + \epsilon \eta \frac{\partial \log(u_\tau)}{\partial X} \frac{\partial}{\partial \eta} \quad (3.34)$$

$$\frac{\partial}{\partial y} = \frac{u_\tau(X)}{\nu} \frac{\partial}{\partial \eta} \quad (3.35)$$

$$\frac{\partial}{\partial z} = \frac{\partial}{\partial z}. \quad (3.36)$$

The modeling ansatz is that the model's velocity components can be

written as

$$u_i(x, X, \eta, z, t) = \mathcal{U}_i(X, \eta) + v_i(x, X, \eta, z, t) \quad (3.37)$$

$$= u_\tau(X)U_i(\eta) + u_\tau(X)u'_i(x, \eta, z, t) \quad (3.38)$$

$$p(x, X, \eta, z, t) = \mathcal{P}(X, \eta) + p'(x, \eta, z, t) \quad (3.39)$$

and that

$$u'_i(x, \eta, z, t) \text{ is homogeneous in } x \text{ and } z. \quad (3.40)$$

The goal is to see what results when this ansatz is inserted into the incompressible Navier Stokes equations in the (x, η, z) coordinates. The final outcome will be a set of new, $\mathcal{O}(\epsilon)$ terms in the momentum equation that model the effect of boundary layer growth on the near wall dynamics, and these equations will then be dubbed the slow-grow near wall patch model.

3.6.2 Multiscale asymptotic analysis

In the (x, η, z) coordinates, the continuity equation becomes

$$\frac{\partial u}{\partial x} + \epsilon \frac{\partial u}{\partial X} + \frac{u_\tau(X)}{\nu} \frac{\partial v}{\partial \eta} + \frac{\partial w}{\partial z} + \epsilon \eta \frac{\partial \log(u_\tau)}{\partial X} \frac{\partial u}{\partial \eta} = 0 \quad (3.41)$$

Inserting the ansatz (3.38) into (3.41) gives

$$\left(\frac{\partial u}{\partial x} + \frac{u_\tau(X)}{\nu} \frac{\partial v}{\partial \eta} + \frac{\partial w}{\partial z} \right) + \epsilon \left(u \frac{\partial \log(u_\tau)}{\partial X} + \eta \frac{\partial \log(u_\tau)}{\partial X} \frac{\partial u}{\partial \eta} \right) = 0 \quad (3.42)$$

so that in (x, y, z) ,

$$\left(\frac{\partial u}{\partial x} + \frac{\partial v}{\partial y} + \frac{\partial w}{\partial z} \right) + \epsilon \left(u \frac{\partial \log(u_\tau)}{\partial X} + \frac{\partial \log(u_\tau)}{\partial X} y \frac{\partial u}{\partial y} \right) = 0 \quad (3.43)$$

$$\Rightarrow \left(\frac{\partial u}{\partial x} + \frac{\partial v}{\partial y} + \frac{\partial w}{\partial z} \right) + \epsilon \frac{\partial \log(u_\tau)}{\partial X} \frac{\partial (yu)}{\partial y} = 0. \quad (3.44)$$

The final identity (3.44) will be used below to put the momentum equation in conservative form. Ultimately, however, the $\mathcal{O}(\epsilon)$ term is dropped in practice as was done by Spalart [203].

For the momentum equation, the time derivative term is unchanged, while the three terms in the Laplacian

$$\left(\frac{\partial^2}{\partial x^2} + \frac{\partial^2}{\partial y^2} + \frac{\partial^2}{\partial z^2} \right) u_i(x, X, \eta, z) \quad (3.45)$$

become

$$\frac{\partial^2}{\partial z^2} u_i(x, X, \eta, z) = \frac{\partial^2 u_i}{\partial z^2}, \quad (3.46)$$

$$\frac{\partial^2}{\partial y^2} u_i(x, X, \eta, z) = \left(\frac{u_\tau(X)}{\nu} \right)^2 \frac{\partial^2}{\partial \eta^2} u_i(x, X, \eta, z) \quad (3.47)$$

$$= \left(\frac{u_\tau(X)}{\nu} \right)^2 \frac{\partial^2 u_i}{\partial \eta^2}, \quad (3.48)$$

and

$$\frac{\partial^2}{\partial x^2} u_i(x, X, \eta, z) = \left(\frac{\partial}{\partial x} + \epsilon \frac{\partial}{\partial X} + \epsilon \eta \frac{\partial \log(u_\tau)}{\partial X} \frac{\partial}{\partial \eta} \right)^2 u_i(x, X, \eta, z) \quad (3.49)$$

$$= \left(\frac{\partial^2}{\partial x^2} + 2\epsilon \left(\frac{\partial}{\partial x} \frac{\partial}{\partial X} + \eta \frac{\partial \log(u_\tau)}{\partial X} \frac{\partial}{\partial \eta} \frac{\partial}{\partial x} \right) \right) u_i(x, X, \eta, z) \\ + \mathcal{O}(\epsilon^2) \quad (3.50)$$

$$= \left(\frac{\partial^2 u_i}{\partial x^2} + 2\epsilon \left(y \frac{\partial \log(u_\tau)}{\partial X} \frac{\partial^2 u_i}{\partial x \partial y} \right) \right) + \mathcal{O}(\epsilon^2). \quad (3.51)$$

The advective term is most important to the slow-grow model and can be written as

$$u \nabla u_i = (\mathcal{N}_1 + \mathcal{N}_2 + \mathcal{N}_3) u_i \quad (3.52)$$

where

$$\mathcal{N}_1 = u \left(\frac{\partial}{\partial x} + \epsilon \frac{\partial}{\partial X} + \epsilon \eta \frac{\partial \log(u_\tau)}{\partial X} \frac{\partial}{\partial \eta} \right) \quad (3.53)$$

$$\mathcal{N}_2 = v \frac{u_\tau(X)}{\nu} \frac{\partial}{\partial \eta} \quad (3.54)$$

$$\mathcal{N}_3 = w \frac{\partial}{\partial z} \quad (3.55)$$

\implies

$$\mathcal{N}_1(u_i) = u \left(\frac{\partial u_i}{\partial x} + \epsilon \left(\frac{\partial u_i}{\partial X} + y \frac{\partial \log(u_\tau)}{\partial X} \frac{\partial u_i}{\partial y} \right) \right) \quad (3.56)$$

$$= u \left(\frac{\partial u_i}{\partial x} + \epsilon \left(u_i \frac{\partial \log(u_\tau)}{\partial X} + y \frac{\partial \log(u_\tau)}{\partial X} \frac{\partial u_i}{\partial y} \right) \right) \quad (3.57)$$

$$= u \left(\frac{\partial u_i}{\partial x} + \epsilon \frac{\partial \log(u_\tau)}{\partial X} \frac{\partial}{\partial y} (yu_i) \right) \quad (3.58)$$

$$\mathcal{N}_2(u_i) = \left(v \left(\frac{u_\tau(X)}{\nu} \right) \frac{\partial u_i}{\partial \eta} \right) \quad (3.59)$$

$$= \left(v \frac{\partial u_i}{\partial y} \right) \quad (3.60)$$

$$\mathcal{N}_3(u_i) = \left(w \frac{\partial u_i}{\partial z} \right) \quad (3.61)$$

Since the pressure field follows the same ansatz as the velocity field, it can be written as

$$p(x, X, \eta, z, t) = \mathcal{P}(X, \eta) + p'(x, \eta, z, t). \quad (3.62)$$

Then

$$\frac{\partial p}{\partial x} = \frac{\partial p}{\partial x} + \epsilon \frac{\partial \mathcal{P}}{\partial X} + \epsilon \eta \frac{\partial \log(u_\tau)}{\partial X} \frac{\partial p}{\partial \eta} \quad (3.63)$$

$$= \frac{\partial p}{\partial x} + \epsilon \frac{\partial \mathcal{P}}{\partial X} + \epsilon y \frac{\partial \log(u_\tau)}{\partial X} \frac{\partial p}{\partial y}, \quad (3.64)$$

while the other terms are ultimately unchanged.

In summary, inserting these terms in the full Navier-Stokes equations in (x, y, z) coordinates

$$\frac{\partial u}{\partial x} + \frac{\partial v}{\partial y} + \frac{\partial w}{\partial z} = 0 \quad (3.65)$$

$$\frac{\partial u_i}{\partial t} + \left(u \frac{\partial}{\partial x} + v \frac{\partial}{\partial y} + w \frac{\partial}{\partial z} \right) u_i + \frac{\partial p}{\partial x_i} - \left(\frac{\partial^2}{\partial x^2} + \frac{\partial^2}{\partial y^2} + \frac{\partial^2}{\partial z^2} \right) u_i = 0 \quad (3.66)$$

results in

$$\left[\frac{\partial u}{\partial x} + \frac{\partial v}{\partial y} + \frac{\partial w}{\partial z} \right] + \epsilon \frac{\partial \log(u_\tau)}{\partial X} \frac{\partial(yu)}{\partial y} = 0 \quad (3.67)$$

$$\begin{aligned} & \left[\frac{\partial u_i}{\partial t} + \left(u \frac{\partial}{\partial x} + v \frac{\partial}{\partial y} + w \frac{\partial}{\partial z} \right) u_i + \frac{\partial p}{\partial x_i} - \left(\frac{\partial^2}{\partial x^2} + \frac{\partial^2}{\partial y^2} + \frac{\partial^2}{\partial z^2} \right) u_i \right] \\ & + \epsilon \left(\delta_{1i} \frac{\partial \mathcal{P}}{\partial X} + \delta_{1i} y \frac{\partial \log(u_\tau)}{\partial X} \frac{\partial p}{\partial y} - 2\nu y \frac{\partial \log(u_\tau)}{\partial X} \frac{\partial^2 u_i}{\partial x \partial y} \right) \\ & + \epsilon \frac{\partial \log(u_\tau)}{\partial X} u \frac{\partial(yu_i)}{\partial y} = 0. \end{aligned} \quad (3.68)$$

For the fixed streamwise location \bar{x} as in the modeling assumptions above, denote $\bar{u}_\tau := u_\tau(\epsilon \bar{x})$. Nondimensionalizing with respect to the velocity, length, and time scales $U = \bar{u}_\tau$, $L = \nu/\bar{u}_\tau$ and $T = \nu/\bar{u}_\tau^2$ results in:

$$\left[\frac{\partial u_j^+}{\partial x_j^+} \right] + \epsilon \frac{\partial \log(u_\tau)}{\partial X^+} \frac{\partial(y^+ u^+)}{\partial y^+} = 0 \quad (3.69)$$

for the continuity equation, where the ‘+’ superscript denotes such a nondimensional quantity, and both here and below Einstein summation notation is

employed for notational ease. The momentum equation becomes

$$\begin{aligned} & \left[\frac{\partial u_i^+}{\partial t^+} + u_j^+ \frac{\partial u_i^+}{\partial x_j^+} + \frac{\partial p^+}{\partial x_i^+} - \frac{\partial^2 u_i^+}{\partial x_j^+ \partial x_j^+} \right] \\ & + \epsilon \left(\delta_{1i} \frac{\partial \mathcal{P}^+}{\partial X^+} + \delta_{1i} y^+ \frac{\partial \log(u_\tau)}{\partial X^+} \frac{\partial p^+}{\partial y^+} - 2 y^+ \frac{\partial \log(u_\tau)}{\partial X^+} \frac{\partial^2 u_i^+}{\partial x^+ \partial y^+} \right) \\ & + \epsilon \frac{\partial \log(u_\tau)}{\partial X^+} u^+ \frac{\partial (y^+ u_i^+)}{\partial y^+} = 0. \end{aligned} \quad (3.70)$$

3.6.3 Slow-growth model equations of motion

Firstly, it is important to note that by the definition of ϵ and L in section 3.6.1,

$$\frac{\partial \log(u_\tau)}{\partial X^+} = \bar{l}_\nu \frac{\partial \log(u_\tau)}{\partial X}(\bar{x}) = \frac{\bar{l}_\nu}{\epsilon} \frac{\partial \log(u_\tau)}{\partial x}(\bar{x}) = L \frac{\partial \log(u_\tau)}{\partial x}(\bar{x}) = 1, \quad (3.71)$$

so that in ‘+’ units, the only parameter to model (i. e. obtain from DNS or experiment) is $\epsilon = \bar{l}_\nu/L$. Since the equations are easier to read, (3.71) is used in the exposition below.

Secondly, the continuity equation (3.69) can be used to write the momentum equation in conservative form, at the “price” of an extra quadratic term. This is an advantageous formulation for the numerical methods em-

ployed in PoongBack. Consider the expression

$$(*) := \frac{\partial (u_j^+ u_i^+)}{\partial x_j} + \epsilon \frac{\partial (u^+ y^+ u_i^+)}{\partial y^+} \quad (3.72)$$

$$\begin{aligned} &= u_i^+ \left[\frac{\partial u_j^+}{\partial x_j^+} + \epsilon \frac{\partial (y^+ u^+)}{\partial y^+} \right] + u_j^+ \frac{\partial u_i^+}{\partial x_j^+} + \epsilon y^+ u^+ \frac{\partial u_i^+}{\partial y^+} \\ &= u_j^+ \frac{\partial u_i^+}{\partial x_j^+} + \epsilon y^+ u^+ \frac{\partial u_i^+}{\partial y^+} + \epsilon u^+ u_i^+ - \epsilon u^+ u_i^+ \\ &= u_j^+ \frac{\partial u_i^+}{\partial x_j^+} + \epsilon u^+ \frac{\partial (y^+ u_i^+)}{\partial y^+} - \epsilon u^+ u_i^+ \\ \implies (*) + \epsilon u^+ u_i^+ &= u_j^+ \frac{\partial u_i^+}{\partial x_j^+} + \epsilon u^+ \frac{\partial (y^+ u_i^+)}{\partial y^+}. \end{aligned} \quad (3.73)$$

Ergo, the momentum equation can be written as

$$\begin{aligned} &\left[\frac{\partial u_i^+}{\partial t^+} + \frac{\partial (u_j^+ u_i^+)}{\partial x_j^+} + \frac{\partial p^+}{\partial x_i^+} - \frac{\partial^2 u_i^+}{\partial x_j^+ \partial x_j^+} \right] \\ &+ \epsilon \left(\delta_{1i} \frac{\partial \mathcal{P}^+}{\partial X^+} + \delta_{1i} y^+ \frac{\partial p^+}{\partial y^+} - 2 y^+ \frac{\partial^2 u_i^+}{\partial x^+ \partial y^+} \right) \\ &+ \epsilon \left(\frac{\partial (y^+ u^+ u_i^+)}{\partial y^+} + u^+ u_i^+ \right) = 0. \end{aligned} \quad (3.74)$$

Finally, the $\epsilon \partial \mathcal{P}^+ / \partial X^+$ term in the momentum equation is identified with the mean pressure gradient dP^+ / dx^+ driving the flow. Futher, following Spalart [203], the pressure term $y^+ \partial p^+ / \partial y^+$ and the viscous term $2y^+ \partial u_i^+ / \partial x^+ \partial y^+$ in the momentum equation are ignored, while the $\partial (y^+ u^+) / \partial y^+$ term in the continuity equation is also ignored. The justification for dropping these terms is partially due to convenience—the velocity-vorticity numerical formulation employed in PoongBack relies on the elimination of pressure in the momentum equations and the imposition of the continuity condition $\nabla \cdot u = 0$. Physically speaking, however, the primary mechanism of momentum transport in

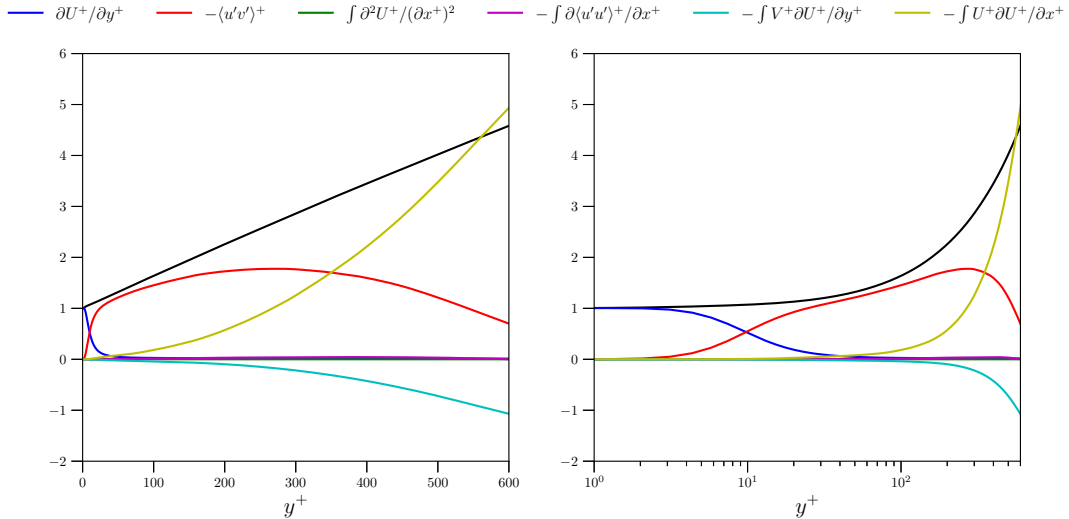


Figure 3.18: Mean stress budget for the $\beta = 1$ APG DNS of Kitsios et al. [127]. The linear, black curve is the sum of all the terms.

a spatially developing boundary layer can be seen in figure 3.18, which shows the total stress budget (3.27) at a fixed streamwise location for the $\beta = 1$ APG DNS of Kitsios et al. [127]. Besides the mean viscous stress $\partial U^+ / \partial y^+$ in the near-wall region and the Reynolds shear stress $-\langle u'v' \rangle$, the significant contributions to the momentum transport are due to convection by the mean quantities $\int V^+ \partial U^+ / \partial y^+$ and $\int U^+ \partial U^+ / \partial x^+$.

After dropping the terms, we thus arrive at the slow-growth model

equations

$$\frac{\partial u_j^+}{\partial x_j^+} = 0 \quad (3.75)$$

$$\begin{aligned} & \left[\frac{\partial u_i^+}{\partial t^+} + \frac{\partial (u_j^+ u_i^+)}{\partial x_j^+} + \frac{\partial p^+}{\partial x_i^+} - \frac{\partial^2 u_i^+}{\partial x_j^+ \partial x_j^+} \right] \\ & + \epsilon \left(u^+ u_i^+ + \frac{\partial (y^+ u^+ u_i^+)}{\partial y^+} \right) = f^+ - dP^+/dx^+ \delta_{1i} \end{aligned} \quad (3.76)$$

where f is the “auxiliary” forcing, as before. Note the slow-growth model simply reduces to the previous NWP model for $\epsilon = 0$.

3.6.4 Velocity-vorticity formulation

In this final section we describe how to transform the equations of motion (3.75) and (3.76) to the velocity-vorticity formulation first described by Kim, Moin, and Moser [126]. This formulation is tailored for the channel flow geometry and relies crucially on the constant Dirichlet and Neumann conditions for (u, v, w) at the locations $y = 0$ and $y = L_y$, respectively, as well as the periodic boundary conditions in x and z . A key advantage is that it allows for the continuity constraint to be imposed exactly.

The first step is to write the momentum equation³ in an abbreviated form

$$\frac{\partial u_i}{\partial t} + H_i + \frac{\partial p}{\partial x_i} - \Delta u_i = f \delta_{1i} \quad (3.77)$$

where Δ is the standard Laplacian operator in Cartesian coordinates, the $-dP/dx$ term has been subsumed into the forcing f (recall this function de-

³Throughout this section the ‘+’ superscripts are implied and dropped for clarity.

pends only on y), and H_i consists of the usual, nonlinear convective terms as well as the slow-growth terms

$$H_i = \frac{\partial(u_j u_i)}{\partial x_j} + \epsilon \left(uu_i + \frac{\partial(yuu_i)}{\partial y} \right). \quad (3.78)$$

The main idea is to evolve the state variables ω_y , ϕ , \bar{u} , and \bar{w} forward in time, instead of the usual u , v , w , and p , where

$$\omega_y = \frac{\partial u}{\partial z} - \frac{\partial w}{\partial x} \quad (3.79)$$

$$\phi = \Delta v \quad (3.80)$$

and \bar{u} and \bar{w} are the 0–0 components in the Fourier series representations of u and w in x and z :

$$\bar{u} = \frac{1}{L_x L_z} \int_0^{L_x} \int_0^{L_z} u(x, y, z) dz dx \quad (3.81)$$

and similarly for \bar{w} , which is simply the average in the $x - z$ plane.

The equation of motion for the wall-normal vorticity ω_y is

$$\frac{\partial \omega_y}{\partial t} + h_{\omega_y} - \Delta \omega_y = 0, \quad (3.82)$$

where

$$h_{\omega_y} = \frac{\partial H_1}{\partial z} - \frac{\partial H_3}{\partial x}, \quad (3.83)$$

while ϕ satisfies

$$\frac{\partial \phi}{\partial t} + h_\phi - \Delta \phi = 0. \quad (3.84)$$

Here

$$h_\phi = -\frac{\partial}{\partial y} \left(\frac{\partial H_1}{\partial x} + \frac{\partial H_3}{\partial z} \right) + \left(\frac{\partial^2}{\partial x^2} + \frac{\partial^2}{\partial z^2} \right) H_2 \quad (3.85)$$

and is derived from the pressure-Poisson equation, which comes from taking the divergence of the momentum equation (3.77) and reads

$$\Delta p = -\frac{\partial H_i}{\partial x_i}. \quad (3.86)$$

Taking the wall normal derivative and adding $\left(\frac{\partial^2}{\partial x^2} + \frac{\partial^2}{\partial z^2}\right) H_2$ to both sides of (3.86) then implies

$$h_\phi = \Delta \frac{\partial p}{\partial y} + \Delta H_2 = -\frac{\partial}{\partial y} \left(\frac{\partial H_1}{\partial x} + \frac{\partial H_3}{\partial z} \right) + \left(\frac{\partial^2}{\partial x^2} + \frac{\partial^2}{\partial z^2} \right) H_2. \quad (3.87)$$

For boundary conditions, periodicity of (u, v, w) implies that ω_y and ϕ are both periodic in x and z and hence admit Fourier series representations. The no-slip condition at $y = 0$ and constant Neumann conditions on u and w at $y = L_y$ imply that

$$\widehat{\omega}_y(k_x, k_z) = 0 \quad \text{at } y = 0 \quad (3.88)$$

$$\frac{\partial}{\partial y} \widehat{\omega}_y(k_x, k_z) = 0 \quad \text{at } y = L_y \quad (3.89)$$

for each nonzero Fourier pair (k_x, k_z) (note: $\overline{\omega_y}$ is identically zero), and the 0–0 modes \overline{u} and \overline{w} satisfy the exact same conditions as u and w at $y = 0$ and L_y .

There are no boundary conditions for ϕ at $y = 0$ and $y = L_y$; instead there are four conditions on v . The no-slip and no-penetration condition give two: $v = 0$ at $y = 0$ and $y = L_y$. The continuity equation and the no-slip condition imply that $\partial v / \partial y = 0$ at $y = 0$, while continuity and the constant,

homogenous Neumann conditions for u and w imply that $\partial^2 v / \partial y^2 = 0$ at $y = L_y$. Since the equation (3.84) for ϕ in Fourier space

$$\frac{\partial \hat{\phi}}{\partial t} + \widehat{h_\phi} - \left(\frac{\partial^2}{\partial y^2} - (k_x^2 + k_z^2) \right) \hat{\phi} = 0 \quad (3.90)$$

is a second order (in y) equation for $\hat{\phi}$, it can be seen as a fourth order equation for \hat{v} , meaning the four conditions just mentioned ensure a unique solution, assuming also there is a well defined initial condition for $\hat{\phi}$. The practical implementation of these four boundary conditions is best described in the semi-discrete context. Supposing (3.84) is discretized in time with some implicit-explicit scheme, a general time step requires the solution of the following system

$$\begin{aligned} L\phi^{n+1} &= f \\ \Delta v^{n+1} &= \phi^{n+1} \\ v(y=0) = v(y=L_y) &= \frac{\partial v}{\partial y}(y=0) = \frac{\partial^2 v}{\partial y^2}(y=L_y) = 0, \end{aligned} \quad (3.91)$$

where L is some linear differential operator and f depends on ϕ and h_ϕ at previous time-steps. Making use of the linearity of L and the Laplacian, this system is then split into three separate systems. Consider

$$\begin{aligned} L\phi_1^{n+1} &= 0 \\ \Delta v_1^{n+1} &= \phi_1^{n+1} \\ \phi_1(y=0) = 1, \phi_1(y=L_y) &= v_1(y=0) = v_1(y=L_y) = 0, \end{aligned} \quad (3.92)$$

$$\begin{aligned} L\phi_2^{n+1} &= 0 \\ \Delta v_2^{n+1} &= \phi_2^{n+1} \end{aligned} \tag{3.93}$$

$$\phi_2(y = L_y) = 1, \phi_2(y = 0) = v_2(y = 0) = v_2(y = L_y) = 0,$$

and

$$\begin{aligned} L\phi_p^{n+1} &= f \\ \Delta v_p^{n+1} &= \phi_p^{n+1} \end{aligned} \tag{3.94}$$

$$\phi_p(y = 0) = \phi_p(y = L_y) = v_p(y = 0) = v_p(y = L_y) = 0.$$

The linear combinations $\phi^{n+1} = c_1\phi_1^{n+1} + c_2\phi_2^{n+1} + \phi_p$ and $v^{n+1} = c_1v_1^{n+1} + c_2v_2^{n+1} + v_p$ clearly satisfy the PDE system in (3.91), while the boundary conditions on the derivatives of v are satisfied with the appropriate choice of c_1 and c_2 .

The averages \bar{u} and \bar{w} satisfy the nonlinear boundary value problems

$$\frac{\partial \bar{u}}{\partial t} + \frac{\partial \bar{u}\bar{v}}{\partial y} + \epsilon \left(\bar{u}\bar{u} + \frac{\partial(\bar{y}\bar{u}\bar{v})}{\partial y} \right) - \frac{\partial^2 \bar{u}}{\partial y^2} = f \tag{3.95}$$

$$\frac{\partial \bar{w}}{\partial t} + \frac{\partial \bar{v}\bar{w}}{\partial y} + \epsilon \left(\bar{w}\bar{w} + \frac{\partial(\bar{y}\bar{u}\bar{w})}{\partial y} \right) - \frac{\partial^2 \bar{w}}{\partial y^2} = 0, \tag{3.96}$$

and, again, satisfy the same Dirichlet and Neumann conditions at $y = 0$ and $y = L_y$, respectively, as u and w .

Finally, given both v and ω_y , the nonzero Fourier modes of both u and

w can be recovered by solving the linear system

$$ik_z \hat{u} - ik_x \hat{w} = \widehat{\omega_y} \quad (3.97)$$

$$ik_x \hat{u} + ik_z \hat{w} = -\frac{\partial \hat{v}}{\partial y}, \quad (3.98)$$

which has a unique solution precisely when $(k_x, k_z) \neq 0$.

Chapter 4

Electrokinetic Flows

4.1 Multiscale Nature of Electrolyte Solutions

Electrolyte solutions are multicomponent fluids with charge-neutral molecules as solvents and charged ions as solutes; an example from everyday life is saltwater. Because electrolytes can conduct electricity through the movement of ions, they exhibit rich dynamics—electric fields generated by the distribution of charged ions exert stresses on the fluid via the Lorentz force. As the fluid accelerates, it advects the ions, rearranging the distribution of charge, creating new electric fields and hence new stresses. Electrokinetic flows occur in a variety of applications, including microfluidic devices, colloid science, and battery technologies [21, 95, 98, 206], often at millimeter scales and below.

Electrolyte solutions are challenging to model because of the wide range of scales relevant to their dynamics. For example, the molecular size (the effective Born radius) of both solvent and solute, the effective hydrodynamic radius of the solute (e.g. of a colloid, cell, or polymer), the ion-ion interaction length (Bjerrum length), the ion-surface interaction length (Gouy-Chapman length), the screening length (Debye length), and hydrodynamic length scales all play a role [57].

In principle, a microscale model such as molecular dynamics (MD) simulation can accurately model the complex range of interactions present in an electrolyte solution. However, this first-principles approach requires accurate inter-molecule potentials for all molecular species and is only computationally feasible for relatively small system sizes, limiting its range of applicability.

Macroscopic models for electrolyte solutions typically take the form of a coupled partial differential equation system consisting of mass transport equations for multicomponent fluid mixtures, the Navier-Stokes (NS) equations of hydrodynamics, and Poisson's equation expressing Gauss' law of electrostatics:

$$\begin{aligned} \partial_t (\rho u) &= -\nabla \cdot \mathcal{F}_{\text{NS}}(u, \rho_1, \dots, \rho_N, \Phi) \\ \partial_t \rho_k &= -\nabla \cdot \mathcal{F}_k(u, \rho_1, \dots, \rho_N, \Phi) \\ -\nabla \cdot (\epsilon \nabla \Phi) &= q(\rho_1, \dots, \rho_N), \end{aligned} \tag{4.1}$$

where u is the fluid velocity, ρ_k and ρ are the fluid component and total fluid densities ($k = 1, \dots, N$, where N is the total number of fluid components), q is the total charge density, ϵ is the permittivity of the fluid (possibly varying in space), and Φ is the electric potential of the fluid mixture. \mathcal{F}_{NS} and \mathcal{F}_k are the hydrodynamic and mass component fluxes, respectively. The specific form of the fluxes, as well as the equation of state necessary to close the system, are usually determined from the phenomenological laws of nonequilibrium thermodynamics, such as the Onsager reciprocal relations and Maxwell-Stefan theory. A relatively simple version of (4.1) applicable for extremely dilute electrolytes is called the Poisson-Nernst-Planck and Navier-Stokes model and in particular

features standard Fickian diffusion in the mass fluxes \mathcal{F}_k .

4.2 Macroscopic Continuum Model for Electrolytes

Below we describe the *deterministic* version of a Fluctuating Hydrodynamics (stochastic) PDE model for electrolyte solutions developed recently by Péraud et al. [179] and then present in sections 4.2.1 and 4.2.2 numerical solutions to the model in two-wall bounded configurations–electro-osmosis (EO) and induced charge electro-osmosis (ICEO). These are prototypical, “building block” flows for transport and mixing, respectively, at the millimeter scale and below. The simulations illustrate how electrolyte solutions develop an asymptotically thin charge, or Debye, layer in the vicinity of the walls. After briefly introducing the Fluctuating Hydrodynamics (FHD) formalism and its merits in section 4.2.3, the deterministic EO and ICEO solution profiles are utilized to explain why FHD *fails* for wall-bounded electrolyte flows. In section 4.2.4 a simple scaling argument is presented showing that a continuum representation for the charged ion densities near walls is generally inappropriate, motivating the hybrid particle-continuum model presented in section 4.3.

Consider now the following isothermal, low-Mach number electrolyte

model with N fluid components due to Péraud et al. [179]:

$$\partial_t(\rho u) + \nabla \cdot (\rho uu) = -\nabla \pi + \nabla \cdot \eta \left(\nabla u + (\nabla u)^T \right) - q(\nabla \Phi + E_{\text{ext}}) \quad (4.2)$$

$$\partial_t \rho_k + \nabla \cdot (\rho_k u) = \nabla \cdot \left(\rho_k \chi_{kj} \left(\frac{\overline{m}}{\rho m_k} \Gamma_{ji} \nabla \rho_i + \frac{\overline{m}}{k_B T} q \frac{\partial \Phi}{\partial x_j} \right) \right) \quad (4.3)$$

$$-\epsilon \Delta \Phi = q \quad (4.4)$$

$$\nabla \cdot u = -\nabla \cdot \left(\sum_{k=1}^N \frac{\mathcal{F}_k}{\overline{\rho_k}} \right) \quad (4.5)$$

for $k = 1, \dots, N$. In the momentum transport equation (4.2), η is the fluid viscosity, $-q\nabla\Phi$ is the Lorentz force density, $q = \sum_{j=1}^N z_j \rho_j$ is the total charge density, z_j is the charge per unit mass of each species, and π is a perturbational pressure resulting from the low-Mach number approximation of the fully compressible Navier-Stokes equations. The approximation can be derived by an asymptotic analysis in the system Mach number [128, 155] and is computationally advantageous because in the resulting equations there is no need to numerically resolve acoustic wave propagation.

In addition to the standard advective flux term, the mass transport equations (4.3) consist of multicomponent diffusion and electrodiffusion terms. χ and Γ are the matrices of diffusion and activity coefficients, respectively—note that Einstein summation notation is implied in (4.3). An expression for χ in terms of the species densities (in “Fickian form”) is available; however, it is nontrivial even to express—see the description in [64]. In general it can be derived from Maxwell-Stefan theory [132]. For intuition, note that for a solution with a single solvent that is extremely dilute, Γ is well approximated by the identity matrix, and the $(N-1) \times (N-1)$ sub-block of χ is approximately

diagonal

$$\chi_{\alpha\alpha} = \frac{m_\alpha D_\alpha}{\bar{m}(\rho_\alpha/\rho)}, \quad (4.6)$$

corresponding to the charged solutes, where D_α are diffusion coefficients. In this limit, the expressions for the mass fluxes reduce to

$$\mathcal{F}_k = D_k \nabla \rho_k - \frac{D_k m_k z_k}{k_B T} \rho_k \nabla \Phi \quad (4.7)$$

for $k = 1, \dots, N-1$ [179]; in other words, the expression reduces to a “standard” diffusion term plus an additional (simplified) electrodiffusive term. In (4.7), (4.6), and (4.3), m_k denotes the mass of a molecule of species k and $\bar{m} = \left(\sum_{k=1}^N \left(\frac{\rho_k}{\rho} \frac{1}{m_k} \right) \right)^{-1}$ is a mixture averaged molecular mass. In equations (4.2) and (4.7), k_B is Boltzmann’s constant.

In the Poisson equation (4.4), the permittivity ϵ is assumed not to vary in space, and finally, in the equation of state (EOS) (4.5), \mathcal{F}_k are the mass fluxes on the right hand side of the mass transport equations (4.3). The EOS is derived from the assumption that the fluid mixture does not change volume upon mixing; see the discussion in [179] for the derivation as well as a precise defintion of the pure-component species densities $\bar{\rho}_k$.

4.2.1 Electro-osmosis (EO)

¹Electro-osmosis refers to the motion of an electrolyte solution in a channel or pipe with charged boundary. The basic setup is illustrated in figure

¹The results in both this section and section 4.2.2 were obtained in collaboration with John B. Bell and Andy Nonaka (Lawrence Berkeley National Laboratory) as well as Alejandro L. Garcia (San Jose State University).

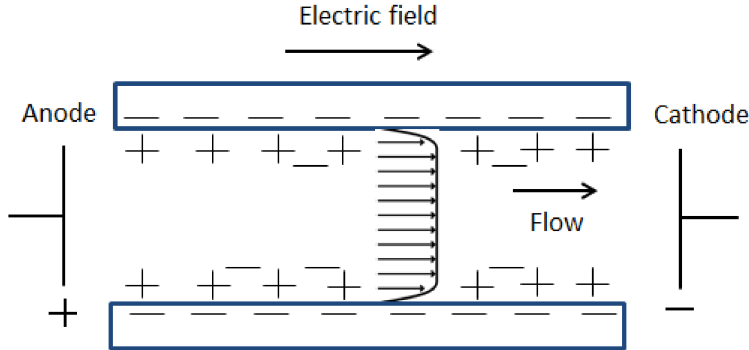


Figure 4.1: Cartoon description of electro-osmosis; image borrowed from [211].

4.1; at chemical equilibrium, oppositely charged ions in the electrolyte solution accumulate at the charged boundary. If an external potential difference is then applied parallel to the channel walls, the charges in the near wall layer accelerate in its direction and produce a shear force on the fluid. This shearing, along with the no-slip condition, produce a plug-flow velocity profile when the ion concentration in the electrolyte is large enough. At lower concentrations, the flow profile resembles classical Poiseuille flow.

Electro-osmosis is technologically important, for example, for transport in microfluidic systems. Traditional transport by pressure gradients in such systems is difficult to realize because the relevant length scales are too small. On the contrary, it is relatively easy to achieve larger flow velocities by increasing the electric field strengths.

The size of the near-wall charge layer, and hence the shape of the velocity flow profile, is related to a fundamental quantity in electrolyte theory

called the Debye, or screening, length

$$\lambda_D = \sqrt{\frac{\epsilon k_B T}{\sum_k n_k q_k^2}} \quad (4.8)$$

which can be interpreted as the length scale that measures how far electrostatic effects persist before they are screened by opposite charges. Here k_B and T are Boltzmann's constant and the fluid temperature, while q_k is the ionic charge of each species. $n_k = N_A \rho_k / m_k^{\text{mol}}$ is number density of each species, where m_k^{mol} is each species' molar mass (which has units of mass per mole), and N_A is Avogadro's number. Note that as the density of the charged species ρ_k increases, λ_D decreases.

For channel flow configuration with no pressure gradient and a constant external electric field $(E_{\text{ext}})_i = E_{\text{ext}} \delta_{1i}$ in the x -direction, electro-osmotic flow is a one-dimensional problem. The isothermal Navier-Stokes and Poisson equations simply reduce to

$$-\eta \frac{d^2 u}{dy^2} = q E_{\text{ext}} \quad (4.9)$$

$$-\epsilon \frac{d^2 \Phi}{dy^2} = q, \quad (4.10)$$

and symmetry about the channel centerline and the no-slip condition then imply that

$$u(y) = \frac{\epsilon}{\eta} (\Phi(y) - \Phi_{\text{wall}}) E_{\text{ext}}, \quad (4.11)$$

so that the flow velocity is directly proportional to the electric potential [52].

To simulate electro-osmotic flow, the equations of motion (4.2)–(4.5) are posed in a channel domain $\Omega = [0, L_x] \times [0, L_y] \times [0, L_z]$ with periodic

boundary conditions for each ρ_k , u , and Φ in the x and z directions. At $y = 0$ and $y = L_y$, the velocity $u = 0$ and $\epsilon \partial\Phi/\partial y = C \in \mathbb{R} \setminus \{0\}$, modeling walls with a fixed charge density. For solvability of the Poisson equation (4.4) the total charge density q due to the ionic species in the domain interior must satisfy a compatibility condition. The densities ρ_k satisfy a no-flux condition at the walls. The external electric field $(E_{\text{ext}})_i = E_{\text{ext}} \delta_{1i}$ is constant and nonzero only in the x direction.

Figure 4.2 shows the results from a numerical implementation of this configuration for saltwater (i.e. a solution of H_2O , Na^+ , and Cl^-) at $T = 300$ K in a $5.12 \times 1.28 \times 1.28$ micron channel. The Debye length $\lambda_D = L_y/10$ and is small enough that the resulting streamwise velocity u has a plug-flow profile. Shown also is the quantity $\epsilon E_{\text{ext}}/\eta (\Phi - \Phi_{\text{wall}})$, illustrating the relation (4.11).

The equations of motion (4.2)–(4.5) were discretized with a structured-grid finite-volume method with cell-averaged densities and staggered (face-averaged) velocities. In general derivatives were computed with second order stencils, and the time marching scheme was a second order predictor-corrector scheme for both the velocities and densities. The mass fluxes in (4.3) were treated explicitly, but each time step requires the solution of a linear system for Φ as well as a linear, saddle point system for u and π . The former was solved with a geometric multigrid algorithm, while the latter was computed with a Stokes solver developed in [38]. The full details of the numerical implementation can be found in the series of works [64, 65, 169, 179].

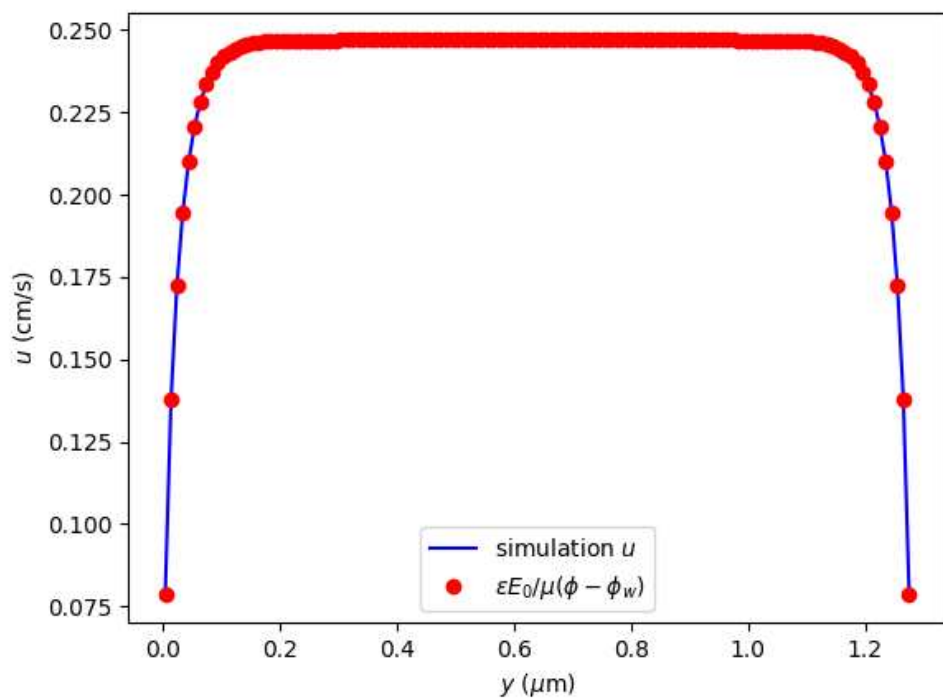


Figure 4.2: Electro-osmotic plug flow velocity profile u is proportional to the electric potential $\Phi - \Phi_{\text{wall}}$ as in equation (4.11). Here E_0 is the external electric field strength, and μ is the fluid viscosity.

4.2.2 Induced-charge electro-osmosis

Just as it becomes difficult to achieve transport through pressure driven flow when system length scales are sufficiently small, so too is it difficult to generate vorticity, and hence facilitate mixing of chemical reactants, e.g. since the associated Reynolds numbers are so low.

A canonical flow configuration that aids in mixing is called induced charge electro-osmosis (ICEO). The basic set up is similar to that of electro-osmosis. Consider a channel domain $\Omega = [0, L_x] \times [0, L_y] \times [0, L_z]$ with periodic boundary conditions in x and z and no-slip (respectively no-flux) walls at $y = 0$ and $y = L_y$ for u (resp. ρ_k). One of the walls, say $y = L_y$, is modeled as a perfect insulator, so that $\partial\Phi/\partial n = 0$, while the other wall consists of a rectangular conducting strip \mathcal{J} along some portion of the boundary with perfect insulators covering the rest of the wall, so that

$$\frac{\partial\Phi}{\partial n} = 0 \quad \text{on } [0, L_x] \times \{y = 0\} \times [0, L_z] \setminus \mathcal{J} \quad (4.12)$$

$$\Phi = 0 \quad \text{on } \mathcal{J} \quad (4.13)$$

where $\mathcal{J} = [a, b] \times \{y = 0\} \times [c, d] \subset [0, L_x] \times \{y = 0\} \times [0, L_z]$.

A cartoon depiction is given in figure 4.3; the dynamics begin when a constant external electric field $(E_{\text{ext}})_i = E_{\text{ext}} e_1$ in the x direction is activated. Since electric fields lines are normal to surfaces of constant potential, the resulting field will cause charged ions in the bulk of the domain to pile up near the conducting strip \mathcal{J} , with positively charged ions congregating on one half of the strip and negatively charged ones on the other. After some initial

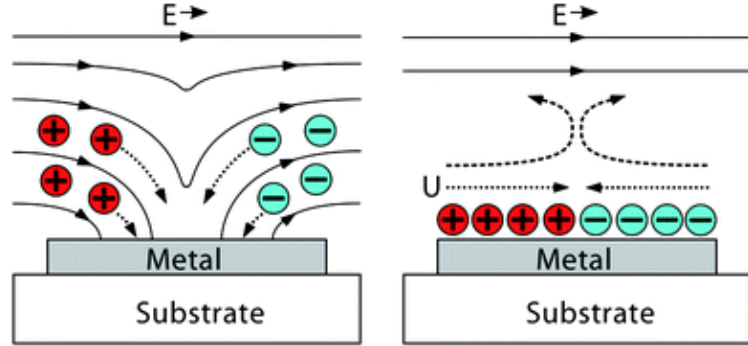


Figure 4.3: Cartoon description of induced charge electro-osmosis; image borrowed from [205].

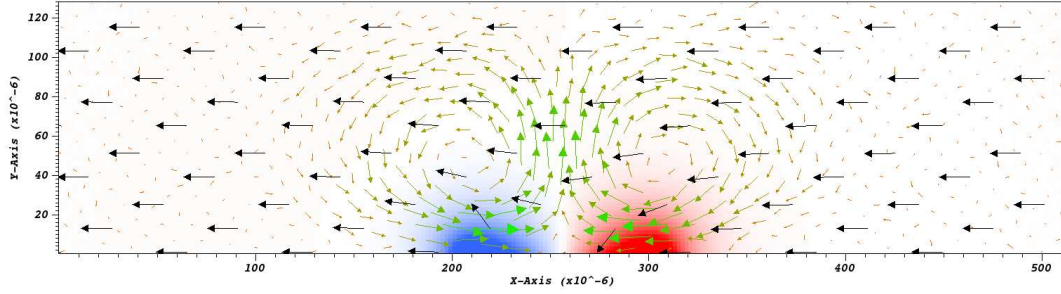
“charging time” there then exists a boundary layer of charge near \mathcal{J} . Similar to electro-osmotic flow, the excess cations (respectively anions) in the vicinity of \mathcal{J} accelerate in the direction (resp. opposite direction) of $E_{\text{ext}} e_1$, resulting in two Lorentz force densities oriented opposite each other. The resulting shears on the fluid then effect two counter-rotating vortices.

An interesting property of this configuration is that the flow velocity field is invariant under a reflection of the sign of the electric field $E_{\text{ext}} e_1 \mapsto -E_{\text{ext}} e_1$ for a 1-1 electrolyte (meaning the cations and anions are equal in molecular mass and molarity and have opposite valences). Because the charge density near the conducting strip also undergoes a reflection $q \mapsto -q$ in this scenario, the Lorentz force density is unchanged and hence neither are the counter-rotating vortices. This property allows for electrokinetic flows to be driven by alternating-current (AC) fields instead of direct current (DC) fields. Figures 4.4(a)–4.4(d) showcase the results from a two-dimensional numerical

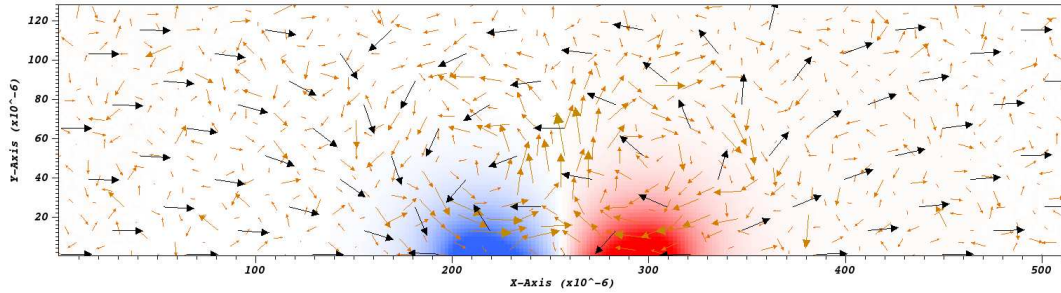
alternating current ICEO simulation at four instances in time and illustrate this symmetry property. The discretized equations of motion (4.2)–(4.5) are solved on a 5.12×1.28 micron channel with periodic boundary conditions in the x direction. The conducting strip $\mathcal{I} = [0.4L_x, 0.6L_x] = [2.0512, 3.0768]$ μm , and the time-dependent external electric field $E_{\text{ext}}(t)$ is a mollified square wave. The electrolyte simulated is 1-1 with a Debye length $\lambda_D \approx 0.1478L_y$. The black arrows in figure 4.4 show $-\nabla\Phi + E_{\text{ext}}$, the green/yellow arrows show the velocity field u , and the red/blue areas show contours of the charge distribution q .

4.2.3 Thermal fluctuations in nonequilibrium systems, stochastic PDEs, and Fluctuating Hydrodynamics

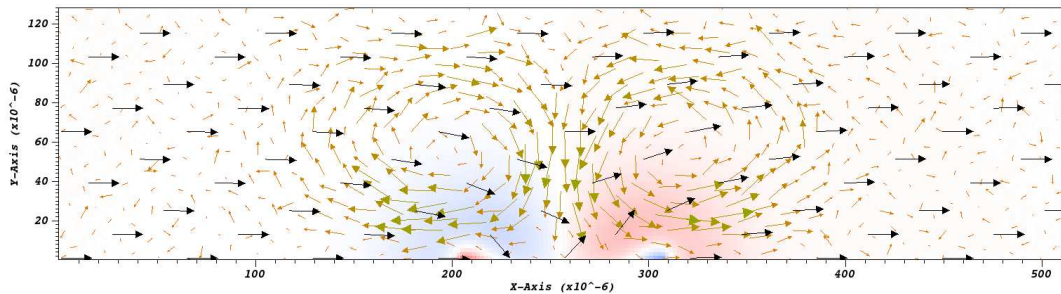
Although (the deterministic version of) the Péraud et al. model (4.2)–(4.5) is demonstrably capable of describing canonical electrokinetic flows, there are cases for which such a macroscopic, deterministic continuum model is inadequate. For example, at large applied voltages the general PDE model (4.1) poorly describes ion-ion interactions and steric or “crowding” effects [22, 123, 124], referring to the fact that the ions have a finite, nonzero size that is especially relevant near electrodes and other boundaries. Another limitation is that (4.1) fails to account for thermal fluctuations *intrinsic* to fluid mixtures at microscopic length scales. In systems held out of thermodynamic equilibrium by, for example, a temperature or concentration gradient, correlations in fluctuations can lead to long range (low wavenumber) features on mesoscopic length scales (loosely defined to be around $\sim 1\text{nm}–1\mu\text{m}$) and even



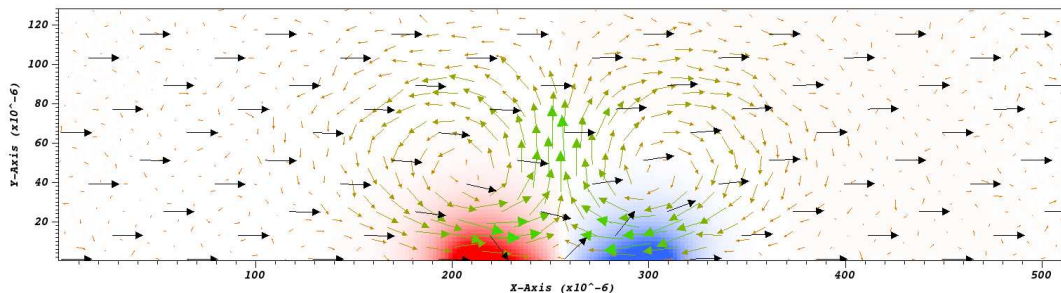
(a) $E_{\text{ext}}(t_1)e_1$ points in the negative x direction.



(b) $E_{\text{ext}}(t_2)e_1 \approx 0$ is changing sign.



(c) $E_{\text{ext}}(t_3)e_1$ now points in the positive x direction, but the charge layer near the conductor \mathcal{I} is rearranging itself.



(d) $E_{\text{ext}}(t_4)e_1$ still points in the positive x direction; the charge layer is now the mirror image of that at t_1 , while the velocity field is unchanged.

Figure 4.4: Alternating current ICEO.

macroscopic scales (up to a millimeter or more) [51, 157, 218].

These so-called “giant fluctuations” can lead to enhanced transport and diffusion [217], cause hydrodynamic instabilities [49, 100, 168], and affect chemical instabilities [125]. The equations of Fluctuating Hydrodynamics (FHD) provide a well-established way to model these mesoscopic effects; see, for example, the book by de Zárate and Sengers [51]. Originally introduced by Landau and Lifshitz [136], the essential idea is to incorporate a stochastic flux term into the traditional, continuum hydrodynamic fluxes in such a way that is consistent with the fluctuation-dissipation theorem of statistical mechanics [133]. The theorem roughly says that at thermodynamic equilibrium (meaning a system is not producing any entropy), the rate at which energy is input into the system is exactly balanced by energy dissipation due to thermal fluctuations.

Consider momentarily a fluid with extremely large Prandtl number, so that the temperature equation can be decoupled from the density and velocity equations [81]. Assume further that the fluid density and thermal conductivity can be taken as constants, and that the temperature varies nontrivially only in one direction. The resulting dynamics are governed by the standard parabolic heat equation

$$\frac{\partial u}{\partial t} = \mathcal{L}u, \quad (4.14)$$

where $\mathcal{L} = \kappa \partial^2 / \partial y^2$. The Fluctuating Hydrodynamics formalism proceeds to add to (4.14) a stochastic flux term

$$du_t = \mathcal{L}u_t dt + \mathcal{K}dW_t, \quad (4.15)$$

where \mathcal{W} is spatio-temporal white noise satisfying

$$\mathbb{E} [\mathcal{W}] = 0 \quad (4.16)$$

$$\mathbb{E} [\mathcal{W}(y, t)\mathcal{W}(y', t')] = \delta(t - t')\delta(y - y'), \quad (4.17)$$

(where δ is the Dirac measure) and \mathcal{K} is a time-indepedent linear operator. (4.15) is a linear stochastic PDE with a well-defined mathematical interpretation using the Itô calculus and “mild-solution”

$$u_t = e^{t\mathcal{L}}u_0 + \int_0^t e^{(t-s)\mathcal{L}}\mathcal{K}d\mathcal{W}_s; \quad (4.18)$$

see the book by De Prato [46]. Using Fourier analysis, one can show that the variance of \hat{u}

$$\mathbb{E} [\hat{u}^*\hat{u}] = 1 \quad (4.19)$$

if the operators \mathcal{L} and \mathcal{K} satisfy the relation

$$\mathcal{L} + \mathcal{L}^* = -\mathcal{K}\mathcal{K}^*, \quad (4.20)$$

where the superscript $*$ in (4.19) denotes the complex conjugate and in (4.20) the operator adjoint. Ergo, if $\mathcal{K} = \sqrt{2\kappa}\partial/\partial y$, then (4.20) will be satisfied. This is the mathematical expression of the fluctuation-dissipation theorem.

As mentioned in the introductory paragraph to this section 4.2, the full Péraud et al. model presented in [179] is an extension of the FHD formalism

to isothermal electrolyte solutions and can be summarized as:

$$\begin{aligned} \partial_t(\rho u) + \nabla \cdot (\rho uu) = \\ \nabla \cdot \mathcal{F}_{\text{NS}}(u, \rho_1, \dots, \rho_N, \Phi) + \nabla \cdot \alpha \left[\mathcal{W}^{\text{NS}} + (\mathcal{W}^{\text{NS}})^T \right] \end{aligned} \quad (4.21)$$

$$\begin{aligned} \partial_t \rho_k + \nabla \cdot (\rho_k u) = \\ -\nabla \cdot \mathcal{F}_k(u, \rho_1, \dots, \rho_N, \Phi) + \nabla \cdot [\beta_{kj}(\rho_1, \dots, \rho_N) \mathcal{W}_j] \end{aligned} \quad (4.22)$$

$$-\nabla \cdot (\epsilon \nabla \Phi) = q(\rho_1, \dots, \rho_N), \quad (4.23)$$

where \mathcal{F}_{NS} and \mathcal{F}_k are the same deterministic fluxes as in equations (4.2) and (4.3). \mathcal{W}^{NS} is a Gaussian, spatiotemporal white noise tensor whose entries are mutually independent and mean zero

$$\mathbb{E} [\mathcal{W}_{ij}^{\text{NS}}(x, t) \mathcal{W}_{kl}^{\text{NS}}(x', t')] = \delta_{ik} \delta_{jl} \delta(x - x') \delta(t - t'), \quad (4.24)$$

and each \mathcal{W}_j is also a mutually independent, mean zero spatiotemporal Gaussian process.

As in the simplified, one-dimensional FHD heat-equation model (4.15), the amplitude of the noise α and β are determined by a fluctuation-dissipation relation. In the momentum equation, the amplitude of the noise α (4.21) is simply a constant: $\alpha = \sqrt{\eta k_B T}$, where, again, η , k_B , and T are the fluid viscosity, Boltzmann's constant, and the fluid temperature. In contrast, the noise amplitude in the mass equation (4.22) β is the square-root of a matrix whose entries depend on the mass densities ρ_k and the diffusivity matrix χ ; see [179] for a full description. The momentum equation noise is said to be

additive, while the mass equation noise is said to be *multiplicative*. Note that for a more general, non-isothermal model, the noise α would be multiplicative.

At their core, the FHD equations (4.21)–(4.23) are a macroscopic, coarse-grained multiscale model for electrolyte solutions. Because the model features multiplicative noise in the mass transport equation, it can be expressed in the HMM framework of equation (1.1). The macroscopic model M is the PDE system (4.2)–(4.4) that is missing the effect of microscopic, thermal motions of fluid molecules. This data D is modeled by stochastic fluxes whose magnitude are determined by the fluctuation-dissipation theorem of statistical mechanics, whose macroscopic model input d is the local space-time values of the component densities ρ_k .

It is important to note that the stochastic PDE (SPDE) system (4.21)–(4.23) are formally ill-defined; because of the stochastic fluxes, the solution variables are probability distributions [118], for which it is nontrivial to give a well-defined meaning to the nonlinear products in the PDEs. In general some sort of regularization is required; a notable example is the theory of regularity structures invented by recent Field medalist Martin Hairer to solve, for example, the KPZ equation with noise [94]. In the present context the regularization ostensibly comes from the finite volume framework used to discretize the SPDEs; however, in this setting the amplitude of the noise increases as the finite volumes shrink, and the nonlinear terms can be shown to diverge [61].

Despite the difficulties in the nonlinear setting, the linearized equations can be analyzed using well established results in the theory of stochastic partial

differential equations [46]. In a series of works [62, 178, 179], Péraud et al. performed Fourier analysis of the linearized SPDEs (4.21)–(4.23) and found that incorporating fluctuations introduces corrections, or a “renormalization”, to the Gibbs free energy and the diffusion coefficients of the fluid mixture that are consistent with the classical theory of electrolytes of Debye, Hückel and Onsager [172, 173]. These results are physically due to electrophoretic and “relaxation” effects [189], which are due to the tendency for a moving ion to drag a “cloud” of oppositely charged ions with it. The numerical simulations based on finite-volume schemes reinforce the theoretical analysis. See Péraud et al. [179] for details of spatial discretization and temporal integration of the stochastic equations, as well as Donev et al. [61] for insightful discussions regarding more general algorithm design for SPDEs.

The works [62, 178, 179] indicate that the Fluctuating Hydrodynamics model is capable of capturing electrokinetic mesoscale phenomena not predicted by the purely deterministic equations (4.2)–(4.4) at a greatly reduced computational cost, relative to a molecular dynamics simulation. Crucially, the theoretical analysis and numerical results were obtained for electrolyte solutions on the torus \mathbb{T}^3 . The presence of solid boundaries, however, presents challenges that are difficult to overcome with the FHD methodology.

4.2.4 Fundamental electrolyte scaling: breakdown of continuum model at walls

A fundamental assumption underlying the Fluctuating Hydrodynamics model for electrolytes is that the number of particles, either solvent or solute, in a given computational grid cell is sufficiently large so that there is a well-defined continuum field representing the particle density [51]. The central limit theorem then can be used to justify the Markovian Gaussian white noise representing thermal fluctuations about the mean fields. There are two important situations for which this assumption is false. The first is when the computational mesh spacing Δx is too fine; it can be said that Δx implicitly defines a “coarse-graining”, mesoscopic length scale, and when Δx approaches microscopic length scales the methodology breaks down. The second situation is when the electrolyte solution to be modeled is too dilute.

When electrolytes interact with solid boundaries, the deterministic, continuum PDE models for electrolytes produce a boundary layer of charge in the near-wall region whose thickness is on the order of a Debye length (4.25)

$$\lambda_D = \sqrt{\frac{\epsilon k_B T}{\sum_k n_k q_k^2}} \quad (4.25)$$

as seen in the EO and ICEO numerical examples in sections 4.2.1 and 4.2.2. Full resolution of this charged boundary layer of course then requires a computational mesh spacing of $\Delta x < \lambda_D$.

For typical electrolyte concentrations, however, a simple calculation shows that the average number of charged ions per cubic λ_D can be less than

one, so the assumption that the charged species' densities can be represented as continuum fields, fluctuating or not, is false.

Consider for simplicity a 1-1 electrolyte mixture, so that the cations and anions are equal in number density n and opposite in charge q . In this case the Debye length simplifies to

$$\lambda_D = \sqrt{\frac{\epsilon k_B T}{2nq^2}}. \quad (4.26)$$

For such an electrolyte, consider the quantity

$$N := n \lambda_D^3 = \left(\frac{\epsilon k_B T}{2q^2} \right)^{3/2} n^{-1/2} \quad (4.27)$$

which can be interpreted as the total number of charged ions one can expect to find in a cubic volume λ_D^3 . If one uses the SI values

$$\epsilon_0 = 8.854 \cdot 10^{-10} F/m$$

$$\epsilon_r = 79.2 \cdot 10^{-10} F/m$$

$$q = 1.6 \cdot 10^{-19} C$$

$$T = 300 K$$

$$k_B = 1.381 \cdot 10^{-23} J/K$$

$$N_A = 6.022 \cdot 10^{23} (\text{mol})^{-1}$$

then N is approximately

$$N = 4.1862 \cdot 10^{11} n^{-1/2} \quad (4.28)$$

$$= 0.53945 w^{-1/2} \quad (4.29)$$

where $w = n/N_A$ is the solution molarity and N_A is Avogadro’s number. At realistic concentrations, *this scaling implies that that total number of ions one can expect to find in a cubic Debye volume is less than one.* For example, a molarity of $w = 0.1 \text{ mol/l} = 10^2 \text{ mol/m}^3 \implies N \approx 0.054$. Hence, when the mesh spacing Δx in a numerical simulation is comparable to the Debye length, the assumption that the charged species’ densities can be represented as continuum fields, fluctuating or not, is false, and new modeling approaches are needed.

4.3 Hybrid Particle-Continuum Stochastic Electrolyte Model

²The results of section 4.2 illustrate the need for alternative multiscale modeling approaches for electrolyte solutions that can simultaneously (i) accurately model the interaction between charged ions and the charge-neutral solvent in regions of low ion density and (ii) account for the effect of thermal fluctuations on mesoscopic dynamics at a reduced cost relative to a full atomistic description. A step in this direction is the following hybrid multiscale model in which the fluid solvent is modeled as a stochastic continuum field in the Fluctuating Hydrodynamics framework, while the charge-carrying solutes are modeled as discrete particles “immersed” in the solvent. The methodology

²The work in this section was performed in collaboration with John Bell, Katherine Klymko, Daniel Ladiges, and Andy Nonaka (LBNL), Guy Moore (University of California, Berkeley), Aleksandar Donev (Courant Institute of Mathematical Sciences), and Alejandro Garcia (San Jose State University).

is based on a stochastic version of immersed boundary method proposed first by Atzberger et al. [17] and then further developed by Atzberger in [16] and Delong et al. in [56].

4.3.1 Model equations

The model proposed herein assumes an overdamped limit, so that the system Schmidt number (measuring the ratio of viscous diffusion to molecular diffusion) is asymptotically large. The charged ions are modeled by the method of Brownian dynamics, in which each discrete particle interact with one another via short-range, Lennard-Jones potentials and Coulomb forces. They also experience hydrodynamic interactions. In turn, the particles exert stresses on the continuum fluid as they accelerate. The stochastic model equations can be summarized as

$$-\eta\Delta_r u + \nabla_r p = \nabla_r \cdot \left[\sqrt{2k_B T \eta} \mathcal{Z} \right] + \mathcal{S}_x [F_{\text{LJ}} + F_{\text{Coulomb}}] + f_{\text{th}} \quad (4.30)$$

$$\nabla_r \cdot u = 0 \quad (4.31)$$

$$\frac{dx_i}{dt} = \mathcal{J}_x [u] + \frac{D_i}{k_B T} (F_{\text{LJ}}^i + F_{\text{Coulomb}}^i) + \sqrt{2D_i} \mathcal{W}_i, \quad 1 \leq i \leq N, \quad (4.32)$$

where the dependent variables are the fluid velocity $u : \mathbb{R}^3 \times [0, \infty) \rightarrow \mathbb{R}^3$, pressure $p : \mathbb{R}^3 \times [0, \infty) \rightarrow \mathbb{R}$, and the particle positions x_i , $i = 1, \dots, N$, where N is the total number of charged ions in the system. Here \mathcal{J}_x and \mathcal{S}_x are the standard interpolation and smoothing operators from the immersed boundary method [180]; consider a smooth, compactly supported function $\varphi_h : C_0^\infty(\mathbb{R}^3) \rightarrow \mathbb{R}$, where h is the diameter of the support of φ_h . The interpolation

operator $\mathcal{J}_x : (L^2(\mathbb{R}^3))^3 \rightarrow \mathbb{R}^{N \times 3}$, while the smoothing operator $\mathcal{S}_x : \mathbb{R}^{N \times 3} \rightarrow (L^2(\mathbb{R}^3))^3$ is its adjoint. For $v \in (L^2(\mathbb{R}^3))^3$, the i -th component of $\mathcal{J}_x[v]$ is defined to be

$$(\mathcal{J}_x[v])_i = \int_{\mathbb{R}^3} \varphi_h(x_i - r)v(r) dr \in \mathbb{R}^3, \quad (4.33)$$

and for $w \in \mathbb{R}^{N \times 3}$,

$$\mathcal{S}_x[w](r) = \sum_{i=1}^N \varphi_h(x_i - r)w_i dr, \quad (4.34)$$

where to be clear, $w_i \in \mathbb{R}^3$ so that $\mathcal{S}_x[w] \in (L^2(\mathbb{R}^3))^3$. From these definitions the adjoint property follows:

$$\langle \mathcal{J}_x[v], w \rangle_{\mathbb{R}^{N \times 3}} = \langle v, \mathcal{S}_x[w] \rangle_{(L^2(\mathbb{R}^3))^3}, \quad (4.35)$$

where $\langle \cdot, \cdot \rangle_{\mathcal{H}}$ denotes the inner product in Hilbert space \mathcal{H} .

In equations (4.30)–(4.32), k_B is Boltzmann's constant, η is the fluid viscosity, and T is the system temperature which is assumed to be constant as in the purely continuum model. The Stokes equation noise $\mathcal{Z} = \mathcal{W}^S + (\mathcal{W}^S)^T$, where, as in section 4.2.3, \mathcal{W}^S is a tensor of Gaussian spatiotemporal white noise whose components are mean-zero and have mutual (co)variances given by

$$\mathbb{E} [W_{ij}^S(r, t)W_{kl}^S(r', t')] = \delta_{ik}\delta_{jl}\delta(r - r')\delta(t - t'), \quad (4.36)$$

and each \mathcal{W}_i is also an independent, Gaussian, mean-zero whitenoise process.

The equations are interpreted in the Itô sense, and f_{th} is a correction term necessary to ensure the long time behavior of the system is consistent with equilibrium statistical mechanics. More specifically, it ensures

that the Fokker-Planck equation corresponding to the coupled particle dynamics (4.32)—governing the probability density function for observing the system particles in some state (x_1, \dots, x_N) at time t —has the Gibbs-Boltzmann distribution

$$p_{\text{eq}}(x) = Z^{-1} e^{-U(x)/k_B T} \quad (4.37)$$

as an equilibrium solution, where $-\nabla_x U(x) = F_{\text{LJ}} + F_{\text{Coulomb}}$. The explicit expression for f_{th} , which is termed the “stochastic drift”, is

$$f_{\text{th}} = k_B T \nabla_x \cdot \mathcal{S}_x. \quad (4.38)$$

If the equations were instead interpreted in the “kinetic” sense (the so-called Klimontovich interpretation, see [129] and [109] for discussions), this correction term would not be necessary.

In the particle evolution equations (4.32), the D_i constants are bare diffusion coefficients, also referred to as “dry” diffusion coefficients for the following reason. Consider momentarily a single spherical particle with radius a suspended in a solvent. It will then undergo standard Brownian motion with a total, or “renormalized” diffusion coefficient given by the Stokes-Einstein relation

$$D^{\text{tot}} = \frac{k_B T}{\zeta \eta a}, \quad (4.39)$$

where ζ is a constant depending on the domain boundary condition. In practice, however, the diffusion a particle experiences from the fluctuating Stokes model (4.30) will depend on the numerical resolution upon discretization. The

fluctuations generated by \mathcal{W}^S will be transmitted to the particle by the interpolation operator \mathcal{J}_x which in turn depends on the support of the kernel φ_h and is set by the numerical mesh spacing Δx . For a given resolution, let D^{wet} denote the diffusion coefficient that results from the particle's interaction with the fluctuating solvent. For a given kernel φ_h , this can be easily measured numerically by averaging over a large number of noninteracting particles. In general, coarsening the numerical resolution (i.e. increasing Δx) will decrease D^{wet} , while in the limit $\Delta x \rightarrow 0 \implies D^{\text{wet}} \rightarrow D^{\text{tot}}$. First described in Español and Donev [75], the approach taken here to ensure that the charged ions diffuse with total coefficient D^{tot} is to add the aforementioned “dry”, or bare diffusion process to the dynamics of $\{x_i\}_i$ so that

$$D_i + D^{\text{wet}} = D^{\text{tot}}. \quad (4.40)$$

The forces F_{LJ}^i and F_{Coulomb}^i on particle i govern the mutual interactions between the charged ions. Coulomb's law gives

$$F_{\text{Coulomb}}^i = \frac{1}{4\pi\epsilon_0} \sum_{j=1, j \neq i}^N \frac{q_i q_j}{|x_i - x_j|^3} (x_i - x_j), \quad (4.41)$$

but in practice an approximation to F_{Coulomb}^i is calculated using the particle-particle, particle-mesh method described in section 4.3.2 below for computational efficiency. The short range force F_{LJ}^i is given by

$$F_{\text{LJ}}^i = \sum_{j \in \Omega_{\text{LJ}}(i)} R_{ij}, \quad (4.42)$$

where $\Omega_{\text{LJ}}(i)$ denotes the set of particles within a given range of particle i , and

$$R_{ij} = -\frac{(x_i - x_j)}{|x_i - x_j|} \left[\frac{\partial U^{\text{LJ}}}{\partial r}(r, \sigma_{ij}, \xi_{ij}) \right] \Big|_{r=|x_i - x_j|}. \quad (4.43)$$

The interaction potential U^{LJ} is taken from the Weeks-Chandler-Anderson model [219], which is a truncated and shifted Lennard Jones potential:

$$U^{\text{LJ}}(r, \sigma, \xi) = \begin{cases} 4\xi ((\sigma/r_{\text{flat}})^{12} - (\sigma/r_{\text{flat}})^6) + \xi, & r \leq r_{\text{flat}} \\ 4\xi ((\sigma/r)^{12} - (\sigma/r)^6) + \xi, & r_{\text{flat}} < r < 2^{1/6}\sigma \\ 0, & 2^{1/6}\sigma \leq r. \end{cases} \quad (4.44)$$

Here σ is the van der Waals diameter, and r_{flat} is a “cutoff” distance below which the potential is mollified so that it does not diverge at the origin. The shift and scaling by ξ ensures that U is not discontinuous at the cutoff, and both σ_{ij} and ξ_{ij} are the values averaged from particles i and j . The parameters used in the numerical pair correlation tests in presented in section 4.3.4 are listed there.

Before presenting the numerical results, the P3M method used to compute the electrostatic forces F_{Coulomb}^i is described in detail in section 4.3.2, and then the temporal integration scheme used to integrate equations (4.30)–(4.32) is detailed in 4.3.3.

4.3.2 Particle-particle, particle-mesh (P3M) description

The particle-particle, particle-mesh (P3M) method for computing long-range, Coulomb interactions among a collection of particles is an example of a “classical” multiscale numerical method and is similar in many ways to Ewald summation and fast multipole techniques. The basic idea is to use a mixed approach to compute pairwise Coulomb forces, and it combines the solution of a so-called Particle-in-Cell (PIC) Poisson equation for “far-field” forces with

a direct calculation of “short-range” Coulomb forces. In general, an extra calculation is needed to supplement these approaches to correct for the fact that the PIC incorrectly accounts for the short range forces. A classic reference for this approach is the Hockney and Eastwood text [102]; see also Frenkel and Smit’s text [76] on molecular simulation methods.

Consider a collection of N point particles with positions $x = \{x_1, x_2, \dots, x_N\}$ and charges $q = \{q_1, q_2, \dots, q_N\}$; each $x_j \in \mathbb{R}^3$ and $q_j \in \mathbb{R}$. The Coulomb force on particle i due to the others is

$$F_C^i = q_i E_C(x_i) \quad (4.45)$$

$$= -q_i \left(\nabla(-\Delta)^{-1} \frac{1}{\epsilon_0} \sum_{j=1, j \neq i}^N q_j \delta_{x_j} \right) (x_i) \quad (4.46)$$

$$= \frac{q_i}{4\pi\epsilon_0} \sum_{j=1, j \neq i}^N \frac{q_j}{|x_i - x_j|^3} (x_i - x_j), \quad (4.47)$$

where δ_x is the Dirac-delta distribution centered at x . The total cost to compute the Coulomb force on every particle due to all the others is $\mathcal{O}(N^2)$, which is prohibitively large for sufficiently large N . A cheaper alternative to compute the electrostatic force on particle i is the PIC approach.

Let $S_a : \mathbb{R}^3 \rightarrow \mathbb{R}$ be a smooth function with fixed compact support of diameter $a > 0$ that integrates to 1, and define the smoothing operator $\mathcal{S}_E(x) : \mathbb{R}^N \rightarrow L^2(\mathbb{R}^3)$

$$\mathcal{S}_E(x)[u](r) := \sum_{j=1}^N S_a(x_j - r) u_j \quad (4.48)$$

and the interpolation operator $\mathcal{J}_E(x) : L^2(\mathbb{R}^3) \rightarrow \mathbb{R}^N$

$$(\mathcal{J}_E(x)[v])_i := \int_{\mathbb{R}^3} S_a(x_i - r)v(r)dr, \quad (4.49)$$

both of which are parameterized by $x \in \mathbb{R}^N \times \mathbb{R}^3$. The smooth kernel S_a and the operators $\mathcal{S}_E(x)$ and $\mathcal{J}_E(x)$ are essentially the same as φ_h and equations (4.33) and (4.34) above; however, the support of the hydrodynamic and electrostatic kernels need not be the same, so different notation is used here. Note also that they map to slightly different spaces.

As above, the $\mathcal{J}_E(x)$ and $\mathcal{S}_E(x)$ operators are adjoints of each other, so that for fixed $x \in \mathbb{R}^N \times \mathbb{R}^3$, any $u \in \mathbb{R}^N$, and any square integrable function v

$$\langle \mathcal{J}_E(x)[v], u \rangle_{\mathbb{R}^N} = \sum_{j=1}^N \left[\int_{\mathbb{R}^3} S_a(x_j - r)v(r)dr \right] u_j \quad (4.50)$$

$$= \int_{\mathbb{R}^3} \left[\sum_{j=1}^N S(x_j - r)u_j \right] v(r)dr \quad (4.51)$$

$$= \int_{\mathbb{R}^3} \mathcal{S}_E(x)[u](r)v(r)dr = \langle v, \mathcal{S}_E(x)[u] \rangle_{L^2(\mathbb{R}^3)}. \quad (4.52)$$

The particle-in-cell (PIC) approach to compute the Coulomb force on particle i due to all the others consists of smoothing the collection of point charges with \mathcal{S}_E , solving Poisson's equation for the potential, taking the negative gradient of that potential, and then interpolating the result with \mathcal{J}_E . Let ϕ solve the Poisson equation

$$-\epsilon_0 \Delta \phi = (\mathcal{S}_E(x)[q]), \quad (4.53)$$

and define $E_P^i := -(\mathcal{J}_E(x) [\nabla \phi])_i$, where \mathcal{J}_E acts on each component of $\nabla \phi$.

The electrostatic force on particle i is then simply computed as

$$F_P^i = q_i E_P^i, \quad (4.54)$$

where the subscript P signifies that the quantities were computed from the solution to Poisson's equation. The numerical solution to (4.53) can be computed relatively quickly using standard Krylov subspace or spectral methods.

By linearity, the electric potential at a point y resulting from the solution to (4.53) is

$$\phi(y) = \frac{1}{\epsilon_0} (-\Delta)^{-1} \left(\sum_{j=1}^N q_j S_a(x_j - r) \right) \quad (4.55)$$

$$= \frac{1}{4\pi\epsilon_0} \sum_{j=1}^N q_j g(x_j, y), \quad (4.56)$$

where

$$g_a(x_j, y) := \int_{\mathbb{R}^3} \frac{S_a(x_j - r)}{|y - r|} dr. \quad (4.57)$$

For fixed y , the $1/|y - r|$ term in the integrand can be written as a multipole expansion about x_j , so that

$$\frac{1}{|y - r|} = \frac{1}{|y - x_j|} + \frac{(y - x_j)}{|y - x_j|^3} \cdot (r - x_j) + \psi(r, y - x_j), \quad (4.58)$$

where ψ represents the quadrupole, octopole, and higher order terms and decays as $|y - x_j|^{-5}$ or faster. Inserting the expansion into g_a gives

$$\begin{aligned} g_a(x_j, y) &= \frac{1}{|y - x_j|} + \frac{y - x_j}{|y - x_j|^3} \cdot \int_{\mathbb{R}^3} (r - x_j) S_a(x_j - r) dr \\ &\quad + \int_{\mathbb{R}^3} S_a(x_j - r) \psi(r, y - x_j) dr, \end{aligned} \quad (4.59)$$

where the fact that S_a integrates to 1 is used. Further assume both here and below that S_a is symmetric, so that $S_a(-r) = S_a(r)$ $\forall r \in \mathbb{R}^3$; it then has vanishing first moment

$$\int_{\mathbb{R}^3} r S_a(r) dr = 0, \quad (4.60)$$

and hence the dipole moment of ϕ will vanish. Therefore,

$$\phi(y) = \frac{1}{4\pi\epsilon_0} \sum_{j=1}^N q_j \left(\frac{1}{|y - x_j|} + \int_{\mathbb{R}^3} S_a(x_j - r) \psi(r, y - x_j) dr \right). \quad (4.61)$$

If the higher order terms in the multipole expansion are neglected, then ϕ is approximated by the sum of monopoles. If ϕ_M denotes this truncated potential, then the resulting electric field is

$$-\nabla \phi_M(y) = \frac{1}{4\pi\epsilon_0} \sum_{j=1}^N \frac{q_j}{|y - x_j|^3} (y - x_j). \quad (4.62)$$

Applying the interpolation operator $\mathcal{J}_E(x)$ to each vector component of (4.62) gives

$$-(\mathcal{J}_E(x) [\nabla \phi_M])_i = - \int_{\mathbb{R}^3} S_a(x_i - y) \nabla \phi_M(y) dy \quad (4.63)$$

$$= \frac{1}{4\pi\epsilon_0} \sum_{j=1, j \neq i}^N \int_{\mathbb{R}^3} S_a(x_i - y) \frac{q_j}{|y - x_j|^3} (y - x_j) dy; \quad (4.64)$$

note the $j = i$ term vanishes due to the assumed symmetry of S_a . Similar to above, the vector $(y - x_j)/|y - x_j|^3$ can be expanded about the point x_i :

$$\frac{y - x_j}{|y - x_j|^3} = \frac{x_i - x_j}{|x_i - x_j|^3} + \left[\nabla_y \left(\frac{y - x_j}{|y - x_j|^3} \right) \Bigg|_{y=x_i} \right] (y - x_i) + \Psi(y, x_i - x_j), \quad (4.65)$$

where, as before, Ψ represents higher order terms in the vector expansion. Since the second order tensor in brackets has no y -dependence, it can be

brought outside the integral. Using again (4.60) and that S_a integrates to 1, (4.64) reduces to

$$-(\mathcal{J}_E(x) [\nabla \phi_M])_i = \frac{1}{4\pi\epsilon_0} \sum_{j=1, j \neq i}^N \left(\frac{x_i - x_j}{|x_i - x_j|^3} + \int_{\mathbb{R}^3} S_a(x_i - y) \Psi(y, x_i - x_j) dy \right). \quad (4.66)$$

Ergo, if one again neglects the higher order terms built into Ψ , equality of (4.45) and (4.54) results, so that the electrostatic force on particle i computed by the PIC approach is equal to the direct $\mathcal{O}(N_p^2)$ Coulomb calculation: $F_C^i = F_P^i$.

Of course, the equality of the two approaches is only approximate, and only correct to the extent that the ψ and Ψ terms in the Taylor expansions (4.58) and (4.65) are asymptotically small, which is true when pairs of point charges are well separated relative to the diameter a of the support of S_a :

$$\frac{|x_i - x_j|}{a} \gg 1. \quad (4.67)$$

In the case when (4.67) does not hold, it is easy to see that in general $F_C^i \neq F_P^i$. Consider a two particle system with charges q_1 and q_2 at the respective positions x_1 and x_2 . For such a configuration, the Poisson equation (4.53) resulting from the PIC approach has solution

$$\phi(y) = \frac{1}{4\pi\epsilon_0} \int_{\mathbb{R}^3} \frac{1}{|y - r|} (q_1 S_a(x_1 - r) + q_2 S_a(x_2 - r)) dr \quad (4.68)$$

with associated electric field

$$-\nabla \phi(y) = \frac{1}{4\pi\epsilon_0} \int_{\mathbb{R}^3} \frac{(y - r)}{|y - r|^3} (q_1 S_a(x_1 - r) + q_2 S_a(x_2 - r)) dr. \quad (4.69)$$

After applying the interpolation operator $\mathcal{J}_E(x)$, one obtains

$$F_P^1 = -q_1 (\mathcal{J}_E(x) [\nabla \phi])_1 = \frac{1}{4\pi\epsilon_0} \int_{\mathbb{R}^3} q_1 S_a(x_1 - y) \int_{\mathbb{R}^3} \frac{(y - r)}{|y - r|^3} (q_2 S_a(x_2 - r)) dr dy \quad (4.70)$$

for the force on particle 1 due to particle 2 (note the particle exerts no force upon itself, again, by symmetry of S_a). A similar result holds for the total force on particle 2, F_P^2 . In general, (4.70) is not equivalent to the standard Coulomb force (4.47); formally this only occurs in the limit $a \rightarrow 0$. Finally, note that if one makes the variable transforms $w = x_1 - r$ and $z = x_1 - y$, (4.70) becomes

$$F_P^1 = \frac{q_1 q_2}{4\pi\epsilon_0} \int_{\mathbb{R}^3} S_a(z) \int_{\mathbb{R}^3} \frac{(w - z)}{|w - z|^3} S_a(w - x_{12}) dw dz, \quad (4.71)$$

$x_{12} = x_1 - x_2$, which is the expression found in the Hockney and Eastwood text [102], as well as various papers in the physics/chemistry literature; see, for example, [7].

The above observations motivate the mixed particle-particle, particle-mesh approach. Let

$$\Omega(i) := \{j \in \{1, \dots, N\}, j \neq i \mid \text{supp } S_a(x_i - \cdot) \cap \text{supp } S_a(x_j - \cdot) \neq \emptyset\} \quad (4.72)$$

$$= \{j \in \{1, \dots, N\}, j \neq i \mid |x_i - x_j| < 2a\} \quad (4.73)$$

define a local neighborhood of particle i . The total force on particle i in the P3M method is computed as

$$F_{P3M}^i = F_{SR}^i + F_{LR}^i - R^i, \quad (4.74)$$

that is, with a short-range, a long-range, and a correction “reference” force. The long range force is computed exactly as in PIC approach described above, so that for ϕ solving (4.53),

$$F_{LR}^i = -q_i (\mathcal{J}_E(x) [\nabla \phi])_i \quad (4.75)$$

$$= \sum_{j=1, j \neq i}^N \frac{q_i q_j}{4\pi\epsilon_0} \int_{\mathbb{R}^3} S_a(x_i - y) \int_{\mathbb{R}^3} \frac{(y - r)}{|y - r|^3} S_a(x_j - r) dr dy. \quad (4.76)$$

The short range force is given as

$$F_{SR}^i = \sum_{j \in \Omega(i)} \frac{q_i q_j}{4\pi\epsilon_0} \frac{(x_i - x_j)}{|x_i - x_j|^3}, \quad (4.77)$$

and the correction force is simply

$$R^i = \sum_{j \in \Omega(i)} \frac{q_i q_j}{4\pi\epsilon_0} \int_{\mathbb{R}^3} S_a(x_i - y) \int_{\mathbb{R}^3} \frac{(y - r)}{|y - r|^3} S_a(x_j - r) dr dy \quad (4.78)$$

$$= \sum_{j \in \Omega(i)} \frac{q_i q_j}{4\pi\epsilon_0} \int_{\mathbb{R}^3} S_a(z) \int_{\mathbb{R}^3} \frac{(w - z)}{|w - z|^3} S_a(w - x_{ij}) dr dy. \quad (4.79)$$

For efficiency, the correction force R^i is pre-computed and tabulated for fixed S_a as a function of $x_{ij} = x_i - x_j$. For appropriately chosen smoothing function S_a , R^i can be treated (approximately) as a function of the separation distance $|x_{ij}|$ only, hence reducing the dimensionality of the “reference” table. The Peskin kernels developed for the immersed boundary method [180] are particularly useful in this regard and are indeed employed in the numerical results presented in section 4.3.4 below.

Inserting each force (4.75), (4.77), (4.78) into the expression (4.74) gives

$$F_{P3M}^i = \sum_{j \in \Omega(i)} \frac{q_i q_j}{4\pi\epsilon_0} \frac{(x_i - x_j)}{|x_i - x_j|^3} \quad (4.80)$$

$$+ \sum_{j \notin \Omega(i)} \frac{q_i q_j}{4\pi\epsilon_0} \int_{\mathbb{R}^3} S_a(x_i - y) \int_{\mathbb{R}^3} \frac{(y - r)}{|y - r|^3} S_a(x_j - r) dr dy. \quad (4.81)$$

Making use of multipole expansions in the same manner as (4.58) and (4.65) above,

$$F_{P3M}^i = \sum_{j \in \Omega(i)} \frac{q_i q_j}{4\pi\epsilon_0} \frac{(x_i - x_j)}{|x_i - x_j|^3} + \sum_{j \notin \Omega(i)} \frac{q_i q_j}{4\pi\epsilon_0} \frac{(x_i - x_j)}{|x_i - x_j|^3} \quad (4.82)$$

$$+ \sum_{j \notin \Omega(i)} \frac{q_i q_j}{4\pi\epsilon_0} \int_{\mathbb{R}^3} S_a(x_i - y) \left(\Psi(y, x_i - x_j) + \int_{\mathbb{R}^3} S_a(x_j - r) \nabla_y \psi(r, y - x_j) dr \right) dy \quad (4.83)$$

$$= F_C^i + \sum_{j \notin \Omega(i)} \frac{q_i q_j}{4\pi\epsilon_0} \int_{\mathbb{R}^3} S_a(x_i - y) \left(\Psi(y, x_i - x_j) + \int_{\mathbb{R}^3} S_a(x_j - r) \nabla_y \psi(r, y - x_j) dr \right) dy. \quad (4.84)$$

Hence, in theory, the force on each particle i resulting from the P3M method is equivalent to Coulomb force (4.45), up to the size of the terms higher order terms Ψ (respectively ψ) in the multipole vector (resp. scalar) expansions of the singular integral kernels.

4.3.3 Temporal integration

The temporal evolution of the hybrid particle-continuum model (4.30)–(4.32) is approximated in the following manner. Assume that at the first

time step t_0 there exists a collection of particles at positions (x_1, \dots, x_N) with charges (q_1, \dots, q_N) .

1. The grid containing charge density, ϱ , is populated using the spreading operation defined by equation (4.48):

$$\varrho = \mathcal{S}_E(x)[q]. \quad (4.85)$$

The Poisson equation (4.53) is solved with a geometric multigrid method, and then the corresponding PIC electric field is computed with as $-\nabla\phi$.

2. This electric field is interpolated to the particle locations using the operator (4.49). The corresponding force on each particle is then computed as (4.54). For particles at close range, the short-range and correction forces featured by the P3M method are also computed, so that the total force on particle i is given by equation (4.74). Additionally, if there is any external electric field E_{ext} being modeled, its effect is included here:

$$F_{\text{Coulomb}}^i = F_{P3M}^i + q_i E_{\text{ext}}. \quad (4.86)$$

Close range WCA interactions are also calculated in this step, and the total force on the particle calculated as per equations (4.42) and (4.43).

3. The force from the particles $F_{\text{LJ}} + F_{\text{Coulomb}}$ is spread to the grid, storing the force density using the smoothing operator defined by equation (4.34). The stochastic drift term (4.38) is computed as

$$f_{\text{th}}(r) = k_B T \nabla_x \cdot \mathcal{S}_x(r) \approx k_B T \left(\mathcal{S}_{x+\delta G/2} \left(\frac{G}{2} \right) - \mathcal{S}_{x-\delta G/2} \left(\frac{G}{2} \right) \right), \quad (4.87)$$

where G is a random vector of $3N$ i.i.d. Gaussian variates with mean-zero and unit variance and is not related to the white noise \mathcal{W}^S or \mathcal{W}_j in equations (4.30) and (4.32). The form of this approximation is motivated by the following lemma:

Lemma 4.3.1. *Let $M_{ij} : \mathbb{R}^d \rightarrow \mathbb{R}^d$ with $M_{ij} \in C^2$ for each $1 \leq i, j \leq N$, and let X, Y be mean-zero Gaussian vectors with covariance $\mathbb{E}[X_i Y_j] = \delta_{ij}$. Then*

$$\lim_{\epsilon \downarrow 0} \frac{1}{\epsilon} \mathbb{E}[M_{ij}(q + \epsilon X)Y_j - M_{ij}(q)Y_j] = \frac{\partial M_{ij}}{\partial q_j}(q). \quad (4.88)$$

Proof:

Using the remainder form of Taylor's theorem,

$$M_{ij}(q + \epsilon X) = M_{ij}(q) + \frac{\partial M_{ij}}{\partial q_\alpha}(q)\epsilon X_\alpha + \frac{\partial^2 M_{ij}}{\partial q_\alpha \partial q_\beta}(q) \frac{\epsilon^2 X_\alpha X_\beta}{2}, \quad (4.89)$$

and the expectation in (4.88) reduces to

$$\frac{1}{\epsilon} \mathbb{E}[M_{ij}(q + \epsilon X)Y_j - M_{ij}(q)Y_j] \quad (4.90)$$

$$= \frac{\partial M_{ij}}{\partial q_\alpha}(q) \mathbb{E}[Y_j X_\alpha] + \mathbb{E}\left[\frac{\partial^2 M_{ij}}{\partial q_\alpha \partial q_\beta}(q) \frac{\epsilon^2 X_\alpha X_\beta}{2} Y_j\right] \quad (4.91)$$

$$= \frac{\partial M_{ij}}{\partial q_j}(q) + \epsilon \mathbb{E}\left[\frac{\partial^2 M_{ij}}{\partial q_\alpha \partial q_\beta}(q) \frac{X_\alpha X_\beta Y_j}{2}\right]. \quad (4.92)$$

Since M_{ij} is C^2 , it's uniformly bounded independent of both ϵ and X , and since X and Y are Gaussians $\mathbb{E}[X_\alpha X_\beta Y_j] < \infty$, the expectation in the final line vanishes as $\epsilon \rightarrow 0$, giving the desired result. \square

The step size δ is a free parameter and should be set to as small a value as possible without incurring numerical roundoff error. The specific value used for the numerical tests below is $\delta = \Delta r$, where Δr is the mesh spacing on which (u, p) is solved. The whitenoise forcing in (4.30) is then generated by pulling a sequence of Gaussian random numbers Z with mean-zero and unit variance, scaling them by $\sqrt{2\eta k_B T / (\Delta t \Delta r^3)}$, and then taking their discrete divergence, as illustrated in figure 4.5. The resulting Stokes system is numerically solved with a preconditioned GMRES solver described in Cai et al. [38].

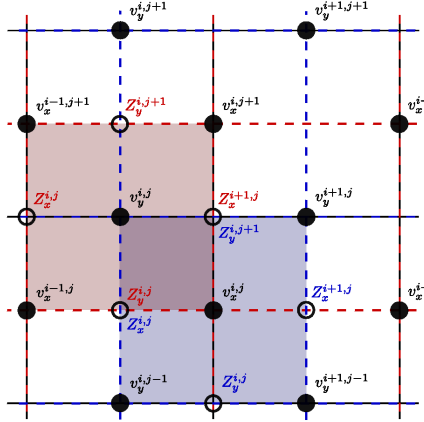


Figure 4.5: 2D illustration courtesy of Daniel Ladiges (LBNL) of the discretization of the $\nabla \cdot \mathcal{W}^S$ term from equation (4.30). Random numbers Z are generated at the faces of control volumes around the points where velocities u are defined so that the divergence may be calculated.

4. The velocity u is interpolated to particle locations using the operator \mathcal{J}_x defined in equation (4.33), yielding the particle velocities, $\mathcal{J}_x[u]$. The temporal discretization of the particle movement is given by the midpoint

update scheme:

$$x_i^{n+1/2} = x_i^n + \frac{\Delta t}{2} \mathcal{J}_{x^n}[u^n] \quad (4.93)$$

$$\begin{aligned} x_i^{n+1} &= x_i^n + \Delta t \mathcal{J}_{x^{n+1/2}}[u^n] + \frac{D_i}{k_B T} ((F_{\text{LJ}}^i)^n + (F_{\text{Coulomb}}^i)^n) \\ &\quad + \sqrt{\frac{2D_i}{\Delta t}} W_i^n, \end{aligned} \quad (4.94)$$

where the superscript n indicate the time step number. Note that this update scheme involves only a single solution of the hydro and electrostatic equations. It is first order in time, as illustrated in Delong et al. [56], where higher order schemes are also discussed.

5. Calculate statistics, output desired fields, and return to step 1.

4.3.4 Numerical results

Here we present a numerical test to verify the implementation of the hybrid continuum-particle electrolyte model. Computed is pair correlation function $g(\hat{x})$, which quantifies the time-averaged density of particles as a function of radius from an arbitrary reference particle, normalized by the total number density of the system.

The stochastic model³ is implemented in the AMReX framework described in Zhang et al. [227] and available online⁴. The numerical simulation is performed for a two species electrolyte with $D_\alpha^{\text{tot}} = 1.17 \cdot 10^{-5} \text{ cm}^2/\text{s}$,

³dubbed SHIBA (“stochastic hybrid immersed boundary algorithm”)

⁴<https://github.com/AMReX-FHD/FHDeX>

$D_\beta^{\text{tot}} = 1.33 \cdot 10^{-5} \text{ cm}^2/\text{s}$, $q_\alpha = 1.6 \cdot 10^{-19} \text{ C}$ and $q_\beta = -q_\alpha$. The solvent is taken to be water, with $T = 295 \text{ K}$, viscosity $\eta = 0.01 \text{ g}/(\text{cm s})$, and permittivity $\epsilon = \epsilon_r \epsilon_0$, where the relative permittivity $\epsilon_r = 78.3$ and ϵ_0 is the vacuum permittivity. The time step $\Delta t = 10^{-13} \text{ s}$ is used, while the spatial grid spacing Δr varies as described below. Note, however, that the grid is isotropic, so that for fixed $\Delta r = \Delta x = \Delta y = \Delta z$. The close range potential parameters $\xi = 10^{-16} \text{ g cm}^2/\text{s}^2$, $\sigma = 0.4 \text{ nm}$, and $r_{\text{flat}} = 0.1 \text{ nm}$.

All numerical parameters were selected by successive refinement until a negligible change in the result was observed. Of particular importance is the selection of the time step, Δt . Setting this too large will result in numerical instability due to the stiffness of both the close range and electrostatic interactions. In MD simulations the time step is typically constrained to less than 10^{-15} s by the bonding forces within water molecules, however even simplified models which coarse grain these features are limited to around 10^{-14} s .[166].

Note that the above parameters yield Schmidt numbers of 854 and 752 for species α and β , respectively, in accordance with the overdamped approximation the model employs.

For a binary system, the pair correlation function between two systems α and β is defined as

$$g_{\alpha\beta}(\hat{x}) = \lim_{\tau \rightarrow \infty} \frac{\mathcal{V}}{N_{\alpha\beta}^2 \tau} \int_0^\tau \sum_{i,j,i \neq j}^N \delta(\hat{x} - r_{ij}(t)) \delta_{\alpha,s_i} \delta_{\beta,s_j} dt. \quad (4.95)$$

\mathcal{V} is the system volume, s_i/s_j are the species of particles i/j , $N_{\alpha\beta}$ is the total number of species pairs, and $r_{ij} = |x_i x_j|$ is the distance between particles i

and j .

For low to moderate ion concentrations, classic Debye-Hückel theory [189] gives the pair correlation function as approximately

$$g_{\alpha\beta}^{\text{DH}}(\hat{x}) = e^{-U_{\alpha\beta}(\hat{x})/k_B T}, \quad (4.96)$$

where the potential

$$U_{\alpha\beta}(\hat{x}) = \frac{q_\alpha q_\beta}{4\pi\epsilon} \frac{e^{-\hat{x}/\lambda_D}}{\hat{x}} + U_{\alpha\beta}^{\text{LJ}}(\hat{x}), \quad (4.97)$$

and $U_{\alpha\beta}^{\text{LJ}}$ is as before in equation (4.44). The Debye length λ_D is as previously defined by equation (4.25).

In figures 4.6 and 4.7, we compare the approximate theoretical expression of equation (4.96) with results obtained from the SHIBA model. In figure 4.6, the comparison is shown for a molar concentration of 0.1M; excellent agreement is observed. Figure 4.7 shows the comparison for 1.0M, for two different ratios of wet and dry diffusion. A negligible difference is observed between the two wet and dry results; this is unsurprising as we can see from equation (4.96) that the pair correlation function contains no hydrodynamic contribution in the classical theory. Reasonable agreement is observed, with some deviation observed in the peak of the opposite charge result. We note that (4.96) is derived in the low concentration limit, so we expect decreasing agreement with increasing concentration.

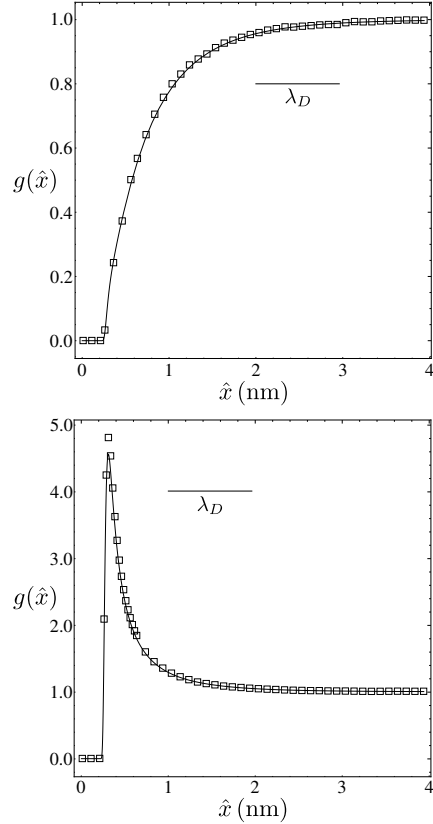


Figure 4.6: Radial distribution for a molarity of 0.1M. The upper plot shows the pair correlation for ions of like charge, also indicated is the Debye length. The lower plot shows the pair correlation for ions of opposite charge. The solid line shows the approximate analytical solution given by (4.96), the squares show the numerical result from the SHIBA mode. These results were collected using a bin width of 0.025 nm, with a sample size of 50,000—the simulation was run for 100,000 steps, with the first 50,000 steps used for equilibration. Note that some points have been omitted for visual clarity. The grid size was set such that the total diffusion of species α was 14.7% wet and 85.3% dry, and for species β , 12.9% wet and 87.1% dry. This corresponds to $\Delta r = 1\text{nm}$, with a $32 \times 32 \times 32$ cell periodic domain.

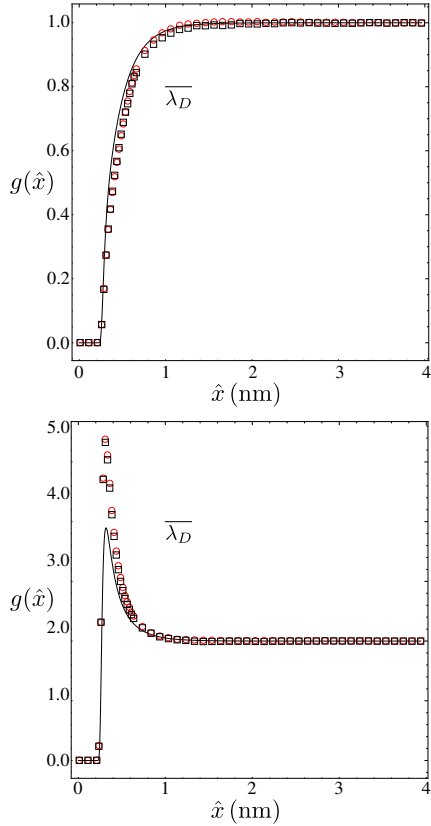


Figure 4.7: Radial distribution for a molarity of 1.0M. The upper plot shows the pair correlation for ions of like charge, also indicated is the Debye length. The lower plot shows the pair correlation for ions of opposite charge. The solid line shows the approximate analytical solution given by (4.96), the boxes and circles show numerical result from the SHIBA model. The numerical parameters are the same as those described for figure 4.6, except that two different grid resolutions are shown. The red circles show the case where the grid size was set such that the total diffusion of species α was 14.7% wet and 85.3% dry, and for species β , 12.9% wet and 87.1% dry. This corresponds to $\Delta r = 1\text{nm}$, with a $16 \times 16 \times 16$ cell periodic domain. The black squares show the case for which the grid size was set such that the total diffusion of species α was 58.9% wet and 41.1% dry, and for species β , 51.8% wet and 41.2% dry. This corresponds to $\Delta r = 0.25\text{nm}$, with a $32 \times 32 \times 23$ cell periodic domain.

4.4 Discussion: Potential Multiscale Modeling for Wall Bounded Electrokinetic Flows

The hybrid particle/continuum model is designed to remain accurate in regions of low ion density, such as the near-wall Debye layer, at a reduced computational cost relative to a fully molecular representation. An application of the method to the situation for which it was originally designed, namely, to wall bounded flows, is still ongoing. Even after sufficient validation, one can argue that at realistic concentrations and sufficiently large length scales, such as those relevant to microfluidic devices and fuel cells, the hybrid particle-continuum approach remains prohibitively expensive.

At these length scales, in which the characteristic system length L is sufficiently large relative to λ_D , electrolytes are effectively electroneutral away from the near-wall Debye layer. Donev et al. [63] recently developed a fluctuating, electroneutral continuum model for such situations, extending the work in [62, 178, 179]. The key advantage of the electroneutral model is the removal of the restrictive electrodiffusive stability constraint $\Delta t < \lambda_D^2/D$, where D is a typical diffusion coefficient.

The drawback to the approach, however, is that it is nontrivial to analytically derive suitable boundary conditions for wall-bounded configurations. Derivations currently available in the literature are based on asymptotic expansions carried out under restrictive physical assumptions, such as no surface conduction and single species mixtures [63, 196, 197].

To extend the capabilities of the electroneutral model and hence en-

able the efficient simulation of wall-bounded electrolyte flows at application scales, I propose an HMM approach. The basic idea is essentially the same as technique employed in chapter 2 and is illustrated in figure 4.4; it consists of coupling together a high-fidelity, particle representation of the charged ions in the near-wall Debye layer—a “microscale” model—to the efficient electroneutral continuum model for the “macroscale” bulk flow.

As with any multiphysics algorithm, such an approach of course comes with nontrivial mathematical, physical modeling, and algorithmic details that must be addressed before successfully deploying it as a modeling tool. For the proposed electrolyte model, some of these issues are well understood. For example, even though the physically correct boundary conditions for the electroneutral model are not known, there of course is a large body of knowledge concerning the mathematical well-posedness of boundary conditions for flow problems.

Another nontrivial, but well understood issue is the proper way to incorporate stochastic fluctuations in both micro and macroscale models in a way that is thermodynamically consistent. Previous researchers have coupled fluctuating, continuum fluid equations to Direct Simulation Monte Carlo schemes [60, 221], as well as MD simulations [50].

Other key modeling issues, however, will comprise the principal areas of investigation. Firstly, it will be crucial to identify metrics by which the accuracy of the macroscale model can be assessed. Without a series of validation cases, there is no way to gauge the microscale’s ability to provide accurate

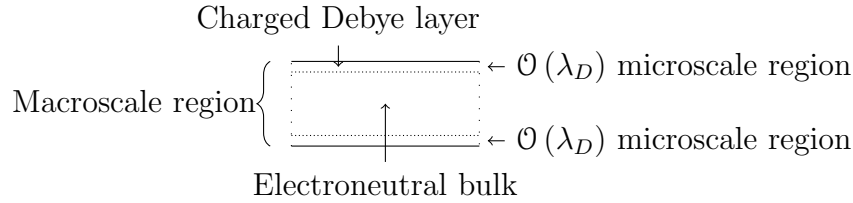


Figure 4.8: Cartoon depiction of proposed heterogeneous multiscale model for a channel configuration.

boundary conditions.

It will also be crucial to identify the proper space of physically important parameters to explore—i.e. what kind of “knobs” to turn—in the microscale model, as this affects the choice of state-variables received from the macroscale model. Examples could be the local value of pressure gradient, ion concentrations, or electric potential. These parameters in turn will affect the choice of “far-field” boundary conditions at the non-physical computational boundary (e.g. the densely dotted lines in figure 4.4), which are required for the microscale model to be complete.

Of course, to some extent the microscale parameters will vary depending on the physical problem at hand, which also affects the choice of the microscale model itself. For example, the hybrid particle/continuum model described in subsection 4.3 is a more computationally efficient choice than an MD model, but the latter may necessary if more complicated physics, such as surface chemistry, need to be modeled in the near-wall region.

4.5 Room Temperature Ionic Liquids (RTILs)

⁵We next turn our attention to ionic liquids (IL), which are liquid salts with dissociated cations and anions such as molten NaCl. Unlike conventional electrolyte solutions (e.g., seawater), an ionic liquid does not require a polar solvent. Of particular interest are ionic liquids composed of complex hydrocarbons that are high-viscosity liquids at room temperature. These room temperature ionic liquids (RTILs) exhibit intriguing physical properties such as high charge density [200, 222] and extremely low vapor pressures [212]. Such properties make them attractive for energy technology applications such as super-capacitors [33], batteries [145], and dye-sensitized photoelectrochemical cells [146]. RTILs also have technological applications as designer solvents in areas such as lubrication of micro-electromechanical machines [202, 229].

Room temperature ionic liquids exhibit a number of interesting physical features. Capacitance measurements with RTILs show different behavior as a function of applied voltage than conventional electrolytes, which reflects overcrowding at the electrode surfaces resulting from the large size of the ions [130]. At low voltages, short-range Coulomb interactions also lead to overscreening in which the layer next to an electrode has excess charge relative to the electrode, resulting in the formation of a subsequent, weaker layer of opposite charge [23]. Molecular dynamics simulations [152, 160, 184] and experimental

⁵The work presented in this section and section 4.6 was performed in collaboration with John Bell, Katherine Klymko, and Andy Nonaka (LBNL) as well as Alejandro Garcia (SJSU).

evidence [174, 208, 220] show that RTILs are heterogeneous at nanoscale levels, forming phase separation of anions and cations on scales of a few nanometers.

Strong inter-ionic correlations and structure render classical models such as Nersnt-Planck used to describe dilute electrolytes inapplicable. Kornyshev and co-workers [88, 130] address the impact of ion size and enthalpy of mixing on the structure of the electrical double layer (EDL) in an ionic liquid. Their model gives a diffuse double-layer capacitance that extends the classical Guoy-Chapman theory and is in agreement with experimental measurements [117]. Bazant, Story, and Kornyshev [24] develop a Landau-Ginzburg-like model that includes effects of ion size and overscreening that is able to predict the structure of the EDL, and improves the prediction of the capacitance. Limmer [147] introduces a mean-field model that incorporates short range repulsion between cations and anions. The interplay of this short-range repulsion with electrostatic forces then determines the morphology of the ionic liquid. Gavish and Yochelis [83] construct a model by adding a Flory-Huggins-like term and an electrostatic term to the free energy of an ideal fluid. The resulting system is similar to the Ohta-Kawasaki model [120, 170] for diblock co-polymers coupled to an electric field. They solve the resulting diffusion equation coupled to the electrostatic equation to study structure in the bulk and how the structure couples to the electric double layer.

Simulation models for ionic liquids generally fall into two categories: coarse-grained lattice models [32, 130, 147] and detailed microscopic models such as molecular dynamics [152, 160] and density functional theory [113, 119].

The former have the advantage of capturing qualitative features of an ionic liquid while being computationally efficient. They have the disadvantage of omitting many physical details required for quantitative predictions. On the other hand, microscopic models capture molecular detail but they are computationally demanding and additionally require delicate tuning of the potentials for the complex molecules in an ionic liquid.

Section 4.6 introduces a new mesoscopic simulation model for ionic liquids. Specifically, we develop a low Mach number fluctuating hydrodynamics model that is similar to the work of Lazaridis et al. [139]. Their model is based on a compressible isothermal formulation that has a more comprehensive description of the fluid than in Gavish and Yochelis [83], albeit with a somewhat idealized thermodynamic representation. The deterministic component of the model here is similar to the quasi-incompressible Cahn-Hilliard fluid model of Lowengrub and Truskinovsky [151] coupled to an electric field. The incorporation of stochastic terms allows our mesoscopic model to capture the effects of thermal fluctuations which cannot be neglected at the nanometer scale, the length scale at which typical structures form in ionic liquids. The low Mach number formulation analytically removes sound waves from the model equations based on the assumption that they do not significantly affect the system dynamics. This eliminates the acoustic time step restriction allowing for time steps that are two or more orders of magnitude larger than the comparable compressible formulation, and significantly more computationally efficient than MD simulations of a similar size.

The outline of the remainder of this chapter is as follows: First, the Gibbs free energy functional is defined and the fluctuating hydrodynamic equations of motion are outlined in section 4.6.1. In particular the free energy contains “excess” and nonlocal (meaning it depends not only on concentration c but also on ∇c) contributions that model repulsive forces between cation and anion and interfacial tension, respectively. These contributions are calibrated to roughly match the feature size of a typical RTIL, and their specific form is determined from a stability analysis of the concentration equation. After a description of the numerical methods used to discretize the equations of motion in sections 4.6.4 and 4.6.5, numerical results are presented in section 4.7 that demonstrate the bulk morphology in both two and three dimensions. Then we discuss the dependence of capacitance on voltage, comparing with the theoretical predictions of Goodwin et al. [88]. We show that the structure of the electric double layer at the electrodes changes significantly if thermal fluctuations are omitted, as previously observed by Lazaridis et al. [139]. Finally, we demonstrate the capability of modeling electrokinetic flows with a simulation of electroosmotic shear. Section 4.7.5 concludes with a discussion of the results and their implications for future work.

4.6 Low Mach Number Fluctuating Hydrodynamics Model for RTILs

4.6.1 Formulation

Our goal here is to develop a low Mach number model for room temperature ionic liquids. We introduce a free energy functional similar to Gavish and Yochelis [83] that includes enthalpy of mixing, interfacial energy, and electrostatic contributions. Based on that free energy functional we then develop a low Mach number fluctuating hydrodynamics model for ionic liquids by extending the methodology developed in a series of papers [63–65, 169, 179] for multispecies mixtures of charged ionic fluids. For simplicity, we adopt an isothermal two-species approximation and assume that the two species, the cation and the anion, have the same molecular mass m and equal but opposite charge. We assume each species is incompressible and has the same density; hence, the velocity field satisfies an incompressibility constraint.

We write the Gibbs free energy as

$$G(c, \nabla c, \phi, \nabla \phi) = \int \left[\rho g(c, \nabla c) + \rho z(2c - 1)\phi - \frac{1}{2}\epsilon|\nabla\phi|^2 \right] d\mathbf{r} \quad (4.98)$$

where c denotes the cation concentration, ϕ is the electric potential, ϵ is the (constant) static permittivity, ρ is the density and z is the charge per mass of cation. The non-electrical contribution to the specific free energy is given by

$$g(c, \nabla c) = \frac{k_B T}{m} \left[g^{\text{id}}(c) + g^{\text{ex}}(c) + \frac{\kappa}{2}|\nabla c|^2 \right] \quad (4.99)$$

where T is temperature, k_B is Boltzmann's constant, and κ is an interfacial parameter, which is assumed to be constant. The entropy of mixing contribution

is

$$g^{\text{id}}(c) = c \log(c) + (1 - c) \log(1 - c) \quad (4.100)$$

and g^{ex} is an excess free energy due to the enthalpy of mixing. Note that Lazaridis et al. [139] include a contribution to the free energy G that depends on $\nabla\rho$; however, the resulting term will vanish in the low Mach number flow limit.

For systems in which the characteristic fluid velocity is asymptotically small relative to the sound speed, we can obtain the low Mach number equations from the fully compressible equations by asymptotic analysis [128, 155]. Taking density, ρ_0 , as constant the equations of motion are

$$\begin{aligned} (\rho_0 c)_t + \nabla \cdot (\rho_0 u c) &= \nabla \cdot \mathcal{F} \\ (\rho_0 u)_t + \nabla \cdot (\rho_0 u u) + \nabla \pi &= \nabla \cdot \tau + \nabla \cdot \sigma + \nabla \cdot \mathcal{R} \\ \nabla \cdot u &= 0 \\ -\epsilon \nabla^2 \phi &= q^f \equiv \rho z(2c - 1), \end{aligned} \quad (4.101)$$

where u is the fluid velocity, π is a perturbational pressure, and q^f is the charge density. Here, \mathcal{F} , τ , σ and \mathcal{R} are the species flux, viscosity tensor, Maxwell stress tensor, and the interfacial reversible stress, respectively.

In the fluctuating hydrodynamics model, the dissipative fluxes, \mathcal{F} and τ , contain both deterministic and stochastic terms, e.g., $\mathcal{F} = \bar{\mathcal{F}} + \tilde{\mathcal{F}}$. The deterministic species flux can be represented in Onsager form as [54]

$$\bar{\mathcal{F}} = L \frac{\nabla_T \mu}{T} \quad (4.102)$$

where μ is the difference in electro-chemical potential between cations and anions, ∇_T refers to the gradient with T held fixed and L is an Onsager coefficient. Differentiation of the specific free energy with respect to c yields

$$\mu(c) = \frac{k_B T}{m} \left[\log(c) - \log(1-c) + \frac{\partial g^{ex}(c)}{\partial c} + \kappa \nabla^2 c \right] + 2z\phi. \quad (4.103)$$

Inserting (4.103) into (4.102) then gives

$$\overline{\mathcal{F}} = L \left[\frac{k_B}{m} \left(\frac{1}{c} + \frac{1}{1-c} + \frac{\partial^2 g^{ex}(c)}{\partial c^2} \right) \nabla c + \frac{k_B \kappa}{m} \nabla \nabla^2 c + 2z \nabla \phi \right]. \quad (4.104)$$

For a two component mixture, the Onsager coefficient is given by [136]

$$L = \frac{\rho m}{k_B} D c (1-c) \quad (4.105)$$

where D is the Fickian binary diffusion coefficient. The species flux expressed in terms of D then is

$$\overline{\mathcal{F}} = \rho D \left(\nabla c + c(1-c) \frac{\partial^2 g^{ex}(c)}{\partial c^2} \nabla c + c(1-c) \kappa \nabla \nabla^2 c + \frac{2zmc(1-c)}{k_B T} \nabla \phi \right). \quad (4.106)$$

The amplitude of the noise satisfies a Fluctuation Dissipation relation [51, 133]

$$\tilde{\mathcal{F}} = \sqrt{2k_B L} \mathcal{Z} = \sqrt{2\rho m D c (1-c)} \mathcal{Z} \quad (4.107)$$

where $\mathcal{Z}(\mathbf{r}, t)$ is a vector of standard, uncorrelated Gaussian white noise.

The viscous stress tensor is given by $\tau = \overline{\tau} + \tilde{\tau}$ where the deterministic component

$$\overline{\tau} = \eta [\nabla u + (\nabla u)^T] \quad (4.108)$$

and η is viscosity. Here, bulk viscosity is neglected because it does not appear in the low Mach number equations. The stochastic contribution to the viscous stress tensor is modeled as,

$$\tilde{\tau} = \sqrt{\eta k_B T} (\mathcal{W} + \mathcal{W}^T), \quad (4.109)$$

where $\mathcal{W}(\mathbf{r}, t)$ is a standard Gaussian white noise tensor with uncorrelated components,

$$\langle \mathcal{W}_{ij}(\mathbf{r}, t) \mathcal{W}_{kl}(\mathbf{r}', t') \rangle = \delta_{ik} \delta_{jl} \delta(\mathbf{r} - \mathbf{r}') \delta(t - t'), \quad (4.110)$$

and, again, the amplitude of the noise satisfies a Fluctuation Dissipation relation [51, 133].

To complete the specification of the model we need to define σ and \mathcal{R} . In the absence of a magnetic field [137], the Maxwell stress is

$$\sigma_{ij} = \epsilon E_i E_j - \frac{1}{2} \epsilon E^2 \delta_{ij}, \quad (4.111)$$

where $E = -\nabla\phi$. Assuming a constant static permittivity, $\epsilon \nabla \cdot E = q^f$, so the resulting force density on the fluid is,

$$\nabla \cdot \sigma = q^f E = -q^f \nabla\phi, \quad (4.112)$$

which is simply the Lorentz force. The interfacial reversible stress

$$\mathcal{R} = \frac{\rho_0 k_B T}{m} \kappa \left(\frac{1}{2} |\nabla c|^2 \mathbb{I} - \kappa \nabla c \otimes \nabla c \right) \quad (4.113)$$

is derived from a variational principle, see section 4.6.2 as well as [139, 151, 198]. Note that since both σ and \mathcal{R} are non-dissipative fluxes, they have no corresponding stochastic fluxes.

The work here considers two different types of boundary conditions: periodic boundaries and no-slip impermeable electrode walls. In the latter case, the velocity at the wall is zero and the electric potential satisfies a Dirichlet condition. For concentration, we specify that both the normal derivative and the total flux vanish at walls. Spatial discretization details for these boundary conditions are described in section 4.6.4.

4.6.2 Derivation of reversible stress term

Here we derive the inviscid form of the momentum equation (4.101) using the calculus of variations. As discussed in Lowengrub and Truskinovsky [151], the viscous dissipation term is best introduced using the phenomenological laws of thermodynamics. It will be useful below to introduce the notation

$$D_t^u f := f_t + u \cdot \nabla f \quad (4.114)$$

for the advective derivative of scalar f with respect to the velocity field u . For the case when f is a vector of functions, equation (4.114) is understood component-wise, so that in Einstein notation

$$(D_t^u f)_i = (f_i)_t + u_j \frac{\partial f_i}{\partial x_j}. \quad (4.115)$$

Starting from the action

$$S = \int \int \left[\frac{1}{2} \rho_0 |u|^2 - \left(\rho_0 g(c, \nabla c) + \rho_0 z(2c - 1)\phi - \frac{1}{2} \epsilon |\nabla \phi|^2 \right) \right] d\mathbf{r} dt, \quad (4.116)$$

which is simply the space-time integral of the kinetic energy of the fluid minus the time integral of the free energy functional G (see eqn. (4.98)), we add the

constraints that the flow u is divergence free and that the concentration c is advected by the flow. The action then becomes

$$S = \int \int \left[\frac{1}{2} \rho_0 |u|^2 - \left(\rho_0 g(c, \nabla c) + \rho_0 z(2c - 1)\phi - \frac{1}{2}\epsilon |\nabla\phi|^2 \right) \right. \\ \left. + \rho_0 \chi (\nabla \cdot u) + \rho_0 \lambda (c_t + \nabla \cdot (uc)) \right] d\mathbf{r} dt, \quad (4.117)$$

where χ and λ are the Lagrange multipliers. These extra constraints are necessary for nontrivial dynamics for the velocity field; enforcing that the action S is stationary with respect to variations in u results in

$$u = c\nabla\lambda + \nabla\chi \quad (4.118)$$

after integrating by parts and assuming the space of trial functions is such that the boundary terms vanish. This is the well-known Clebsch representation [42, 192]. Variations with respect to ϕ and χ result in the Poisson equation of electrostatics and the divergence-free constraint

$$-\epsilon \nabla^2 \phi = \rho_0 z(2c - 1) = q^f \quad (4.119)$$

$$\nabla \cdot u = 0. \quad (4.120)$$

Variations with respect to λ and using (4.120) result in the constraint

$$D_t^u c = 0. \quad (4.121)$$

Consider now the advective derivative of the Clebsch representation (4.118), and note that D_t^u is a linear operator that obeys the standard product rule of differential calculus $D_t^u(fg) = gD_t^u f + fD_t^u g$, as well as the commutation relation

$$D_t^u (\nabla f) = \nabla (D_t^u f) - \nabla u \nabla f, \quad (4.122)$$

where the second term is a matrix-vector product and $(\nabla u)_{ij}$ is defined as $\partial u_i / \partial x_j$. Hence

$$D_t^u u = D_t^u (c \nabla \lambda) + D_t^u (\nabla \chi) \quad (4.123)$$

$$= c D_t^u (\nabla \lambda) + (D_t^u c) \nabla \lambda + D_t^u (\nabla \chi), \quad (\text{Eq. (4.122)}) \quad (4.124)$$

$$= c \nabla (D_t^u \lambda) - c \nabla u \nabla \lambda + \nabla (D_t^u \chi) - \nabla u \nabla \chi \quad (D_t^u c = 0) \quad (4.125)$$

$$= c \nabla (D_t^u \lambda) + \nabla (D_t^u \chi - |u|^2/2) \quad (u = c \nabla \lambda + \nabla \chi). \quad (4.126)$$

The term $c \nabla (D_t^u \lambda)$ will be the source of the Lorentz force density (4.112) and the divergence of the interfacial reversible stress (4.113).

It remains to consider variations of the action S with respect to the concentration c . Grouping together the contributions to the specific free energy modeling the enthalpy and entropy of mixing into a single term

$$g^{\text{loc}}(c) := \frac{k_B T}{m} (g^{\text{id}}(c) + g^{\text{ex}}(c)), \quad (4.127)$$

eqn. (4.99) becomes

$$g(c, \nabla c) = g^{\text{loc}}(c) + \frac{k_B T}{m} \frac{1}{2} \kappa |\nabla c|^2. \quad (4.128)$$

Variations with respect to c then result in

$$D_t^u \lambda = -\frac{\partial g^{\text{loc}}}{\partial c} + \frac{k_B T}{m} \kappa \nabla^2 c - 2z\phi \quad (4.129)$$

$$\implies c \nabla (D_t^u \lambda) = -c \nabla \left(\frac{\partial g^{\text{loc}}}{\partial c} \right) + \frac{k_B T}{m} \kappa c \nabla (\nabla^2 c) - 2zc \nabla \phi \quad (4.130)$$

After manipulating the three terms on the right hand side of (4.130), we will insert them into (4.126). The third term can be written as

$$-2zc\nabla\phi = -z(2c-1)\nabla\phi - z\nabla\phi \quad (4.131)$$

$$= -\left(\frac{1}{\rho_0}\right)q^f\nabla\phi - z\nabla\phi \quad (4.132)$$

$$= \frac{1}{\rho_0}\nabla\cdot\sigma - z\nabla\phi \quad (4.133)$$

using the definition of the Maxwell stress tensor (4.112). The second term can be written by combining the two product rule identities:

$$c\nabla(\nabla^2c) = \nabla(c\nabla^2c) - \nabla^2c\nabla c \quad (4.134)$$

and

$$\nabla^2c\nabla c = \nabla\cdot(\nabla c\otimes\nabla c) - \frac{1}{2}\nabla(|\nabla c|^2) \quad (4.135)$$

$$= \nabla\cdot\left(\nabla c\otimes\nabla c - \frac{1}{2}|\nabla c|^2\mathbb{I}\right) \quad (4.136)$$

so that

$$\frac{k_B T}{m}\kappa c\nabla(\nabla^2c) = \nabla\left(\frac{k_B T}{m}\kappa c\nabla^2c\right) - \frac{k_B T}{m}\kappa\nabla\cdot\left(\nabla c\otimes\nabla c - \frac{1}{2}|\nabla c|^2\mathbb{I}\right) \quad (4.137)$$

$$= \nabla\left(\frac{k_B T}{m}\kappa c\nabla^2c\right) + \frac{1}{\rho_0}\nabla\cdot\left(\frac{\rho_0 k_B T \kappa}{m}\left[\frac{1}{2}|\nabla c|^2 - \nabla c\otimes\nabla c\right]\right) \quad (4.138)$$

$$= \nabla\left(\frac{k_B T}{m}\kappa c\nabla^2c\right) + \frac{1}{\rho_0}\nabla\cdot\mathcal{R} \quad (4.139)$$

by definition of the interfacial reversible stress tensor (4.113). Lastly, the first term on the right hand side of equation (4.130) can be re-written using the

Gibbs-Duhem relation of thermodynamics [54], which says for our isothermal, two-component mixture

$$\nabla p = \rho_1 \nabla \mu_1 + \rho_2 \nabla \mu_2 \quad (4.140)$$

where p is the thermodynamic pressure and $\mu_k = \partial g^{\text{loc}} / \partial c_k$. Since $\rho_k = \rho_0 c_k$, $c = c_1$, and $c_2 = 1 - c_1$,

$$\frac{\partial g^{\text{loc}}}{\partial c_2} = -\frac{\partial g^{\text{loc}}}{\partial c_1}, \quad (4.141)$$

and hence the Gibbs-Duhem relation reduces to

$$\nabla p = \rho_0(2c - 1) \nabla \left(\frac{\partial g^{\text{loc}}}{\partial c} \right) \quad (4.142)$$

$$\implies -c \nabla \left(\frac{\partial g^{\text{loc}}}{\partial c} \right) = -\frac{1}{2} \frac{\nabla p}{\rho_0} - \frac{1}{2} \nabla \left(\frac{\partial g^{\text{loc}}}{\partial c} \right). \quad (4.143)$$

Inserting the relations (4.143), (4.139), and (4.133) into the $c \nabla (D_t^u \lambda)$ term in (4.126) then results in

$$D_t^u u = c \nabla (D_t^u \lambda) + \nabla (D_t^u \chi - |u|^2/2) \quad (4.144)$$

$$\begin{aligned} &= \frac{1}{\rho_0} \nabla \cdot \mathcal{R} + \frac{1}{\rho_0} \nabla \cdot \sigma \\ &\quad + \nabla \left(D_t^u \chi + \frac{k_B T \kappa}{m} c \nabla^2 c - \frac{1}{2} |u|^2 - \frac{1}{2} \frac{1}{\rho_0} p - \frac{1}{2} \frac{\partial g^{\text{loc}}}{\partial c} - z \phi \right), \end{aligned} \quad (4.145)$$

and after identifying

$$\pi := - \left(\rho_0 D_t^u \chi + \frac{\rho_0 k_B T \kappa}{m} c \nabla^2 c - \frac{1}{2} \rho_0 |u|^2 - \frac{1}{2} p - \frac{1}{2} \rho_0 \frac{\partial g^{\text{loc}}}{\partial c} - \rho_0 z \phi \right) \quad (4.146)$$

as a perturbational pressure, we arrive at the inviscid form of the momentum equation in (4.98)

$$(\rho_0 u)_t + \nabla \cdot (\rho_0 u u) + \nabla \pi = \nabla \cdot \sigma + \nabla \cdot \mathcal{R} \quad (4.147)$$

as desired.

4.6.3 Numerical methods

The equations of motion (4.101) consist of species transport and momentum evolution with an incompressibility constraint on the velocity field coupled to a Poisson equation for the electric potential. The system is discretized in a structured-grid finite-volume approach with cell-averaged concentrations and face-averaged (staggered) velocities, and integration in time is performed with a predictor-corrector scheme. Below we summarize our spatial and temporal discretization, noting that we are building off the explicit electrodiffusion approach used in [63], except we do not consider reactions here. Here, the two primary additions are the additional terms in the deterministic mass flux (4.106) (the term containing the Gibbs free energy and the fourth-order term) and the reversible stress tensor in the momentum equation (4.113).

4.6.4 Spatial Discretization

As detailed in [61, 65], the spatial discretization of the equations for mass and momentum transport is based on standard second-order stencils for derivatives and spatial averaging to ensure a discrete fluctuation-dissipation balance. The electrodiffusion term in the species fluxes and the Lorentz force in the momentum equation are computed from the electric potential. This potential is obtained by solving Poisson's equation with a cell-centered multi-

grid solver [179]. The multigrid solver uses standard second-order stencils, and supports user-specified Dirichlet conditions on the potential for electrode wall boundary conditions. For the velocity/pressure equations, the boundary condition for π at walls is homogeneous Neumann. For velocity we set the normal velocity on walls to zero, set the evaluation of the viscous, advective, and stochastic terms on the wall to zero, and linearly extrapolate tangential velocity to ghost cells to retain the use of the same stencils everywhere. The random numbers for the stochastic contribution to the viscous stress tensor are generated on shifted control volumes about each cell face. We note that for tangential velocities adjacent to no-slip walls, there is a stochastic flux on the wall itself; this noise term has twice the variance of the noise in the bulk [19].

Since the interfacial tension term in (4.99) introduces a new, fourth-order term in the species flux \mathcal{F} and a reversible stress tensor in the momentum equation, their discretization is described in detail here. The center of the cells in two dimensions are indexed by (i, j) and the faces along x, y as $(i + 1/2, j), (i, j + 1/2)$, where $i = 1, \dots, N_x, j = 1, \dots, N_y$. The species diffusion fluxes are computed on the faces of the grid based on (4.106) and (4.107), and the divergence of the flux is approximated with

$$(\nabla \cdot \mathcal{F})_{i,j} \approx \Delta x^{-1} \left[\mathcal{F}_{i+1/2,j}^{(x)} - \mathcal{F}_{i-1/2,j}^{(x)} \right] + \Delta y^{-1} \left[\mathcal{F}_{i,j+1/2}^{(y)} - \mathcal{F}_{i,j-1/2}^{(y)} \right]. \quad (4.148)$$

The new, fourth order term in the species flux equation (4.106) (i.e., the term proportional to $\kappa \nabla \nabla^2 c$) is computed by first approximating $\nabla^2 c$ at cell centers.

Here, nine and twenty-one point stencils in two and three dimensions, respectively, are used so that the discrete Laplacian is more isotropic numerically and hence reflective of the isotropic contribution $\kappa/2|\nabla c|^2$ to the free energy density. Specifically, if the undivided difference operator in two dimensions is defined as

$$\delta_x^2 c_{i,j} = c_{i+1,j} - 2c_{i,j} + c_{i-1,j}$$

(with δ_y^2 defined analogously), then the Laplacian is approximated by

$$\nabla^2 c_{i,j} \approx \left[\left(I + \frac{\delta_y^2}{6} \right) \frac{\delta_x^2}{\Delta x^2} + \left(I + \frac{\delta_x^2}{6} \right) \frac{\delta_y^2}{\Delta y^2} \right] c_{i,j}. \quad (4.149)$$

The generalization to three dimensions is then:

$$\begin{aligned} \nabla^2 c_{i,j,k} \approx & \left[\left(I + \frac{\delta_y^2}{6} \right) \left(I + \frac{\delta_z^2}{6} \right) \frac{\delta_x^2}{\Delta x^2} + \left(I + \frac{\delta_x^2}{6} \right) \left(I + \frac{\delta_z^2}{6} \right) \frac{\delta_y^2}{\Delta y^2} \right. \\ & \left. + \left(I + \frac{\delta_y^2}{6} \right) \left(I + \frac{\delta_z^2}{6} \right) \frac{\delta_z^2}{\Delta z^2} \right] c_{i,j,k}. \end{aligned} \quad (4.150)$$

Discrete gradients of the Laplacian are then computed at cell faces and added to the other terms in the deterministic species diffusion flux. Concerning boundary conditions, on impermeable walls we set the total mass fluxes to zero. Physically, the stochastic mass fluxes on walls are zero, and the combination of all the deterministic fluxes sum to zero so it is not necessary to specify boundary conditions on the mass densities themselves.

The other new term in the low Mach model is the reversible stress tensor (4.113) in the momentum equation. The discretization here is somewhat more complex because of the use of staggered velocities; terms appearing in

the x velocity need to be evaluated at x faces, etc. The first step is to compute the gradients of $c_{i,j}$ at grid nodes—in two dimension these are

$$(G_x^n c)_{i+\frac{1}{2},j+\frac{1}{2}} = \frac{1}{2\Delta x} (c_{i+1,j} - c_{i,j} + c_{i+1,j+1} - c_{i,j+1}) \quad (4.151)$$

$$(G_y^n c)_{i+\frac{1}{2},j+\frac{1}{2}} = \frac{1}{2\Delta y} (c_{i,j+1} - c_{i,j} + c_{i+1,j} - c_{i+1,j+1}). \quad (4.152)$$

The nodal gradients are then averaged to cell centers

$$(G_x^{cc} c)_{i,j} = \frac{1}{4} \left[(G_x^n c)_{i+\frac{1}{2},j+\frac{1}{2}} + (G_x^n c)_{i-\frac{1}{2},j+\frac{1}{2}} + (G_x^n c)_{i+\frac{1}{2},j-\frac{1}{2}} + (G_x^n c)_{i-\frac{1}{2},j-\frac{1}{2}} \right] \quad (4.153)$$

$$(G_y^{cc} c)_{i,j} = \frac{1}{4} \left[(G_y^n c)_{i+\frac{1}{2},j+\frac{1}{2}} + (G_y^n c)_{i-\frac{1}{2},j+\frac{1}{2}} + (G_y^n c)_{i+\frac{1}{2},j-\frac{1}{2}} + (G_y^n c)_{i-\frac{1}{2},j-\frac{1}{2}} \right]. \quad (4.154)$$

From this one can define a second order approximation to $\nabla \cdot \mathcal{R}$ by using conservative differences of the nodal and cell averaged gradients as:

$$\begin{aligned} (\nabla \cdot \mathcal{R})_{x,i+\frac{1}{2},j} &\approx -\frac{\rho_0 k_B T \kappa}{m} \frac{1}{\Delta y} \left[(G_x^n c)_{i+\frac{1}{2},j+\frac{1}{2}} (G_y^n c)_{i+\frac{1}{2},j+\frac{1}{2}} \right. \\ &\quad \left. - (G_x^n c)_{i+\frac{1}{2},j-\frac{1}{2}} (G_y^n c)_{i+\frac{1}{2},j-\frac{1}{2}} \right] \\ &\quad + \frac{\rho_0 k_B T \kappa}{m} \frac{1}{\Delta x} \left[\frac{1}{2} ((G_y^{cc} c)_{i+1,j}^2 - (G_x^{cc} c)_{i+1,j}^2) \right. \\ &\quad \left. - \frac{1}{2} ((G_y^{cc} c)_{i,j}^2 - (G_x^{cc} c)_{i,j}^2) \right] \\ (\nabla \cdot \mathcal{R})_{y,i,j+\frac{1}{2}} &\approx -\frac{\rho_0 k_B T \kappa}{m} \frac{1}{\Delta x} \left[(G_x^n c)_{i+\frac{1}{2},j+\frac{1}{2}} (G_y^n c)_{i+\frac{1}{2},j+\frac{1}{2}} \right. \\ &\quad \left. - (G_x^n c)_{i-\frac{1}{2},j+\frac{1}{2}} (G_y^n c)_{i-\frac{1}{2},j+\frac{1}{2}} \right] \\ &\quad + \frac{\rho_0 k_B T \kappa}{m} \frac{1}{\Delta y} \left[\frac{1}{2} ((G_y^{cc} c)_{i,j+1}^2 - (G_x^{cc} c)_{i,j+1}^2) \right. \\ &\quad \left. - \frac{1}{2} ((G_y^{cc} c)_{i,j}^2 - (G_x^{cc} c)_{i,j}^2) \right], \end{aligned}$$

The reversible stress tensor in three dimensions is treated analogously.

4.6.5 Temporal Discretization

The basic temporal discretization is a predictor-corrector scheme for both concentration and velocity. Given the values c^n and u^n at the beginning of time step t^n , the method consists of a preliminary step to obtain the concentration and velocity at $t^{n+\frac{1}{2}}$. Using these values, the concentration at t^{n+1} is then computed with a midpoint corrector, and the velocity u^{n+1} is determined from midpoint and trapezoidal source terms. More details can be found in [63], but the main steps are summarized here; note the discretizations for the spatial gradients are not included for ease of presentation.

Step 1: Calculate the predictor species fluxes, \mathcal{F}^n , and predictor reversible stress tensor, \mathcal{R}^n , using

$$\begin{aligned}\mathcal{F}^n = & \rho_0 D \left[\nabla c + c(1-c) \frac{\partial^2 g^{\text{ex}}(c)}{\partial c^2} \nabla c + c(1-c)\kappa \nabla \nabla^2 c \right]^n \\ & + \left[\frac{2zmc(1-c)}{k_B T} \right]^n \nabla \phi^n + \left(\sqrt{\frac{2\rho_0 m}{\Delta t \Delta V}} D c (1-c) \right)^n \mathcal{Z}^n\end{aligned}\quad (4.155)$$

where \mathcal{Z}^n are the i.i.d. normal random variables and the electric potential is computed by solving the Poisson equation

$$-\nabla \cdot (\epsilon \nabla \phi^n) = (q^f)^n \quad (4.156)$$

with a cell-centered multigrid solver. Compute the predictor reversible stress tensor as

$$\mathcal{R}^n = \frac{\rho_0 k_B T \kappa}{m} \left[\frac{1}{2} |\nabla c|^2 \mathbb{I} - \kappa \nabla c \otimes \nabla c \right]^n . \quad (4.157)$$

Step 2: Compute the predictor velocity and pressure, $u^{*,n+1}$ and $\pi^{*,n+\frac{1}{2}}$, by solving the linear, saddle-point Stokes system [38]:

$$\begin{aligned} \frac{\rho_0 u^{*,n+1} - \rho_0 u^n}{\Delta t} + \nabla \pi^{*,n+\frac{1}{2}} &= -\nabla \cdot (\rho_0 u u^T)^n + \frac{1}{2} (\eta \nabla^2 u^n + \eta \nabla^2 u^{n+1,*}) \\ &\quad + \nabla \cdot \sqrt{\frac{\eta k_B T}{\Delta t \Delta V}} (\mathcal{W}_{\text{mom}} + \mathcal{W}_{\text{mom}}^T)^n \quad (4.158) \\ &\quad + [\nabla \cdot (\epsilon \nabla \phi) \nabla \phi]^n + \nabla \cdot \mathcal{R}^n \end{aligned}$$

$$\nabla \cdot u^{*,n+1} = 0, \quad (4.159)$$

where ΔV is the volume of a grid cell.

Step 3: Compute the predictor concentration $c^{*,n+\frac{1}{2}}$

$$\rho_0 c^{*,n+\frac{1}{2}} = \rho_0 c^n + \frac{\Delta t}{2} (-\nabla \cdot \mathcal{F}^n) - \frac{\Delta t}{2} \nabla \cdot \rho_0 c^n \left(\frac{u^n + u^{*,n+1}}{2} \right). \quad (4.160)$$

Step 4: Calculate the corrector species fluxes, $\mathcal{F}^{*,n+1/2}$, and corrector reversible stress tensor, $\mathcal{R}^{*,n+1/2}$, using

$$\begin{aligned} \mathcal{F}^{*,n+1/2} &= \rho D \left[\nabla c + c(1-c) \frac{\partial^2 g^{\text{ex}}(c)}{\partial c^2} \nabla c + c(1-c)\kappa \nabla \nabla^2 c \right]^{*,n+1/2} \\ &\quad + \left[\frac{2zmc(1-c)}{k_B T} \right]^{*,n+1/2} \nabla \phi^{*,n+1/2} \quad (4.161) \\ &\quad + \left(\sqrt{\frac{2\rho_0 m}{\Delta t \Delta V}} D c (1-c) \right)^{*,n+\frac{1}{2}} \left(\frac{(\mathcal{Z}_{(1)})^n + (\mathcal{Z}_{(2)})^n}{\sqrt{2}} \right), \end{aligned}$$

where $\nabla \phi^{*,n+\frac{1}{2}}$ comes from the multigrid solution to

$$-\nabla \cdot (\epsilon \nabla \phi^{*,n+1/2}) = (q^f)^{*,n+1/2}, \quad (4.162)$$

and the corrector reversible stress tensor is

$$\mathcal{R}^{*,n+1/2} = \frac{\rho_0 k_B T \kappa}{m} \left[\frac{1}{2} |\nabla c|^2 \mathbb{I} - \nabla c \otimes \nabla c \right]^{*,n+1/2}. \quad (4.163)$$

Step 5: Compute the corrector concentration c^{n+1}

$$\rho_0 c^{n+1} = \rho_0 c^n + \Delta t (-\nabla \cdot \mathcal{F}^{*,n+1/2}) - \Delta t \nabla \cdot \rho_0 c^{*,n+1/2} \left(\frac{u^n + u^{*,n+1}}{2} \right). \quad (4.164)$$

Step 6: Finally, compute the corrector velocity and pressure, u^{n+1} and $\pi^{n+1/2}$, by solving the Stokes system

$$\begin{aligned} \frac{\rho_0 u^{n+1} - \rho_0 u^n}{\Delta t} + \nabla \pi^{n+\frac{1}{2}} &= -\frac{1}{2} \nabla \cdot [(\rho_0 u u^T)^n + (\rho_0 u u^T)^{*,n+1}] \\ &\quad + \frac{1}{2} (\eta \nabla^2 u^n + \eta \nabla^2 u^{n+1}) \\ &\quad + \nabla \cdot \sqrt{\frac{\eta k_B T}{\Delta t \Delta V}} (\mathcal{W}_{\text{mom}} + \mathcal{W}_{\text{mom}}^T)^n \quad (4.165) \\ &\quad + \{\nabla \cdot (\epsilon \nabla \phi) \nabla \phi\}^{*,n+1/2} + \nabla \cdot \mathcal{R}^{*,n+1/2} \end{aligned}$$

$$\nabla \cdot u^{n+1} = 0. \quad (4.166)$$

4.7 RTIL Simulation Results

4.7.1 Parameter Calibration

To calibrate the model parameters, we select a specific RTIL that has been studied extensively both experimentally and with molecular dynamics, namely, 1-butyl-3-methylimidazolium hexafluorophosphate or [DMPI+][F6P-]. Properties of [DMPI+][F6P-] (also known as [C₄min⁺][PF₆⁻]) are summarized in Table 4.1. From the data in this table we can define the parameters needed by the code as summarized in Table 4.2.

PubChem CID	CAS ID	Mass (g/mol)	Density (g/cm ³)
2734174	174501-64-5	284.19	1.38
Viscosity (cP)	Conductivity (C s ² g ⁻¹ cm ⁻³)	Relative Permittivity (-)	Sound speed (cm/s)
272	1.5×10^{-10}	10.2 ± 0.4	144000
Cation D (cm ² /s)	Anion D (cm ² /s)	Melting T (K)	Entropy (J/(mol K))
5.5×10^{-8}	4.3×10^{-8}	282	493

Table 4.1: RTIL properties of [DMPI+][F6P-] at standard conditions from NIST database <https://ilthermo.boulder.nist.gov/>; ion diffusion coefficients from [89, 213]

Density (g/cm ³)	1.38
Molecular mass (anion and cation) (g)	2.4×10^{-22}
Temperature (K)	300
Charge per mass (C/g)	6.8×10^2
Relative Permittivity (-)	10.4
Binary diffusion coefficient (cm/s ²)	$5. \times 10^{-8}$
Viscosity (cP)	270.

Table 4.2: Parameters used in the simulation

To complete the specification of the model it remains to specify the excess Gibbs free energy, $g^{\text{ex}}(c)$ and the interfacial tension parameter, κ . Experimental measurements and molecular dynamics simulations show that the repulsive forces between cations and anions are strong enough to overcome the electrostatic forces and induce phase separation, where the morphological details depend on the specific ionic liquid under consideration. In the model, this repulsive force is represented by the excess free energy. From a mathematical perspective, phase separation corresponds to an instability of the system. To assess this instability, we consider the linearized form of the concentration equation.

For the case considered here, where the cations and anions are of equal

mass, the concentration equation linearized around $c = 1/2$ must be unstable for the phases to separate. The equation for a perturbation δc about one half is

$$\delta c_t = D \left[\left(1 + \frac{1}{4} \frac{\partial^2 g^{\text{ex}}(c)}{\partial c^2} \Big|_{c=\frac{1}{2}} \right) \nabla^2 \delta c - \frac{1}{4} \kappa \nabla^4 \delta c + \frac{zm}{2k_B T} \nabla^2 \phi \right] \quad (4.167)$$

Observing that

$$-\epsilon \nabla^2 \phi = 2\rho_0 z \delta c \quad (4.168)$$

we then obtain

$$\delta c_t = D \left[\left(1 + \frac{1}{4} \frac{\partial^2 g^{\text{ex}}(c)}{\partial c^2} \Big|_{c=\frac{1}{2}} \right) \nabla^2 \delta c - \frac{1}{4} \kappa \nabla^4 \delta c - \frac{\rho_0 z^2 m}{\epsilon k_B T} \delta c \right]. \quad (4.169)$$

Taking the Fourier transform of (4.169) gives

$$\hat{\delta c}_t = D \left[- \left(\frac{1}{4} \frac{\partial^2 g^{\text{ex}}(c)}{\partial c^2} \Big|_{c=\frac{1}{2}} + 1 \right) k^2 - \frac{1}{4} \kappa k^4 - \frac{\rho z^2 m}{\epsilon k_B T} \right] \hat{\delta c}. \quad (4.170)$$

where k is the magnitude of the wave vector. From this equation, one sees that both the electric field and the fourth-order term inhibit the growth of perturbations and hence act to inhibit phase separation. For the system to be unstable, the coefficient of $\hat{\delta c}$ on the right hand side must be positive. In general, this requires that the second derivative of g^{ex} be sufficiently negative and κ be sufficiently small for there to be a range of unstable k . The g^{ex} term will then set the larger scale of the features, while the k^4 term will regularize finer scale features.

The excess Gibb's free energy can be expressed in polynomial form [228]; here we use,

$$g^{\text{ex}}(c) = \alpha [c(1 - c)]^n \quad (4.171)$$

Experimental data indicates that the characteristic feature size of [DMPI+][F6P-] is approximately 2-3 nm [97, 99]. Accordingly, g^{ex} and κ are chosen so that wavelengths, $\lambda = 2\pi/k$ in the 4-6 nm range (twice the feature size) are in the unstable range. From the parameters describing [DMPI+][F6P-], we can estimate the electric force term in (4.170) to be approximately $4 \times 10^{16} \text{ cm}^{-2}$. We choose $\alpha = 4.0 \times 10^3 \text{ cm}^{-1} \text{ s}^{-1}$ and $n = 2$ in (4.171) so the coefficient of k^2 in (4.170) is approximately $1124 \text{ cm}^{-1} \text{ s}^{-1}$, so that, ignoring interfacial tension, wavelengths shorter than approximately 10 nm are unstable. Finally, for $\kappa = 1 \times 10^{-11} \text{ cm}^{-3} \text{ s}^{-1}$ wavelengths between 3.3 and 9.4 nm are stable so we take that as our baseline. It should be noted that we experimented with different forms for g^{ex} (different values of α and n) while maintaining the value of the second derivative at $c = 1/2$ and found that the specific form did not change the qualitative structure significantly.

4.7.2 Bulk morphology

First we consider quasi-two-dimensional systems with periodic boundary conditions. All quasi-two-dimensional simulations in this paper use $192 \times 192 \times 1$ cells with grid spacings $\Delta x = \Delta y = \Delta z = 0.5 \text{ nm}$ and time step $\Delta t = 0.2 \text{ ps}$. As discussed in Section 4.7.1, we take $\kappa = 1 \times 10^{-11} \text{ cm}^{-2}$ for our baseline case; see Table 4.2 for other parameters. Figure 4.9 shows the development of patterns that form in a simulation of the RTIL starting from a homogeneous initial condition of $c = \frac{1}{2}$. By $t = 5 \text{ ns}$, the morphology nearly reaches the final configuration we show at $t = 10 \text{ ns}$. In fact, at a later time of

$t = 50$ ns (not pictured), the morphology is nearly identical to the $t = 10$ ns frame. This stable feature size reflects the competition between the phase separation and electrostatic forces as discussed in Section 4.7.1. Also, note that all figures in this paper use the same colorbar for cation concentration used in Figure 4.9 unless otherwise noted.

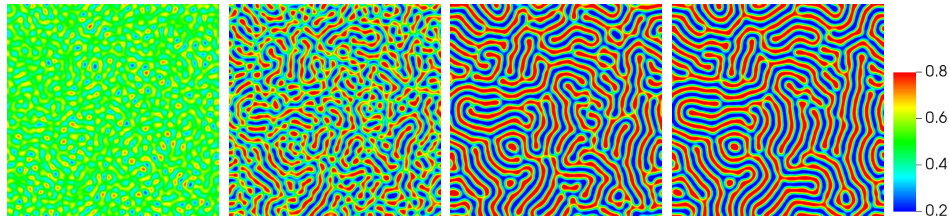


Figure 4.9: Time evolution of cation concentration profiles illustrating structural pattern formation at $t = 1, 2, 5$, and 10 ns for $\kappa = 1 \times 10^{-11} \text{ cm}^{-2}$. All figures in this paper use the same colorbar unless otherwise noted.

In Figure 4.10 we show the analogous spinodal decomposition as in Figure 4.9 but for the case of uncharged species ($z = 0$); here the patterns coarsen quickly and increasingly with time. We repeat the simulations, but

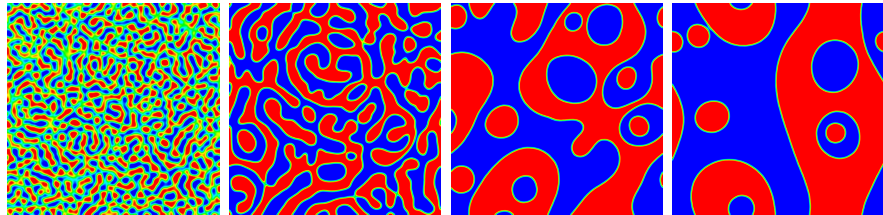


Figure 4.10: Time evolution of pattern formation as in Figure 4.9 with uncharged species ($z = 0$) at $t = 1, 2, 5$, and 10 ns. In this case the regions will continue to coarsen.

in three dimensions (see Figure 4.11) using a cubical domain of $192 \times 192 \times 192$ cells with the same mesh spacing and time step as before. As in two

dimensions, the case with charges evolves to a pattern with fixed feature sizes and then stabilizes whereas the uncharged case coarsens quickly and continues to coarsen over time.

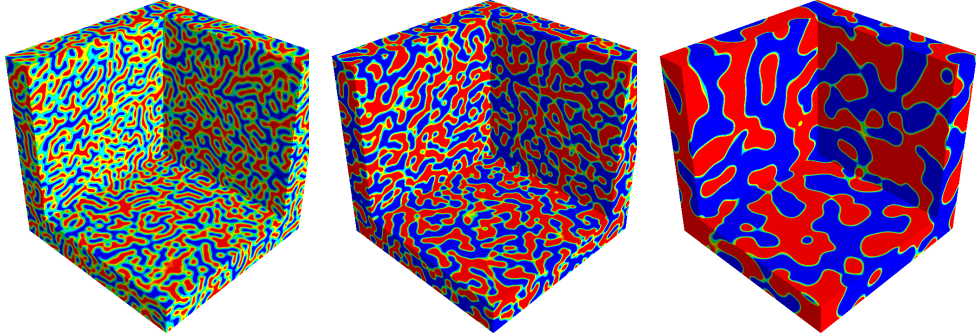


Figure 4.11: Cation concentration profiles from three-dimensional simulations (interior cut-out image). The left panel shows the stable pattern ($t = 10$ ns) reached by the RTIL; compare with the last frame in Figure 4.9. The other two panels show the evolution of pattern formation of the cation concentration in three dimensions for the uncharged case at $t = 2$ ns and $t = 5$ ns; compare with the second and third frames in Figure 4.10.

Next we examine how the morphology depends on the interfacial tension parameter, κ . Figure 4.12 shows the patterns formed at four additional values of κ . As κ increases, the dynamic range of phase separation concentrations decreases. For the largest value shown ($\kappa = 2.5 \times 10^{-11} \text{ cm}^{-2}$) the phase separation is almost completely suppressed. In addition, as κ increases, the feature size in these patterns becomes larger. To quantify this observation we measured the static structure factor, which is the Fourier transform of the equal time covariance of the concentration,

$$S(\mathbf{k}) = \left\langle \left(\widehat{\delta c_{\mathbf{k}}} \right) \left(\widehat{\delta c_{\mathbf{k}}} \right)^* \right\rangle, \quad (4.172)$$

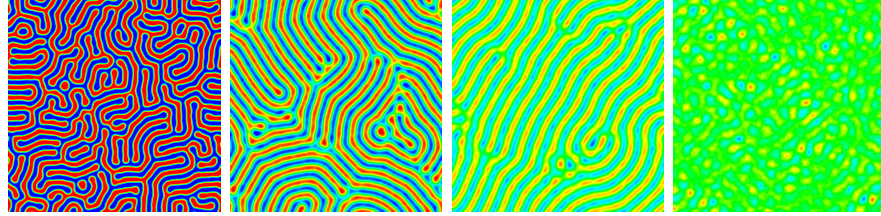


Figure 4.12: Cation concentration profiles illustrating spinodal decomposition for the $t = 50$ ns configuration for $\kappa = 0.5, 1.5, 2.0$, and $2.5 \times 10^{-11} \text{ cm}^{-2}$, respectively. Compare to final image in Figure 4.9. We note that the colorbar for the $\kappa = 2.5 \times 10^{-11} \text{ cm}^{-2}$ case only has been changed to range from 0.4 to 0.6 in order to see the structure.

where the brackets $\langle \rangle$ denote an equilibrium average over time and

$$\widehat{\delta c_{\mathbf{k}}}(t) = \int \delta c(\mathbf{x}, t) e^{-i\mathbf{k}\cdot\mathbf{x}} d\mathbf{x}. \quad (4.173)$$

In each case, we capture statistics for the structure factor by sampling at every time step for 1 ns beginning at $t = 50$ ns. Figure 4.13 shows the structure factor for the $\kappa = 1. \times 10^{-11} \text{ cm}^{-2}$ and $\kappa = 2. \times 10^{-11} \text{ cm}^{-2}$ cases. For each value of κ , the structure factor has a maximum at a radius of $|\mathbf{k}| = k_r$. We note that for $\kappa = 2. \times 10^{-11} \text{ cm}^{-2}$, we see only a partial ring that reflects the fact that most of the stripes in Figure 4.12 are oriented in the same direction. The corresponding patterns feature a length scale (i.e., the width of the red or blue structures) that can be found using $\ell = \pi/k_r$. We compute k_r by considering $S(\mathbf{k})$ to be a probability density function and computing its expected value,

$$k_r = \frac{\sum_{k_x} \sum_{k_y} \sqrt{k_x^2 + k_y^2} S(k_x, k_y)}{\sum_{k_x} \sum_{k_y} S(k_x, k_y)}, \quad (4.174)$$

where we only include points in the sum where $S(\mathbf{k})$ is above 1% of the peak value, which effectively acts as a white noise filter.

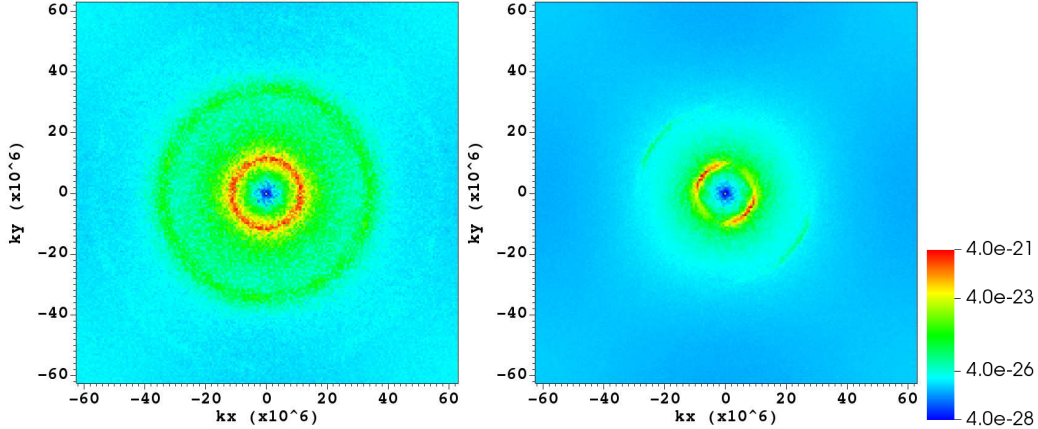


Figure 4.13: Structure factor in logscale for the cation concentration, $S(\mathbf{k})$ for $\kappa = 1 \times 10^{-11} \text{ cm}^{-2}$ (left) and $\kappa = 2 \times 10^{-11} \text{ cm}^{-2}$ (right). The radius of the ring, k_r , is inversely proportional to the morphological feature size as $\ell \sim \pi/k_r$. The anisotropic ring in the right panel is consistent with the striped features favoring a single orientation in physical space, as seen in the third panel in Figure 4.12.

Table 4.3 lists the values of k_r and ℓ for all five values of κ that we consider (the cases not pictured in Fig. 4.12 have rings similar to the $\kappa = 1. \times 10^{-11} \text{ cm}^{-2}$ case). We note that the results for the baseline $\kappa = 1. \times 10^{-11} \text{ cm}^{-2}$ case with $\ell = 2.9 \text{ nm}$ are consistent with experimental measurements [97, 215, 216] and molecular dynamics simulations [148, 167] for the RTIL discussed in section 4.7.1; for a review see [99]. As κ increases, the associated ℓ increases as well, which is consistent with the patterns in Figures 4.9 and 4.12. Finally, our three-dimensional simulations using $\kappa = 1. \times 10^{-11} \text{ cm}^{-2}$ show a spherical structure factor (not pictured) with $k_r \sim 1.1 \times 10^7 \text{ cm}$, which matches the two-dimensional case.

Table 4.3: The radius corresponding to the maximum value of the structure factor, k_r , and the associated pattern feature scale, $\ell = \pi/k_r$ as a function of κ .

$\kappa [10^{-11} \text{ cm}^{-2}]$	$k_r [\text{nm}^{-1}]$	$\ell [\text{nm}]$
0.5	1.35	2.33
1.0	1.14	2.76
1.5	1.03	3.05
2.0	0.96	3.27
2.5	0.92	3.41

4.7.3 Double Layer Capacitance

Consider a charged fluid, either an electrolyte solution or an ionic liquid, confined in a parallel plate capacitor with electrodes at $y = 0$ and $y = L$. The specific differential capacitance of the double layer is defined as $C = d\sigma_s/dV$ where σ_s is the surface-charge density and V is the overall potential drop between the bulk of electrolyte and the electrode surface. By Gauss' law, for the electrode wall at $y = 0$,

$$\sigma_s = -\epsilon \frac{d\phi}{dy} \Big|_{\text{wall}} \quad (4.175)$$

With this,

$$C(V) = -\epsilon \frac{d}{dV} \frac{d\phi}{dy} \Big|_{\text{wall}} \quad (4.176)$$

From Gouy-Chapman theory, for a 1:1 electrolyte solution,

$$C_e = \frac{\epsilon}{\lambda_D} \cosh \Phi \quad \text{where} \quad \Phi = \frac{eV}{2k_B T} \quad (4.177)$$

and

$$\lambda_D = \sqrt{\frac{\epsilon k_B T}{z^2 m \rho_0}} \quad (4.178)$$

is the Debye length.

To account for steric effects in ionic liquids Kornyshev [130] formulated a lattice model with a lattice saturation parameter γ defined as the ratio of the total number of ions to the number of available sites ($0 \leq \gamma \leq 1$). This formulation was improved [88] by accounting for the enthalpy of mixing contribution to the free energy, which adds another parameter, α , to the model ($0 \leq \alpha \leq 1$). For this model the capacitance of the double layer for an ionic liquid with equal size ions is

$$C = \frac{\epsilon}{\lambda_D} \frac{\sqrt{\alpha} \cosh(\alpha\Phi)}{1 + f} \sqrt{\frac{f}{\ln(1 + f)}} \quad \text{where} \quad f = 2\gamma \sinh^2(\alpha\Phi) \quad (4.179)$$

This reduces to the Gouy-Chapman result for $\alpha = 1$ in the limit $\gamma \rightarrow 0$. Qualitatively the capacitance $C(V)$ has the so-called “bell” curve shape for large γ while for small γ the capacitance shows a dip near $V = 0$ (“camel” shape). The former case is typical of ionic liquids for which the double layer thickness increases with voltage. The latter case corresponds to dilute electrolyte solutions, where $dC/dV > 0$ for small voltages and the thickness decreases with voltage until steric effects become significant.

We measure the differential capacitance using a series of quasi-two-dimensional simulations. Our simulations use a parallel plate capacitor geometry with no-slip, impermeable, fixed voltage walls in the y direction, and periodic in the x direction. For each simulation, the voltage at the top and bottom walls are equal in magnitude but opposite in sign; otherwise the parameters used were identical to those used in the periodic simulations in section

4.7.2. We performed simulations using ± 1 , 2 , 4 , 8 , 16 , 32 , 64 , and 128 V at the walls for the baseline case of $\kappa = 1.0 \times 10^{-11} \text{ cm}^{-2}$.

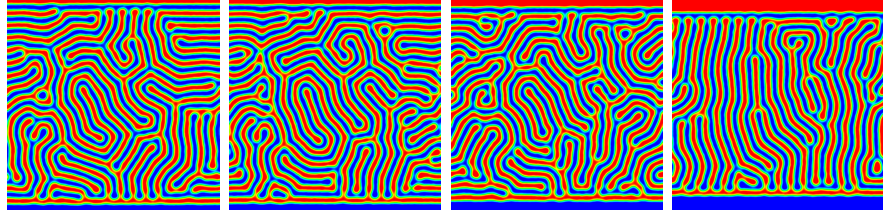


Figure 4.14: Cation concentrations for capacitance simulations. Electrode wall voltages (top and bottom) are ± 2 , 8 , 32 , and 128 V.

Figure 4.14 shows the cation concentration after equilibration for several of the cases with varying electrode voltages. The equilibration time depends on the voltage at the walls, with smaller electrode voltages taking longer to fully form the double layer structure, which is why for most of the simulations the voltage was above the electrochemical window of the RTIL [37]. The simulations ran until equilibration, where the patterns had reached a steady configuration (80 ns for runs with $|V| \geq 16$ V, up to 400 ns for the $|V| = 1$ case). Note that for the largest voltage presented (128V), the morphology features a vertical striped pattern parallel to the strong electric field.

To calculate the capacitance from the simulation data we computed the surface charge density $-\epsilon d\phi/dy$ by horizontally averaging ϕ and then approximating the normal derivative at the wall using a second-order finite difference approximation using the boundary potential and two interior values. In Figure 4.15 we show plots of the horizontally-averaged electric potential for the cases depicted in Figure 4.14. First, we see that the normal derivative of ϕ steepens

with increasing voltage. The double layer thickness also clearly increases with voltage. We also observe that the amplitude of the patterns a few nanometers away from the wall is similar for all voltages.

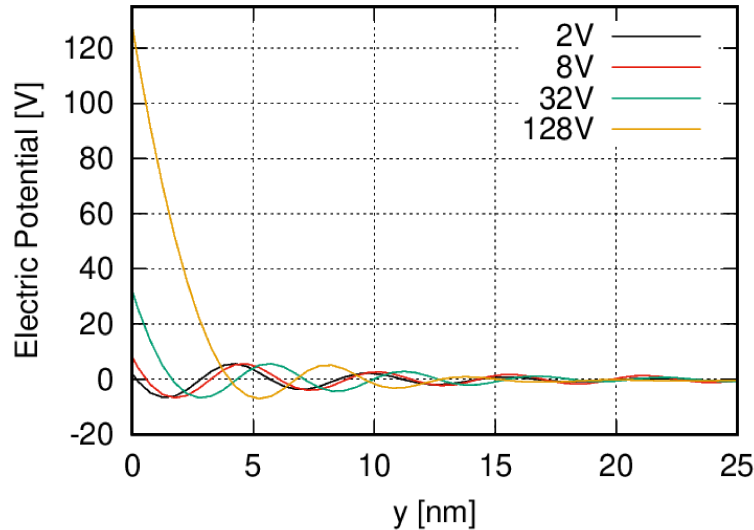


Figure 4.15: Horizontally-averaged potential for the capacitance cases in Figure 4.14.

From these simulations we compute the differential capacitance using (4.176) by estimating the derivative of the surface charge density with respect to voltage using a second-order finite difference approximation. The measured differential capacitance as a function of electrode voltage is shown in Figure 4.16. The simulation data was curve fit to (4.179) and the parameter values for the optimal fit were $\gamma = 1.0$ and $\alpha = 1.0$; the corresponding curve is also shown in Figure 4.16. For larger voltages we are able to recover the predicted differential capacitance. For smaller potentials our simulations under-predict the differential capacitance.

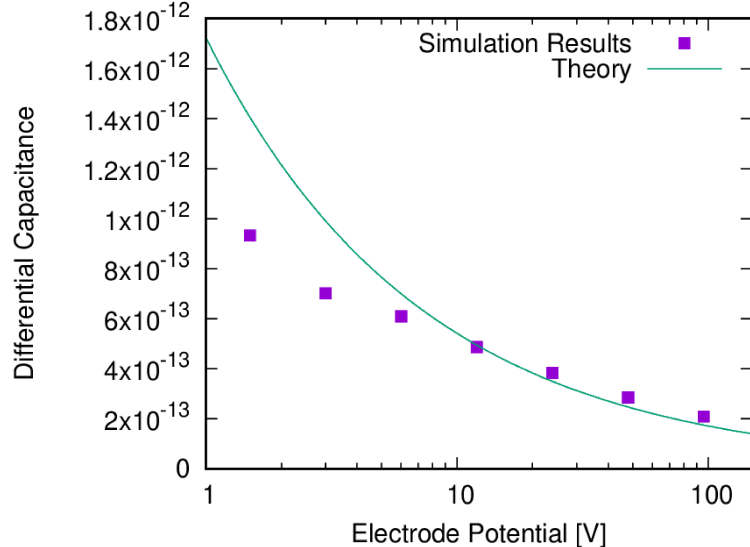


Figure 4.16: Differential capacitance as a function of electrode potential compared to theory (4.179).

Next we illustrate the effect of the thermal fluctuations in the fluctuating hydrodynamic model of the RTIL. We consider two cases in which the simulations were performed with the stochastic fluxes turned off: a deterministic simulation with a random initial perturbation (first running one time step of the full stochastic algorithm and then turning off the noise terms); and a fully deterministic simulation with a homogeneous initial condition. For the periodic systems considered in section 4.7.2 we found little difference between the fully stochastic and the randomly perturbed deterministic simulations. However, if we consider the steady state cation concentration in capacitance simulations with ± 8 V electrode potentials as shown in Fig. 4.17, we see that the results for the two deterministic cases are very different from the results for the fully stochastic simulation. The initially perturbed deterministic sim-

ulation has a similar morphology, except that horizontal stripes are preferred in the vicinity of the walls. In the fully deterministic simulation, horizontal stripes quickly form across the domain. These stripes do not have a consistent structure size; they are thinner at the center of the domain and thickest near the walls.

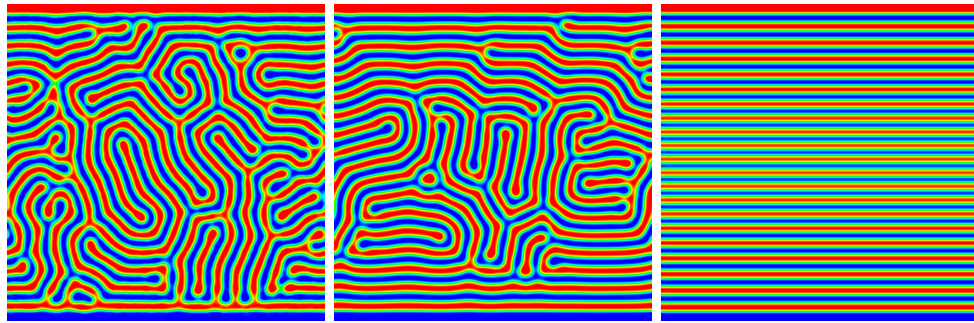


Figure 4.17: Cation concentrations for ± 8 V capacitance simulations. (Left) Stochastic simulation, (Middle) deterministic simulation with an initial stochastic perturbation, and (Right) purely deterministic simulation.

In Figure 4.18 we show horizontally-averaged profiles of the electric potential for these same three cases which further confirm these observations. The perturbed deterministic simulation shows a slower decrease in the potential away from the wall due to the horizontal striping (constructive interference in the horizontal averaging), and in the purely deterministic case the wavelength of the oscillations is clearly smaller.

4.7.4 Electroosmotic shear flow

Electroosmotic flow occurs when an external electric field is applied parallel to the electric double layer near an electrode wall. Since the double

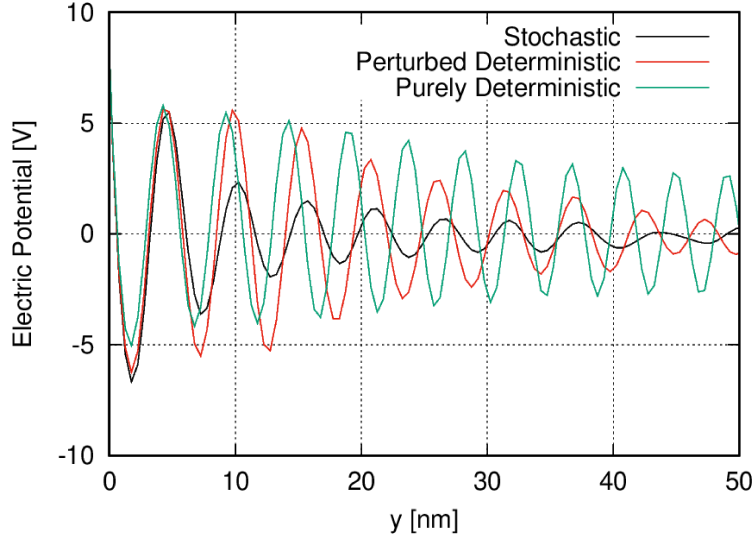


Figure 4.18: Horizontally-averaged potential for the cases in Figure 4.17. The perturbed deterministic case has a large amplitude near the walls due to the horizontal striping, but the same wavelength as the stochastic case. The purely deterministic case has striping features with smaller wavelength.

layer is not electroneutral the ions near the wall experience a Lorentz force, which results in a body force on the fluid. For channel walls of equal potential (or surface charge density) electroosmosis results in a plug flow for wide channels ($L \gg \lambda_D$) and Poiseuille-type flow in narrow channels. Here we consider electrode walls of opposite potential, as in the parallel plate capacitor geometry described in the previous section, which results in electroosmotic shear flow. Specifically we consider electrodes with potentials of $\pm 8\text{V}$ and impose an external electric field in the x direction corresponding to a 500V potential drop across the domain. The resulting shear rate from the electroosmotic flow is about 0.4 ns^{-1} .

The temporal evolution of the resulting sheared system is shown in

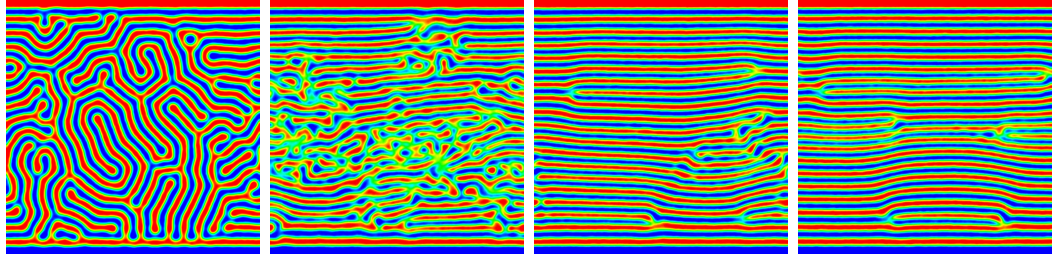


Figure 4.19: Time evolution of the cation concentration in the RTIL under electroosmotic shear; images are at $t = 0, 2, 5$, and 20 ns.

Figure 4.19. For the strong imposed electric field considered in this example, the shearing first destroys the serpentine patterns and then structure is restored, developing a striated pattern parallel to the imposed electric field with a few long-lived defects. Molecular dynamics studies also indicate that nanostructures in RTILs persist in the presence of a strong shear [36, 185].

4.7.5 Discussion

The computational model presented here is the first step towards a mesoscale simulation capability for room temperature ionic liquids that includes both hydrodynamics and thermal fluctuations. The fluctuating hydrodynamics formulation for RTILs is a useful intermediary, mesoscale theory bridging microscopic models, such as molecular dynamics, and macroscopic models. The low Mach number formulation avoids the severe time step restriction associated with previous compressible formulations. We have demonstrated in both two and three dimensions that resulting methodology reproduces the microscopic structuring observed in RTILs. We also used the methodology to show that the differential capacitance decreases with applied

voltage which is a characteristic of ionic liquids. The morphology patterns observed in this capacitance geometry were significantly different depending on whether the simulations included or excluded thermal fluctuations. Finally, the shear electroosmosis example shows that the methodology can be used to model electrokinetic flows.

The present model can be enhanced and extended in several important directions in the future. In this paper we considered a two-component ionic fluid with symmetric ions; however, the RTIL model can be generalized to arbitrary multi-component mixtures. (See [179] for a more general FHD model of multicomponent electrolyte solutions.) This will allow us to consider RTILs composed of dissimilar ions as well as investigate the effect of a polar solvent on the structural, thermodynamic, and electrical properties.

As is commonly assumed in RTIL modeling we assumed the permittivity to be a constant. A more realistic version of the model makes the permittivity a function of concentration, which is important for the study of RTIL mixtures. The implementation requires modifying the calculation of the Poisson equation and the Maxwell stress tensor; a greater challenge is determining an accurate functional form of $\epsilon(c)$. A related extension is to include dielectric relaxation [207] by treating the local permittivity (or equivalently, the local polarization density) as a stochastic quantity whose dynamics are given by a Langevin equation.

The increased time step associated with the low Mach number fluctuating hydrodynamics model makes it possible to investigate long time dynamics

and three dimensional effects. Many ionic liquids tend to have glassy behaviors [77, 195] that make the equilibration of molecular dynamics simulations particularly challenging. Our fluctuating hydrodynamics model permits numerical explorations of RTIL regimes with slow dynamics. The capability to perform three dimensional simulations is particularly important for future investigations of the structure and dynamics of the double layer. The transitions between lateral arrangements of counter and co-ions at electrified interfaces greatly affects the capacitance and dynamics of the double layers, and this is related to the three-dimensional nature of the double layer in ionic liquids [131]. As part of this type of investigation, more physically realistic boundary conditions that can capture wetting effects at electrode-RTIL interfaces will need to be introduced.

Generalization of the methodology to more complex boundary conditions and geometries would allow us to explore capacitance enhancement in nanopores [176], which are important in the development of supercapacitors based on nanostructured electrodes. The treatment of electrochemical effects at electrode boundaries would be a topic for future work.

Finally, the FHD methodology presented here lays the foundation for the macroscopic component of an HMM-style hybrid method described in section 1.3. For heterogeneous models that couple to microscopic descriptions such as DSMC or MD, it is known that the continuum model must include thermal fluctuations in order to correctly capture the behavior in the region being modeled with the microscopic model [60]; see also [55, 82]. This type

of hybrid model would enable simulations to use a microscopic representation locally where molecular-level accuracy is desired, such as near electrode surfaces, while using a less expensive continuum-based model in the remainder of the domain.

Chapter 5

Reduction of the cell resonance error in numerical homogenization

5.1 Introduction

¹This chapter is concerned with developing methods for the numerical homogenization of the multiscale elliptic equation

$$\begin{aligned} -\nabla \cdot (a^\epsilon \nabla u^\epsilon) &= f, & \Omega \subset \mathbb{R}^d \\ u^\epsilon &= g, & \partial\Omega \end{aligned} \tag{5.1}$$

where $0 < \epsilon \ll 1$, $|\Omega| = \mathcal{O}(1)$, and a^ϵ is assumed to be symmetric, positive-definite, and bounded, so that $\forall w \in \mathbb{R}^d$, $x \neq 0$,

$$\lambda|w|^2 \leq \sup_{x \in \Omega} \langle w, a^\epsilon(x)w \rangle \leq \Lambda|w|^2, \tag{5.2}$$

for some $\lambda, \Lambda > 0$. a^ϵ is assumed to oscillate rapidly, that is, with frequencies $\sim 1/\epsilon$, which in turn implies the solution to the elliptic equation u^ϵ is oscillatory as well. Equation (5.1) models, for instance, steady-state heat conduction in a composite material, as well as porous media flow through material with highly variable permeability [66].

¹The work presented in this chapter is part of an ongoing collaboration with Milica Dussinger and Björn Engquist.

The mathematical study of the behavior of the solution to (5.1) as $\epsilon \rightarrow 0$ has a long history; see [25, 41, 114]. It is well known that when a^ϵ is periodic, $u^\epsilon \rightarrow \bar{u}$ weakly in $H^1(\Omega)$ and strongly in $L^2(\Omega)$, where \bar{u} satisfies the homogenized equation

$$\begin{aligned} -\nabla \cdot (\bar{a} \nabla \bar{u}) &= f, & \Omega \\ \bar{u} &= g, & \partial\Omega. \end{aligned} \tag{5.3}$$

The entries in the homogenized tensor \bar{a} are given by

$$\bar{a}_{ij} = \frac{1}{|Y|} \int_Y \left(a_{ij}(y) + a_{ik} \frac{\partial \chi^j}{\partial y_k}(y) \right) dy, \tag{5.4}$$

where summation over repeated indices is implied, and χ^j solves the cell problem posed in the unit cell $Y = [0, 1]^d$

$$\begin{aligned} -\nabla \cdot a \nabla \chi^j &= \nabla \cdot (a e_j), & Y \\ \chi^j &\text{ } Y\text{-periodic and mean zero,} \end{aligned} \tag{5.5}$$

and e_j is the standard unit basis vector in \mathbb{R}^d . With a slight modification, a similar result holds for locally periodic media. In $d = 1$, the cell problem reduces to a two-point boundary value problem, and it is easy to show that \bar{a} is given by the harmonic average of a

$$\bar{a} = \left(\int_0^1 \frac{1}{a(s)} ds \right)^{-1}. \tag{5.6}$$

In more general settings, the theory of Γ -convergence provides sufficient conditions for u^ϵ to limit to some \bar{u} ; however, there does not in general exist a

closed expression for \bar{a} , and numerical homogenization techniques are required in order to approximate the homogenized tensor.

There exist many strategies for the numerical homogenization of (5.1), for example, the multiscale finite element method [73, 103, 104], upscaling techniques [13], the variational multiscale method [107], and the heterogeneous multiscale method (HMM) [1, 6, 69], but they all typically involve solving a microscale problem in order to estimate some missing data from the macroscopic model. In practice, the choice of both the size of the microscale domain and the boundary conditions prescribed for the microscale problem play a crucial role in the accuracy of the homogenization procedure.

A common way to study the effect that the choice of microscale domain size and boundary conditions has on numerical homogenization techniques is the setting of periodic oscillations, where analytic results are known, but where the period is assumed to be unknown. In this context, Ming et al. [71] first proved that if the microscale, or “cell”, problem is solved on a domain whose length η does not coincide with the true period of the heterogeneous media ϵ , a boundary, or “cell resonance” error results that is proportional to ϵ/η and $\epsilon/\eta + \eta$ for truly periodic and locally periodic data, respectively. Yue and E [226] performed a numerical study of this boundary error as a function of domain length η for Dirichlet, Neumann, and periodic boundary conditions and found results consistent with the theory from [71]. Since an $\mathcal{O}(\epsilon/\eta)$ error will dominate discretization error in any sensible numerical homogenization scheme, its reduction is of great practical importance. One strategy to reduce

the cell resonance error is to simply take $\eta \gg \epsilon$. This, however, will of course greatly increase the overall computational cost of the homogenization procedure. Instead, it is preferable to devise strategies to asymptotically reduce the cell resonance error to $\mathcal{O}(\epsilon/\eta)^r$ for some $r > 1$, so that greater accuracy can be obtained at a lower cost.

Many techniques exist in the literature to address the cell resonance error based on, for example, oversampling [101, 105] and filtering [28]. There are a few notable examples that achieve an asymptotic reduction of the cell resonance error based on the idea of reducing influence from the boundary. In [86], Gloria modified the microscale elliptic problem to include a zeroth order term. Since the Green's function associated to the modified elliptic operator decays exponentially fast, the influence from the boundary is lessened, and a convergence rate of $\mathcal{O}(\epsilon/\eta)^4$ for the cell resonance error was obtained in the periodic setting. The approach was improved in a follow up work [87] using Richardson extrapolation. In [14], Arjmand and Runborg proposed to solve a time-dependent hyperbolic PDE on the microscale, based on the idea that the finite speed of the propagation of initial data prevents the boundary error from affecting the solution in interior of the domain, provided the domain is sufficiently large. Using averaging kernels with special regularity and vanishing moment properties, they were able to rigorously obtain in the periodic setting a convergence rate of $\mathcal{O}(\epsilon/\eta)^q$ for arbitrary q , depending on the regularity properties of the averaging kernel. More recently, Abdulle et al. proposed [2] and then described [3, 4] two separate but related methods to reduce the

influence from the boundary. The first approach solves a parabolic microscale problem over a time interval T that depends on the domain length η and the bounds for the oscillatory tensor a (5.2). Similar to [86], the method is based on the exponential decay of the parabolic Green's function. The second approach solves a modified elliptic equation with a forcing term of the form

$$f = \sum_{k=1}^N e^{-\lambda_k T} \langle \nabla \cdot a, \varphi_k \rangle \varphi_k, \quad (5.7)$$

where $\{\lambda_k, \varphi_k\}_{k=1}^N$ are the first N dominant eigenvalues and eigenfunctions of the operator $A := -\nabla \cdot (a \nabla)$, and is a spectral truncation of the solution operator e^{-AT} for the parabolic problem from semigroup theory. With careful selections for the parameters T and N , the authors prove exponential decay of the boundary error.

We present below an alternative method for the reduction of the cell resonance error based on the simple observation that the error as a function of the microscale domain size η is oscillatory. By sampling this error at multiple different values of η and taking a weighted average, we are able to asymptotically reduce the cell resonance error. More specifically, we rely on averaging kernels $K \in \mathbb{K}^{-p,q}$, defined below, that have special regularity and vanishing “negative” moment properties in order to average out the boundary error. These kernels are similar to, but distinct from, the averaging kernels found in [14] and [74].

In section 5.2 below, the space of averaging kernels $\mathbb{K}^{-p,q}$ is introduced, and some elementary facts regarding their properties are proved. Those re-

sults are then used in section 5.3 to prove that the boundary error can be averaged and reduced to $\mathcal{O}(\epsilon/\eta)^r$ in the case $d = 1$, where $r = r(p, q)$, and the numerical examples presented in section 5.4 bolster the theory. In section 5.5 we propose an extension of the strategy for $d \geq 2$ and then conclude in section 5.6 with a discussion of the computational complexity of the proposed method as compared to the existing methods in the literature.

5.2 Averaging Kernels

Definition 5.2.1. For continuous g let $g^{[0]}(x) = g(x)$, and define the primitive

$$g^{[k+1]}(x) := \int_0^x g^{[k]}(s) ds + c_{k+1}, \quad k = 0, 1, \dots, \quad (5.8)$$

where the constant is chosen so that $\int_0^1 g^{[k+1]}(s) ds = 0$.

Lemma 5.2.1. Let $g \in C(\mathbb{R})$ be 1-periodic, so that $g(x+1) = g(x) \forall x \in \mathbb{R}$, and let g be mean zero, so that $\int_0^1 g(x) dx = 0$. Then the primitive $g^{[1]}(x)$ defined above is also continuous, 1-periodic, and bounded.

Proof: By continuity of g , both the left and right-handed limits exist for all x : $|g^{[1]}(x \pm \Delta x) - g^{[1]}(x)| \rightarrow 0$ as $\Delta x \rightarrow 0$, so that $g^{[1]}$ is continuous. Furthermore,

$$\begin{aligned} g^{[1]}(x+1) &= \int_0^{x+1} g(s) ds = \int_0^x g(s) ds + \int_x^{x+1} g(s) ds \\ &= g^{[1]}(x) + \int_0^1 g(s) ds = g^{[1]}(x) \end{aligned} \quad (5.9)$$

from the assumption that g is mean zero. Lastly, note that continuous, periodic functions are bounded. \square

Consider the “incorrect” average of an oscillatory function. Let $f \in C(\mathbb{R})$ be 1-periodic, and fix $\epsilon > 0$ and $\eta > \epsilon$ with $\eta/\epsilon \notin \mathbb{N}$. Without loss of generality, take f to be mean-zero. Then the error in taking the incorrect average of length η can be bounded as

$$\begin{aligned} \left| \frac{1}{\eta} \int_0^\eta f\left(\frac{x}{\epsilon}\right) dx \right| &= \left| \frac{1}{\eta} \left(\int_0^{\lfloor \eta/\epsilon \rfloor \epsilon} f\left(\frac{x}{\epsilon}\right) dx + \int_{\lfloor \eta/\epsilon \rfloor \epsilon}^\eta f\left(\frac{x}{\epsilon}\right) dx \right) \right| \\ &= \left| \frac{1}{\eta} \left(\lfloor \eta/\epsilon \rfloor \int_0^\epsilon f\left(\frac{x}{\epsilon}\right) dx + \int_0^{\eta - \lfloor \eta/\epsilon \rfloor \epsilon} f\left(\frac{x}{\epsilon}\right) dx \right) \right| \quad (5.10) \\ &= \left| \frac{\epsilon}{\eta} \int_0^{\eta/\epsilon - \lfloor \eta/\epsilon \rfloor} f(u) du \right| \leq C \|f\|_\infty \left(\frac{\epsilon}{\eta} \right), \end{aligned}$$

where $C = (\eta/\epsilon - \lfloor \eta/\epsilon \rfloor) \in (0, 1)$. Thus, the error decreases like $1/x$, where x is the averaging length, in units of ϵ . This error rate can be asymptotically improved if the average is taken against smooth kernels with nice regularity properties.

Theorem 5.2.2. *Let $K \in C_0^q([0, 1]) \cap W^{q+1, \infty}([0, 1])$, and let $\int_0^1 K(x) dx = 1$.*

Define $K_\eta(x) := \frac{1}{\eta} K(x/\eta)$ so that

$$K_\eta^{(l)}(0) = K_\eta^{(l)}(\eta) = 0, \quad l = 0, 1, \dots, q, \quad (5.11)$$

where $K_\eta^{(l)} := \frac{d^l K_\eta}{dx^l}$. Let $f \in C(\mathbb{R})$ be 1-periodic, and let $\langle f \rangle = \int_0^1 f(s) ds$.

Then

$$\left| \int_0^\eta K_\eta(x) f\left(\frac{x}{\epsilon}\right) dx - \bar{f} \right| \leq C \left(\frac{\epsilon}{\eta} \right)^{q+1} \quad (5.12)$$

where C is independent of ϵ and η , and depends on q , f , and K .

Proof: First define $g(x) := f(x) - \bar{f}$, so that g is mean-zero. One can integrate by parts to get

$$\int_0^\eta K_\eta(x)g\left(\frac{x}{\epsilon}\right)dx = \left[\epsilon K_\eta g^{[1]}\left(\frac{x}{\epsilon}\right)\right]_{x=0}^{x=\eta} - \frac{\epsilon}{\eta} \int_0^\eta K_\eta^{(1)}(x)g^{[1]}\left(\frac{x}{\epsilon}\right)dx \quad (5.13)$$

$$= -\frac{\epsilon}{\eta} \int_0^\eta K_\eta^{(1)}(x)g^{[1]}\left(\frac{x}{\epsilon}\right)dx, \quad (5.14)$$

since K_η is compactly supported and $g^{[1]}$ is bounded. By assumption on the regularity of K_η , this process can be repeated q more times to get

$$\int_0^\eta K_\eta(x)g\left(\frac{x}{\epsilon}\right)dx = (-1)^{q+1} \left(\frac{\epsilon}{\eta}\right)^{q+1} \int_0^\eta K_\eta^{(q+1)}(x)g^{[q+1]}\left(\frac{x}{\epsilon}\right)dx \quad (5.15)$$

$$\implies \left| \int_0^\eta K_\eta(x)f\left(\frac{x}{\epsilon}\right)dx - \bar{f} \right| \leq \left(\frac{\epsilon}{\eta}\right)^{q+1} \int_0^\eta \left| \frac{1}{\eta} K^{(q+1)}\left(\frac{x}{\eta}\right) g^{[q+1]}\left(\frac{x}{\epsilon}\right) \right| dx \quad (5.16)$$

$$\leq \left(\frac{\epsilon}{\eta}\right)^{q+1} \|K^{(q+1)}\|_{L^\infty([0,1])} \|g^{[q+1]}\|_{L^\infty([0,1])}, \quad (5.17)$$

giving the desired the result, since $g^{[q+1]}$ is bounded by consequence of 5.2.1.

□

Next, define the averaging kernels that possess “negative moments” used in the numerical homogenization procedure:

Definition 5.2.2. $K \in \mathbb{K}^{-p,q}([1, 2])$ if both $K \in C_0^q([1, 2]) \cap W^{q+1,\infty}([1, 2])$, so that for $l = 0, 1, \dots, q$

$$\frac{d^l}{dx^l} K(x) = 0, \quad x = 1, x = 2, \quad (5.18)$$

and

$$\int_1^2 K(x)x^{-r}dx = \begin{cases} 1, & r = 0 \\ 0, & r = 1, \dots, p. \end{cases} \quad (5.19)$$

Note that for $K_\eta := \frac{1}{\eta} K(x/\eta)$, $K \in \mathbb{K}^{-p,q}([1, 2]) \iff K_\eta \in \mathbb{K}^{-p,q}([\eta, 2\eta])$.

The following theorem establishes the bounds needed to prove the main result concerning the reduction of the cell resonance error.

Theorem 5.2.3. *Let $K \in \mathbb{K}^{-p,q}([1, 2])$, and let $K_\eta(x) := \frac{1}{\eta} K(x/\eta)$ for $\eta > 0$. Let $f \in C(\mathbb{R})$ be 1-periodic, and let $\langle f \rangle = \int_0^1 f(s)ds$. Then for $r \in \mathbb{N}$:*

$$\begin{aligned} \left| \int_{\eta}^{2\eta} K_\eta(x) x^{-r} f\left(\frac{x}{\epsilon}\right) dx \right| &\leq C_1 \|f\|_{\infty} r^{q+1} \left(\frac{\epsilon}{\eta}\right)^{q+1} \eta^{-r} \\ &\quad + |\langle f \rangle| \|K\|_{\infty} \eta^{-r} \mathbf{1}_{\{r>p\}} \end{aligned} \quad (5.20)$$

where C_1 is independent of ϵ , η , and r , and depends only on q , K and its derivatives.

Proof: Define $F^{[0]}(x) = f(x) - \langle f \rangle$, and let $F^{[n+1]}$ be the $n+1$ primitive, as in definition 5.2.1. Note

$$\frac{d^{n+1}}{dx^{n+1}} F^{[n+1]}(x) = F^{[0]}(x), \quad (5.21)$$

so that

$$F^{[0]}(x/\epsilon) = \epsilon^{n+1} \frac{d^{n+1}}{dx^{n+1}} F^{[n+1]}(x/\epsilon). \quad (5.22)$$

Furthermore, note that $\|F^{[q+1]}\|_\infty \leq 2^{q+1} \|f\|_\infty$. Then by integration by parts,

$$\begin{aligned}
\int_{\eta}^{2\eta} K_\eta(x) x^{-r} f\left(\frac{x}{\epsilon}\right) dx &= \int_{\eta}^{2\eta} K_\eta(x) x^{-r} F^{[0]}(x/\epsilon) dx + \langle f \rangle \int_{\eta}^{2\eta} K_\eta(x) x^{-r} dx \\
&= \epsilon^{q+1} \int_{\eta}^{2\eta} K_\eta(x) x^{-r} \frac{d^{q+1}}{dx^{q+1}} F^{[q+1]}(x/\epsilon) dx \\
&\quad + \langle f \rangle \int_{\eta}^{2\eta} K_\eta(x) x^{-r} dx \\
&= (-1)^{q+1} \epsilon^{q+1} \int_{\eta}^{2\eta} \frac{d^{q+1}}{dx^{q+1}} (K_\eta(x) x^{-r}) F^{[q+1]}(x/\epsilon) dx \\
&\quad + \langle f \rangle \int_{\eta}^{2\eta} K_\eta(x) x^{-r} dx.
\end{aligned}$$

Since $K_\eta \in \mathbb{K}^{-p,q}$, the second integral vanishes if $r \leq p$; otherwise,

$$\left| \langle f \rangle \int_{\eta}^{2\eta} K_\eta(x) x^{-r} dx \right| \leq |\langle f \rangle| \|K\|_\infty \eta^{-r}. \quad (5.23)$$

For the first integral,

$$\left| \epsilon^{q+1} \int_{\eta}^{2\eta} \frac{d^{q+1}}{dx^{q+1}} (K_\eta(x) x^{-r}) F^{[q+1]}(x/\epsilon) dx \right| \quad (5.24)$$

$$\leq \epsilon^{q+1} \|F^{[q+1]}\|_\infty \sup_{x \in [\eta, 2\eta]} \left| \frac{d^{q+1}}{dx^{q+1}} (K(x/\eta) x^{-r}) \right| \quad (5.25)$$

$$\leq C(q, K) 2^{q+1} \|f\|_\infty r^{q+1} \epsilon^{q+1} \eta^{-(r+q+1)} \quad (5.26)$$

$$= C(q, K) \|f\|_\infty r^{q+1} \left(\frac{\epsilon}{\eta}\right)^{q+1} \eta^{-r}, \quad (5.27)$$

where the factor of 2^{q+1} was absorbed into C . By the general Leibniz rule for differentiating products of functions, C depends on q , K , and the supremum of derivatives of K up to order $q+1$. \square

5.3 Reduction of the Cell Resonance Error: $d = 1$

Here and throughout the section, let $a : \mathbb{R} \rightarrow \mathbb{R}$ be a 1-periodic, continuous function that satisfies

$$0 < \lambda < a(s) < \Lambda, \quad \forall s \in \mathbb{R} \quad (5.28)$$

with harmonic average

$$\bar{a} := \left(\int_0^1 \frac{1}{a(s)} ds \right)^{-1} = \left(\frac{1}{\epsilon} \int_0^\epsilon \frac{1}{a^\epsilon(s)} ds \right)^{-1} \quad (5.29)$$

where $a^\epsilon(s) = a(s/\epsilon)$ and $\epsilon > 0$. In the absence of knowledge of the true period ϵ of a^ϵ , one could approximate \bar{a} with

$$\rho^\epsilon(x) := \left(\frac{1}{x} \int_0^x \frac{1}{a^\epsilon(s)} ds \right)^{-1} = \left(\frac{\epsilon}{x} \int_0^{x/\epsilon} \frac{1}{a(s)} ds \right)^{-1}. \quad (5.30)$$

After a simple algebraic rearrangement, a calculation similar to (5.10) gives

$$|\bar{a} - \rho^\epsilon(\eta)| \leq C \left(\frac{\epsilon}{\eta} \right), \quad (5.31)$$

which is the one-dimensional version of the cell-resonance error derived in [71]. The goal of this section is to show that by sampling ρ^ϵ at different values of η and taking a weighted average, the cell resonance error can be asymptotically reduced.

Definition 5.3.1. Define for $K \in \mathbb{K}^{-p,q}([1, 2])$, $K_\eta(x) = \frac{1}{\eta} K(x/\eta)$, the “smoothed” average

$$S^\epsilon(\eta) := \int_\eta^{2\eta} K_\eta(x) \rho^\epsilon(x) dx. \quad (5.32)$$

Theorem 5.3.1. Let $K \in \mathbb{K}^{-p,q}([1, 2])$ and $\epsilon, \eta > 0$ such that

$$\bar{a} B < \frac{\eta}{\epsilon} \quad (5.33)$$

$$\left(1 + \frac{1}{p+1}\right)^{q+1} < \frac{\eta}{\epsilon}, \quad (5.34)$$

where

$$B = \left\| \frac{1}{a} - \int_0^1 \frac{1}{a(s)} ds \right\|_{L^\infty(\mathbb{R})}, \quad (5.35)$$

is the supremum of the fluctuations about the mean for the function $1/a$. Let S^ϵ be defined by (5.32). Then

$$|S^\epsilon(\eta) - \bar{a}| \leq C \left(\frac{\epsilon}{\eta} \right)^{\min\{p+1, q+2\}}, \quad (5.36)$$

where C depends on p, q, K , its derivatives, \bar{a} and B .

Proof: Let $b(s) := 1/a(s)$, $\langle b \rangle := \int_0^1 b(s) ds$ and rewrite ρ^ϵ as

$$\rho^\epsilon(x) = \left(\frac{\epsilon}{x} \int_0^{x/\epsilon} b(s) ds \right)^{-1} \quad (5.37)$$

$$= \left(\langle b \rangle + \frac{\epsilon}{x} \int_0^{x/\epsilon} (b(s) - \langle b \rangle) ds \right)^{-1} \quad (5.38)$$

$$= \bar{a} \left(1 + \bar{a} \frac{\epsilon}{x} \int_0^{x/\epsilon} (b(s) - \langle b \rangle) ds \right)^{-1} \quad (5.39)$$

$$= \bar{a} \left(1 + z \left(\frac{x}{\epsilon} \right) \right)^{-1} \quad (5.40)$$

since $\langle b \rangle^{-1} = \bar{a}$ is the harmonic average. Here $z(x/\epsilon) = \bar{a} (\epsilon/x) \int_0^{x/\epsilon} (b(s) - \langle b \rangle) ds$.

The main idea is to expand ρ^ϵ in a power series

$$(1 + z)^{-1} = 1 - z + z^2 - z^3 + \dots, \quad (5.41)$$

and insert the expansion in the smoothed average (5.32). The condition (5.34) ensures that the power series sum converges uniformly, so that the order of the sum and the integral can be interchanged. The resulting expression is

$$S^\epsilon(\eta) = \int_\eta^{2\eta} K_\eta(x) \rho^\epsilon(x) dx \quad (5.42)$$

$$= \bar{a} + \sum_{r=1}^{\infty} (-1)^r \bar{a}^r \epsilon^r \int_\eta^{2\eta} \left[K_\eta(x) x^{-r} \left(\int_0^{x/\epsilon} (b(s) - \langle b \rangle) ds \right)^r \right] dx, \quad (5.43)$$

which implies

$$|S^\epsilon(\eta) - \bar{a}| \leq \sum_{r=1}^{\infty} \overbrace{\bar{a}^r \epsilon^r \left| \int_\eta^{2\eta} K_\eta(x) x^{-r} G_r(x/\epsilon) dx \right|}^{:= F_r}, \quad (5.44)$$

where $G_r(x/\epsilon) := \left(\int_0^{x/\epsilon} (b(s) - \langle b \rangle) ds \right)^r$. Fixing r , each individual term in the summations can be bounded using theorem 5.2.3. Since $b - \langle b \rangle$ is periodic and mean zero, lemma 5.2.1 implies G_r is periodic as well. Hence, the assumptions of theorem 5.2.3 are satisfied, which implies

$$F_r \leq \bar{a}^r \epsilon^r \cdot \begin{cases} C(q, K) \|G_r\|_\infty r^{q+1} \left(\frac{\epsilon}{\eta} \right)^{q+1} \eta^{-r}, & r \leq p \\ C(q, K) \|G_r\|_\infty r^{q+1} \left(\frac{\epsilon}{\eta} \right)^{q+1} \eta^{-r} + |\langle G_r \rangle| \|K\|_\infty \eta^{-r}, & r > p \end{cases} \quad (5.45)$$

$$= \begin{cases} C(q, K) \|G_r\|_\infty r^{q+1} \bar{a}^r \left(\frac{\epsilon}{\eta} \right)^{r+q+1}, & r \leq p \\ C(q, K) \|G_r\|_\infty r^{q+1} \bar{a}^r \left(\frac{\epsilon}{\eta} \right)^{r+q+1} + |\langle G_r \rangle| \|K\|_\infty \bar{a}^r \left(\frac{\epsilon}{\eta} \right)^r, & r > p. \end{cases} \quad (5.46)$$

Furthermore, because $b - \langle b \rangle$ is periodic and mean zero,

$$\sup_{s \in \mathbb{R}} \left| \int_0^{x/\epsilon} (b(s) - \langle b \rangle) ds \right| \leq B, \quad (5.47)$$

$$\implies \|G_r\|_\infty \leq \begin{cases} B^r, & B > 1 \\ B, & B \leq 1 \end{cases} \quad (5.48)$$

as a result. An identical bound exists for $|\langle G_r \rangle|$. The infinite sum (5.44) can be broken up into two parts, at which point the bounds (5.46) and (5.48) can be inserted to bound the difference between the true harmonic average and $S^\epsilon(\eta)$ by three parts:

$$|S^\epsilon(\eta) - \bar{a}| \leq \sum_{r=1}^p F_r + \sum_{r=p+1}^{\infty} F_r \quad (5.49)$$

$$\leq \sum_{r=1}^p C(q, K) r^{q+1} (\bar{a}B)^r \left(\frac{\epsilon}{\eta} \right)^{r+q+1} \quad (5.50)$$

$$+ \sum_{r=p+1}^{\infty} C(q, K) r^{q+1} (\bar{a}B)^r \left(\frac{\epsilon}{\eta} \right)^{r+q+1} \quad (5.51)$$

$$+ \sum_{r=p+1}^{\infty} \|K\|_\infty (\bar{a}B)^r \left(\frac{\epsilon}{\eta} \right)^r, \quad (5.52)$$

where the case $B > 1$ is assumed without loss of generality (an identical computation to the one below holds for the case $B \leq 1$). The first part (5.50) is a finite sum from which

$$(5.50) \leq C(q, K, \bar{a}, B) \left(\frac{\epsilon}{\eta} \right)^{q+2} \quad (5.53)$$

follows. The third, (5.52), is simply the tail of a geometric series. The assumption (5.34) implies

$$(5.52) = \|K\|_\infty \left(\bar{a}B \frac{\epsilon}{\eta} \right)^{p+1} \left(1 - \bar{a}B \frac{\epsilon}{\eta} \right)^{-1} \quad (5.54)$$

$$\leq \|K\|_\infty \frac{(\bar{a}B)^{p+1}}{2} \left(\frac{\epsilon}{\eta} \right)^{p+1} \quad (5.55)$$

The second part (5.51) can be bounded with the “integral test” from elementary calculus, which says

$$\sum_{r=p+1}^{\infty} f(r) \leq f(p+1) + \int_{p+1}^{\infty} f(r) dr, \quad (5.56)$$

provided f is a monotonically decreasing function of r . Here

$f(r) = r^{q+1}(\bar{a}B)^r \left(\frac{\epsilon}{\eta}\right)^r$, and $f(r+1) < f(r)$ for every $r > p$ under the assumption (5.34). Hence

$$(5.51) \leq C(q, K) \left((p+1)^{q+1} (\bar{a}B)^{p+1} \left(\frac{\epsilon}{\eta}\right)^{p+q+2} \right. \\ \left. + \left(\frac{\epsilon}{\eta}\right)^{q+1} \underbrace{\int_{p+1}^{\infty} r^{q+1} (\bar{a}B)^r \left(\frac{\epsilon}{\eta}\right)^r dr}_{(*)} \right). \quad (5.57)$$

With $z = \bar{a}B\epsilon/\eta$, the integral $(*)$ can be estimated with $q+1$ applications of integration by parts:

$$(*) = - \int_{p+1}^{\infty} (q+1)r^q (\log(z))^{-1} z^r dr + (p+1)^{q+1} (-\log(z))^{-1} z^{p+1} \quad (5.58)$$

$$= \int_{p+1}^{\infty} (q+1)! (-\log(z))^{-(q+1)} z^r dr \quad (5.59)$$

$$+ \sum_{k=1}^{q+1} \frac{(q+1)!}{(q+2-k)!} (p+1)^{q+2-k} (-\log(z))^{-k} z^{p+1} \\ = (q+1)! (-\log(z))^{-(q+2)} z^{p+1} \quad (5.60)$$

$$+ \sum_{k=1}^{q+1} \frac{(q+1)!}{(q+2-k)!} (p+1)^{q+2-k} (-\log(z))^{-k} z^{p+1}$$

Because of the prefactor $(\epsilon/\eta)^{q+1}$ in front of the integral $(*)$, the logarithmic growth as a function of z is dominated by the algebraic decay of z . Comparing

the exponents on the (ϵ/η) terms in (5.53), (5.55) and (5.60), the desired result is shown:

$$|S^\epsilon(\eta) - \bar{a}| \leq C(p, q, K, \bar{a}, B) \left(\frac{\epsilon}{\eta} \right)^{\min\{p+1, q+2\}} \quad (5.61)$$

□

5.3.1 Numerical strategy, $d = 1$

In order to generate the smoothed average (5.32) as an estimate for the true harmonic average \bar{a} , one must have two quadrature schemes in hand. Given a smoothing kernel $K_\eta \in \mathbb{K}^{-p,q}([\eta, 2\eta])$, the procedure is then as follows:

1. Fix a set of quadrature nodes $\{s_j\}_{j=1}^J \in [\eta, 2\eta]$.
2. For each $1 \leq j \leq J$, estimate the integral (5.30) with

$$\rho^\epsilon(s_j) \approx \rho_j^\epsilon := \left(\frac{1}{s_j} \sum_{k=1}^K \omega_k 1/a^\epsilon(\sigma_k) \right)^{-1} \quad (5.62)$$

where the nodes and weights $\{\sigma_k, \omega_k\}_{k=1}^K$ depend on j .

3. Estimate the integral (5.32) using $\{\rho_j^\epsilon\}_{j=1}^J$

$$S^\epsilon(\eta) \approx \sum_{j=1}^J w_j K_\eta(s_j) \rho_j^\epsilon. \quad (5.63)$$

5.4 Numerical Results, $d = 1$

The results of a comparison between the smoothed harmonic average (5.32) and the true harmonic average \bar{a} are shown in figures 5.1-5.3 for the

cases of a smooth periodic, discontinuous periodic, and smooth quasi-periodic oscillatory function a^ϵ .

The quadrature formula (5.63) chosen to estimate the integral (5.32) is the composite trapezoidal rule; note that it has an arbitrarily high rate of convergence on account of the compact support of K_η . For a given quadrature point s_j , the average ρ_j^ϵ (5.62) is itself estimated with Gaussian quadrature.

The black curve in each figure shows that the cell resonance error (5.31) in the one dimensional case indeed decays like $\mathcal{O}(\epsilon/\eta)$. In addition, it is evident that the error exhibits oscillatory behavior in between the asymptotic bounds of (5.31).

The difference between the smoothed error and the true harmonic average is shown in the colored curves in the figures. For intermediate, “practical” values of η , for instance, $3\epsilon \lesssim \eta \lesssim 10\epsilon$, the left panels of each figure illustrate that the smoothed error is lower than the error obtained by taking the harmonic average of function using a “guess” for its period.

The rate of convergence of both the smoothed error (5.36) and the cell resonance error (5.31) are also shown in the right panels in figures 5.1-5.3. The bound (5.36) is clearly realized, and the convergence rates for the smoothed error either match or exceed the predicted convergence rate of

$$\mathcal{O}(\epsilon/\eta)^{\min\{p+1,q+2\}}. \quad (5.64)$$

In all of the numerical examples presented, the kernels $K \in \mathbb{K}^{-p,q}([1, 2])$

are of the form

$$K(x) = (a_p x^p + a_{p-1} x^{p-1} + \dots + a_1 x + a_0) (x-1)^{q+1} (x-2)^{q+1} \quad (5.65)$$

where the constants a_p, \dots, a_0 are chosen to satisfy (5.19).

For the averaging kernels, there is a balance between obtaining a better convergence rate and performing satisfactorily at practical values of η . For large (p, q) , the kernels themselves have large local mins/maxima that can “amplify” the cell resonance error; see figure 5.4. These are not seen asymptotically, but care must be taken when using a kernel with too large (p, q) . For example, figure 5.5 shows that for $K \in \mathbb{K}^{-7,7}$, the averaging strategy outperforms the simple harmonic average (5.30) only for $8\epsilon \lesssim \eta$.

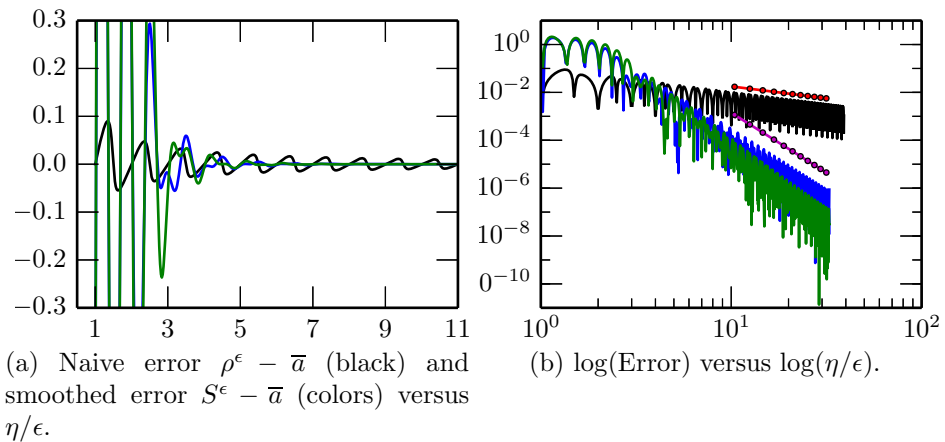


Figure 5.1: Results for $a^\epsilon(x) = 1.1 + \cos(2\pi x/\epsilon)$. (Blue) $K \in \mathbb{K}^{-2,2}$; (Green) $K \in \mathbb{K}^{-2,3}$; (Red) $\mathcal{O}(\epsilon/\eta)$; (Magenta) $\mathcal{O}(\epsilon/\eta)^5$

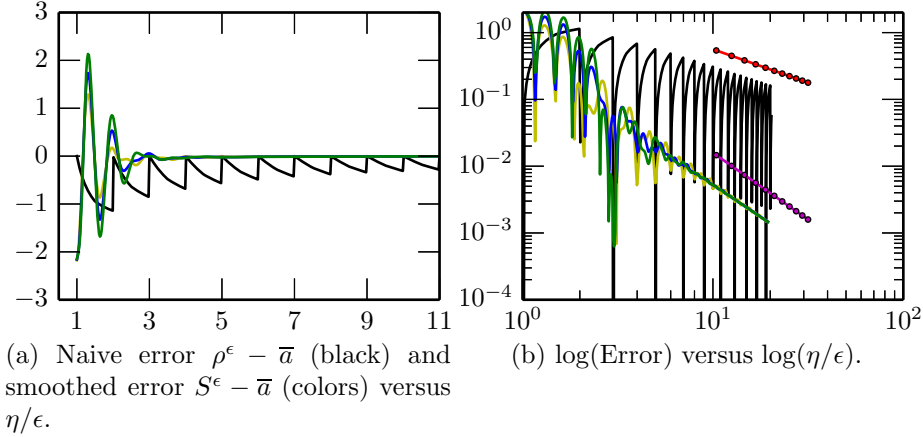


Figure 5.2: Results for the discontinuous, oscillatory step-function $a^\epsilon(x) = 3\chi_{[0,\epsilon/2)}(x) + 4\chi_{[\epsilon/2,\epsilon)}(x)$, periodically extended to \mathbb{R} . (Yellow) $K \in \mathbb{K}^{-1,1}$; (Blue) $K \in \mathbb{K}^{-1,2}$; (Green) $K \in \mathbb{K}^{-1,3}$; (Red) $\mathcal{O}(\epsilon/\eta)$; (Magenta) $\mathcal{O}(\epsilon/\eta)^2$

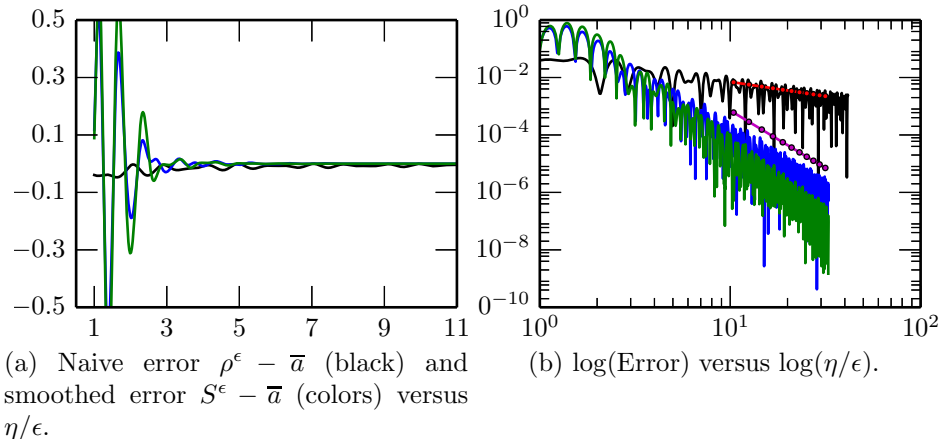


Figure 5.3: Results for the quasi-periodic oscillatory function $a^\epsilon(x) = (2.2 + \sin(2\pi x/\epsilon) + \sin(\sqrt{2} 2\pi x/\epsilon))^{-1}$. (Blue) $K \in \mathbb{K}^{-2,1}$; (Green) $K \in \mathbb{K}^{-2,2}$; (Red) $\mathcal{O}(\epsilon/\eta)$; (Magenta) $\mathcal{O}(\epsilon/\eta)^4$

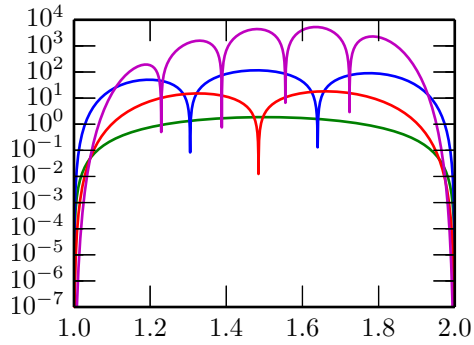


Figure 5.4: Absolute values of various smoothing kernels shown on a log-scale as a function of $x \in [1, 2]$. (Green) $K \in \mathbb{K}^{0,1}$; (Red) $K \in \mathbb{K}^{-2,2}$; (Blue) $K \in \mathbb{K}^{-1,3}$; (Magenta) $K \in \mathbb{K}^{-7,7}$. The local extrema of K grow as a function of (p, q) .

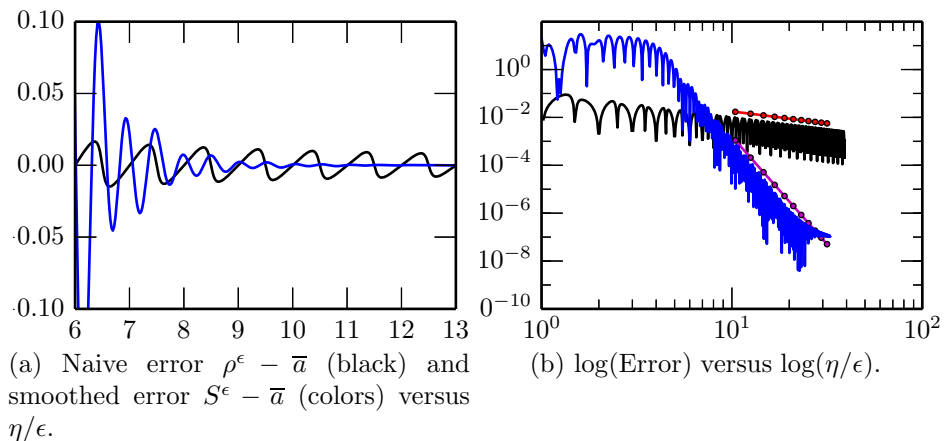


Figure 5.5: Results for $a^\epsilon(x) = 1.1 + \cos(2\pi x/\epsilon)$. (Blue) $K \in \mathbb{K}^{-7,7}$; (Red) $\mathcal{O}(\epsilon/\eta)$; (Magenta) $\mathcal{O}(\epsilon/\eta)^9$

5.5 Numerical Strategy, $d \geq 2$

We now present a method for generating smoothed approximations to the entries in the homogenized tensor (5.4) in the case when the dimension $d > 1$. For domain $I_\eta := [-\eta/2, \eta/2]^d$, define the set of mean zero, periodic functions on I_η

$$W_{\text{per}}(I_\eta) := \{v \in H_{\text{per}}^1(I_\eta) : \int_{I_\eta} v = 0\}. \quad (5.66)$$

For symmetric, oscillatory tensor $a^\epsilon : \mathbb{R}^d \rightarrow \mathbb{R}^d$ satisfying (5.2), define ϕ_η^j to be the solution to the variational problem

$$\int_{I_\eta} a^\epsilon(s) \nabla \phi_\eta^j \cdot \nabla v \, ds = - \int_{I_\eta} a^\epsilon(s) e_j \cdot \nabla v \, ds, \quad \forall v \in W_{\text{per}}(I_\eta), \quad (5.67)$$

whose existence and uniqueness is guaranteed by the Lax-Milgram theorem. ϕ_η^j is indexed by the direction $1 \leq j \leq d$ (here e_j is the standard unit vector in \mathbb{R}^d) and domain size η . (5.67) is essentially the weak form of the rescaled cell problem (5.5). For $1 \leq i, j \leq d$, define the generalization to (5.30)

$$\rho_{ij}^\epsilon(\eta) := \frac{1}{|I_\eta|} \int_{I_\eta} a_{ik}^\epsilon(s) \left(\delta_{kj} + \frac{\partial \phi_\eta^j}{\partial s_k}(s) \right) ds, \quad (5.68)$$

where δ_{kj} is the Kronecker delta function. The ρ_{ij}^ϵ are meant to be approximations to (5.4), and when $\eta = N\epsilon/2$, $N \in \mathbb{N}$, $\rho^\epsilon(\eta) = \bar{a}_{ij}$ holds, i.e. the true homogenized tensor is recovered. From [71] it is known that when a^ϵ is periodic and $2\eta/\epsilon \notin \mathbb{N}$

$$\|\bar{a} - \rho^\epsilon(\eta)\|_F \leq C \frac{\epsilon}{\eta}, \quad (5.69)$$

where $\|\cdot\|_F$ is the Frobenius norm. For averaging kernel $K \in \mathbb{K}^{-p,q}([1, 2])$, define the generalization to the smoothed average (5.32)

$$S_{ij}^\epsilon(\eta) := \int_\eta^{2\eta} K_\eta(s) \rho_{ij}^\epsilon(s) ds. \quad (5.70)$$

Given a quadrature scheme, a numerical method for solving the variational problem (5.67), and a smoothing kernel $K_\eta \in \mathbb{K}^{-p,q}([\eta, 2\eta])$, the procedure to generate (5.70) is:

1. Fix a set of quadrature nodes $\{s_l\}_{l=1}^L \in [\eta, 2\eta]$.
2. For each $1 \leq l \leq L$, solve (5.67) on I_{s_l} for $\phi_{s_l}^j$, $1 \leq j \leq d$.
3. Estimate (5.68) $\rho_{ij}^\epsilon(s_l)$.
4. Using $\{\rho_{ij}^\epsilon(s_l)\}_{l=1}^L$, estimate (5.70)

$$S_{ij}^\epsilon(\eta) \approx \sum_{l=1}^L w_l K_\eta(s_l) \rho_{ij}^\epsilon(s_l). \quad (5.71)$$

Note that in the case that the heterogeneous media is locally periodic, so that the tensor a^ϵ can be written in the form $a^\epsilon(x) = a(x, x/\epsilon)$ and $a(x, y) = a(x, y + 1)$, the procedure above is easily generalized. In this case, the true homogenized tensor varies as a function of the slow variable: $\bar{a} = \bar{a}(x)$, and the approximations S^ϵ and ρ^ϵ also depend on this slow variable x . The only modification to the method described above is that the tensor a^ϵ is collocated in the slow variable, so that in (5.67) and (5.68) $a^\epsilon(s)$ is replaced with $a(x, s/\epsilon)$.

5.6 Computational Cost and Discussion

The computational cost associated to reducing the cell resonance error is now analyzed in the case of periodic media in dimension $d > 1$. Several cases are considered, namely: (i) solving a single, unmodified, elliptic problem (the “naive” case analyzed in [71]); (ii) solving a single elliptic problem that includes a zeroth order term, analyzed in [86]; (iii) solving a time-dependent hyperbolic problem, analyzed in [14]; and (iv) solving a sequence of unmodified elliptic problems, proposed in the present work. *It is assumed* that 5.3.1 proven in 5.3 generalizes to higher dimensions.

Assume that a linear system with N degrees of freedom can be solved with computational cost proportional to N^α . For example, $\alpha = 3$ for straightforward LU decomposition, or $\alpha = 2$ (respectively 2.5) for a direct method that takes advantage of the sparsity that results from the discretization of an elliptic operator in two (resp. three) dimensions. In an ideal scenario, $\alpha = 1$ could be achieved with multigrid; however, for microscopic domain length η sufficiently large relative to ϵ , it is not clear that a multigrid iteration will converge since the coarse grids will not be able to resolve the oscillatory nature of the solution. Lastly, because the microscale problems are typically posed with periodic boundary conditions on squares/cubes, one can use pseudo-spectral methods, which has the advantage of quasi-optimal complexity for the case of an analytic tensor a^ϵ , see [5]. Furthermore, assume that the cost of estimating the homogenized coefficients, using a quadrature formula for instance, given the solution to the microscale problem, is dominated by the cost of the linear

solve necessary to obtain the solution. In all cases, let τ denote some fixed error tolerance for the cell resonance error.

For an elliptic microsolver, the number of degrees of freedom is proportional to $(\eta/\epsilon)^d$; hence, the total computational cost is proportional to $(\eta/\epsilon)^{\alpha d}$. The strategy proposed in the present work requires solving a sequence of elliptic problems on domains with lengths that range from η to 2η in order to approximate ρ^ϵ . Since ρ^ϵ can oscillate with period ϵ , in general η/ϵ elliptic solves are required, each of which cost $(\eta/\epsilon)^{\alpha d}$. For the hyperbolic solver, a time step $\Delta t \sim \epsilon$ is required and their total time of integration $T \sim \eta$. Ergo, the total computational cost is proportional to $\eta/\epsilon \cdot (\eta/\epsilon)^{\alpha d}$.

The total computational cost associated to reducing the the cell resonance error below some tolerance τ is summarized in table 5.1. The cost is a function of dimension d , linear solver complexity α , and the order of the boundary error reduction strategy for the cases (i)-(iv) above.

It is important to note that in any serious application that requires the use of numerical homogenization, the performance of the microsolver at relatively low values of η determines its utility; depending on the application, this could mean η is several times the assumed period, or correlation length, ϵ of the heterogeneous media. The cost estimates in table 5.1 assume the asymptotic rates of the proposed methods have been reached, which might not be true until $\eta = \mathcal{O}(10\epsilon)$ or larger. A comparison of the existing numerical homogenization methods proposed in the literature at such “practical” values of η is beyond the scope of the present work. We believe that such a study,

Micro problem	Computational cost	Error	Cost for a fixed tolerance
Unmodified elliptic	$(\eta/\epsilon)^{\alpha d}$	ϵ/η	$\tau^{-\alpha d}$
Elliptic w/ zeroth order term	$(\eta/\epsilon)^{\alpha d}$	$(\epsilon/\eta)^4$	$\tau^{-\alpha d/4}$
Sequence of elliptic problems	$\eta/\epsilon \cdot (\eta/\epsilon)^{\alpha d}$	$(\epsilon/\eta)^s$	$\tau^{-(\alpha d+1)/s}$
Hyperbolic	$\eta/\epsilon \cdot (\eta/\epsilon)^{\alpha d}$	$(\epsilon/\eta)^q$	$\tau^{-(\alpha d+1)/q}$

Table 5.1: Comparison of the computational cost associated to reducing the cell resonance error below some fixed tolerance for some of the microscale problems proposed in the literature. Here the decay rate $s = \min\{p+1, q+2\}$ for averaging kernel $K \in \mathbb{K}^{-p,q}$ is assumed to generalize for the case $d \geq 2$ in the present work. The averaging kernels in the hyperbolic solver from [14] are defined slightly differently than those in the present work, but the meaning of q is identical.

especially if conducted in collaboration with researchers in the engineering community, is likely to be valuable to streamline research in numerical homogenization. In addition, serious applications of numerical homogenization are most likely implemented in a high-performance computing environment in which effective use of parallelization strategies is crucial. Hence, this is also an important factor for practitioners to consider when selecting a multiscale computational strategy.

Bibliography

- [1] Assyr Abdulle. The finite element heterogeneous multiscale method: a computational strategy for multiscale pdes. *GAKUTO International Series Mathematical Sciences and Applications*, 31:135–184, 2009.
- [2] Assyr Abdulle, Doghonay Arjmand, and Edoardo Paganoni. Exponential decay of the resonance error in numerical homogenization via parabolic and elliptic cell problems. *Comptes Rendus Mathematique*, 357(6):545 – 551, 2019.
- [3] Assyr Abdulle, Doghonay Arjmand, and Edoardo Paganoni. An elliptic local problem with exponential decay of the resonance error for numerical homogenization. *ArXiv e-prints, arXiv:2001.06315*, 2020.
- [4] Assyr Abdulle, Doghonay Arjmand, and Edoardo Paganoni. A parabolic local problem with exponential decay of the resonance error for numerical homogenization. *ArXiv e-prints, arXiv:2001.05543*, 2020.
- [5] Assyr Abdulle and Björn Engquist. Finite element heterogeneous multiscale methods with near optimal computational complexity. *SIAM Multiscale modeling & simulation*, 6(4):1059–1084, 2007.
- [6] Assyr Abdulle, E Weinan, Björn Engquist, and Eric Vanden-Eijnden. The heterogeneous multiscale method. *Acta Numerica*, 21:187, 2012.

- [7] S. Aboud, D. Marreiro, M. Saraniti, and R. Eisenberg. A poisson p3m force field scheme for particle-based simulations of ionic liquids. *Journal of Computational Electronics*, 3(2):117–133, Apr 2004.
- [8] Y. Achdou, O. Pironneau, and F. Valentin. Effective boundary conditions for laminar flows over periodic rough boundaries. *J. Comput. Phys.*, 147(1):187–218, 1998.
- [9] Y. Achdou, P. Le Tallec, F. Valentin, and O. Pironneau. Constructing wall laws with domain decomposition or asymptotic expansion techniques. *Comput. Methods Appl. Mech. Engrg.*, 151:215–232, 1998.
- [10] Yves Achdou. Effet d'un mince revetement metallise mince sur la reflexion d'une onde electromagnetique. *C.R. Acad. Sci. Paris Ser. I*, 314(3):217–222, 1992.
- [11] Yves Achdou and O. Pironneau. Analysis of wall laws. *C.R. Acad. Sci. Paris Ser. I*, 320:541–547, 1995.
- [12] Youcef Amirat, Olivier Bodart, Umberto De Maio, and Antonio Gaudiello. Effective boundary condition for stokes flow over a very rough surface. *Journal of Differential Equations*, 254(8):3395 – 3430, 2013.
- [13] Todd Arbogast. Numerical subgrid upscaling of two-phase flow in porous media. In Zhangxin Chen, Richard E. Ewing, and Zhong-Ci Shi, editors, *Numerical Treatment of Multiphase Flows in Porous Media*, pages 35–49, Berlin, Heidelberg, 2000. Springer Berlin Heidelberg.

- [14] Doghonay Arjmand and Olof Runborg. A time dependent approach for removing the cell boundary error in elliptic homogenization problems. *Journal of Computational Physics*, 314:206 – 227, 2016.
- [15] M. Artola and M. Cessenat. Diffraction d'une onde electromagnetique par une couche composite mince accolée à un conducteur épais. *C.R. Acad. Sci. Paris Ser. I*, 313:231–236, 1991.
- [16] Paul J. Atzberger. Stochastic eulerian lagrangian methods for fluid-structure interactions with thermal fluctuations. *Journal of Computational Physics*, 230(8):2821 – 2837, 2011.
- [17] Paul J. Atzberger, Peter R. Kramer, and Charles S. Peskin. A stochastic immersed boundary method for fluid-structure dynamics at microscopic length scales. *Journal of Computational Physics*, 224(2):1255 – 1292, 2007.
- [18] Frederic Aulery, Dorian Dupuy, Adrien Toutant, Francoise Bataille, and Ye Zhou. Spectral analysis of turbulence in anisothermal channel flows. *Computers and Fluids*, 2016.
- [19] F. Balboa Usabiaga, J.B. Bell, R. Delgado-Buscalioni, A. Donev, T.G. Fai, B.E. Griffith, and C. Peskin. Staggered schemes for fluctuating hydrodynamics. *Multiscale Modeling & Simulation*, 10(4):1369–1408, 2012.

- [20] Arnaud Basson and David Grard-Varet. Wall laws for fluid flows at a boundary with random roughness. *Communications on Pure and Applied Mathematics*, 61(7):941–987, 2008.
- [21] Martin Z. Bazant, Mustafa Sabri Kilic, Brian D. Storey, and Armand Ajdari. Towards an understanding of induced-charge electrokinetics at large applied voltages in concentrated solutions. *Advances in Colloid and Interface Science*, 152(1):48 – 88, 2009.
- [22] Martin Z. Bazant, Mustafa Sabri Kilic, Brian D. Storey, and Armand Ajdari. Towards an understanding of induced-charge electrokinetics at large applied voltages in concentrated solutions. *Advances in Colloid and Interface Science*, 152(1):48 – 88, 2009.
- [23] Martin Z Bazant, Brian D Storey, and Alexei A Kornyshev. Double layer in ionic liquids: Overscreening versus crowding. *Physical Review Letters*, 106(4):046102, 2011.
- [24] Martin Z. Bazant, Brian D. Storey, and Alexei A. Kornyshev. Double layer in ionic liquids: Overscreening versus crowding. *Phys. Rev. Lett.*, 106:046102, Jan 2011.
- [25] A. Bensoussan, J. Lions, and G. Papanicolaou. *Asymptotic analysis for periodic structures*. North-holland, 1978.
- [26] H. J. C. Berendsen, J. P. M. Postma, W. F. van Gunsteren, A. DiNola, and J. R. Haak. Molecular dynamics with coupling to an external bath.

The Journal of Chemical Physics, 81(8):3684–3690, 1984.

- [27] L.C. Berselli, T. Iliescu, and W.J. Layton. *Mathematics of Large Eddy Simulation of Turbulent Flows*. Scientific Computation. Springer, 2006.
- [28] Xavier Blanc and Claude Le Bris. Improving on computation of homogenized coefficients in the periodic and quasi-periodic settings. Research report, May 2009. Published in "Networks and Heterogeneous Media", 2010, vol. 5, no 1, p. 1-29 <http://hal-enpc.archives-ouvertes.fr/hal-00625537/fr/>.
- [29] Guillem Borrell, Juan A. Sillero, and Javier Jiménez. A code for direct numerical simulation of turbulent boundary layers at high Reynolds numbers in BG/P supercomputers. *Computers and Fluids*, 80:37–43, July 2013.
- [30] Sanjeeb T. Bose and George Ilhwan Park. Wall-modeled large-eddy simulation for complex turbulent flows. *Annual Review of Fluid Mechanics*, 50(1):535–561, 2018.
- [31] Olivier Botella and Karim Shariff. B-spline Methods in Fluid Dynamics. *International Journal of Computational Fluid Dynamics*, 17(2):133–149, 2003.
- [32] David J Bozym, Betl Uralcan, David T Limmer, Michael A Pope, Nicholas J Szamreta, Pablo G Debenedetti, and Ilhan A Aksay. Anomalous capacitance maximum of the glassy carbon–ionic liquid interface through

dilution with organic solvents. *The journal of physical chemistry letters*, 6(13):2644–2648, 2015.

- [33] A. Brandt, S. Pohlmann, A. Varzi, A. Balducci, and S. Passerini. Ionic liquids in supercapacitors. *MRS Bulletin*, 38(7):554–559, 2013.
- [34] Didier Bresch and David Gérard-Varet. Roughness-induced effects on the quasi-geostrophic model. *Communications in Mathematical Physics*, 253(1):81–119, Jan 2005.
- [35] D. M. Bushnell and K. J. Moore. Drag reduction in nature. *Annual Review of Fluid Mechanics*, 23(1):65–79, 1991.
- [36] Simon N. Butler and Florian Mller-Plathe. Nanostructures of ionic liquids do not break up under shear: A molecular dynamics study. *Journal of Molecular Liquids*, 192:114 – 117, 2014. Fundamental Aspects of Ionic Liquid Science.
- [37] Marisa C. Buzzeo, Russell G. Evans, and Richard G. Compton. Non-haloaluminate room-temperature ionic liquids in electrochemistrya review. *ChemPhysChem*, 5(8):1106–1120, 2004.
- [38] Mingchao Cai, Andy Nonaka, John B. Bell, Boyce E. Griffith, and Aleksandar Donev. Efficient variable-coefficient finite-volume stokes solvers. *Communications in Computational Physics*, 16(5):12631297, 2014.
- [39] R. Car and M. Parrinello. Unified approach for molecular dynamics and density-functional theory. *Phys. Rev. Lett.*, 55:2471–2474, Nov 1985.

- [40] Alexandre Chorin and J.E. Marsden. *A Mathematical Introduction to Fluid Mechanics*. Springer-Verlag New York, 1993.
- [41] D. Cioranescu and P. Donato. *An introduction to homogenization*. Oxford University Press, 1999.
- [42] A. Clebsch. Ueber die integration der hydrodynamischen gleichungen. *Journal fr die reine und angewandte Mathematik*, 1859(56):1 – 10, 1859.
- [43] C. A. Coclici and W.L. Wendland. Analysis of a heterogeneous domain decomposition for compressible viscous flow. *Mathematical Models and Methods in Applied Sciences*, 11(4):565–599, 2001.
- [44] G. N. Coleman, A. Garbaruk, and P. R. Spalart. Direct Numerical Simulation, Theories and Modelling of Wall Turbulence with a Range of Pressure Gradients. *Flow, Turbulence and Combustion*, 95(2):261–276, 2015.
- [45] Tim Colonius. Modeling Artificial Boundary Conditions for Compressible Flow. *Annual Review of Fluid Mechanics*, 36:315–345, 2004.
- [46] G. Da Prato. *Kolmogorov Equations for Stochastic PDEs*. Birkhauser, 2004.
- [47] Anne-Laure Dalibard and David Grard-Varet. Effective boundary condition at a rough surface starting from a slip condition. *Journal of Differential Equations*, 251(12):3450 – 3487, 2011.

- [48] Henry Darcy. Recherches expérimentales relatives au mouvement de l'eau dans les tuyaux. *Mém. Savants Etrang. Acad. Sci. Paris*, 17:1–268, 1854.
- [49] Benny Davidovitch, Esteban Moro, and Howard A. Stone. Spreading of viscous fluid drops on a solid substrate assisted by thermal fluctuations. *Phys. Rev. Lett.*, 95:244505, Dec 2005.
- [50] Gianni De Fabritiis, Rafael Delgado-Buscalioni, and Peter Coveney. Multiscale modeling of liquids with molecular specificity. *Physical review letters*, 97:134501, 10 2006.
- [51] José de Zárate and Jan Sengers. *Hydrodynamic Fluctuations in Fluids and Fluid Mixtures*. Elsevier Science, 2007.
- [52] William Murray Deen. *Analysis of transport phenomena*. Oxford University Press, 2013.
- [53] David B. DeGraaff and John K. Eaton. Reynolds-number scaling of the flat-plate turbulent boundary layer. *Journal of Fluid Mechanics*, 422:319–346, 2000.
- [54] S. R. DeGroot and P. Mazur. *Non-Equilibrium Thermodynamics*. North-Holland Publishing Company, Amsterdam, 1963.
- [55] Luigi Delle Site, Matej Praprotnik, John B. Bell, and Rupert Klein. Particlecontinuum coupling and its scaling regimes: Theory and applications. *Advanced Theory and Simulations*, n/a(n/a):1900232, 2020.

- [56] Steven Delong, Florencio Balboa Usabiaga, Rafael Delgado-Buscalioni, Boyce E Griffith, and Aleksandar Donev. Brownian dynamics without green's functions. *The Journal of chemical physics*, 140(13):134110, 2014.
- [57] Mingge Deng, Zhen Li, Oleg Borodin, and George Em Karniadakis. cdpd: A new dissipative particle dynamics method for modeling electrokinetic phenomena at the mesoscale. *Journal of Chemical Physics*, 145(14), 10 2016.
- [58] Giulia Deolmi, Wolfgang Dahmen, and Siegfried Mller. Effective boundary conditions: A general strategy and application to compressible flows over rough boundaries. *Communications in Computational Physics*, 21(2):358400, 2017.
- [59] Q.V. Dinh, R. Glowinski, J. P\'eriaux, and G. Terrasson. On the coupling of viscous and inviscid models for incompressible fluid flows via domain decomposition. *First International Symposium on Domain Decomposition Methods for Partial Differential Equations*, pages 350–369, 1987.
- [60] A. Donev, John B. Bell, Alejandro J. Garcia, and Berni J. Alder. A hybrid particle-continuum method for hydrodynamics of complex fluids. *Multiscale Model. Simul.*, 8:871–911, 2010.
- [61] A. Donev, E. Vanden-Eijnden, A. L. Garcia, and J. B. Bell. On the accuracy of finite-volume schemes for fluctuating hydrodynamics. *Comm.*

Appl. Math and Comp. Sci., 5(2):149, 2010.

- [62] Aleksandar Donev, Alejandro L. Garcia, Jean-Philippe Péraud, Andrew J. Nonaka, and John B. Bell. Fluctuating hydrodynamics and debye-hückel-onsager theory for electrolytes. *Current Opinion in Electrochemistry*, 13:1 – 10, 2019.
- [63] Aleksandar Donev, Andrew J Nonaka, Changho Kim, Alejandro L Garcia, and John B Bell. Fluctuating hydrodynamics of electrolytes at electroneutral scales. *Physical Review Fluids*, 4(4):043701, 2019.
- [64] Aleksandar Donev, Andy Nonaka, Amit Kumar Bhattacharjee, Alejandro L Garcia, and John B Bell. Low mach number fluctuating hydrodynamics of multispecies liquid mixtures. *Physics of Fluids*, 27(3):037103, 2015.
- [65] Aleksandar Donev, Andy Nonaka, Yifei Sun, Thomas Fai, Alejandro Garcia, and John Bell. Low mach number fluctuating hydrodynamics of diffusively mixing fluids. *Communications in Applied Mathematics and Computational Science*, 9(1):47–105, 2014.
- [66] Louis J. Durlofsky. Coarse scale models of two phase flow in heterogeneous reservoirs: volume averaged equations and their relationship to existing upscaling techniques. *Computational Geosciences*, 2(2):73–92, Mar 1998.

- [67] E.B. Dussan. On the spreading of liquids on solid surfaces: Static and dynamic contact lines. *Annu. Rev. Fluid Mech.*, 11:371–400, 1979.
- [68] W. E and B. Engquist. The heterogeneous multiscale methods. *Commun. Math. Sci.*, 1(1):87–132, 2003.
- [69] W. E, B. Engquist, X. Li, W. Ren, and E. Vanden-Eijnden. Heterogeneous multiscale methods: A review. *Commun. Comput. Phys.*, 2:367–450, 2007.
- [70] Weinan E. *Principles of Multiscale Modeling*. Cambridge University Press, 2011.
- [71] Weinan E, Pingbing Ming, and Pingwen Zhang. Analysis of the heterogeneous multiscale method for elliptic homogenization problems. *Journal of the American Mathematical Society*, 18(1):121–156, 2005.
- [72] Y. Efendiev and T.Y. Hou. *Multiscale finite element methods: theory and applications*, volume 4 of *Surveys and Tutorials in the Applied Mathematical Sciences*. Springer New York, 2009.
- [73] Yalchin Efendiev and Tom Hou. *Multiscale Finite Element Methods*. Surveys and Tutorials in the Applied Mathematical Sciences. Springer-Verlag New York, 1 edition, 2009.
- [74] Björn Engquist and Yen-Hsi Tsai. Heterogeneous multiscale methods for stiff ordinary differential equations. *Mathematics of Computation*, 74(252):1707–1742, 2005.

- [75] Pep Español and Aleksandar Donev. Coupling a nano-particle with isothermal fluctuating hydrodynamics: Coarse-graining from microscopic to mesoscopic dynamics. *The Journal of Chemical Physics*, 143(23):234104, 2015.
- [76] Daan Frenkel and Berend Smit. *Understanding molecular simulation: from algorithms to applications*, volume 1. Elsevier, 2001.
- [77] Falk Frenzel, Pia Borchert, Arthur Markus Anton, Veronika Strehmel, and Friedrich Kremer. Charge transport and glassy dynamics in polymeric ionic liquids as reflected by their inter-and intramolecular interactions. *Soft matter*, 15(7):1605–1618, 2019.
- [78] E. Friedmann. The optimal shape of riblets in the viscous sublayer. *J. Math. Fluid. Mech.*, 12:243–265, 2010.
- [79] E. Friedmann and T. Richter. Optimal microstructures drag reducing mechanism of riblets. *J. Math. Fluid. Mech.*, 13(3):429–447, 2011.
- [80] B. Ganapathisubramani, N. Hutchins, J. P. Monty, D. Chung, and I. Marusic. Amplitude and frequency modulation in wall turbulence. *Journal of Fluid Mechanics*, 712:61–91, 2012.
- [81] A. Garcia, M. Mansour, G. Lie, and E. Clementi. Numerical integration of the fluctuating hydrodynamic equations. 47:209–228, 1987.

- [82] Alejandro L Garcia, John B Bell, William Y Crutchfield, and Berni J Alder. Adaptive mesh and algorithm refinement using direct simulation monte carlo. *Journal of Computational Physics*, 154(1):134 – 155, 1999.
- [83] Nir Gavish and Arik Yochelis. Theory of phase separation and polarization for pure ionic liquids. *The Journal of Physical Chemistry Letters*, 7(7):1121–1126, 2016. PMID: 26954098.
- [84] Christophe Geuzaine and Jean-Franois Remacle. Gmsh: A 3-d finite element mesh generator with built-in pre- and post-processing facilities. *International Journal for Numerical Methods in Engineering*, 79(11):1309–1331, 2009.
- [85] S. Ghosal and P. Moin. The basic equations for the large eddy simulation of turbulent flows in complex geometry. *Journal of Computational Physics*, 118(1):24 – 37, 1995.
- [86] Antoine Gloria. Reduction of the resonance error. Part 1: Approximation of homogenized coefficients. *Mathematical Models and Methods in Applied Sciences*, 21(8):1601–1630, 2011.
- [87] Antoine Gloria and Zakaria Habibi. Reduction in the Resonance Error in Numerical Homogenization II: Correctors and Extrapolation. *Found. Comput. Math.*, 16(1):217–296, February 2016.
- [88] Zachary A.H. Goodwin, Guang Feng, and Alexei A. Kornyshev. Mean-field theory of electrical double layer in ionic liquids with account of

short-range correlations. *Electrochimica Acta*, 225:190 – 197, 2017.

- [89] Martin Gouverneur, Jakob Kopp, Leo van Wllen, and Monika Schnhoff. Direct determination of ionic transference numbers in ionic liquids by electrophoretic nmr. *Phys. Chem. Chem. Phys.*, 17:30680–30686, 2015.
- [90] W.W. Grabowski. Coupling cloud processes with the large-scale dynamics using the cloud-resolving convection parameterization (crcp). *J. Atmos. Sci.*, 58(9):978–997, 2001.
- [91] Ian Grooms and Andrew J. Majda. Efficient stochastic superparameterization for geophysical turbulence. *Proceedings of the National Academy of Sciences*, 110(12):4464–4469, 2013.
- [92] Max D. Gunzburger. *Finite Element Methods for Viscous Incompressible Flows: A Guide to Theory, Practice, and Algorithms*. Academic Press, 1989.
- [93] GHL Hagen. Über den bewegung des wassers in engen cylindrischen röhren. *Poggendorfs Ann. Phys. Chem.*, 46:423–42, 1839.
- [94] Martin Hairer. Solving the kpz equation. *Annals of Mathematics*, 178:559–664, 2013.
- [95] Christopher K. Haluska, Karin A. Riske, Valérie Marchi-Artzner, Jean-Marie Lehn, Reinhard Lipowsky, and Rumiana Dimova. Time scales of membrane fusion revealed by direct imaging of vesicle fusion with high

- temporal resolution. *Proceedings of the National Academy of Sciences*, 103(43):15841–15846, 2006.
- [96] James M. Hamilton, John Kim, and Fabian Waleffe. Regeneration mechanisms of near-wall turbulence structures. *Journal of Fluid Mechanics*, 287:317–348, 1995.
- [97] Christopher Hardacre, John D. Holbrey, Claire L. Mullan, Tristan G. A. Youngs, and Daniel T. Bowron. Small angle neutron scattering from 1-alkyl-3-methylimidazolium hexafluorophosphate ionic liquids ([cnmim][pf₆], n=4, 6, and 8). *The Journal of Chemical Physics*, 133(7):074510, 2010.
- [98] D. Jed Harrison, Karl Fluri, Kurt Seiler, Zhonghui Fan, Carlo S. Effenhauser, and Andreas Manz. Micromachining a miniaturized capillary electrophoresis-based chemical analysis system on a chip. *Science*, 261(5123):895–897, 1993.
- [99] Robert Hayes, Gregory G. Warr, and Rob Atkin. Structure and nanoscale in ionic liquids. *Chemical Reviews*, 115:6357–6426, 2015.
- [100] Y. Hennequin, D. G. A. L. Aarts, J. H. van der Wiel, G. Wegdam, J. Eggers, H. N. W. Lekkerkerker, and Daniel Bonn. Drop formation by thermal fluctuations at an ultralow surface tension. *Phys. Rev. Lett.*, 97:244502, Dec 2006.
- [101] Patrick Henning and Daniel Peterseim. Oversampling for the multiscale

- finite element method. *Multiscale Modeling and Simulation*, 11:1149–1175, 2013.
- [102] R. W. Hockney and J. W. Eastwood. *Computer Simulation Using Particles*. Taylor & Francis, Inc., Bristol, PA, USA, 1988.
- [103] Thomas Y. Hou, Xiao hui Wu, and Zhiqiang Cai. Convergence of a multiscale finite element method for elliptic problems with rapidly oscillating coefficients. *Math. Comput.*, pages 913–943, 1999.
- [104] Thomas Y. Hou and Xiao-Hui Wu. A multiscale finite element method for elliptic problems in composite materials and porous media. *Journal of Computational Physics*, 134(1):169 – 189, 1997.
- [105] Thomas Y. Hou, Wu Xiao-hui, and Yu Zhang. Removing the cell resonance error in the multiscale finite element method via a petrov-galerkin formulation. 2004.
- [106] Sergio Hoyas and Javier Jiménez. Reynolds number effects on the Reynolds-stress budgets in turbulent channels. *Physics of Fluids*, 20:101511, 2008.
- [107] Thomas J.R. Hughes, Gonzalo R. Feijo, Luca Mazzei, and Jean-Baptiste Quincy. The variational multiscale methoda paradigm for computational mechanics. *Computer Methods in Applied Mechanics and Engineering*, 166(1):3 – 24, 1998. Advances in Stabilized Methods in Computational Mechanics.

- [108] Nicholas Hutchins and Ivan Marusic. Large-scale influences in near-wall turbulence. *Philosophical Transactions of the Royal Society A: Mathematical, Physical and Engineering Sciences*, 365:647–664, 2007.
- [109] Markus Hütter and Hans Christian Öttinger. Fluctuation-dissipation theorem, kinetic stochastic integral and efficient simulations. *J. Chem. Soc., Faraday Trans.*, 94:1403–1405, 1998.
- [110] W. Jäger and A. Mikelić. On the interface boundary condition of beavers, joseph, and saffman. *SIAM J. Appl. Math.*, 60(4):1111–1127, 2000.
- [111] W. Jäger and A. Mikelić. On the roughness-induced effective boundary conditions for an incompressible viscous flow. *J. Differential Equations*, 170(1):96–122, 2001.
- [112] J. Jeong, F. Hussain, W. Schoppa, and J. Kim. Coherent structures near the wall in a turbulent channel flow. *Journal of Fluid Mechanics*, 332:185–214, 1997.
- [113] De-en Jiang, Dong Meng, and Jianzhong Wu. Density functional theory for differential capacitance of planar electric double layers in ionic liquids. *Chemical Physics Letters*, 504(4-6):153–158, 2011.
- [114] V. Jikov, S. Kozlov, and O. Oleinik. *Homogenization of differential operators and integral functionals*. Springer-Verlag, 1994.

- [115] Javier Jiménez and Parviz Moin. The minimal flow unit in near-wall turbulence. *Journal of Fluid Mechanics*, 225:213–240, 1991.
- [116] Javier Jiménez and Alfredo Pinelli. The autonomous cycle of near-wall turbulence. *Journal of Fluid Mechanics*, 389:335–359, 1999.
- [117] Monchai Jitvisate and James RT Seddon. Direct measurement of the differential capacitance of solvent-free and dilute ionic liquids. *The journal of physical chemistry letters*, 9(1):126–131, 2018.
- [118] Ionnis Karatzas and Steven Shreve. *Brownian Motion and Stochastic Calculus*. Springer Verlag, 1998.
- [119] Sergey A Katsyuba, Elena E Zvereva, Ana Vidiš, and Paul J Dyson. Application of density functional theory and vibrational spectroscopy toward the rational design of ionic liquids. *The Journal of Physical Chemistry A*, 111(2):352–370, 2007.
- [120] Kyozi Kawasaki, Takao Ohta, and Mitsuharu Kohrogi. Equilibrium morphology of block copolymer melts. 2. *Macromolecules*, 21:2972–2980, 1988.
- [121] Ionannis G. Kevrekidis, C. William Gear, James M. Hyman, Panagiotis G. Kevrekidis, Olof Runborg, and Constantinos Theodoropoulos. Equation-free, coarse-grained multiscale computation: enabling microscopic simulators to perform system-level analysis. *Comm. Math. Sci.*, 1(4):715–762, 2003.

- [122] G. Khujadze and M. Oberlack. DNS and scaling laws from new symmetry groups of ZPG turbulent boundary layer flow. *Theoretical Computational Fluid Dynamics*, 18:391–411, 2004.
- [123] Mustafa Sabri Kilic, Martin Z. Bazant, and Armand Ajdari. Steric effects in the dynamics of electrolytes at large applied voltages. i. double-layer charging. *Phys. Rev. E*, 75:021502, Feb 2007.
- [124] Mustafa Sabri Kilic, Martin Z. Bazant, and Armand Ajdari. Steric effects in the dynamics of electrolytes at large applied voltages. ii. modified poisson-nernst-planck equations. *Phys. Rev. E*, 75:021503, Feb 2007.
- [125] Changho Kim, Andy Nonaka, John B. Bell, Alejandro L. Garcia, and Aleksandar Donev. Fluctuating hydrodynamics of reactive liquid mixtures. *The Journal of Chemical Physics*, 149(8):084113, 2018.
- [126] John Kim, Parviz Moin, and Robert Moser. Turbulence statistics in fully developed channel flow at low Reynolds number. *Journal of Fluid Mechanics*, 177:133–166, 1987.
- [127] V. Kitsios, A. Sekimoto, C. Atkinson, J. A. Sillero, G. Borrell, A. G. Gungor, J. Jimnez, and J. Soria. Direct numerical simulation of a self-similar adverse pressure gradient turbulent boundary layer at the verge of separation. *Journal of Fluid Mechanics*, 829:392–419, 2017.

- [128] Sergiu Klainerman and Andrew Majda. Compressible and incompressible fluids. *Communications on Pure and Applied Mathematics*, 35(5):629–651, 1982.
- [129] Yu.L. Klimontovich. Ito, stratonovich and kinetic forms of stochastic equations. *Physica A: Statistical Mechanics and its Applications*, 163(2):515 – 532, 1990.
- [130] Alexei A. Kornyshev. Double-layer in ionic liquids: paradigm change? *The Journal of Physical Chemistry B*, 111(20):5545–5557, 2007. PMID: 17469864.
- [131] Alexei A. Kornyshev and Rui Qiao. Three-dimensional double layers. *The Journal of Physical Chemistry C*, 118(32):18285–18290, 2014.
- [132] Rajamani Krishna. Diffusion in multicomponent electrolyte systems. *The Chemical Engineering Journal*, 35(1):19 – 24, 1987.
- [133] R Kubo. The fluctuation-dissipation theorem. *Reports on Progress in Physics*, 29(1):255–284, 1966.
- [134] Wai Yip Kwok, Robert D. Moser, and Javier Jimnez. A critical evaluation of the resolution properties of b-spline and compact finite difference methods. *Journal of Computational Physics*, 174(2):510 – 551, 2001.
- [135] Ugis Lācis and Shervin Bagheri. A framework for computing effective boundary conditions at the interface between free fluid and a porous medium. *Journal of Fluid Mechanics*, 812:866–889, 2017.

- [136] L. D. Landau and E. M. Lifshitz. *Fluid Mechanics, Course of Theoretical Physics, Vol. 6*. Pergamon Press, 1959.
- [137] LD Landau, EM Lifshitz, and LP Pitaevskii. Electrodynamics of continuous media, 1984. *Moscow Science*, 1992.
- [138] William Layton. *Introduction to the Numerical Analysis of Incompressible Viscous Flows*. Society for Industrial and Applied Mathematics, Philadelphia, PA, USA, 2008.
- [139] Konstantinos Lazaridis, Logan Wickham, and Nikolaos Voulgarakis. Fluctuating hydrodynamics for ionic liquids. *Physics Letters A*, 381(16):1431 – 1438, 2017.
- [140] Myoungkyu Lee, Nicholas Malaya, and Robert D. Moser. Petascale direct numerical simulation of turbulent channel flow on up to 786K cores. In *the International Conference for High Performance Computing, Networking, Storage and Analysis*, pages 1–11, New York, New York, USA, 2013. ACM Press.
- [141] Myoungkyu Lee and Robert D. Moser. Direct numerical simulation of turbulent channel flow up to $\text{Re}_\tau = 5200$. *Journal of Fluid Mechanics*, 774:395–415, June 2015.
- [142] Myoungkyu Lee and Robert D. Moser. Large-scale Motions in Turbulent Poiseuille & Couette flows. In *Tenth International Symposium*

on Turbulence and Shear Flow Phenomena, Chicago, Illinois, USA, July 2017.

- [143] Myoungkyu Lee and Robert D. Moser. Spectral analysis of the budget equation in turbulent channel flows at high reynolds number. *Journal of Fluid Mechanics*, 860:886–938, 2019.
- [144] Myoungkyu Lee, Rhys Ulerich, Nicholas Malaya, and Robert D. Moser. Experiences from Leadership Computing in Simulations of Turbulent Fluid Flows. *Computing in Science Engineering*, 16(5):24–31, September 2014.
- [145] Andrzej Lewandowski and Agnieszka widerska Mocek. Ionic liquids as electrolytes for li-ion batteriesan overview of electrochemical studies. *Journal of Power Sources*, 194(2):601 – 609, 2009.
- [146] Qinghua Li, Qunwei Tang, Benlin He, and Peizhi Yang. Full-ionic liquid gel electrolytes: Enhanced photovoltaic performances in dye-sensitized solar cells. *Journal of Power Sources*, 264:83 – 91, 2014.
- [147] David T. Limmer. Interfacial ordering and accompanying divergent capacitance at ionic liquid-metal interfaces. *Phys. Rev. Lett.*, 115:256102, Dec 2015.
- [148] Zhiping Liu, Shiping Huang, and Wenchuan Wang. A refined force field for molecular simulation of imidazolium-based ionic liquids. *The Journal of Physical Chemistry B*, 108(34):12978–12989, 2004.

- [149] Anders Logg, Kent-Andre Mardal, Garth N. Wells, et al. *Automated Solution of Differential Equations by the Finite Element Method*. Springer, 2012.
- [150] Anders Logg, Garth N. Wells, and Johan Hake. *DOLFIN: a C++/Python Finite Element Library*, chapter 10. Springer, 2012.
- [151] J. Lowengrub and L. Truskinovsky. Quasiincompressible CahnHilliard fluids and topological transitions. *Proceedings of the Royal Society, A*, 454:2617–2654, 1998.
- [152] Edward J Maginn. Atomistic simulation of the thermodynamic and transport properties of ionic liquids. *Accounts of chemical research*, 40(11):1200–1207, 2007.
- [153] A.J. Majda. Multiscale models with moisture and systematic strategies for superparameterization. *J. Atmos. Sci.*, 64(7):2726–2734, 2007.
- [154] A.J. Majda and M.J. Grote. Mathematical test models for superparameterization in anisotropic turbulence. *PNAS*, 106(14):5470–5474, 2009.
- [155] Andrew Majda and James Sethian. The derivation and numerical solution of the equations for zero mach number combustion. *Combustion Science and Technology*, 42(3-4):185–205, 1985.
- [156] Andrew J. Majda and Ian Grooms. New perspectives on superparameterization for geophysical turbulence. *Journal of Computational Physics*, 271:60 – 77, 2014. Frontiers in Computational Physics.

- [157] M. Mareschal, M. Malek Mansour, G. Sonnino, and E. Kestemont. Dynamic structure factor in a nonequilibrium fluid: A molecular-dynamics approach. *Phys. Rev. A*, 45:7180–7183, May 1992.
- [158] Ivan Marusic, Romain Mathis, and Nicholas Hutchins. High Reynolds number effects in wall turbulence. *International Journal of Heat and Fluid Flow*, 31(3):418–428, June 2010.
- [159] Romain Mathis, Nicholas Hutchins, and Ivan Marusic. A predictive inner–outer model for streamwise turbulence statistics in wall-bounded flows. *Journal of Fluid Mechanics*, 681:537–566, 2011.
- [160] Cline Merlet, David T. Limmer, Mathieu Salanne, Ren van Roij, Paul A. Madden, David Chandler, and Benjamin Rotenberg. The electric double layer has a life of its own. *The Journal of Physical Chemistry C*, 118(32):18291–18298, 2014.
- [161] Andro Mikelić. Rough boundaries and wall laws. *unpublished notes*, 2009.
- [162] Clark B. Millikan. A critical discussion of turbulent flows in channels and circular tubes. In *Proceedings of the fifth International Congress for Applied Mechanics*, pages 386–392, 1938.
- [163] Yoshinori Mizuno. Spectra of turbulent energy transport in channel flows. In *15th European Turbulence Conference*, Delft, The Netherlands, 2015.

- [164] Yoshinori Mizuno. Spectra of energy transport in turbulent channel flows for moderate Reynolds numbers. *Journal of Fluid Mechanics*, 805:171–187, September 2016.
- [165] Yoshinori Mizuno and Javier Jiménez. Wall turbulence without walls. *Journal of Fluid Mechanics*, 723:429–455, 2013.
- [166] Valeria Molinero and Emily B Moore. Water modeled as an intermediate element between carbon and silicon. *The Journal of Physical Chemistry B*, 113(13):4008–4016, 2009.
- [167] Timothy I. Morrow and Edward J. Maginn. Molecular dynamics study of the ionic liquid 1-n-butyl-3-methylimidazolium hexafluorophosphate. *The Journal of Physical Chemistry B*, 106(49):12807–12813, 2002.
- [168] Michael Moseler and Uzi Landman. Formation, stability, and breakup of nanojets. *Science*, 289(5482):1165–1169, 2000.
- [169] Andrew Nonaka, Yifei Sun, John Bell, and Aleksandar Donev. Low mach number fluctuating hydrodynamics of binary liquid mixtures. *Communications in Applied Mathematics and Computational Science*, 10(2):163–204, 2015.
- [170] Takao Ohta and Kyozi Kawasaki. Equilibrium morphology of block copolymer melts. *Macromolecules*, 19(10):2621–2632, 1986.

- [171] Todd A. Oliver, Nicholas Malaya, Rhys Ulerich, and Robert D. Moser. Estimating uncertainties in statistics computed from direct numerical simulation. *Physics of Fluids*, 26:035101, March 2014.
- [172] L. Onsager and R.M Fuoss. Irreversible processes in electrolytes. diffusion, conductance and viscous flow in arbitrary mixtures of strong electrolytes. *J. Phys. Chem.*, 1932:2689, 1932.
- [173] Lars Onsager and Shoon Kyung Kim. The relaxation effects in mixed strong electrolytes. *The Journal of Physical Chemistry*, 61(2):215–229, 1957.
- [174] Ge-Bo Pan and Werner Freyland. 2d phase transition of pf6 adlayers at the electrified ionic liquid/au(111) interface. *Chemical Physics Letters*, 427(1):96 – 100, 2006.
- [175] Andrea Pascarelli, Ugo Piomelli, and Graham V. Candler. Multi-block large-eddy simulations of turbulent boundary layers. *Journal of Computational Physics*, 157(1):256–279, 2000.
- [176] Clarisse Péan, Céline Merlet, Benjamin Rotenberg, Paul Anthony Madden, Pierre-Louis Taberna, Barbara Daffos, Mathieu Salanne, and Patrice Simon. On the dynamics of charging in nanoporous carbon-based supercapacitors. *ACS nano*, 8(2):1576–1583, 2014.
- [177] Joseph Pedlosky. *Geophysical Fluid Dynamics*. Springer-Verlag New York, 1987.

- [178] Jean-Philippe Péraud, Andrew J Nonaka, John B Bell, Aleksandar Donev, and Alejandro L Garcia. Fluctuation-enhanced electric conductivity in electrolyte solutions. *Proceedings of the National Academy of Sciences*, 114(41):10829–10833, 2017.
- [179] Jean-Philippe Péraud, Andy Nonaka, Anuj Chaudhri, John B. Bell, Aleksandar Donev, and Alejandro L. Garcia. Low mach number fluctuating hydrodynamics for electrolytes. *Phys. Rev. Fluids*, 1:074103, Nov 2016.
- [180] Charles S Peskin. The immersed boundary method. *Acta numerica*, 11:479–517, 2002.
- [181] Ugo Piomelli and Elias Balaras. Wall-layer models for large-eddy simulations. *Annual Review of Fluid Mechanics*, 34(1):349–374, 2002.
- [182] Stephen B. Pope. *Turbulent Flows*. Cambridge University Press, 2000.
- [183] A. Quarteroni and L. Stolcis. Homogeneous and heterogeneous domain decomposition for compressible fluid flows at high reynolds numbers. *Numerical Methods for Fluid Dynamics*, 5:113–128, 1995.
- [184] Nav Nidhi Rajput, Joshua Monk, and Francisco R Hung. Structure and dynamics of an ionic liquid confined inside a charged slit graphitic nanopore. *The Journal of Physical Chemistry C*, 116(27):14504–14513, 2012.

- [185] S G Raju and S Balasubramanian. Intermolecular correlations in an ionic liquid under shear. *Journal of Physics: Condensed Matter*, 21(3):035105, dec 2008.
- [186] W. Ren and W. E. Heterogeneous multiscale method for the modeling of complex fluids and microfluidics. *J. Comput. Phys.*, 204(1):1–26, 2005.
- [187] O. Reynolds. On the Dynamical Theory of Incompressible Viscous Fluids and the Determination of the Criterion. *Philosophical Transactions of the Royal Society of London Series A*, 186:123–164, 1895.
- [188] David H. Richter. Turbulence modification by inertial particles and its influence on the spectral energy budget in planar Couette flow. *Physics of Fluids*, 27(6):063304, June 2015.
- [189] R. A. Robinson and R. H. Stokes. *Electrolyte Solutions: Second Revised Edition*. Dover Books on Chemistry Series. Dover Publications, Incorporated, 2012.
- [190] P. Sagaut, S. Deck, and M. Terracol. *Multiscale and Multiresolution Approaches in Turbulence*. Imperial College Press, 2006.
- [191] Pierre Sagaut. *Large Eddy Simulation for Incompressible Flows: An Introduction*. Springer, 3rd edition edition, 2005.
- [192] Rick Salmon. Hamiltonian fluid mechanics. *Annual review of fluid mechanics*, 20(1):225–256, 1988.

- [193] M. Samie, I. Marusic, N. Hutchins, M. K. Fu, Y. Fan, M. Hultmark, and A. J. Smits. Fully resolved measurements of turbulent boundary layer flows up to $Re_\tau = 20\,000$. *Journal of Fluid Mechanics*, 851:391–415, 2018.
- [194] Neil D. Sandham, Roderick Johnstone, and Christian T. Jacobs. Surface-sampled simulations of turbulent flow at high reynolds number. *International Journal for Numerical Methods in Fluids*, 85(9):525–537, 2017.
- [195] Joshua R Sangoro and Friedrich Kremer. Charge transport and glassy dynamics in ionic liquids. *Accounts of chemical research*, 45(4):525–532, 2012.
- [196] Ory Schnitzer and Ehud Yariv. Induced-charge electro-osmosis beyond weak fields. *Physical review. E*, 86, 12 2012.
- [197] Ory Schnitzer and Ehud Yariv. Macroscale description of electrokinetic flows at large zeta potentials: Nonlinear surface conduction. *Phys. Rev. E*, 86, 2012.
- [198] Barry Z Shang, Nikolaos K Voulgarakis, and Jhih-Wei Chu. Fluctuating hydrodynamics for multiscale simulation of inhomogeneous fluids: Mapping all-atom molecular dynamics to capillary waves. *The Journal of chemical physics*, 135(4):044111, 2011.
- [199] Juan A. Sillero, Javier Jimnez, and Robert D. Moser. One-point statistics for turbulent wall-bounded flows at Reynolds numbers up to $\delta^+ \approx$

2000. *Physics of Fluids*, 25(10):105102, 2013.
- [200] D. Silvester and R. Compton. Electrochemistry in room temperature ionic liquids: A review and some possible applications. *Zeitschrift für Physikalische Chemie*, 220:1247–1274, 2009.
- [201] Mark P. Simens, Javier Jimnez, Sergio Hoyas, and Yoshinori Mizuno. A high-resolution code for turbulent boundary layers. *Journal of Computational Physics*, 228(11):4218 – 4231, 2009.
- [202] Anthony E. Somers, Patrick C. Howlett, Douglas R. MacFarlane, and Maria Forsyth. A review of ionic liquid lubricants. *Lubricants*, 1(1):3–21, 2013.
- [203] Philippe R. Spalart. Direct simulation of a turbulent boundary layer up to $Re_\theta = 1410$. *Journal of Fluid Mechanics*, 187:61–98, 1988.
- [204] Philippe R. Spalart, Robert D. Moser, and Michael M. Rogers. Spectral Methods for the Navier-Stokes Equations with One Infinite and Two Periodic Directions. *Journal of Computational Physics*, 96:297–324, 1991.
- [205] Todd M. Squires. Induced-charge electrokinetics: fundamental challenges and opportunities. *Lab on a Chip*, 9:2477–2483, 2009.
- [206] Todd M. Squires and Martin Z. Bazant. Induced-charge electro-osmosis. *Journal of Fluid Mechanics*, 509:217–252, 2004.

- [207] Alexander Stoppa, Richard Buchner, and Glenn Hefter. How ideal are binary mixtures of room-temperature ionic liquids? *Journal of Molecular Liquids*, 153(1):46 – 51, 2010.
- [208] Yu-Zhuan Su, Yong-Chun Fu, Jia-Wei Yan, Zhao-Bin Chen, and Bing-Wei Mao. Double layer of au(100)/ionic liquid interface and its stability in imidazolium-based ionic liquids. *Angewandte Chemie International Edition*, 48(28):5148–5151, 2009.
- [209] E. B. Tadmor, M. Ortiz, and R. Phillips. Quasicontinuum analysis of defects in solids. *Philosophical Magazine A*, 73(6):1529–1563, 1996.
- [210] Yifeng Tang and Rayhaneh Akhavan. Computations of equilibrium and non-equilibrium turbulent channel flows using a nested-les approach. *Journal of Fluid Mechanics*, 793:709748, 2016.
- [211] Luong Duy Thahn and Rudolf Sprik. Zeta potential measurement using electroosmosis in porous media. *VNU Journal of Science: Natural Sciences and Technology*, 31(4), 2015.
- [212] Hiroyuki Tokuda, Seiji Tsuzuki, Md. Abu Bin Hasan Susan, Kikuko Hayamizu, and Masayoshi Watanabe. How ionic are room-temperature ionic liquids? an indicator of the physicochemical properties. *The Journal of Physical Chemistry B*, 110(39):19593–19600, 2006.
- [213] Hiroyuki Tokuda, Seiji Tsuzuki, Md. Abu Bin Hasan Susan, Kikuko Hayamizu, and Masayoshi Watanabe. How ionic are room-temperature

- ionic liquids? an indicator of the physicochemical properties. *The Journal of Physical Chemistry B*, 110(39):19593–19600, 2006.
- [214] A. A. Townsend. *The Structure of Turbulent Shear Flow*. Cambridge University Press, 2nd edition edition, 1976.
- [215] Alessandro Triolo, Andrea Mandanici, Olga Russina, Virginia Rodriguez-Mora, Maria Cutroni, Christopher Hardacre, Mark Nieuwenhuyzen, Hans-Jurgen Bleif, Lukas Keller, and Miguel Angel Ramos. Thermodynamics, structure, and dynamics in room temperature ionic liquids: the case of 1-butyl-3-methyl imidazolium hexafluorophosphate ([bmim][pf6]). *The Journal of Physical Chemistry B*, 110(42):21357–21364, 2006.
- [216] Alessandro Triolo, Olga Russina, Hans-Jurgen Bleif, and Emanuela Di Cola. Nanoscale segregation in room temperature ionic liquids. *The Journal of Physical Chemistry B*, 111(18):4641–4644, 2007.
- [217] A. Vailati and M. Giglio. Giant fluctuations in a free diffusion process. *Nature*, 390:262–265, 1997.
- [218] A. Vailati and M. Giglio. Nonequilibrium fluctuations in time-dependent diffusion processes. *Phys. Rev. E*, 58:4361–4371, 1998.
- [219] John D. Weeks, David Chandler, and Hans C. Andersen. Role of repulsive forces in determining the equilibrium structure of simple liquids. *The Journal of Chemical Physics*, 54(12):5237–5247, 1971.

- [220] Rui Wen, Bjrn Rahn, and Olaf M. Magnussen. Potential-dependent adlayer structure and dynamics at the ionic liquid/au(111) interface: A molecular-scale *in situ* video-stm study. *Angewandte Chemie International Edition*, 54(20):6062–6066, 2015.
- [221] Sarah Williams, John Bell, and Alejandro Garcia. Algorithm refinement for fluctuating hydrodynamics. *Multiscale Model. Simul.*, 6:1256–1280, 2008.
- [222] James Wishart. Energy applications of ionic liquids. *Royal Society of Chemistry*, 2:956–961, 2009.
- [223] Xiaohua Wu and Parviz Moin. Direct numerical simulation of turbulence in a nominally zero-pressure-gradient flat-plate boundary layer. *Journal of Fluid Mechanics*, 630:5–41, 2009.
- [224] G. Yalla, T. Oliver, S. Haering, B. Engquist, and R. Moser. On the effects of resolution inhomogeneity in les. *arXiv e-prints*, page 2003.02355, 2020.
- [225] Xin Yong and Lucy T. Zhang. Thermostats and thermostat strategies for molecular dynamics simulations of nanofluidics. *The Journal of Chemical Physics*, 138(8):084503, 2013.
- [226] Xingye Yue and Weinan E. The local microscale problem in the multiscale modeling of strongly heterogeneous media: Effects of boundary

- conditions and cell size. *Journal of Computational Physics*, (222):556–572, 2006.
- [227] Weiqun Zhang, Ann Almgren, Vince Beckner, John Bell, Johannes Blaschke, Cy Chan, Marcus Day, Brian Friesen, Kevin Gott, Daniel Graves, et al. Amrex: a framework for block-structured adaptive mesh refinement. *Journal of Open Source Software*, 4(37), 2019.
- [228] Hongbo Zhao, Brian D. Storey, Richard D. Braatz, and Martin Z. Bazant. Learning the physics of pattern formation from images. *Phys. Rev. Lett.*, 124:060201, Feb 2020.
- [229] Feng Zhou, Yongmin Liang, and Weimin Liu. Ionic liquid lubricants: designed chemistry for engineering applications. *Royal Society of Chemistry*, 38:2590–2599, 2009.